I: DYNAMICS OF FLOWING POLYMER SOLUTIONS

II: THE MEASUREMENT OF VELOCITY GRADIENTS BY HOMODYNE LIGHT SCATTERING SPECTROSCOPY

Thesis by

Gerald Gendall Fuller

In Partial Fulfillment of the Requirements

for the Degree of

Doctor of Philosophy

California Institute of Technology

Pasadena, California

1980

(Submitted January 30, 1980)

dedicated to

my family

ACKNOWLEDGEMENT

I wish to thank my advisor, Professor L. G. Leal, for his guidance and his support and for his personal interest in my career development. I have benefitted a great deal through the association with him and his research group. Professor C. J. Pings has participated in this research program as a co- investigator and I thank him fo his efforts and for the use of his laboratory.

Throughout the course of this work, I have been supported by a National Research Council of Canada Postgraduate Scholarship for which I am truly grateful. I also wish to thank Caltech for several Institute Tuition Scholarships and the Office of Naval Research for support of the research program.

Caltech has offered an exceptional atmosphere for research through its fine staff and facilities. In particular, I must thank Messrs. Hollis Reamer, George Griffith, Chic Nakawatase, and John Yehle. Their practical insights and fine craftsmanship contributed greatly.

There are a great many friends, too numerous to list individually, who have helped to make the years spent at

Caltech a rewarding experience. In particular, however, I want to thank Mr. Lance O'Steen for his sense of humor and for acting as a sounding board for many ideas and frustrations. I also benefitted from Drs Claude Cohen, Ray Schmidt and John Rallison through many discussions and by their example.

The opportunity to achieve this goal in my life has come from my parents to whom I sincerely express my love and my gratitude. Their sacrifice and encouragement have been a prime source of inspiration and motivation. I wish to thank my entire family for their support and love. Most importantly, I thank my wife Darci for making my life a happy one.

Abstract

This thesis is presented in two parts. In the first part the results of flow birefringence experiments and modelling efforts on both concentrated and dilute polymer solutions are discussed. The second part presents theoretical developments and complementary experiments which demonstrate the utility of the technique of homodyne light scattering spectroscopy to the measurement of velocity gradients in laminar flow fields.

The flow birefringence experiments were performed using a four roll mill which was designed in order to allow the simulation of a wide range of two dimensional flows ranging from purely extensional flows to purely rotational flows. Flow visualization and homodyne light scattering spectroscopy experiments were used to characterize the flow fields.

Using this device the flow birefringence of concentrated polyethylene/water and polystyrene/tricresyl phosphate solutions was measured. Birefringence measurements of the Polyox solutions over a wide range of flow types indicated that the birefringence could be well correlated against the eigenvalue of the velocity gradient

tensor, in agreement with model calculations. Transient experiments were performed in which the birefringence was measured as purely extensional flows were started from rest. Both polymer/solvent systems showed a pronounced overshoot in the birefringence. Turbidity measurements were also performed on the polyox solutions and a 30% increase in the turbidity was measured which persisted for many hours after the cessation of flow (whereas the birefringence decayed to zero in a fraction of a second). This increased turbidity and its persistence with time suggests the occurence of flow induced crystallization of the polymer.

These experiments involving concentrated polymer systems were compared to model calculations using the Yamamoto network theory. Several choices of the polymer entanglements creation and destruction functions were analyzed and it is demonstrated that analytical results can be obtained using these choices. A variety of nonlinear phenomena can be predicted including the correlation of the birefringence with the eigenvalue of the velocity gradient tensor and the overshoot of birefringence for the start up of purely extensional flows. The predicted response of the stress tensor is also presented and discussed.

Flow birefringence experiments were also carried out in

the dilute concentration range. Measurements were taken on three molecular weight samples ($2\text{-}8\times10^6$ MW, $M_w/M_N=1.14\text{-}1.3$) in a viscous polychlorinated biphenyl solvent in the range of 50-100 ppm subjected to a wide range of two dimensional flows. The birefringence was again found to be well correlated against the eigenvalue of the velocity gradient tensor. The normalized birefringence, corrected for concentration, $(\Delta n/nc)$, was observed to approach a saturation value at high velocity gradients in purely extensional flow. This saturation value was independent of both the molecular weight and the concentration c, in agreement with theory. In addition, the magnitude of the saturation value is consistent with nearly fully extended chains and suggests extensions in the range of 20-50 times the rest state size. The experiments were complemented by simple dumbbell model calculations which incorporated the nonlinear spring, internal viscosity and variable hydrodynamic friction. The model was found to simulate the experimental data very well if the effects of molecular weight distribution and finite transit times in the flow were taken into account.

The results of a detailed investigation of the dumbbell model used to analyze the dilute solution experiments is also included. The effects of the nonlinear spring, variable

friction factor and internal viscosity to the response of the dumbbell to steady state and transient two dimensional flows are exposed. A perturbation solution for the dumbbell with a small amount of internal viscosity is presented and it is demonstrated that this problem can be solved analytically.

The technique of homodyne light scattering spectroscopy applied to suspensions in laminar flow is investigated. It is demonstrated both theoretically and experimentally that use of this method allows direct measurement of velocity gradients without the need for differentiating velocity data which is the normal method used. This technique was used to characterize the spatial distribution of velocity gradients existing in the four roll mill simulating purely extensional flow.

TABLE OF CONTENTS

Table of Contents (Continued)

Table of Contents (Continued)

I: DYNAMICS OF FLOWING POLYMER SOLUTIONS

Flow Birefringence of Concentrated Polymer Solutions in Two-Dimensional Flows

by

G. G. Fuller and L. G. Leal

Department of Chemical Engineering
California Institute of Technology
Pasadena, California 91125

Abstract

The results of flow birefringence measurements of polymer solutions of moderate concentration subjected to a wide range of two dimensional flows generated by a four roll mill are reported. The flows generated in the flow device were characterized and it is demonstrated that use of the four roll mill enables one to systematically vary the ratio of the vorticity to the rate of strain in the flow while holding the velocity gradient constant. Steady state flow birefringence data collected over a wide range of flow types showed that the birefringence can be correlated against the eigenvalue of the velocity gradient tensor in agreement with the criterion for strong and weak flows from model calculations (Tanner (1976), Olbricht et al (1980)). Transient birefringence measurements in which purely extensional flows were started from rest are also reported. It was observed that the birefringence went through a pronounced overshoot in time for two different polymer/solvent systems. Flow induced increases in the solution turbidity were also observed and the increased turbidity remained constant over a period of many hours after extensional flows were arrested. The birefringence, on the other hand, decayed to zero almost immediately after the flows were stopped. These changes in the turbidity

suggest that crystallization of the polymer was occurring.

The qualitative results of the experiments are compared to recent network model calculations (Fuller and Leal (1980a)) using the theory of Yamamoto (1956, 1957) for concentrated polymer systems. It is found that this model can predict qualitatively many of the experimental observations if the function describing the breakage of polymer chain entanglements is allowed to depend on the conformation of the polymer segments bridging the entanglements. In particular, this dependency of the entanglement breakage on the conformation of the network segments allows the overshoot of birefringence when purely extensional flows are started from rest to be predicted. It is also demonstrated through this model that birefringence data taken over a wide range of flow types can be used to estimate the degree to which the network deforms affinely with the flow field.

I. Introduction

Non-Newtonian flow properties of polymer solutions or melts are a consequence of flow-induced changes in the statistical conformation of the polymer molecules. One approach to the development of a constitutive equation to describe these non-Newtonian properties is therefore to first understand and model the macromolecular conformation changes and then pass to a macroscopic description of the solution or melt via an appropriate averaging process. This procedure, which is known as the "kinetic theory" approach to theoretical rheology, has recently been reviewed in some detail by Bird et. al. (1977).

The present paper is concerned with the use of flow birefringence to determine the response of macromolecular conformation to an imposed flow for moderately concentrated polymer solutions that are subjected to a wide variety of two-dimensional shearing flows. In this concentration range, the polymer molecules interact directly with each other, and these direct interactions are usually described via the so-called temporary entanglement network picture in which the molecules are viewed as being connected at a number of junction points that are continuously created and destroyed. The polymer segments which bridge these

junctions are assumed to respond as linear, elastic springs with equilibrium length proportional to the square root of the number of subunits N making up the segment. Following the original work of Yamamoto (1956), many models of this general type have been proposed which differ primarily in the forms assumed for the functions that describe the rate of creation and destruction of the segments, and in the presence or absence of affine deformation of the network relative to the deformation of the solution (or melt) as a whole. In spite of the relatively advanced and sophisticated appearance of these models, however, relatively little is known of the predicted response of the network structure to the action of an imposed bulk flow. Solutions for the probability distribution function describing the state of the network have not generally been obtained, except for the cases of simple, linear shear flow and, in some instances a uniaxial extensional flow. Furthermore, it must always be recognized that the network models are truly models, and therefore bear an essentially unknown relationship to real macromolecular solutions or melts. Recently, we have obtained theoretical predictions for the segment probability distribution function for several of the more commonly used network models and from this, predictions of the bulk birefringence and rheological behavior for general two-dimensional flows. The primary

motivation for the present study, as well as continuing research in this area, is to develop a data base for the behavior of real polymers in a flowing solution which can be used to test the validity of the many network models that have been proposed.

Previous applications of flow birefingence for measurement for macromolecular conformation in a flowing solution or melt have almost exclusively considered either a simple shear flow or a purely extensional flow (Tsvetkov et al. (1964), Crowley et al. (1976), and Pope and Keller (1977)). One notable exception to this is the work of Frank and Mackley (1976) who studied flow birefringence in flows generated by two co-rotating rollers. This work is important because the ratio of vorticity to strain rate, which determines the type of flow, is between the two cases of simple shear flow and purely extensional flow. However, both the magnitude of the velocity gradient and the flow type are dependent on the separation of the two rollers and can therefore not be varied independently in a convenient way. The results of these previous investigations clearly point out the importance of flow type in determining the effectiveness of a flow field in deforming the polymer chains.

Theoretical studies of the role of flow type in the deformation process indicate that simple shear and purely extensional flows are two limiting cases for the class of two dimensional motions which we shall consider here. Purely extensional flow, also known as hyperbolic flow in the two-dimensional case, represents the strongest type of flow insofar as polymer deformation is concerned, for a given velocity gradient. In a simple shear flow, on the other hand, the magnitude of the vorticity and the rate of strain are equal, and we thus have a neutral case lying at the boundary between "weak" flows which contain a greater amount of vorticity and cannot induce significant macromolecular deformation, and "strong" flows with less vorticity that can produce a large degree of macromolecular deformation if the velocity gradient is large enough. It is important, therefore, that the response of real polymer solutions to a wide variety of flow types be understood, and it is to this end that the present study has been directed.

We have constructed a four roll mill which can simulate a wide range of two dimensional flows in which the ratio of vorticity to the rate of strain can be systematically varied at a given velocity gradient. These flow types have been well characterized for a Newtonian fluid and for concentrated polyethylene oxide solutions. Flow

birefringence has then been used to measure the degree of macromolecular deformation and orientation in concentrated polymer solutions and it is shown that data taken over a range of flow types (including both steady and unsteady flows) can be interpreted in terms of molecular characteristics which distinguishes between certain features of the network models.

II. Theoretical Developments

We are concerned in this paper with conformational features of flowing polymer solutions in the range of moderate concentrations where there are direct interactions between the polymer molecules. As indicated in the preceding sections these interactions are modelled via the so-called entanglement network concept in which the molecules are viewed as being temporarily connected at a number of junction points that are constantly being created and destroyed. Between the network junctions are polymer segments, modelled as linear, elastic springs connecting the two junctions, with an equilibrium length proportional to the square root of the number of subunits in the segment. We have recently investigated the response of the network to a variety of two-dimensional bulk flows for several different variations of the basic network theory of

Yamamoto (1956), and it is convenient to summarize the theoretical calculations in order to facilitate comparison between the predictions from these models and the experimental birefringence data which we will present later in this paper.

In the basic theory of Yamamoto, the state of the network is described through a probability distribution function $f(\underline{x},N,t)$ such that fd^3x represents the number of segments with end to end vector $\underline{x}$ which are composed of N subunits at a time t. The conservation equation for f is then

$$\frac{\partial f}{\partial t} + \nabla(\dot{\underline{x}}f) = G(x,N) - \beta(\underline{x})f \qquad (1)$$

where $\dot{\underline{x}}$ is the rate of change of the end to end segment vector, G is the distribution function describing the rate of creation of the segments and β is the rate of destruction of the segments. Network models of this general form have been proposed by many authors (Lodge (1956), Wiegel (1969), Phan-Thien and Tanner (1977)). These models differ mainly in the forms assumed for the junction creation and destruction functions, G and β, as we shall shortly discuss in some detail. However, an additional difference is the nature of the network deformation that is assumed

when the bulk motion of the solution as a whole is given by

$$\underline{u} = \underline{\underline{\Gamma}} \cdot \underline{r}$$

where $\underline{\underline{\Gamma}}$ is the velocity gradient tensor and $\underline{r}$ a position vector. All of the older network models assumed that the network deformation was "affine" with the deformation of the solutions as a whole, so that

$$\dot{\underline{x}} = \underline{\underline{\Gamma}} \cdot \underline{x} \tag{2a}$$

More recently, however, Phan-Thien and Tanner (1977) and Johnson and Segalman (1977) have independently suggested that this affine deformation assumption should be relaxed. In the most plausible formulation, it is assumed that

$$\dot{\underline{x}} = (\underline{\underline{\Gamma}} - \xi \underline{\underline{D}}) \cdot \underline{x} \tag{2b}$$

where $\underline{\underline{D}}$ is the bulk rate of strain tensor, $(\underline{\underline{\Gamma}} + \underline{\underline{\Gamma}}^{+})/2$ and ξ is the so-called slip coefficient. The motivation for inclusion of a non-affine deformation of this form probably originated with the description of an anisotropic fluid by Ericksen (1960), and has subsequently appeared in almost all modern theories of dilute suspensions and solutions. The effect this slip mechanism is that the velocity gradient tensor is replaced by an "effective" velocity gradient

tensor $\hat{\underline{\underline{\Gamma}}}=(\underline{\underline{\Gamma}} - \xi\underline{\underline{D}})$.

Equation (1), with either equation (2a) or (2b), can be solved for any reasonable choice of G and β using the method of characteristics. In a recent investigation, Fuller and Leal (1980), we have obtained solutions for four specific combinations of G and β, including both the affine and non-affine network deformation assumption. The different models considered are outlined in table 1, and can be seen to include what we shall call the constant destruction model, the quadratic law model, the square well model and, finally, a model which only differs from Phan-Thien and Tanner's model in the fact that they used a pre-averaged form for β, i.e. $\beta = \beta_o(1.+ \sigma\langle r^2\rangle)$ and replaced $\langle\underline{r}^2\rangle$ by $3NkT(\text{tr}\ \underline{\underline{\tau}})$ where $\underline{\underline{\tau}}$ is the stress tensor and kT is the Boltzmann temperature.

The parameters appearing in table 1 are defined as follows:

> $\underline{x}$-the segmental end to end vector which has been made nondimensional with respect to the maximum end to end distance of a segment, Na (where a is the length scale of a segment subunit)

σ -the square of the ratio of the maximum end to end distance of a segment to the length scale over which the function β changes. (σ is assumed to be in the range $N >> \sigma >> 1$)

β_o, L -the rate of junction destruction and creation respectively (units of inverse time)

R- the length of segments (nondimensionalized by Na) above which the probability of breakage is unity in the square well model

All of the models which we have analyzed have used the Gaussian assumption (Lodge (1968) , Schowalter (1978)) for the creation function G and, with the exception of the Phan-Thien and Tanner model, have also assumed that the rate of creation L is constant.

The simplest choice for β is the constant destruction model in which the junctions leave the network at a constant rate, independent of the conformation of the segments. This model can be shown to be equivalent to the Lodge network model with a single relaxation time (Lodge (1968)) and it was pointed out by Yamamoto (1957) that this choice for β has serious shortcomings (shear rate independent viscosity

and a zero second normal stress difference). In order to improve upon the predictive power of the model, Yamamoto proposed the square well model in which the destruction function becomes infinite whenever the end to end distance of a segment is greater than R, forcing such segments to leave the network. Yamamoto demonstrated that this choice for β leads to a shear thinning viscosity although he did not arrive at completely analytical results. In the same spirit, Phan-Thien and Tanner have taken the quadratic form for β where the destruction function is assumed to be proportional to r^2. They also made an additional preaveraging assumption and replaced r^2 by $\langle r^2 \rangle$ and showed that a variety of nonlinear phenomena can be described by the resulting model.

Following specification of G and β, macroscopic properties of the network can be determined. The velocity gradient tensor which we have considered is

$$\underline{\underline{\Gamma}} = \frac{\gamma}{2} \begin{pmatrix} (1+\lambda) & (1-\lambda) & 0 \\ -(1-\lambda) & -(1+\lambda) & 0 \\ 0 & 0 & 0 \end{pmatrix} \tag{3}$$

which, as will be demonstrated later can be simulated by the four roll mill used in the experiments. The parameter γ is

the magnitude of the local velocity gradient and λ is a parameter which describes the type of flow. If λ is 1 the flow is purely extensional and when λ is -1 the flow is purely rotational. As λ varies between these two limits, the flow is a linear superposition of pure extension and pure rotation with simple shear flow being simulated at λ equal to zero. The ratio of the vorticity to the rate of strain in the flow field is $w=(1-\lambda)/(1+\lambda)$. The "effective" velocity gradient tensor acting on the network when the slip mechanism is considered is

$$\underline{\underline{E}} = \frac{\gamma}{2}\begin{pmatrix} (1-\xi)(1+\lambda) & (1-\lambda) & 0 \\ -(1-\lambda) & -(1-\xi)(1+\lambda) & 0 \\ 0 & 0 & 0 \end{pmatrix} \qquad (4)$$

which produces an "effective" ratio of vorticity to the rate of strain equal to $(1-\lambda)/(1-\xi)(1+\lambda)$.

The problem solved in Fuller and Leal (1980) was the time dependent start up of the flow field, equation (3) from rest at t=0. From equation (1) it is clear that the initial probability distribution function for this situation is

$$f_o(x_1 y_1 z) = G(x_1 y_1 z_i N)/\beta(x_1 y_1 z)$$

A detailed account of the solution of equation (1) for all of the models described in table 1 can be found in

Fuller and Leal (1980) which presents the predictions for the stress tensor and birefringence of the deformed network. These macroscopic quantities are related to the moments of the distribution function $\langle x^2 \rangle$, $\langle y^2 \rangle$, $\langle xy \rangle$ and $\langle z^2 \rangle$. In addition the average $n=\langle 1 \rangle$ can also be calculated which is interpreted as the concentration of segments remaining in the network at any given time.

The birefringence from the segments making up the network can be derived in a manner directly analogous to that used for the dilute solution dumbbell model, in which the birefringence is calculated from the average polarizibility tensor of the segments. When the network is distorted in a two dimensional flow, this tensor becomes

$$\underline{\underline{\mu}} = \begin{pmatrix} \mu_{xx} & \mu_{xy} & 0 \\ \mu_{xy} & \mu_{yy} & 0 \\ 0 & 0 & \mu_{zz} \end{pmatrix} \tag{5}$$

Since the birefringence Δn is proportional to the difference in the major axes of the refractive index tensor, the birefringence will be proportional to the average of the difference in the eigenvalues of this tensor, i. e.

$$\Delta n = \Delta \left\langle (\mu_{xx} - \mu_{yy})^2 + 4\mu_{xy}^2 \right\rangle^{\frac{1}{2}} \tag{6}$$

where A is a constant of proportionality which depends on the solution properties. Following Kuhn and Grun (1942), the polarizability of a segment is related to the end to end distance by

$$\mu_{\|} = p + 2q(x^2 + y^2 + z^2)$$

$$\mu_{\perp} = p - q(x^2 + y^2 + z^2) \tag{8}$$

where $\mu_{\|}$ is the polarizibility parallel to x and $\mu_{\perp}$ is the polarizibility normal to $\underline{x}$. The constants p and q are independent of $\underline{x}$ and depend on the polarizibility of monomer units making up the chain. Using the relationship in equation (7), the birefringence is seen to be following function of the moments of the segments

$$\Delta n = B\left\{\left(\langle x^2\rangle - \langle y^2\rangle\right)^2 + 4\langle xy\rangle^2\right\}^{\frac{1}{2}} \tag{9}$$

where B is a constant of proportionality. In using this relation we are neglecting the contribution of form birefringence which should be a good approximation for concentrated systems (Peterlin (1976)).

A summary of the qualitative results for the four models is shown in table 2. It is interesting to note that

for constant β, the model produces precisely the same results as would be obtained from the linear dumbbell model of dilute solutions. The case of constant β is also equivalent to the model of Lodge (1956) with a single relaxation time, as pointed out previously by Lodge (1968). For this case n is unity. This would mean that for constant β , the number of entanglement junctions remains at the rest state value and is not affected by the flow. In addition, for constant β, the model also possesses a singularity (as can be seen in the response of the birefringence in table 2) at a critical value of the dimensionless velocity gradient $\alpha = \gamma/\beta_o$

$$\alpha = \frac{1}{\sqrt{v}} \tag{9}$$

where

$$v = (1 - \xi)^2(1 + \lambda)^2 - (1 - \lambda)^2 \tag{10}$$

The incorporation of a destruction function which is dependent on the end to end vector $\underline{x}$ removes this singularity. The effect of this dependence of β on $\underline{x}$ is also to make n a diminishing function of the velocity gradient for all flows except those which are purely rotational in nature. This is demonstrated in figure 1 which displays the results for simple shear and purely

extensional flows for the quadratic law model. The square well model and the model of Phan-Thien and Tanner show a similar trend and those results are not reproduced here.

Using equation (8), the birefringence can be calculated for all four models. As pointed out above, the singularity inherent in the constant destruction model is removed when β becomes a function of conformation. Both the quadratic model and the model of Phan-Thien and Tanner predict that the birefringence approaches a constant asymptote at sufficiently large values of the velocity gradient. This saturation effect results from the fact that the increase in birefringence from the deformation of the segments remaining in the network at any given value of the velocity gradient is exactly balanced by the diminishing junction concentration as the network deforms. For the square well model on the other hand, a bound is placed on the allowable segment end to end distance and, at some point the drop in the entanglement junction concentration must cause a net decrease in the birefringence. This leads to an extremum in the predicted birefringence/velocity gradient curve. Since the birefringence and stress are directly related in this network model, such an extremum will also be a point of flow instability as pointed out by Doi and Edwards (1979). Experimentally, therefore, such a maximum may not be

directly measurable but rather will be manifested by an instability in the flow following a leveling off of the birefringence with the velocity gradient.

The effect of flow type can also be studied as the parameter λ is varied. Figure 2 shows the predicted steady state birefringence for several different values of the parameter ξ plotted against the eigenvalue of the velocity gradient tensor $\sqrt{\lambda\alpha}$ for the quadratic law model. It is seen that the curves fall in close proximity to each other for a large range of λ as long as ξ does not become too large. This correlation with the eigenvalue of the velocity gradient tensor is predicted for all the models considered and does not distinguish between the various forms for the functional dependence of G and β. It may be noted, however, that the criteria for correlation of the birefringence against $\sqrt{\lambda\alpha}$ is that $v=(1-\xi)^2(1+\lambda)^2-(1-\lambda)^2$ not be too close to zero. Therefore, experimental data could be used to estimate the magnitude of ξ by determining the range of the parameter λ where the correlation with $\sqrt{\lambda\alpha}$ holds.

The reason that the birefringence can be well correlated with the eigenvalue of the velocity gradient tensor can be seen by performing a linear stability analysis on equation 1. This has been done for the case of the linear dumbbell by Tanner (1976) and more recently for a somewhat more general model by Olbricht et al (1980). The analysis of Olbricht et al included the effect of the slip mechanism (i. e. finite ξ) and showed that the point of neutral stability coincides with the singularity condition of equation (9). Therefore, if $\alpha\sqrt{v}>1$, the network model will predict significant deformation whereas if the flow is weak ($\alpha\sqrt{v}<1$), the steady state is only a slight departure from the rest state configuration. The quantity $\alpha\sqrt{v}$, therefore, directly prescribes the strength of the flow and the amount of deformation. For this reason the birefringence, which is a measure of the deformation, should scale with the group $\alpha\sqrt{v}$. This correlation will break down when $\alpha\sqrt{v}=0$ because the Brownian forces which have been built into the model by the choice of G, force the model to achieve a finite length scale for the segments when the flows are weak. When ξ is zero, $\alpha\sqrt{v}$ tends to $2\sqrt{\lambda\alpha}$ which is twice the eigenvalue of the velocity gradient tensor. Therefore, one would expect the birefringence to scale with $\sqrt{\lambda\alpha}$ over a range of the flow type parameter λ and that this range of correlation would depend on the magnitude of ξ.

For a given value of ξ the following lower bound on the range of λ for the correlation to hold can be found from the criteria $\alpha\sqrt{v}=0$ or

$$\lambda_{1.b} = \frac{\xi}{2-\xi} \tag{11}$$

Therefore, when $\xi=0.2$, the lower bound is at $\lambda=.11$ and when λ is lower than this value (for example, the curve in figure 2 for $\lambda=0.1$) there will be a marked departure from the correlation. For $\xi=0.3$ the bound is at $\lambda=.176$ and this is reflected in the departure of the $\lambda=0.2$ curve from the correlation in this case in figure 2.

The growth of birefringence in time as the flow is started from rest can also be calculated. As in the case of the linear dumbbell, the constant breakage model predicts simple monotonic growth for all flows when $v>0$. The nonlinear models, with conformation dependent destruction functions, however, show overshoot in the birefringence when the velocity gradient is large enough. The predicted response of the quadratic law model to the start up of purely extensional flow and a simple shear flow can be seen in figure 3. All four models will also show oscillatory growth in the birefringence when the parameter v is less than zero and this corresponds to the case in which the

effective ratio of the vorticity to the rate of strain becomes greater than unity. In this situation the network segments rotate at a faster rate than the rate at which they are deformed.

The presence of an overshoot for simple shear flow is an expected result and has recently been measured by Osaki et al (1979). The prediction of an overshoot for purely extensional flows is, however, somewhat unexpected and is linked to the nonconstant segment density n when β is nonconstant. The overshoot results from the competing processes of segment deformation and junction destruction which dictate the level of birefringence. When the time scale of segment deformation becomes faster than the time scale of the destruction process, an overshoot in the birefringence is manifested.

The model of Aceirno et al. (1976) also shows this overshoot effect in extensional flows and their structure parameter, which is directly related to the segment concentration, is a diminishing function of the velocity gradient. The model of Phan-Thien and Tanner (1977) although similar in many respects to the third model presented here shows a monotonic rise in the birefringence which is a consequence of the preaveraging approximation

used in their destruction function. The preaveraging forces the segment density to be constant. The model of Doi and Edwards (1979) also leads to a constant segment density and would predict a monotonic rise in the birefringence for the start up of purely extensional flows.

The technique of flow birefringence offers the possibility of testing the qualitative trends noted here and may be used to suggest the attributes that a network model should possess in order to simulate the actual physical situation. As will be demonstrated in a later section, the existence of a correlation of birefringence with the eigenvalue of the velocity gradient tensor can be explored experimentally and used to provide an upper bound for the magnitude of the slip coefficient ξ. Existence of an asymptote in the degree of birefringence or a flow instability at sufficiently high velocity gradients can suggest how strong the functional dependence of the destruction function on the conformation should be. Finally, the measurement of the growth of birefringence after the start up of flow (especially purely extensional flows) can offer important information concerning the nature of the creation and destruction processes operating on the temporary junctions of the network. Existence of overshoot for the case of pure extension would seem to suggest that

the correct model of the network should lead to diminished junction concentration as the network deforms. Monotonic growth would suggest that this concentration remains constant and that the network retains its integrity over the time scales important to the flow process.

III. Experimental

The experimental arrangement is shown in figure 4. The four roll mill was situated on a cross slide rotary table which allowed translation and orientation of the flow device independent of the optics. The rollers were powered by four independent motors which were connected to the rollers through electronic clutches that could be engaged simultaneously in order to initiate the flow immediately. The motors were connected to controllers which could hold their speeds constant to within one or two percent and which could electronically brake the rollers simultaneously in order to arrest the flow. The speed of each motor was monitored through electromagnetic sensors which sent a signal to a digital tachometer.

The light source was generated using a 4 watt argon ion laser which produced polarized light at a wave length of 4880 Å. The light was directed through the four roller

apparatus from below using a mirror. For the purpose of birefringence measurements, the light was sent vertically through the device and a polarizer was positioned between the mirror and the flow device instead of before the mirror as shown in the figure. The light intensity was detected with a 13 stage photomultiplier tube which was mounted onto a wide angle goniometer. A polarizer and interference filter were mounted on the goniometer in front of the photo tube. For the birefringence measurements the pinholes were removed and the goniometer was rotated into the vertical position. The signal was processed with photon counting equipment which provided the total intensity of the light striking the phototube. For systems where the light intensity of the birefringence was sufficiently strong and for the transient experiments where it was important to have a fast response, a laser power meter was used in place of the photo multiplier. Both detection systems were checked against each other and found to produce equivalent results for steady state flows and for the start up of flows where the response of the system was slow compared to the response time of the photon counting equipment.

In the birefringence experiment the first polarizer is used to define the polarization of the incident beam and the second polarizer has its polarization vector crossed at 90^{0}

to the first. The polarizers used were capable of producing an extinction of 10^{-5} to 10^{-7}. The polymer solution when deformed by the flow field will be characterized by an anisotropic refractive index which can be described as a tensor with major and minor axes at an orientation which is directly related to the average orientation of the polymer chains in the flow. The various polarization vectors in the experiment can be represented by the vector diagram of figure 5. The light intensity seen by the phototube is then

$$I = I_o \sin^2 2\theta \sin^2 \frac{\delta}{2} \tag{12}$$

where θ is the orientation of the principal axis of the refractive index with respect to the incident polarization vector and I_o is the incident beam intensity. The quantity δ is related to the birefringence $\Delta n=(n_{||}-n_{\perp})$ by

$$\delta = \frac{2\pi}{\lambda} (n_{||} - n_{\perp}) d$$

where λ is the wave length of light and d is the thickness of the sample. The birefringence experiment therefore offers the possibility of measuring both the orientation of the polymer and the degree of deformation through Δn. The orientation of the polymer is found by rotating the flow device while keeping the optics fixed and determining the angle which produces a maximum in the birefringence intensity. Measurement of the intensity at that angle

produces the birefringence which, as shown by the simple model of the previous section, is related to the degree of deformation of the segments making up the concentrated polymer network.

The polymer systems studied were polyethylene oxide/water solutions in the concentration range from .75% to 1.5% and a 500 ppm solution of polystyrene in tricresyl phosphate. The WSR-30 Polyox sample was donated by Union Carbide Corp. and the polystyrene was obtained from the Japan Synthetic Rubber Co.. The polystyrene was characterized by JSR through intrinsic viscosity and sedimentation measurements as having a molecular weight of 18×10^6 and a molecular weight ratio Mw/Mn of 1.35. The experiments using the polyox solutions were run at a temperature of $20^{\circ}C$ while the polystrene solutions were studied at $12.8^{\circ}C$. The viscosity of the tricresyl phosphate at $12.8^{\circ}C$ was 1.7 poise.

The polyethylene oxide solutions were prepared by first placing the polymer in a small amount of isopropanol and then slowly adding this dispersion into the vortex of a flask of water undergoing moderate mixing by a propeller. The solution was mixed for one day and then subjected to a vacuum which helped remove inhomogeneities. The solution

was then passed through a course filter (50 microns) and allowed to sit for several days. The initial solution prepared was of 2% polymer by weight and the three concentrations studied (.75%,1.0%,1.5%) were made by dilution of this parent solution. This was important as it was noticed that it was difficult to duplicate the measurements from two solutions prepared seperately at the same concentration unless the steps used in preparation were reproduced exactly. The polystrene solutions were prepared by first dissolving the polymer in dichloromethane (a volatile solvent) and then adding this mixture to the tricresyl phosphate. This final solution was allowed to sit heated from below to approximately 50°C for several days which provided gentle thermal mixing of the constituents. The solution was then placed under vacuum to draw off the dichloromethane and finally passed through a 1 micron teflon filter. The concentration was 500 ppm which, although appearing superficially to be dilute, was actually quite concentrated due to the high molecular weight and the large degree of swelling caused by the solvent.

IV. Characterization of the Four Roll Mill

The four roll mill was invented by G. I. Taylor (1934) who used it to study drop deformation and breakup in

extensional flows. The device consists of four rollers positioned on the corners of a square. Giesekus (1962) demonstrated that if the rates and direction of rotation of a pair of rollers on one diagonal of the square is varied with respect to the remaining pair, the ratio of vorticity to the rate of extension can be systematically controlled. It is this feature which was exploited in our experiment.

The schematic diagram in figure 6 describes the various modes of operation of the four roll mill. If λ is identified with the negative of the ratio of the angular velocities of rollers 1 and 3 with respect to 2 and 4, the flow generated at the center of the device is well approximated by a linear flow field with the velocity gradient tensor of equation (3). The streamlines for this flow field are given by the following family of curves

$$(x + y)^2 - (x - y)^2 = c \qquad (13)$$

where c is an arbitrary constant. The ratio of vorticity to extension is $w=(1-\lambda)/(1+\lambda)$. For the cases where $0<\lambda<1$, the streamlines are open and are characterized by inlet and exit streamlines which are oriented at an angle ϕ (see figure 6) with respect to each other. This angle is related to λ by

$$\tan(\phi/2) = \sqrt{\lambda} \qquad (14)$$

Alternatively, if $0>\lambda\gtrsim-1$, the streamlines form a family of ellipses with major axis a and minor axis b (see figure 6) related to λ by

$$\frac{b}{a} = \sqrt{\lambda} \tag{15}$$

Equations (14) and (15) can therefore be used to determine how well the actual local velocity near the center stagnation point in the four roll mill is simulated by equation (3). In particular, the relationship between the actual value of λ which characterizes the flow field and the setting of the relative angular velocities of the rollers can be measured. It is also possible to derive simple expressions from which the velocity gradient can be determined. In particular, it is a simple matter to show that the trajectory of a particle starting at (x_o, y_o) is given by

$$x = x_o \frac{(1+\lambda)}{2\sqrt{\lambda}} \sinh\sqrt{\lambda}\gamma t + x_o \cosh\sqrt{\lambda}\gamma t + y_o \frac{(1-\lambda)}{2} \sinh\sqrt{\lambda}\gamma t \tag{16}$$

$$y = -x_o \frac{(1-\lambda)}{2\sqrt{\lambda}} \sinh\sqrt{\lambda}\gamma t - y_o \frac{(1+\lambda)}{2\sqrt{\lambda}} \sinh\sqrt{\lambda}\gamma t + y_o \cosh\sqrt{\lambda}\gamma t$$

Therefore if the transit time for a particle to travel from (x_1,y_1) to (x_2,y_2) is τ, the velocity gradient is given by

$$\gamma = \frac{1}{\sqrt{\lambda}\,\Delta t} \sinh^{-1}\left[\frac{2\sqrt{\lambda}\,(x_2y_1 - x_1y_2)}{(x_1^2 + y_1^2)(1 - \lambda) + 2(1 + \lambda)x_1y_1}\right] \qquad (17)$$

The above formula is most useful when λ is positive. When λ is negative and the streamlines are closed ellipses, it is more convenient to measure the time for a particle to make a complete orbit. If this time is measured to be Δt the velocity gradient is

$$\gamma = \frac{2\pi}{\sqrt{\lambda}\,\Delta t} \qquad (18)$$

Using equations (13-18) the flow type parameter λ and the velocity gradient can, in principle, be determined experimentally for any given rate and direction of rotation of the rollers.

The device which was actually constructed is seen in figure 7. The ratio of the roller diameters to the diagonal distance defined by the rollers was set at .546. This ratio was chosen as it produced the best fit between a hyperbola and the circular surface of a roller. The procedure for deciding on the best fit is shown in figure 8 where the ratio of the roller diameter to the diagonal distance of the square defined by the roller centers was varied in order

that the area between the two curves go to zero. The rollers were mounted on a pyrex plate which formed the lid of the container and the bottom was also made of a pyrex plate. The walls of the container were formed from a brass jacket containing grooved channels to support circulating water for temperature control. Temperature was measured by inserting a thermister into the thermometer well and could be measured to within 0.01° C. In a typical operation however, temperature gradients were observed to exist in the system which were manifested by periodic variations in the temperature of about 0.1°C as the fluid circulated in the device.

Flow visualization experiments were carried out using the four roll mill in order to characterize the flows produced by the device. The polyethylene oxide solutions of at 1% and 1.5% concentration were studied as well as glycerin. The flow visualization was accomplished by replacing the brass jacket of the four roll mill with one made of lucite. A plane of light of approximately 0.125 inches in thickness was directed into the sides of the jacket at half height which illuminated tiny particles residing in the liquid. The particles were tiny ceramic spheres of about 100 microns in diameter. The flow was then visualized through a camera with a close up lens system.

Figure 9 shows a series of photographs taken of the glycerin system at several values of the flow type parameter λ. From these pictures and the equations (14) and (15), the relationship between the ratio of roller speeds λ_M and the value of the flow type parameter for the flow, λ_F could be determined. The results of this procedure for the glycerin and polyethylene oxide solutions are seen in figure 10 which indicates that the trend for the concentrated polymer solutions is not significantly different from that for the glycerin. It is important to note that the angles measured for the case of positive values of λ are those extrapolated from the center stagnation point. The angles could be measured to within about 3° which represents a 10% spread in the value of λ. The simulation of the flow field tensor of equation (3) is seen to be very reasonable except when λ is much smaller that about 0.1. The case of λ equal to zero, which should simulate simple shear flow, was noticeably different than the simple empirical model and contained circulating regions due to the presence of the two stationary rollers.

Using equations (17) and (18) the relationship between the angular velocity of the rollers and the local velocity gradient at the stagnation point can be determined by measuring the transit times of particles in the flow. This

was done for the glycerin system for several values of the parameter λ. Figure 11 shows the measured velocity gradients versus the angular velocity of the rollers. The plot indicates that the values for all the values of λ studied fell on a single straight line from which the following relation between the gradient γ and the angular velocity of the fastest pair of rollers ω was obtained

$$\gamma = 0.678\omega \tag{19}$$

where ω is measured in radians/sec.

For negative values of λ the velocity gradients were obtained by measuring the orbit time of the particles. For the case of purely extensional flow (λ=1) the data were obtained by taking photographs of a given time exposure and calculating the velocity gradient required for particles to produce the streaklines in the photographs in that given amount of time. This procedure, although accurate for low values of γ becomes less reliable at high velocity gradients as the particles move faster and the exposure times have to be reduced causing the streaks to be fainter. For that reason data using this technique for purely extensional flow only covered the range from 1 to 7 radians/sec. In order to study the dependence of the velocity gradient on the angular

velocity of the rollers the technique of homodyne light scattering spectroscopy was used for the glycerin system. The results of this work (Fuller et al (1980)) demonstrated that the velocity gradient was a linear function of the roller velocities over the range from 0 to 35 radians/sec which was the maximum range accessible in the experiment. The homodyne light scattering experiment allows direct measurement of the velocity gradients in the system and also showed that the region over which the velocity gradient is constant is confined to an area of dimension equal to the gap width between two adjacent rollers. Unfortunately, it was not possible to perform such experiments on the polyethylene oxide solutions due to the multiple scattering effects inherent with such turbid solutions.

V. Results

A. Birefringence Measurements

Flow birefringence measurements were taken on the three polyethylene oxide solutions of concentrations 0.75%, 1.0% and 1.5%. This system was also studied by Pope and Keller (1977) and Crowley et al (1976) in purely extensional flow produced by a four roll mill. The results obtained from the present work for purely extensional flow can be seen in

figure 12. The birefingence is linear in the velocity gradient for the 1.0% and 0.75% solutions in agreement with the observations of Pope and Keller (1977). The magnitude of birefringence for the 1% solution was compatible with their measurements as can be seen by comparing the birefringence (corrected for concentration) at a velocity gradient of 10 sec^{-1}. The reported value of Pope and Keller was $4.8x10^{-5}$ (read off of their figure 4) while the result from this work was $4.2x10^{-5}$. Since the characteristic relaxation time for such concentrated solutions is a strong function of concentration it is expected that the birefringence will exhibit a stronger than linear dependence on concentration. This was in fact observed by Pope and Keller and again in this work. The measurements of the 1.5% solution, however, showed a noticeable departure from the linear dependence of birefringence on the velocity gradient and in fact the flow was observed to become unstable above velocity gradients of 13-14 sec^{-1}. This instablility did not occur for the lower concentrations studied over the entire range of velocity gradients. From the discussion of the theoretical section, the existence of levelling off of the birefringence followed by the onset of a flow instability for the 1.5% solution, suggests that the elongational stress may possess an extremum with respect to the velocity gradient.

One of the most important (although predictable) observations of prior studies of flow birefringence in extensional flows is the extreme localization of the region over which the birefringence exists. This is a manifestation of the finite time required for the polymer to deform and the fact that the molecules start from a nearly undeformed state just inside the entrance of the four rollers. Figure 13 shows the degree of localization for the 1.5% solution at a gradient of 7.1 sec^{-1}. It is seen that the thickness of the region of appreciable birefringence is about 0.015 inches. Since the incident laser beam used in the experiment was measured to be roughly Gaussian in shape with a width of between 0.004 and 0.006 inches, the real signal, which is the deconvolution of the measured curve of figure 13 with the laser beam profile, is actually somewhat narrower than 0.015 inches and probably in the neighborhood of 0.009 to 0.011 inches.

One of the principal objectives of this work was to study the effect of flow type on the deformation of polymer solutions. As was pointed out in the previous section the four roll mill offers an excellent means by which this can be accomplished. The procedure which was followed in carrying out this study was to first set the angular

velocities of the four rollers to achieve a desired velocity gradient and flow type parameter λ. Following this the flow device must be rotated so that the birefringence signal is at a maximum. The results for a velocity gradient of 9.47 sec^{-1} and for three different values of λ for the 1.5% solution can be seen in figure 14. As expected from equation (12), the birefringence attains a maximum for pure extension ($\lambda = 1$) at θ equal to ± 45 . As vorticity is added to the flow by decreasing λ, the orientation of the polymer shifts towards zero and the magnitude of the birefringence is decreased. The magnitude of the birefringence at the maximum point for two separate velocity gradients as a function of λ for the 1.5% solution is plotted in figure 15. This figure demonstrates the effect that vorticity has in the deformation of polymers in flow. The same data were obtained for the 1% solution and it was noticed that the birefringence for constant velocity gradient was a linear function of $\sqrt{\lambda}$. This is shown in figure 16 which has the birefringence plotted against $\sqrt{\lambda}$. Since the birefringence for purely extensional flow was also linear in the velocity gradient for the 1% solution, this suggests that the birefringence for this system could be well correlated with $(\sqrt{\lambda}\gamma)$ which is the eigenvalue of the velocity gradient tensor of equation (3). It is important to note that the values for λ which were used for figures 15 and 16 were obtained

from figure 10. If the ratio of roller velocities is used instead of the corresponding value measured from the flow visualization studies, the correlation of the birefringence with $\sqrt{\lambda\gamma}$ is still quite good but is improved when the actual measured values are used. When the data for the 1.5% solution are plotted against $\sqrt{\lambda\gamma}$ as in figure 17, a good correlation was obtained for this system as well.

As was pointed out in section 2, the fact that the data seem to be well correlated with $\sqrt{\lambda\gamma}$, the eigenvalue of the velocity gradient tensor, may be interpreted in terms of molecular charcteristics. Indeed, the simple model discussed in section 2 would suggest that the slip parameter should have a maximum magnitude of about 0.27 or less. This value was obtained from equation (11) using the value of 0.16 for λ_{lb}. This was the lowest value of λ which could be produced with confidence where the birefringence was still well correlated. In order to determine a more precise value for ξ it would be necessary to achieve lower values of the flow type parameter λ than was possible with the present system.

Besides the magnitude of the birefringence, one can also obtain the orientation angle of the deformed polymer system. From plots such as figure 14, the orientation of

the polymer is found by determining that angle at which the birefringence achieves a maximum. The results of this procedure for the 1.5% solution at two velocity gradients is shown in figure 18. In plotting this figure we have taken the angle of polymer orientation as 45° minus the angle associated with the maximum. The orientation angle has then been plotted against $(45°-\arctan(\sqrt{\lambda}))$ which is the orientation of the principal axis of extension for the flows of the four roll mill. It is seen that the data appear to fall close to the 45° line which represents the strong flow limit where the polymer is aligned completely with the principal axis of extension. It must be pointed out, however, that the error in determining the angle of orientation increases substantially with the decrease in λ as the level of birefringence drops off and the maximum becomes broader.

We have also performed transient experiments in which birefringence was recorded as purely extensional flows were initiated from rest. This was done by first setting the motors to a desired speed and then engaging the electromagnetic clutches. The signal was sent to the laser power meter instead of the photon counting equipement as the power meter had a faster response time. The intensity detected at the power meter was then sent to either a

storage oscilloscope or an x-y recorder which recorded the signal as a function of time. The results for the 1.5% polyethlene oxide solution for three different velocity gradients are presented in figure 19 which shows the presence of an overshoot in the birefringence. The magnitude of the overshoot increased with the velocity gradient while the time taken to reach the maximum decreased. It was noticed that the overshoot effect was only observed if sufficient time was given between the arrest of flow and the initiation of a new flow or if the solution residing at the center stagnation point after stopping the flow was pushed aside prior to start up. Figure 20 shows a series of runs with successively decreased time intervals between shut down and start up. As this time is reduced to less than 10 seconds, the overshoot effect appears to diminish. The waiting time could not be reduced to less than about 5 or 6 seconds as it took this amount of time for the motors to regain speed after braking them. It should be noted that the birefringence decays to zero very quickly upon braking the motors. The time scale of the decay is in fact of the same order as the characteristic time of electronic transients in the detection equipment. The bouncing at the end of the shut down resulted from the inertial response of the laser power meter responding to such a fast decrease.

The overshoot effect was not seen to occur for the 1.0% solution. This can be attributed to the fact that this lower concentration system would have a much faster characteristic time scale, which could either make any overshoot occur too quickly for the system to respond or simply be nonexistent for the range of velocity gradients studied.

Startup experiments were also performed on 18x10 MW polystrene/tricresyl phosphate solutions of 500 ppm. These solutions were visibly very viscoelastic and the addition of the polymer increased the viscosity of the solvent by 50% as measured using a Cannon-Fenske viscometer. Figure 21 shows the results of start-up experiments for several velocity gradients at a temperature of 12.8°C. It was necessary to decrease the temperature to this level in order to achieve a sufficient level of birefringence. This figure shows the appearance of an overshoot which is now oscillatory in nature. The time scale of the overshoot again has an inverse relationship with the velocity gradient and the magnitude of the overshoot increased with the gradient. The reason for the oscillations is not clear to us and requires further investigation.

In order to try to isolate the overshoot effect from

experimental artifact, we have carried out a number of tests in order to eliminate a number of such sources. After the overshoot effect had passed and steady state was achieved, the area of localized birefringence was passed across the laser beam by translating the flow device in order to ensure that the steady state did not surpass the maximum in the overshoot. This was necessary as, when starting the flow from rest, it was impossible to ensure that the laser beam was passing through the stagnation point due to small, random fluctuations in the roller velocities and the extreme localization of the birefringence region. For this reason the device used in this investigation with four independent rollers is not best suited for the study of the start-up of purely extensional flows. Care was also taken that the speed of the motors did not "bounce" when the clutches were engaged. This effect was measured to be only a fraction of a percent due to the large inertia and torque of the motors used. Measurements were also performed with the flow field in a steady state condition at a velocity gradient where overshoot was seen to occur but with the laser beam blocked from passing through the flow device. At a given time the laser beam was unblocked and the response of the detection system to an instantaneous rise in the signal was recorded in time. The system did show a slight overshoot following this procedure due to inertia in the power meter, but the

magnitude of this overshoot was never greater than 10% of the overshoot caused by flow initiation.

Overshoot in birefringence in simple shear flows has been recently measured by Osaki et al (1979). However, for this flow type this is not an unexpected result due to the precedent set through the measurement of the overshoot effect in rheological functions. There have been very few studies of transient behaviour in purely extensional flows due to the difficulty in creating such flows and the majority of studies that do exist have been performed by the drawing of filaments of polymer melts (Meissner (1971)). Although these studies report a sharp upturn in the normal stress with time, steady state was not approached before breakage of the filaments. Recently, however, Munstedt and Laun (1979) have achieved steady state levels of the normal stresses and observed a pronounced overshoot when the velocity gradient was sufficiently high. This overshoot, which was observed by experiments in two different devices does seem to be consistent with the transient results reported here.

Overshoot in simple shear can be predicted by a number of molecular models (Doi and Edwards (1979), Phan-Thien and Tanner (1977), Acerino et al (1976) and Bird and Carreau

(1968)). For the case of purely extensional flow, however, it would appear that only models with nonconstant entanglement junction density such as the model of Acerino et al and the models presented in section 2 with conformation dependent destruction functions, will show an overshoot in these flows. The existence of the overshoot effect therefore offers important information about the nature of entanglement creation and destruction in flow and we feel that additional work in this regard is certainly warranted. It would be interesting to determine the dependence of the presence of overshoot on the type of polymer studied, its molecular weight and concentration. Experiments should also be performed in devices more suited to the rapid initiation of flow rather than in one with the mechanical complexities of the four roll mill.

There is relatively little experimental data on the transient response of birefringence and stresses in purely extensional flows. This is a reflection on the difficulty in creating ideal extensional flows. Recently, however, Munstedt and Laun (1979) have measured the time-dependent tensile stress for low density polyethylene melts and observed a pronounced overshoot in the stress in pure extension when the rate of strain was increased to large values. This observation does seem consistent with the

birefringence experiments reported here and the predictions of the network models with conformation dependent destruction functions.

B. Turbidity Measurements

The polyethylene solutions were noticeably turbid upon preparation and remained so after aging for several weeks. It was noticed that the extensional flows induced an increased turbidity which was as highly localized as the birefringence effect. For the 1.5% solution the turbidity was seen to increase by about 30% when subjected to purely extensional flow . The dependence of this percent increase on the velocity gradient can be seen in figure 22 and was largely insensitive to the velocity gradient and reached the plateau of 30% very soon. Unfortunately, it was not possible to produce velocity gradients much lower than 1 sec before the motors became unstable. The turbidity was observed to remain for a duration of up to 4 to 5 hours after the flow was arrested, unlike the birefringence which fell to zero almost immediately after stoppage of the flow. This effect is shown in figure 23 which also displays the fact that the turbidity remained highly localized for many hours. This turbidity increase may be explained by possible crystallization of the polymer by the flow field. An

increase in turbidity has been observed by several investigators studying the phenomena of flow induced crystallization (Torza (1975) and Frank et al. (1971)).

VI. Conclusions

The four roll mill, when designed with the flexibility to simulate a wide class of two dimensional flow, provides a useful tool by which the properties of polymers in flowing solutions can be investigated. We have shown how the flow simulated by the device may be characterized with regard to the flow type and velocity gradients which exist locally at the center. When the flow type was varied in the device the measured birefringence for concentrated polyethylene oxide solutions was seen to correlate well with the eigenvalue of the velocity gradient tensor which describes the four roll mill flow fields. This correlation can be interpreted in terms of molecular characteristics, and the simple models discussed in section 2 suggest that it may be associated with the ability of the solution to deform affinely. However the correspondence of this model to the real system should not be taken too far as it clearly cannot describe many of the observed phenomena, namely the increased turbidity in the flow and its persistence with time. The presence of an overshoot in birefringence upon the

initiation of purely extensional flow has important consequences and needs to be further verified, particularly with flow devices which are more suited to a startup experiment. The presence of an overshoot is related to the nature of the entanglements forming the solution and, when several current models are compared, seems to be linked to the level of entanglement junctions and would suggest that the concentration of such junctions should diminish as the flow deforms the system.

ACKNOWLEDGEMENT

This research was supported by the Office of Naval Research. One of us (G.G.F.) is indebted to the National Research Council of Canada for fellowship support.

The authors have benifitted from cooperation and discussion with Dr. R. L. Schmidt of Chevron Oil Field Research Company, La Habra, Ca.

References

Acierno, D., La Mantia, F. P., Marrucci, G., Rizzo, G. and Titomanlio, G., J. Non-Newt. Fluid Mech. 1,125(1976).

Bird, R. B. and Carreau, P. J., Chem. Eng. Sci. 23,427(1968).

Bird, R. B., Armstrong, R. C. and Hassager, O., Dynamics of Polymeric Liquids Volume II: Kinetic Theory, Wiley, 1977.

Crowley, P. G., Frank, F. C., Mackely, M. R. and Stephenson, R. G., J. Polym. Sci. Polym. Phys. Ed. 14,1111(1976).

Doi, M. and Edwards, S. F., J.C.S. Faraday II 75,38(1979).

Ericksen, J., Kolloid Z. 173, 117 (1960).

Frank, F. C. and Mackley, H. H., J. Polym. Sci. Polym. Phys. Ed. 14,1121(1976).

Frank, F. C., and Keller, A., Colloid and Polymer Science 255,633(1977).

Frank, F. C., Keller, A. and Mackley, M. R., Polymer 12,467(1971).

Fuller, G. G. and Leal, L. G., Network Models of Concentrated Polymer Solutions Derived from the Yamamoto Network Theory, forthcoming publication (1980).

Fuller, G. G., Rallison, J. M., Schmidt, R. L. and Leal, L. G., The Measurement of Velocity Gradients by

Homodyne Light Scattering Spectroscopy, forthcoming publication (1980).

Giesekus, V. H., Rheol. Acta 2,113(1962).

Johnson, M. W. and Segalman, D., J. Non-Newt. Fluid Mech. 2,255(1977).

Kuhn ,W. and Grun, F., Kolloid Z. 101,248(1942).

Lodge, A. S., Rheol. Acta. 7,379(1968).

Lodge, A. S., Trans. Faraday Soc. 52,120(1956).

Meissner, J., Rheol. Acta 10,230(1971).

Munstedt, H. and Laun, H. M., Rheol. Acta 18, 492(1979).

Olbricht, W. L., Rallison, J. M. and Leal, L. G., A Criterion for Strong Flows Based on Microstructure Deformation, forthcoming publication, (1980).

Osaki K., Bessho, N., Kojimoto, T. and Kurata, M., J. Rheol. 23,457(1979).

Peterlin, A., Ann. Rev. Fluid Mech. 8,35(1976).

Phan-Thien, N. and Tanner, R. I., J. Non-Newt. Fluid Mech. 2,353(1977).

Pope, D. P. and Keller, A., Colloid and Polymer Sci. 255,633(1977).

Schowalter, W. R., Mechanics of Non-Newtonian Fluids, Pergamon Press, 1978.

Tanner, R. I., AICHE J. 22,910(1976).

Taylor, G. I., Proc. Royal Soc. (London) 146,501(1934).

Torza, S., J. Polym. Sci. Phys. Ed. 13,43(1975).

Tsvetkov, V. N., Eskin, V. E. and Frenkel, S. Y.,
Structure of Macromolecules in Solution, Volume 3,
National Lending Library for Science and Technology, 1971.

Wiegel, F. M., Physica 42, 156(1969).

Yamamoto, M, ibid. 12,1148(1957).

Yamamoto, M, Phys. Soc. Japan 11,413(1956).

Table 1. Newwork Models Investigated

Affine and Non-Affine	Destruction Function $\beta(\underline{x})$	Creation Function $G(\underline{x},N)$
Constant Breakage Model	$\beta = \beta_0$ (constant)	$G(\underline{x},N) = L \left(\frac{3N}{2\pi}\right)^{3/2} e^{\frac{3N}{2}(x^2+y^2+z^2)}$
Quadratic Law Model	$\beta = \beta_0\left[1 + \sigma(x^2+y^2+z^2)\right]$	"
Square Well Model	$\beta = \begin{cases} \beta_0: & x^2+y^2+z^2 \le R^2 \\ \infty: & x^2+y^2+z^2 > R^2 \end{cases}$	"
Phan-Thien Tanner Model	$\beta = \beta_0\left[1 + \sigma(x^2+y^2+z^2)\right]$	$G(\underline{x},N) = L \left(\frac{3N}{2\pi}\right)^{3/2}\left[1+\frac{3\sigma}{2N}\right]^{-1}\left[1+\sigma(x^2+y^2+z^2)\right] e^{-\frac{3N}{2}(x^2+y^2+z^2)}$

Table 2. Model Predictions

	$n \equiv \langle 1 \rangle$ vs α	Birefringence vs α	Correlation of Birefringence Against $\sqrt{\lambda}\alpha$	Growth of Birefringence Upon Startup of Flow
Constant Breakage Model	Constant	Possesses Asingularity at $\alpha = 1/\sqrt{v}$	Good as Long as $v = (1-\xi)^2(1+\lambda)^2-(1-\lambda)^2$ Does not Approach Zero	Monotonically Increasing Unless $v < 0$, where it is oscillatory.
Quadratic Law Model	Monotonically Decreasing	Reaches Asymptote	"	Overshoots for all Flows if α is large enough. Oscillatory if $v < 0$.
Square Well Model	"	Possesses an Extremum	"	"
Phan-Thien Tanner Model	"	Qualitatively the Same as the Quad-Law Model	"	"

Figure Captions

Figure 1. Normalized entanglement juction concentration versus α ; ----- simple shear flow, ——— purely extensional flow

Figure 2. $\Delta n/B$ versus $\sqrt{\lambda}\alpha$

Figure 3. $\Delta n/B$ versus t

Figure 4. Experimental apparatus

Figure 5. Orientation of polarization vectors and sample refractive index tensor

Figure 6. Flow field simulation in the four roll mill

Figure 7. Schematic diagram of the four roll mill

Figure 8. Quality of fit between a roller surface and hyperbolic streamline.

Figure 9. Flow visualization photographs - λ : A) 1., B) 0., C) -1., D) 1., E) .8, F) .4, G) 0., H) -.2, I) -1.

Figure 10. λ_F versus λ_M for glycerin and polyethylene oxide solutions.

Figure 11. Velocity gradient versus angular velocity of the fastest pair of rollers for several values of λ .

Figure 12. Δn versus velocity gradient in pure extensional flows for solutions of polyethylene oxide in water.

Figure 13. Light intensity due to birefringence versus the distance along center incoming streamline for

1.5% polyethylene oxide solution versus the velocity gradient in purely extensional flow.

Figure 23. Light intensity transmitted through the 1.5% ethylene oxide solution. At point (a) the flow field was initiated and at point (b) the flow was arrested. At point (c) the flow device was translated so that the center stagnation point of the original flow was passed back across the laser beam in order to demonstrate the persistence of the increased turbidity and the localization of the effect.

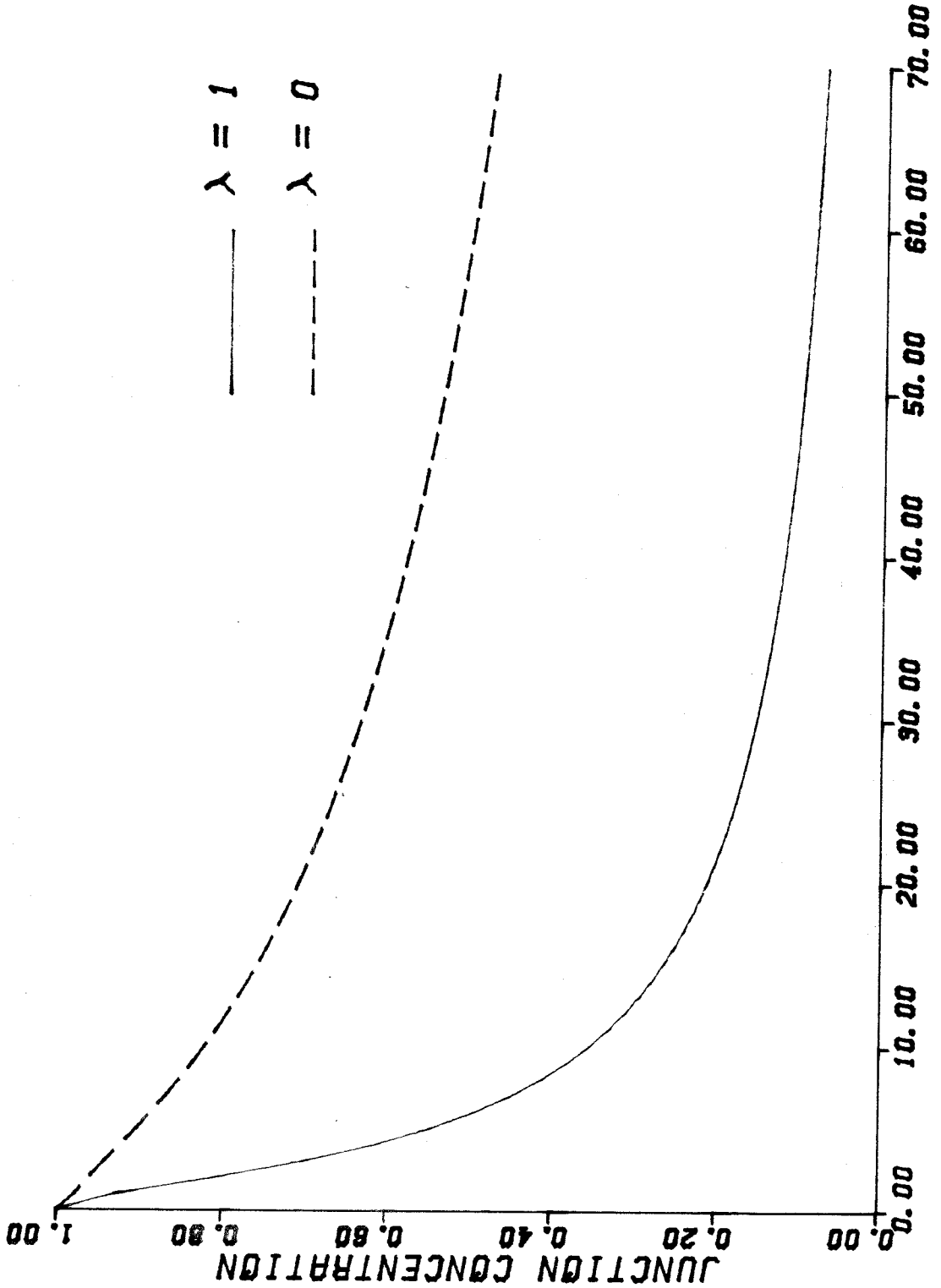
JUNCTION CONCENTRATION
0.00
0.20
0.40
0.60
0.80
1.00
0.00
10.00
20.00
30.00
40.00
50.00
60.00
70.00
α
λ = 0
λ = 1

Fig. 1

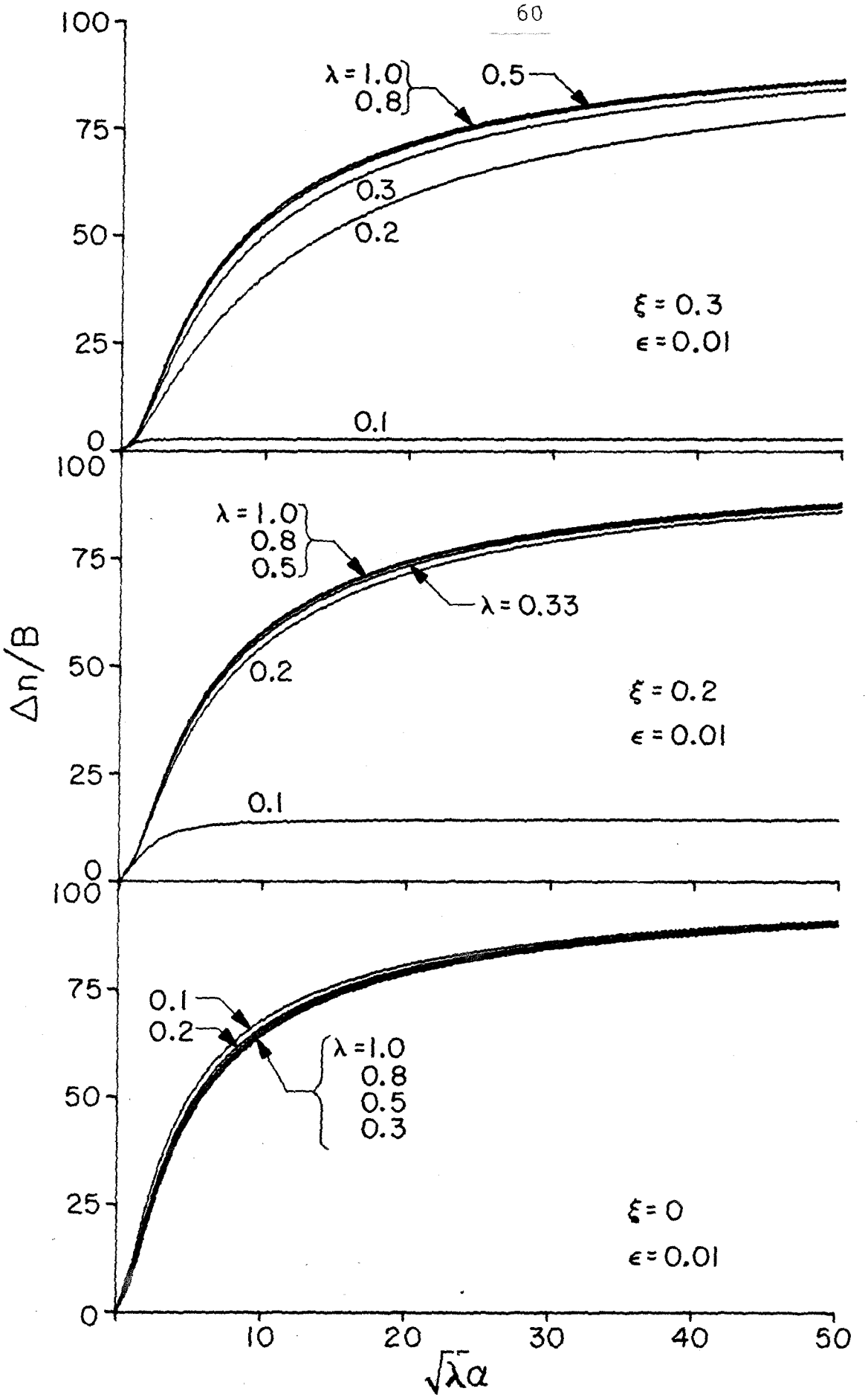
100
75
50
25
0
λ = 1.0
0.8
0.5
0.3
0.2
0.1
ξ = 0.3
ϵ = 0.01
λ = 1.0
0.8
0.5
λ = 0.33
0.2
0.1
ξ = 0.2
ϵ = 0.01
0.1
0.2
λ = 1.0
0.8
0.5
0.3
ξ = 0
ϵ = 0.01
Δn/B
10
20
30
40
50
√λα

Fig. 2

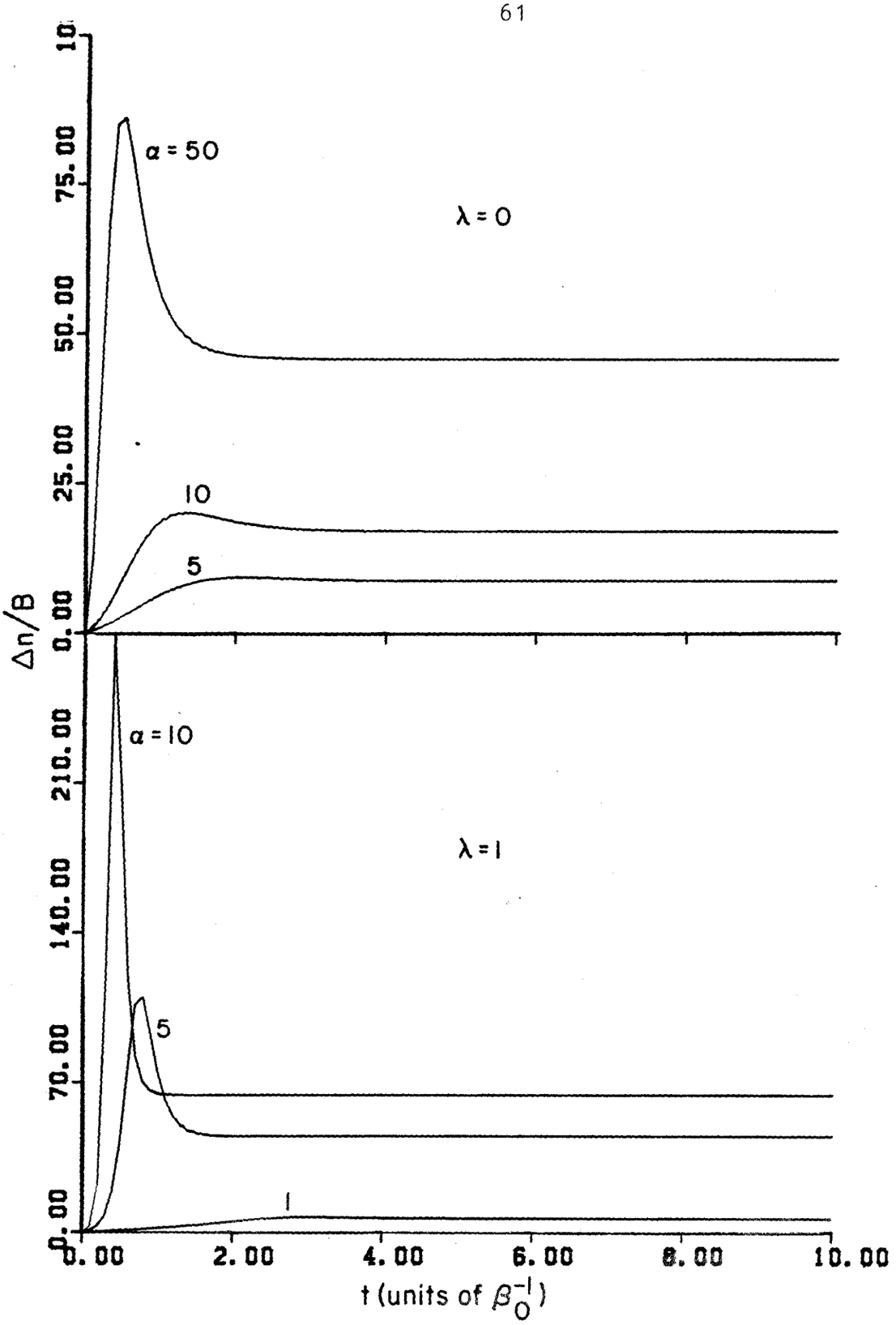
α = 50
λ = 0
10
5
α = 10
λ = 1
5
1
Δn/B
0.00
25.00
50.00
75.00
10
0.00
70.00
140.00
210.00
0.00
2.00
4.00
6.00
8.00
10.00
t (units of β_0^{-1})

Fig. 3

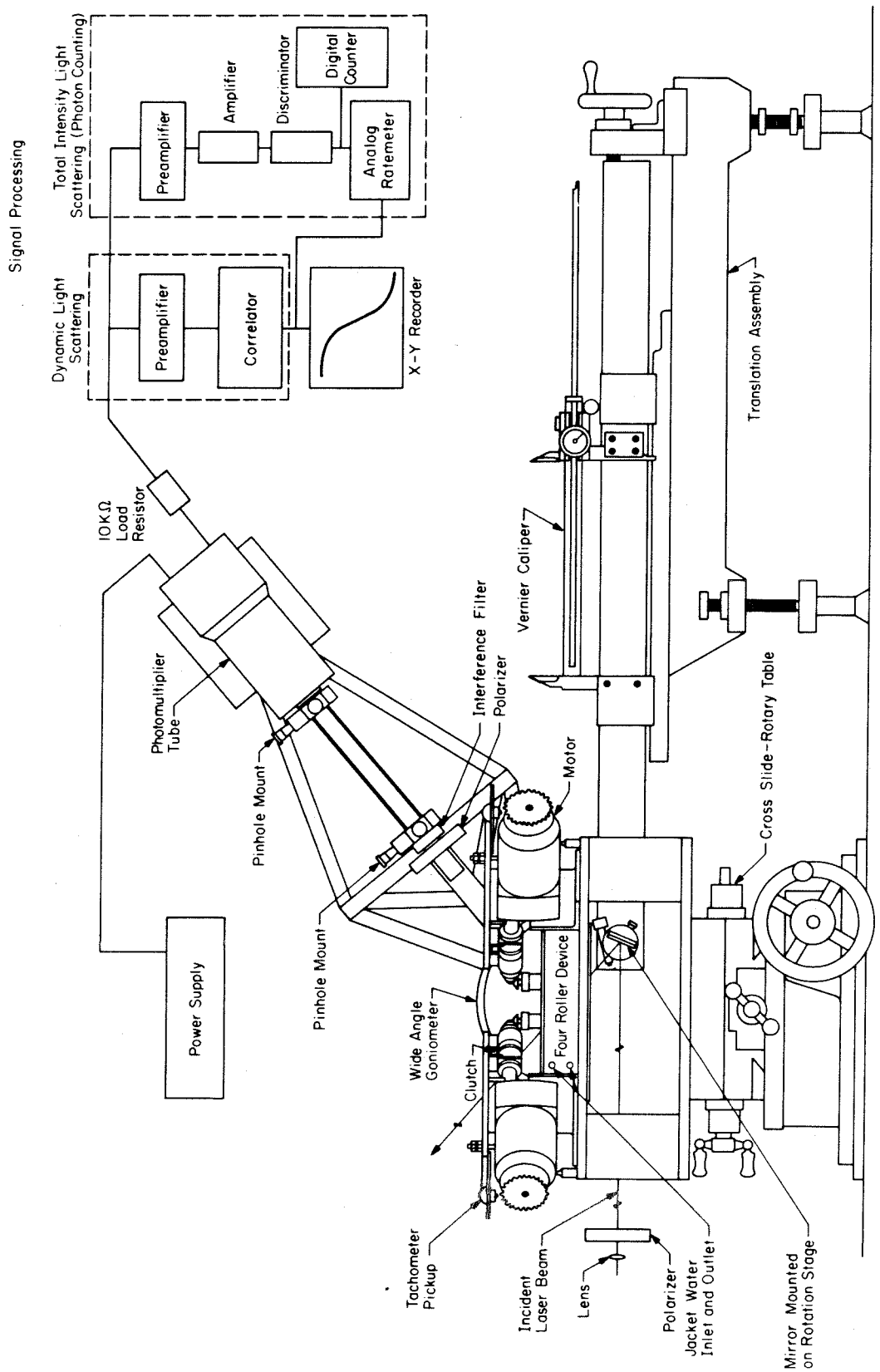
Signal Processing
Total Intensity Light Scattering (Photon Counting)
Preamplifier
Amplifier
Discriminator
Digital Counter
Analog Ratemeter
Dynamic Light Scattering
Preamplifier
Correlator
X-Y Recorder
10KΩ Load Resistor
Photomultiplier Tube
Pinhole Mount
Pinhole Mount
Interference Filter
Polarizer
Vernier Caliper
Translation Assembly
Motor
Cross Slide-Rotary Table
Power Supply
Wide Angle Goniometer
Clutch
Four Roller Device
Tachometer Pickup
Incident Laser Beam
Lens
Polarizer
Jacket Water Inlet and Outlet
Mirror Mounted on Rotation Stage

Fig. 4

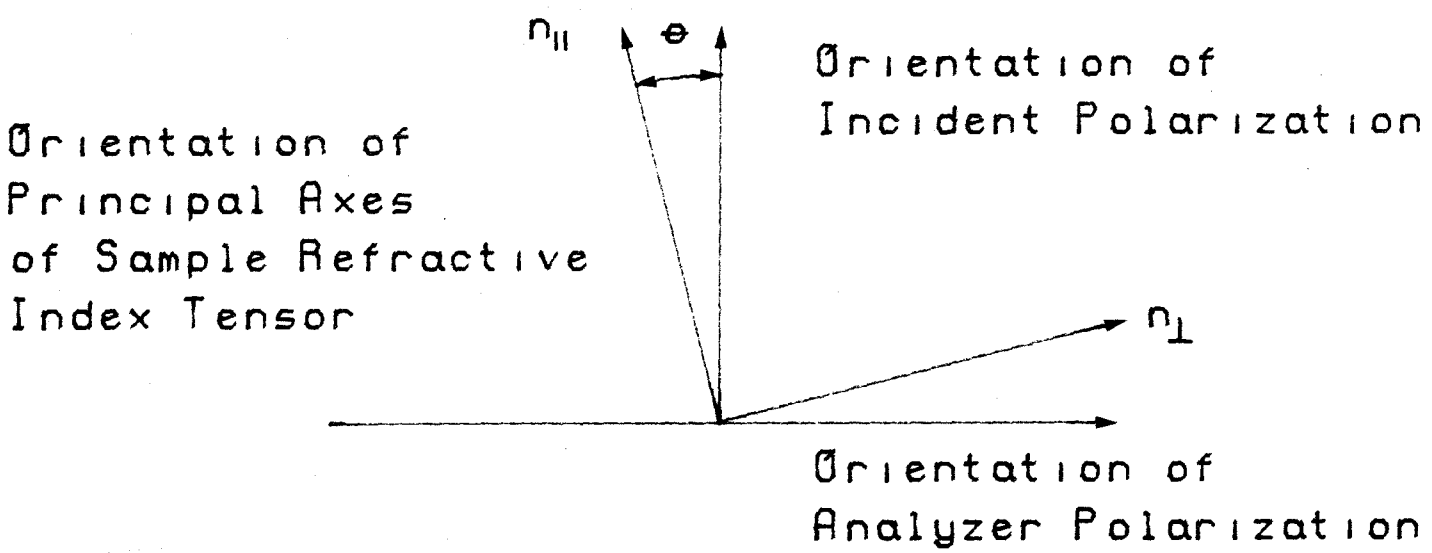
$n_{\parallel}$
θ
Orientation of
Incident Polarization
Orientation of
Principal Axes
of Sample Refractive
Index Tensor
$n_{\perp}$
Orientation of
Analyzer Polarization

Fig. 5

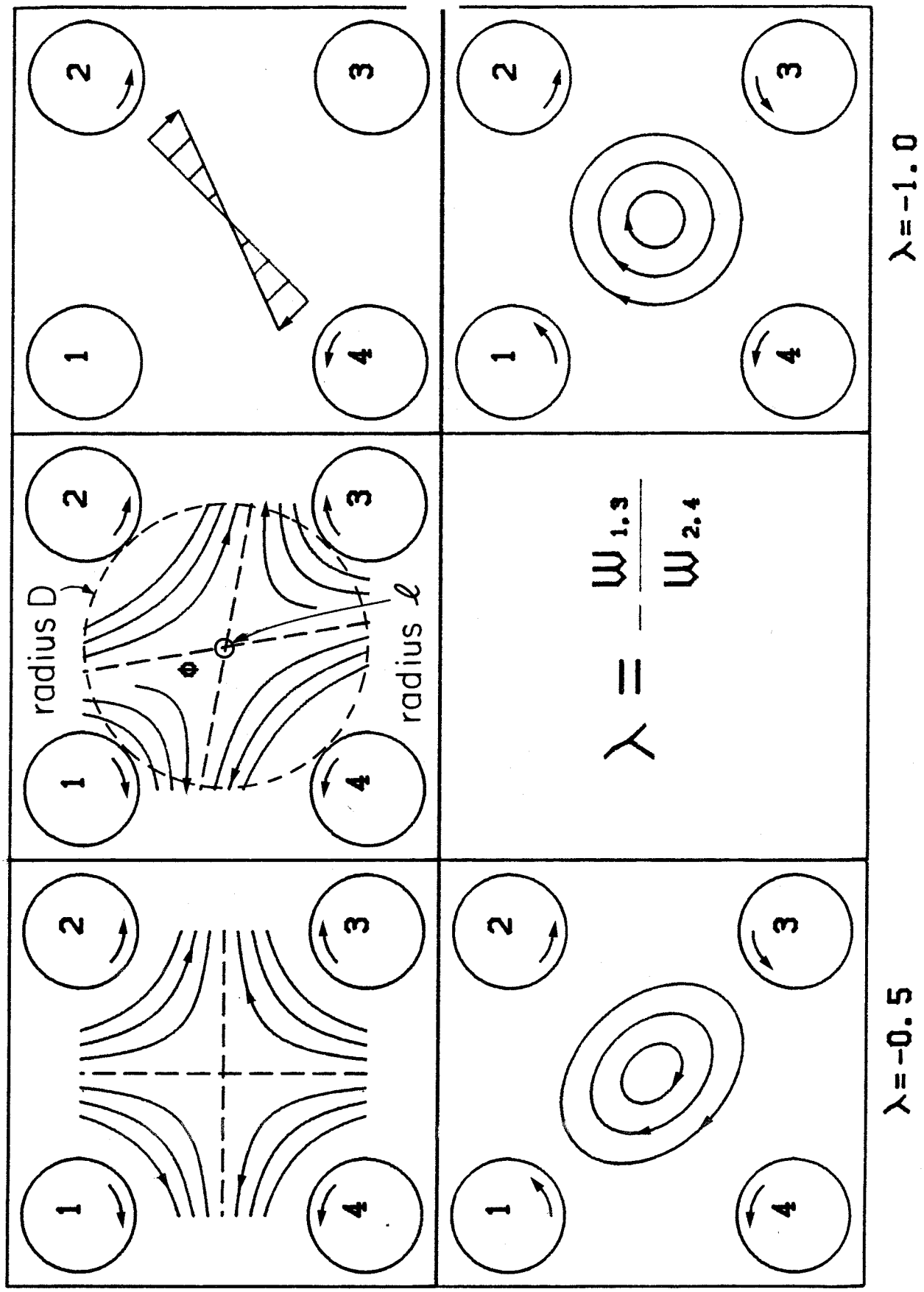

Fig. 6

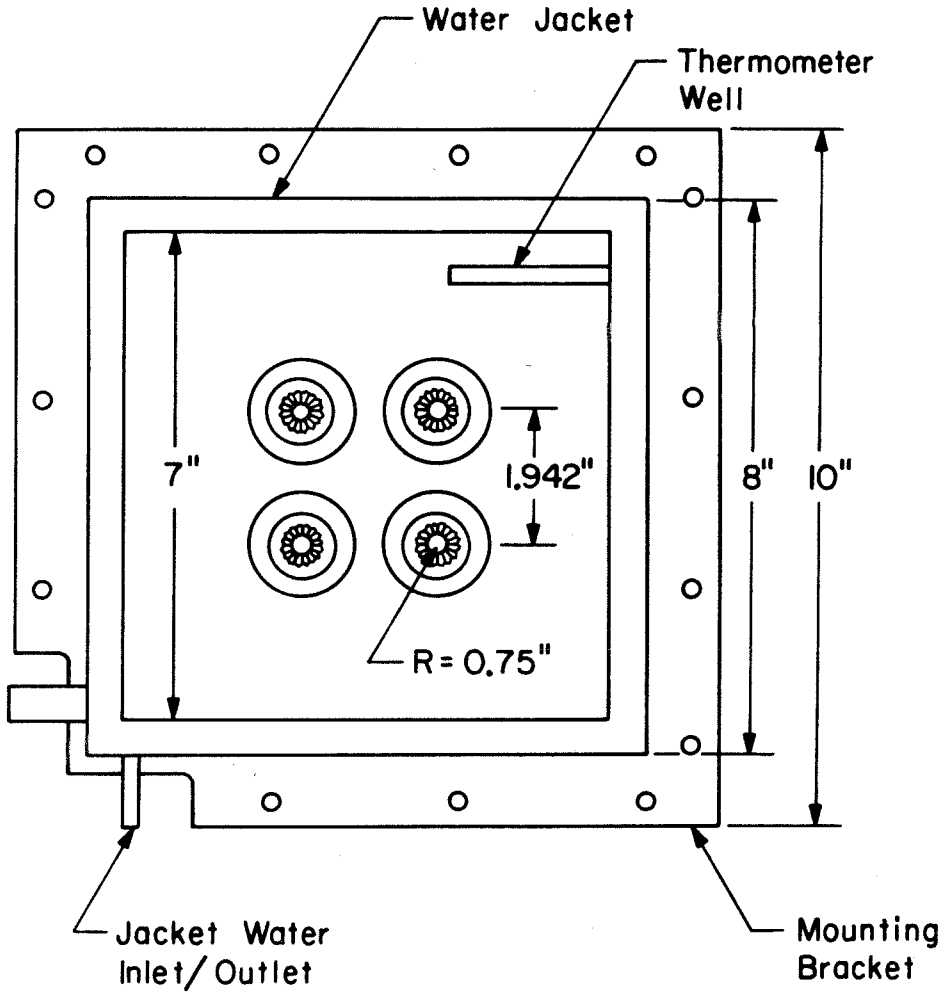
Water Jacket
Thermometer Well
7"
1.942"
8"
10"
R = 0.75"
Jacket Water Inlet/ Outlet
Mounting Bracket

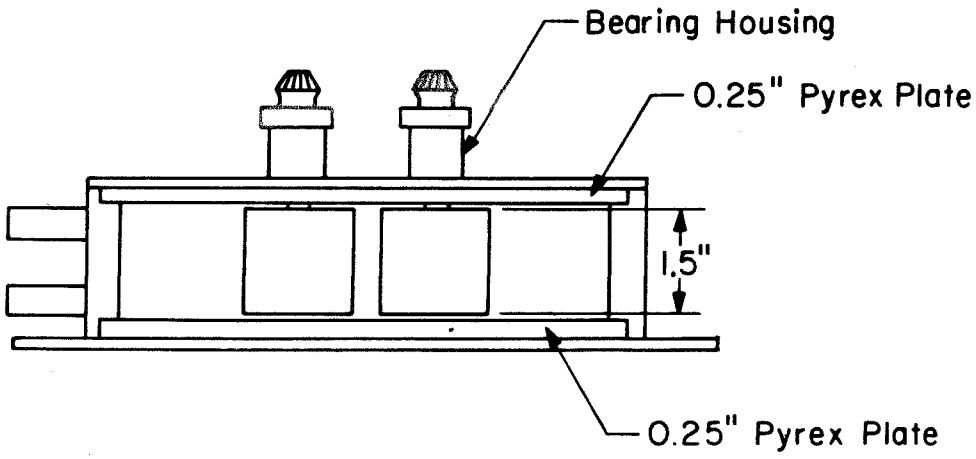
Bearing Housing
0.25" Pyrex Plate
1.5"
0.25" Pyrex Plate

Fig. 7

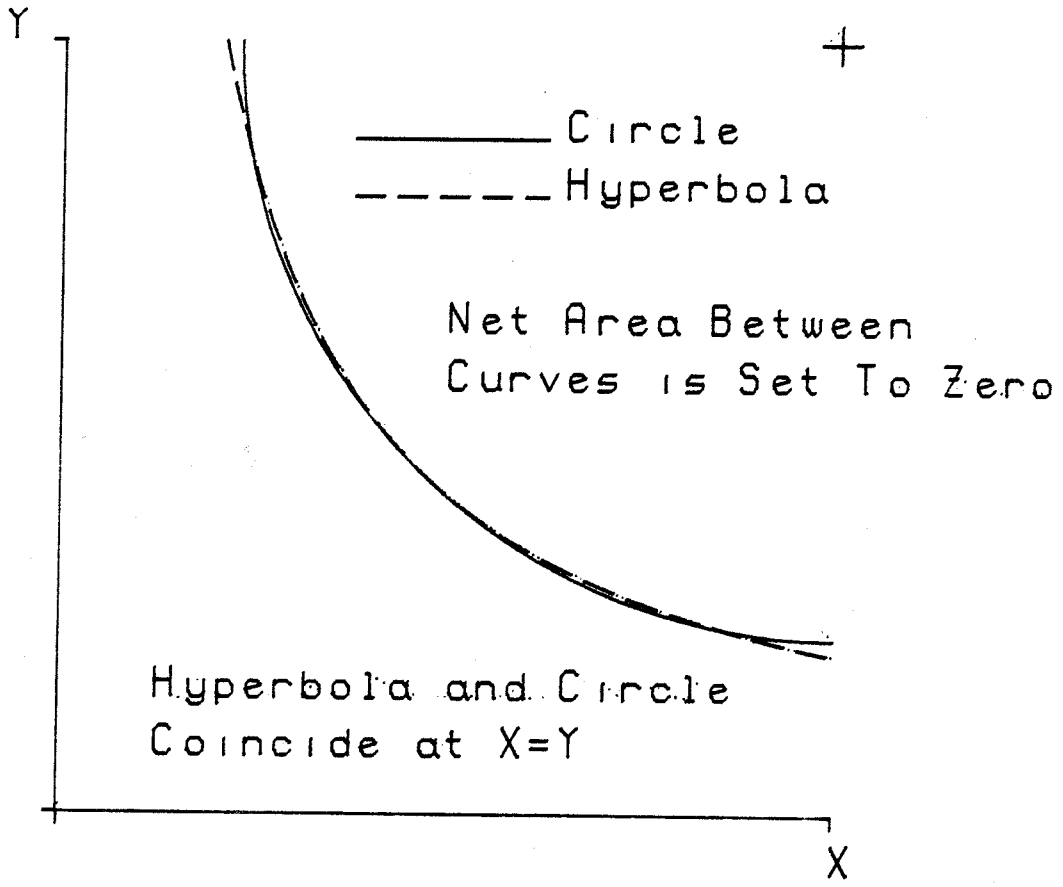
Y
Circle
Hyperbola
Net Area Between
Curves is Set To Zero
Hyperbola and Circle
Coincide at X=Y
X

Fig. 8

A

λ=1.0

B

λ=0.0

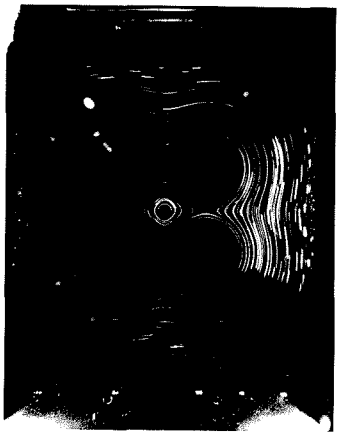

C

λ=-1.0

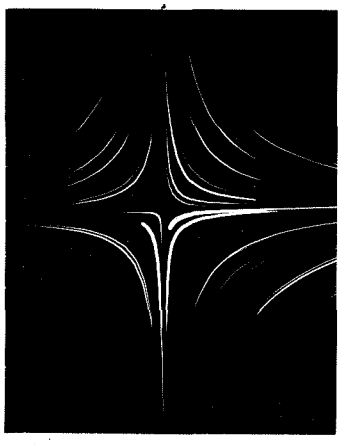

D

λ=1.0

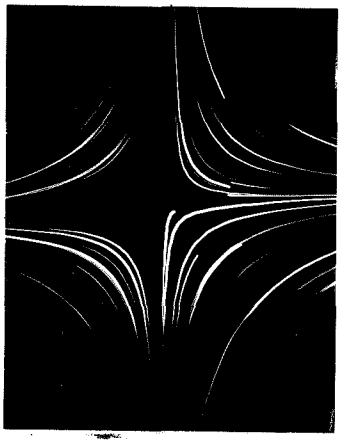

E

λ=0.8

F

λ=0.4

G

λ=0.0

H

λ=-0.2

I

λ=-1.0

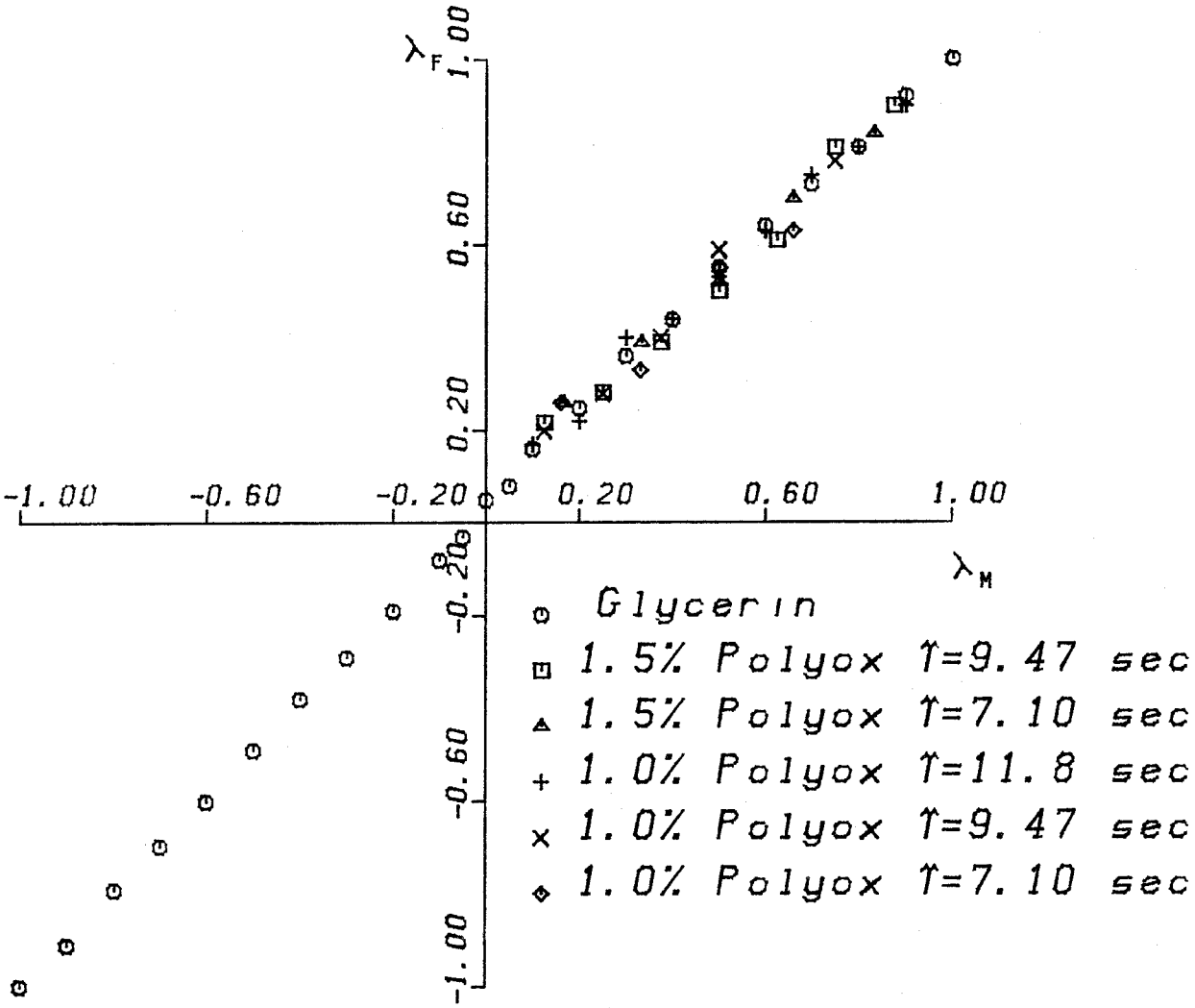
λF
1.00
0.60
0.20
-1.00
-0.60
-0.20
0.20
0.60
1.00
λM
-0.20
-0.60
-1.00
Glycerin
1.5% Polyox τ=9.47 sec
1.5% Polyox τ=7.10 sec
1.0% Polyox τ=11.8 sec
1.0% Polyox τ=9.47 sec
1.0% Polyox τ=7.10 sec

Fig. 10

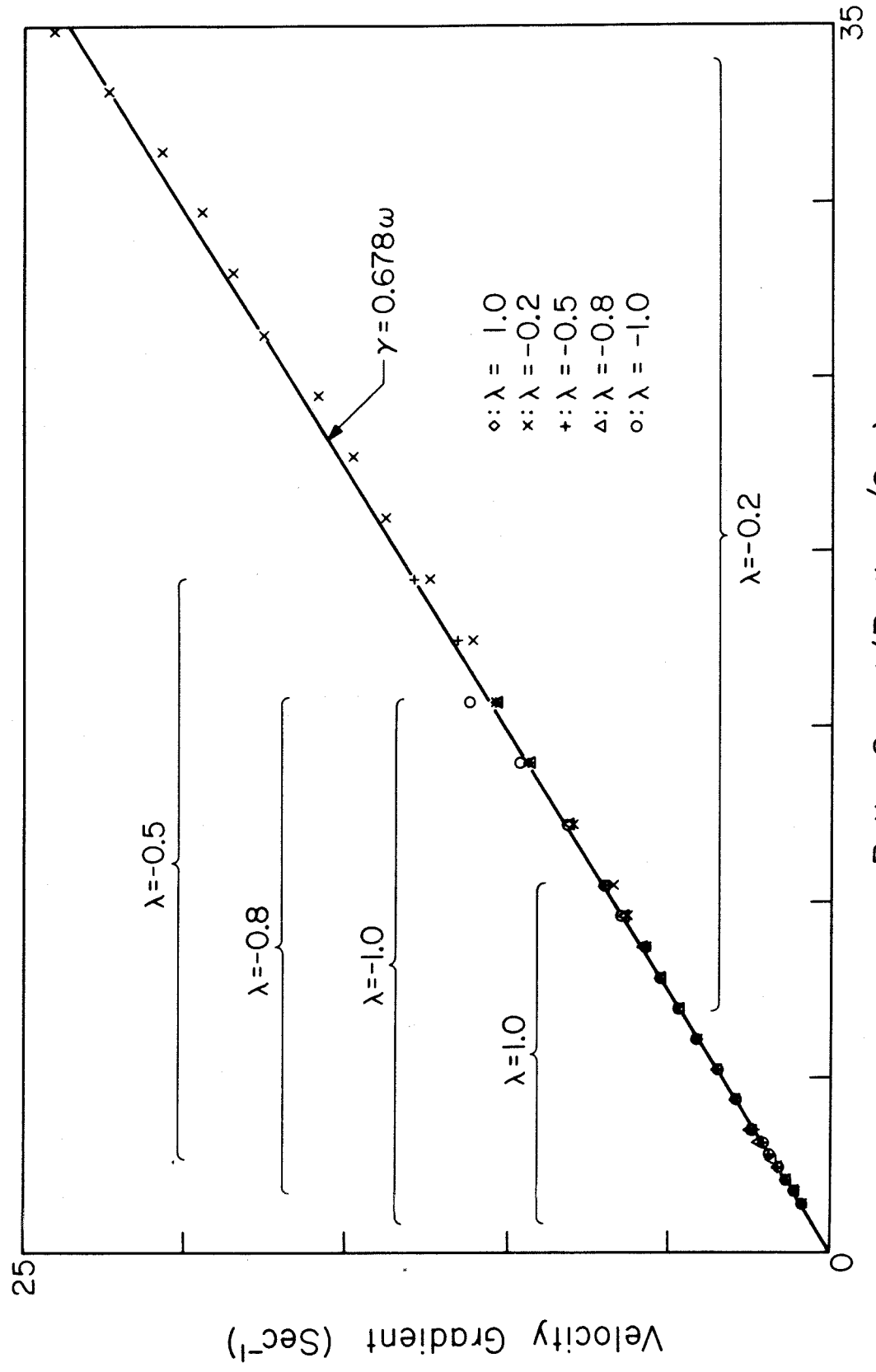
Velocity Gradient (Sec⁻¹)
25
0
35
Roller Speed (Radians/Sec)
γ=0.678ω
◇: λ = 1.0
×: λ = −0.2
+: λ = −0.5
△: λ = −0.8
○: λ = −1.0
λ=-0.5
λ=-0.8
λ=-1.0
λ=1.0
λ=-0.2

Fig. 11

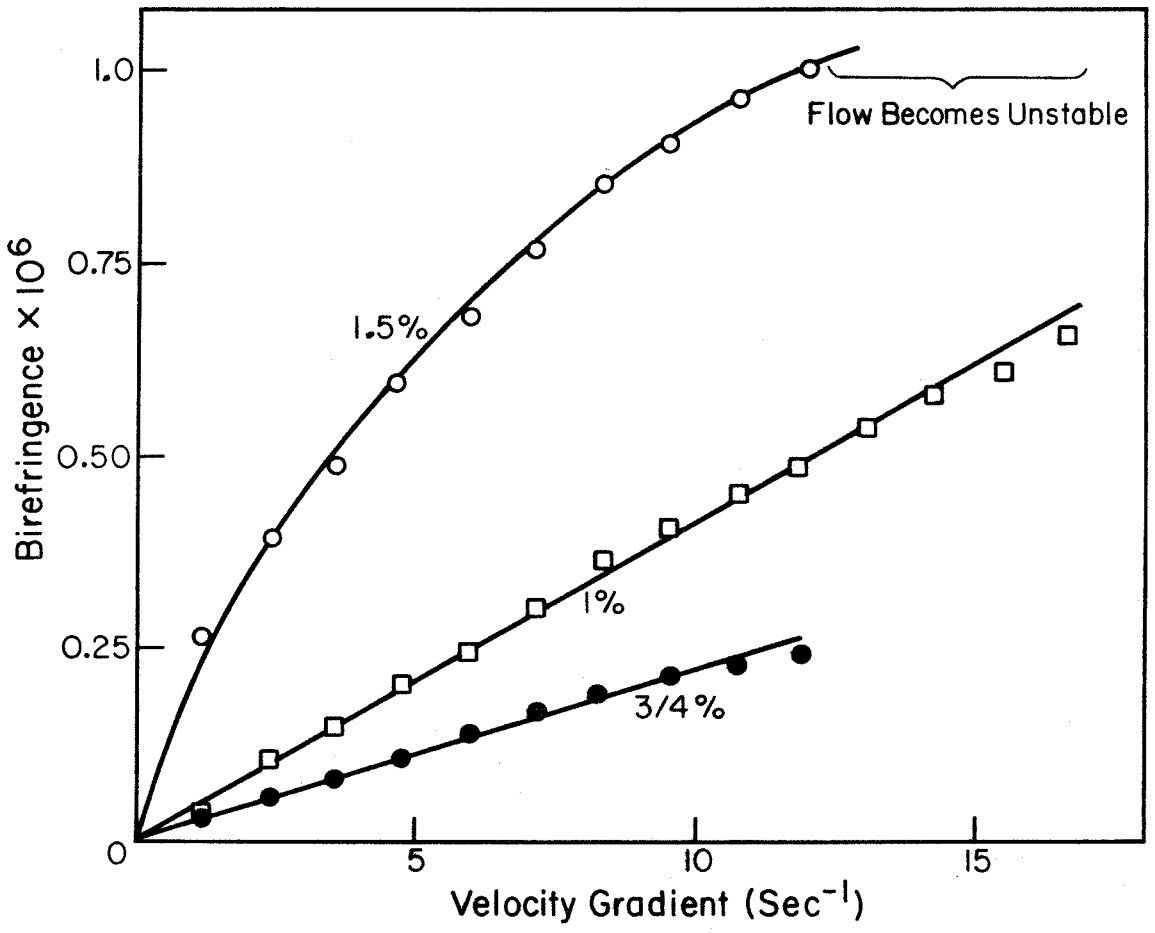
1.0
0.75
0.50
0.25
0
Birefringence x 10^6
Flow Becomes Unstable
1.5%
1%
3/4%
5
10
15
Velocity Gradient (Sec^-1)

Fig. 12

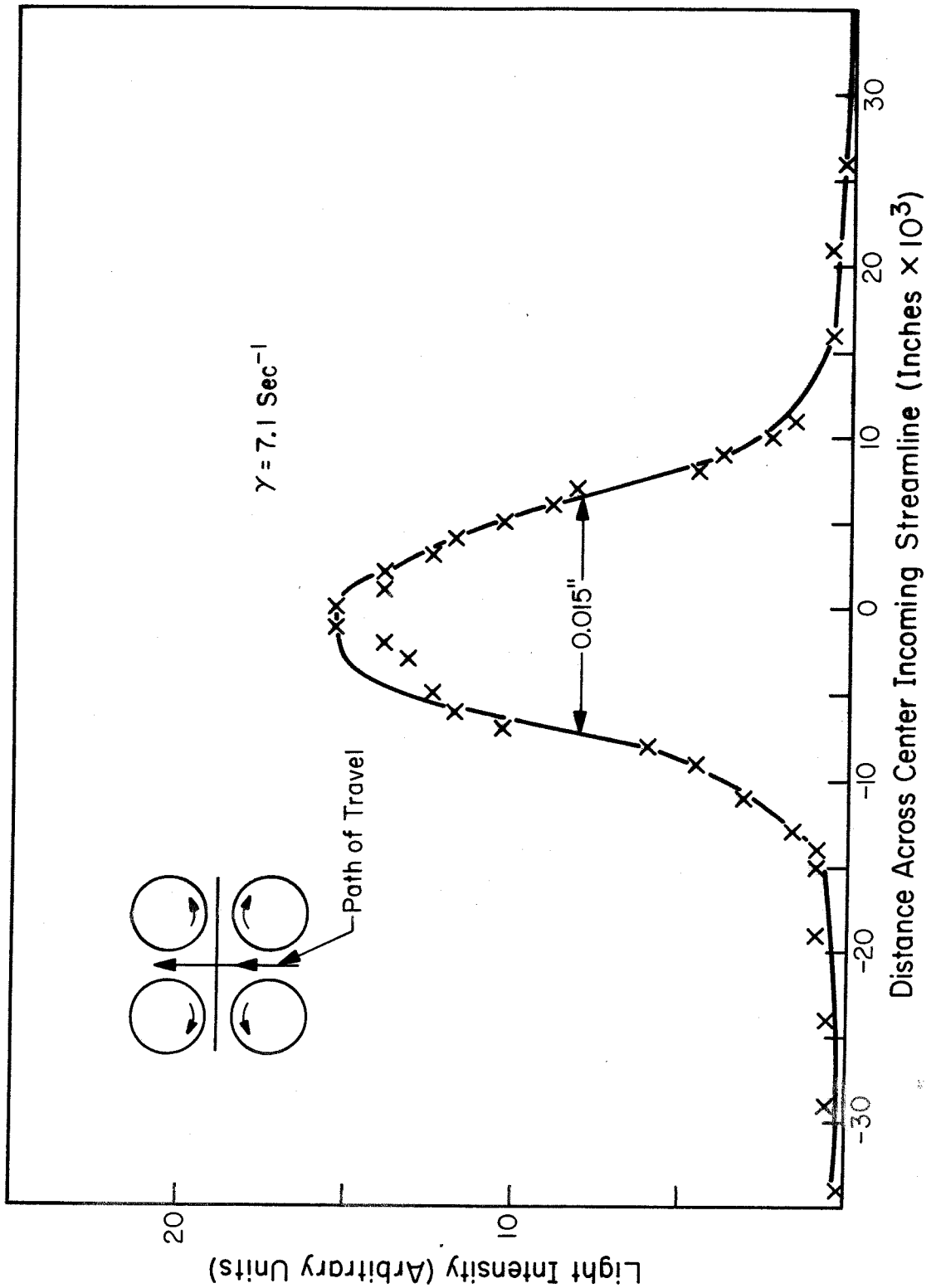
Light Intensity (Arbitrary Units)
20
10
$\gamma = 7.1\ Sec^{-1}$
0.015"
Path of Travel
-30
-20
-10
0
10
20
30
Distance Across Center Incoming Streamline (Inches × 10^3)

Fig. 13

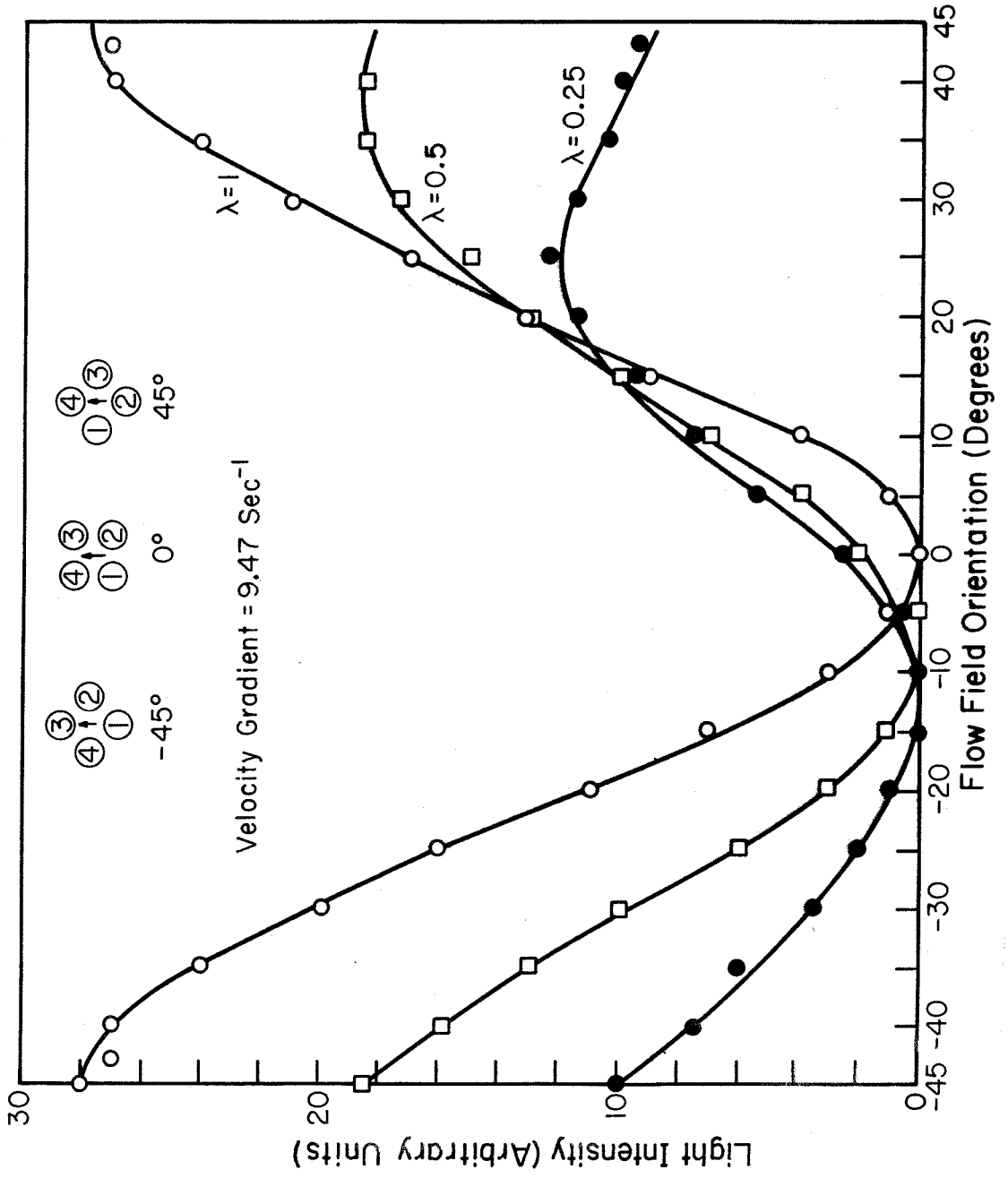
Light Intensity (Arbitrary Units)
Flow Field Orientation (Degrees)
Velocity Gradient = 9.47 Sec⁻¹
λ=1
λ=0.5
λ=0.25
-45°
0°
45°

Fig. 14

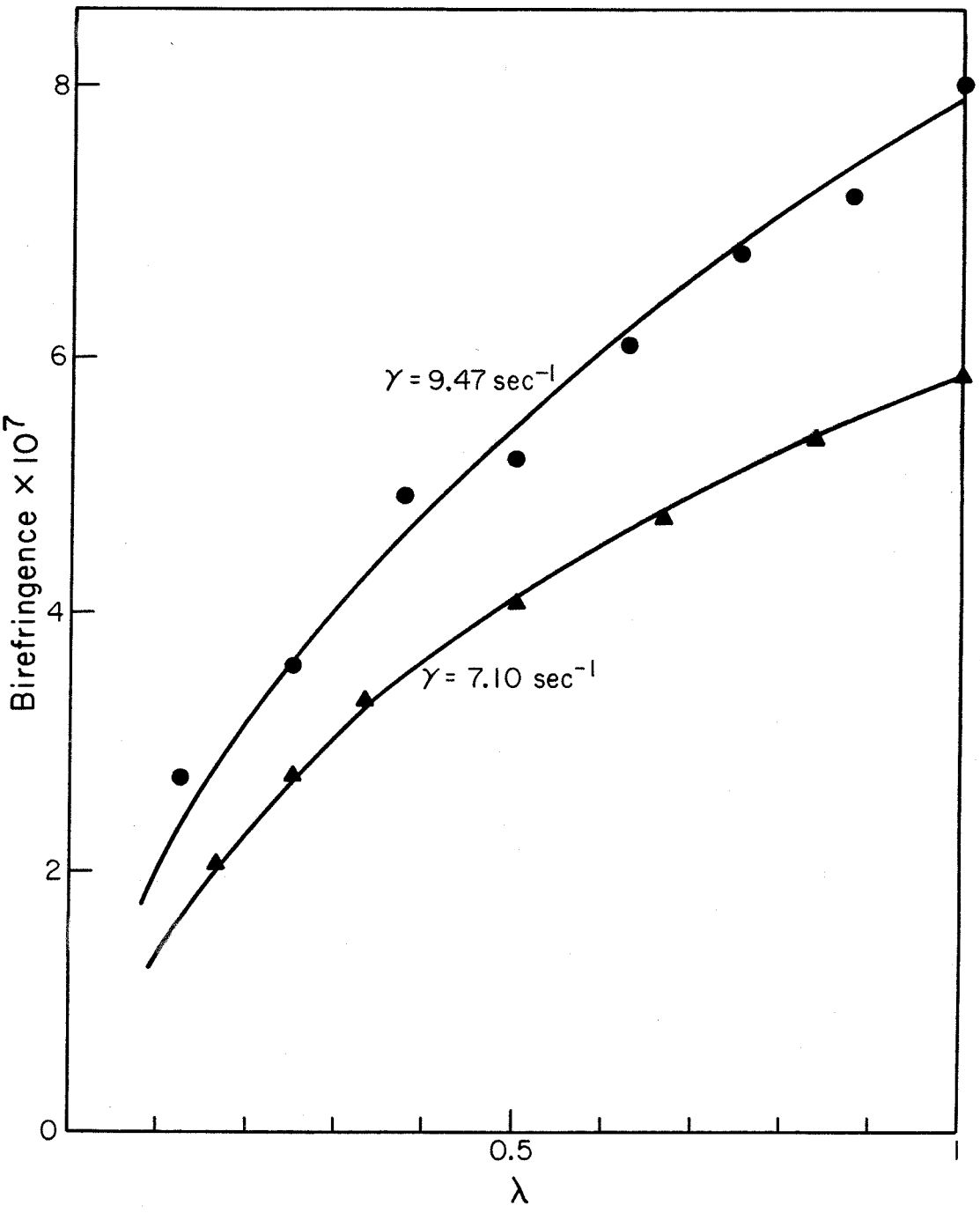

Fig. 15

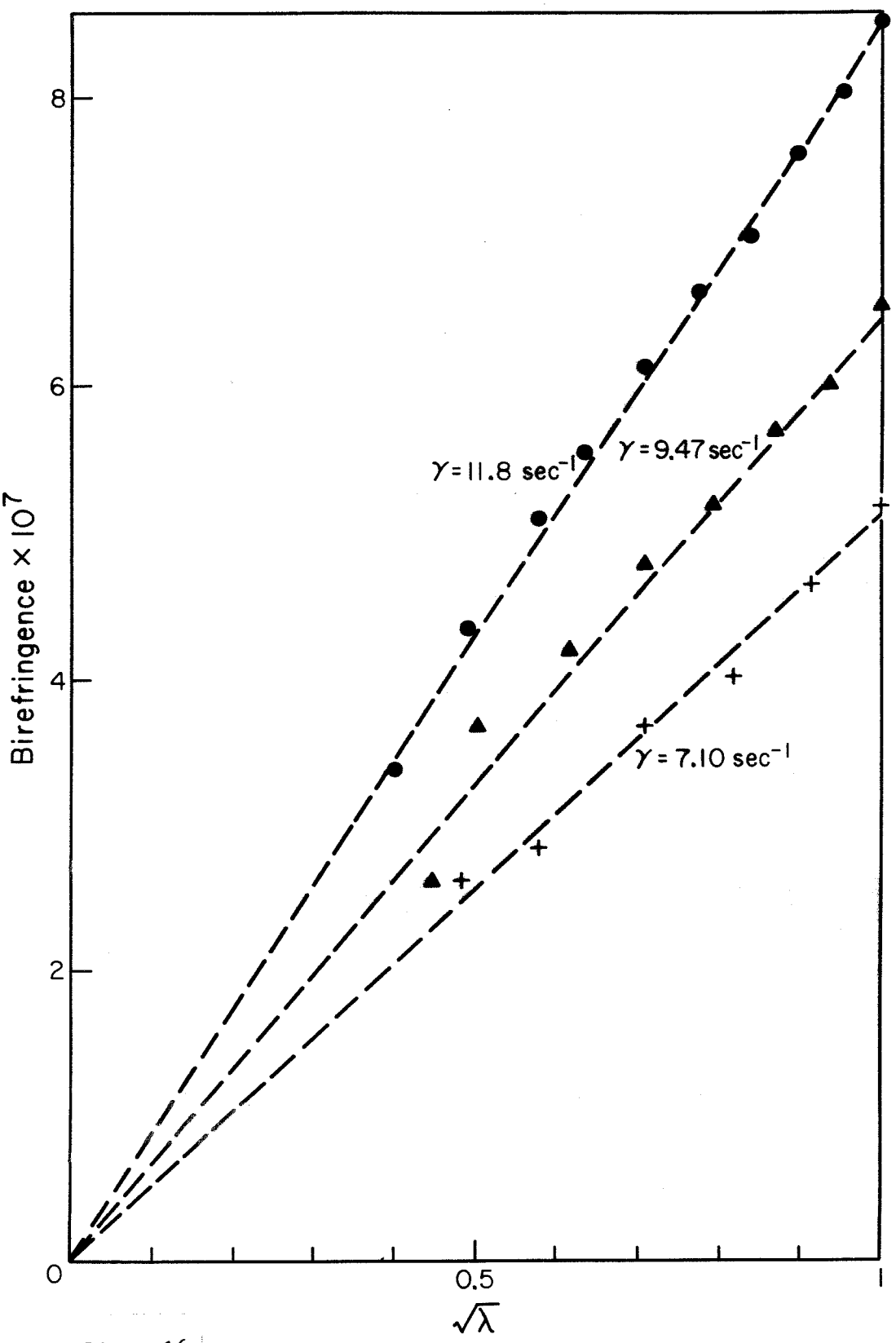

Fig. 16

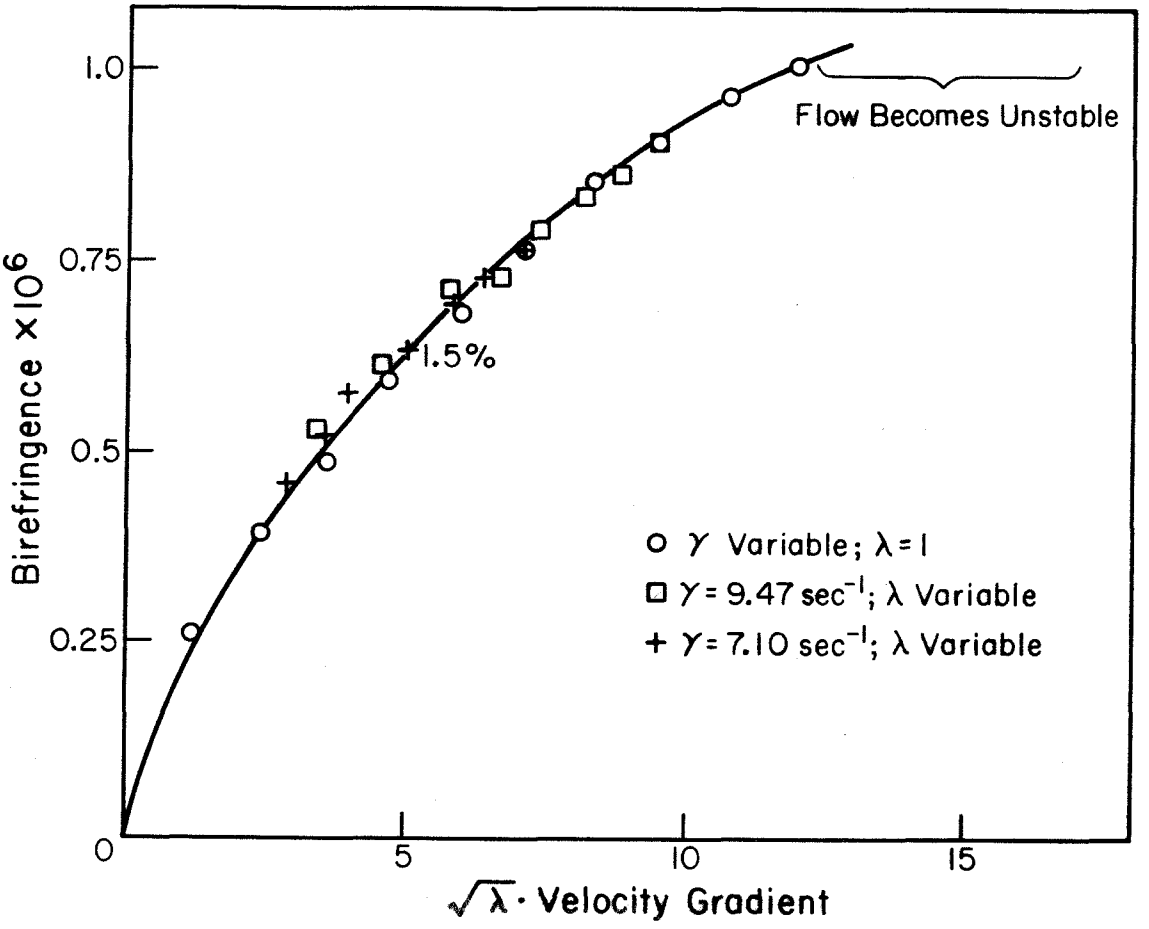
1.0
0.75
0.5
0.25
0
Birefringence ×10⁶
5
10
15
√λ · Velocity Gradient
Flow Becomes Unstable
1.5%
○ γ Variable; λ = 1
□ γ = 9.47 sec⁻¹; λ Variable
+ γ = 7.10 sec⁻¹; λ Variable

Fig. 17

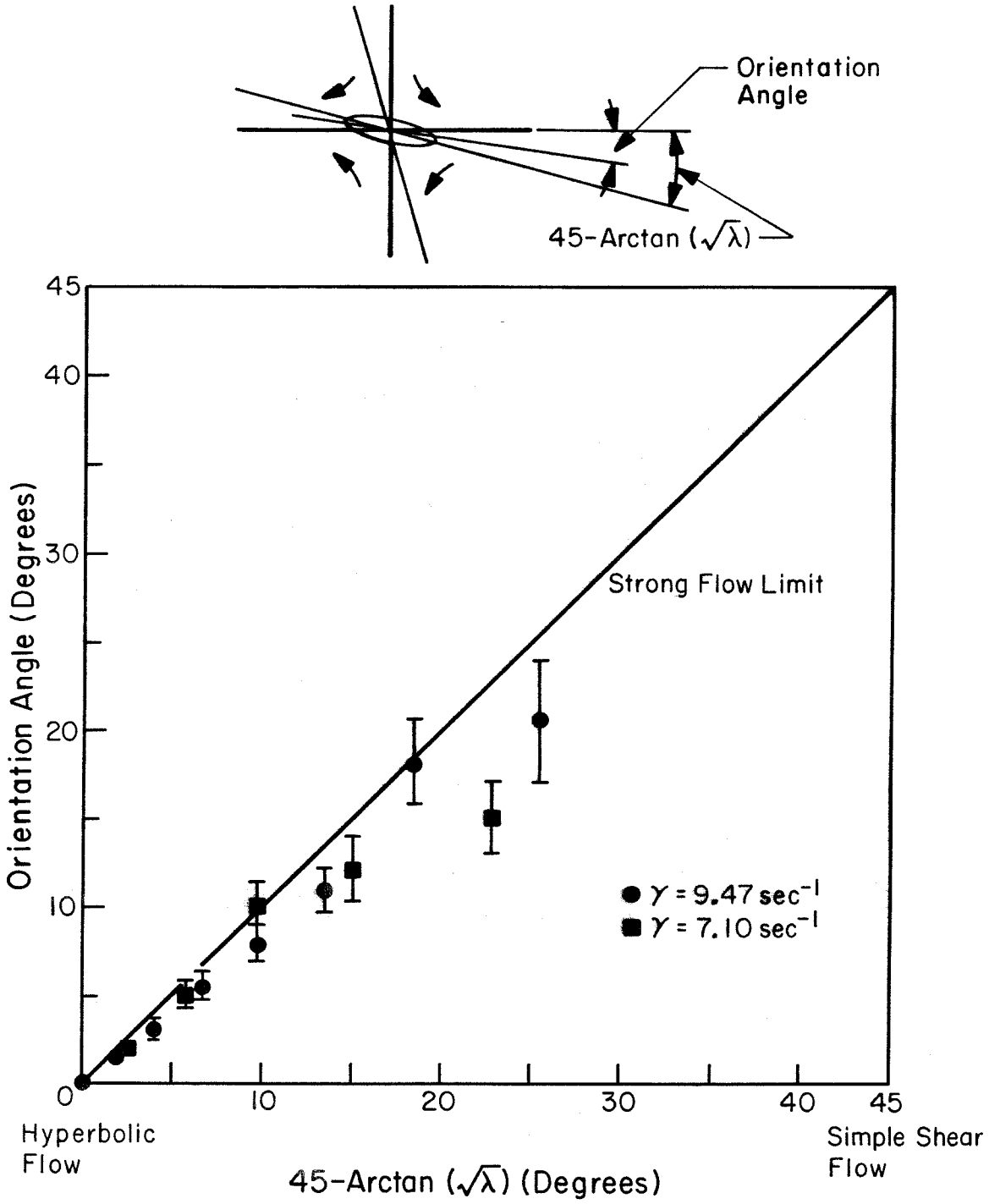
Orientation Angle
45-Arctan (√λ)
Strong Flow Limit
● γ = 9.47 sec⁻¹
■ γ = 7.10 sec⁻¹
Orientation Angle (Degrees)
45-Arctan (√λ) (Degrees)
Hyperbolic Flow
Simple Shear Flow
0
10
20
30
40
45

Fig. 18

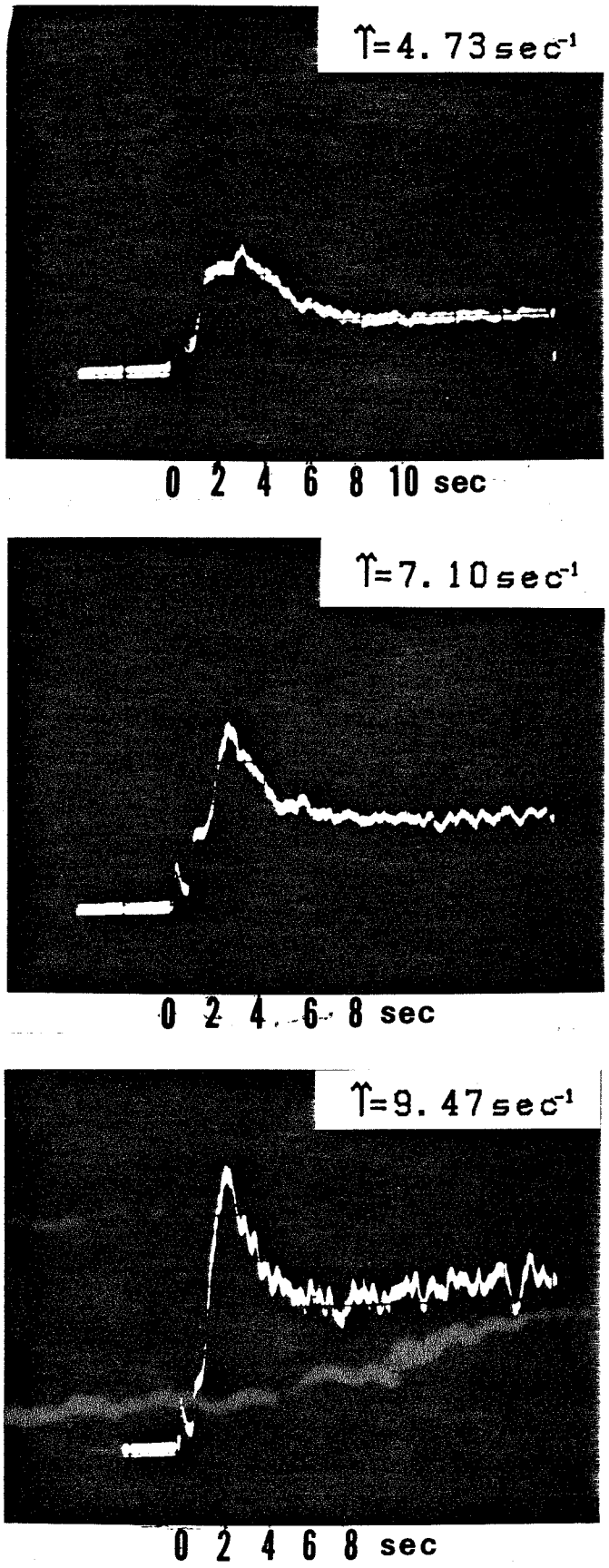

Fig. 19

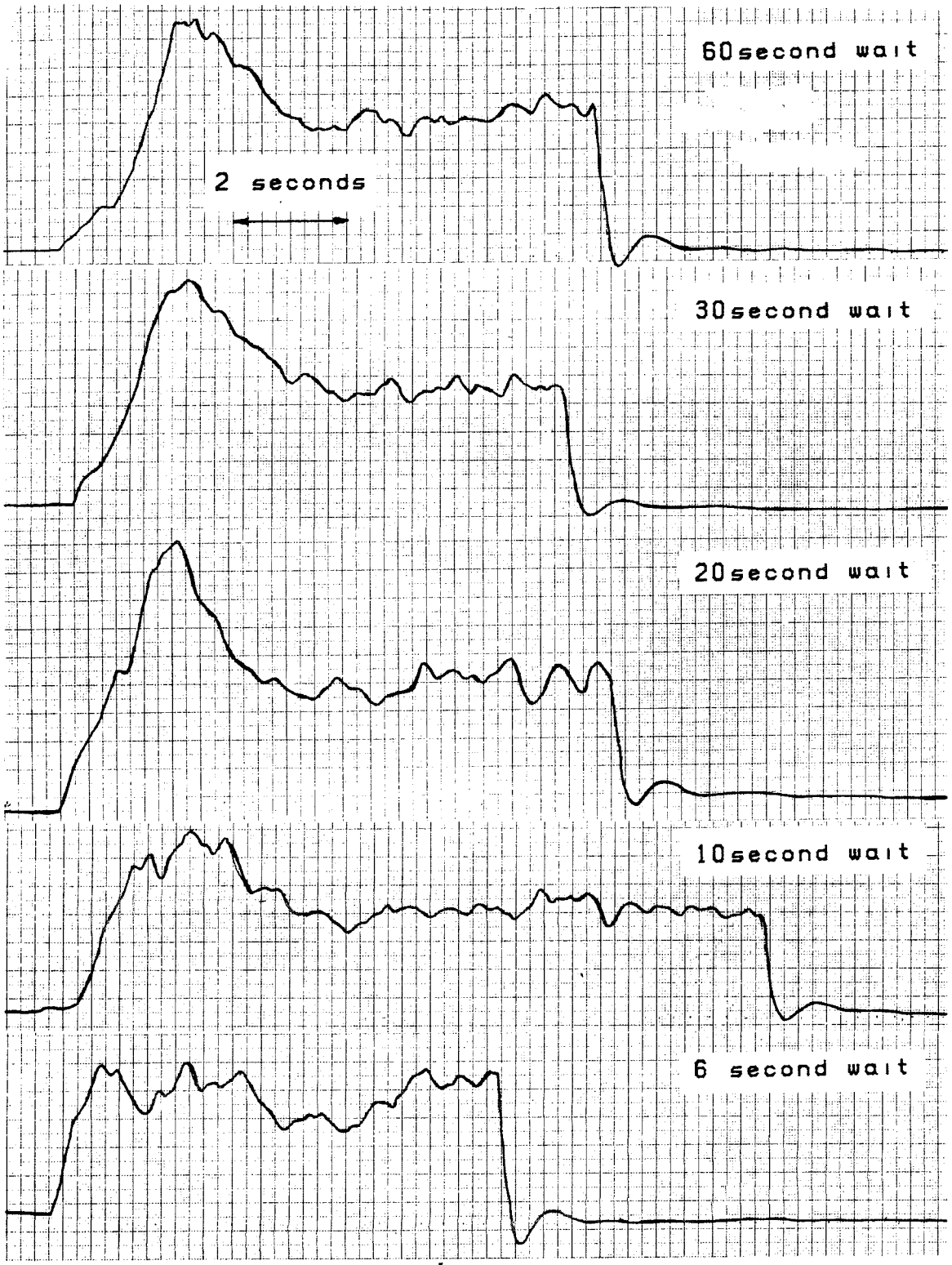
60 second wait
2 seconds
30 second wait
20 second wait
10 second wait
6 second wait

Fig. 20

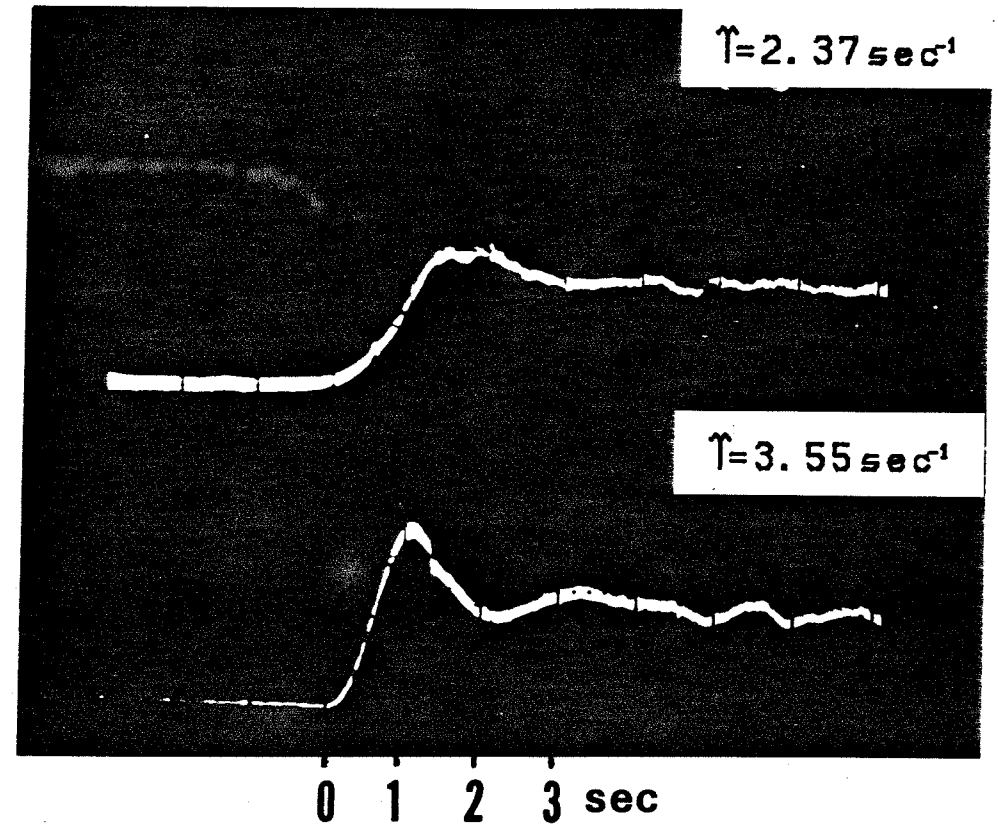

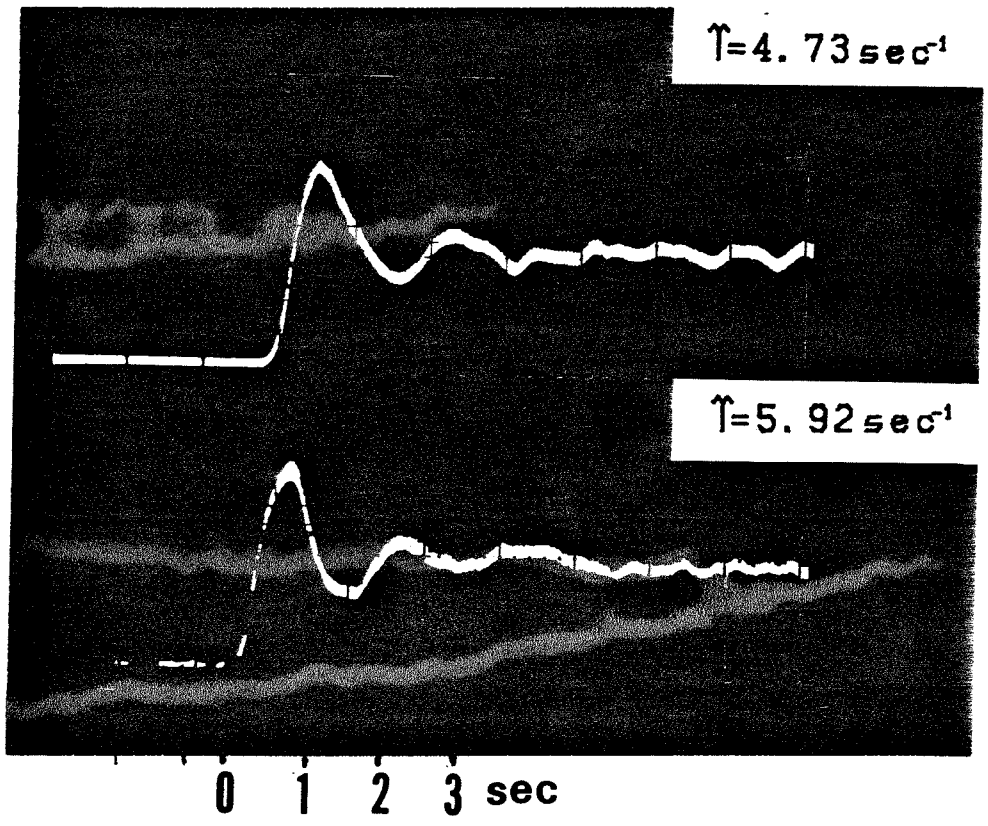

Fig. 21

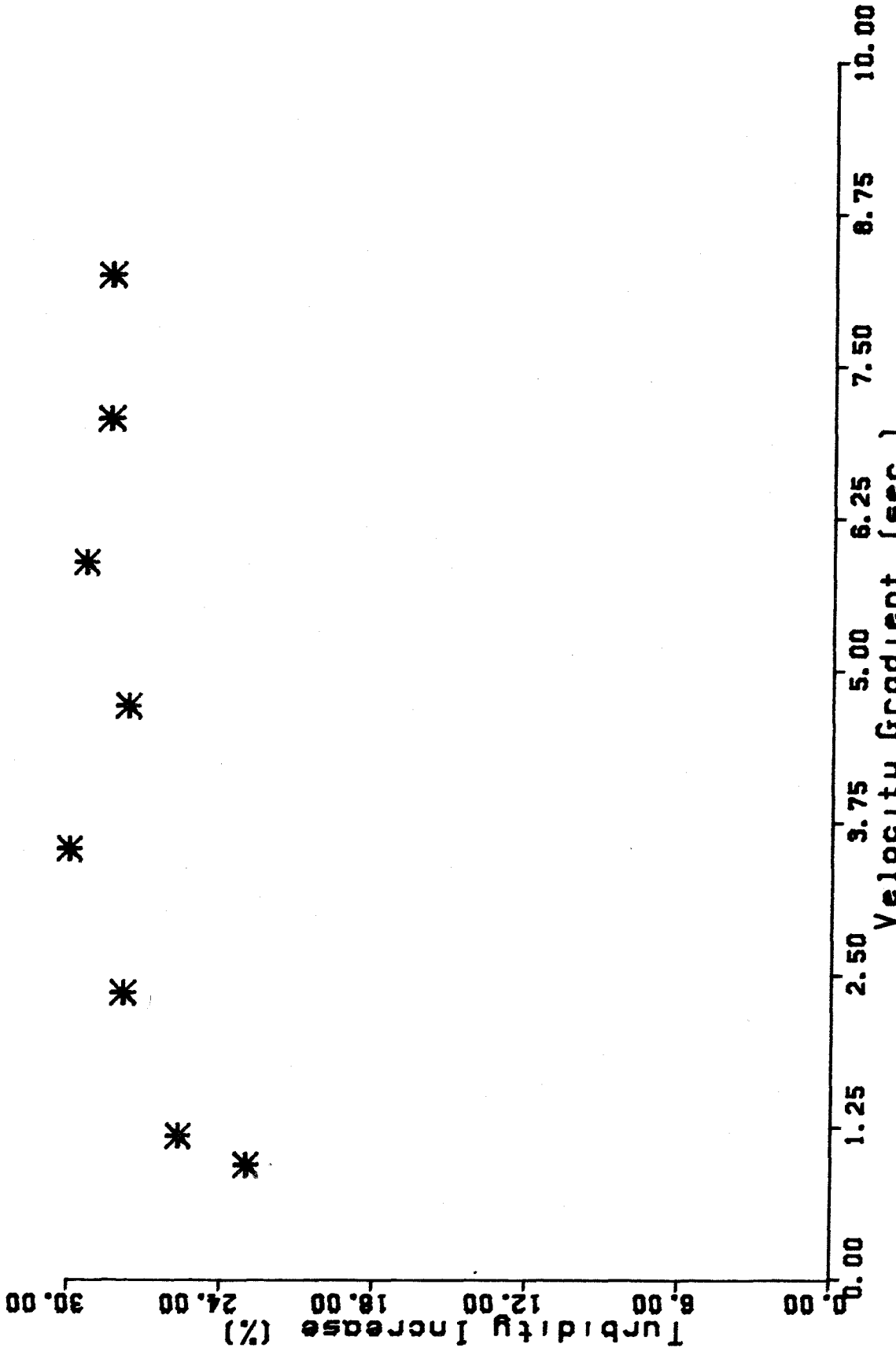
Turbidity Increase (%)
0.00
8.00
12.00
18.00
24.00
30.00
0.00
1.25
2.50
3.75
5.00
6.25
7.50
8.75
10.00
Velocity Gradient (sec)

Fig. 22

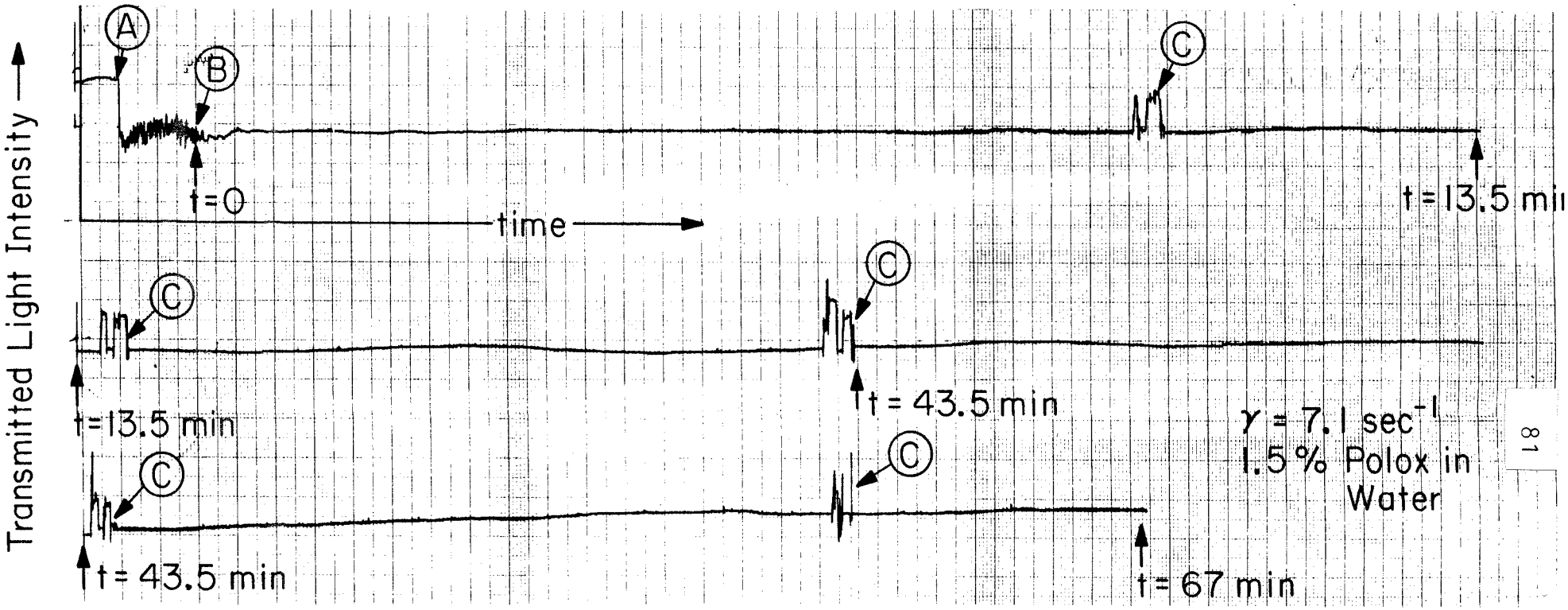
Transmitted Light Intensity
A
B
t=0
time
C
t=13.5 min
C
t = 43.5 min
C
t = 43.5 min
C
t = 67 min
t = 13.5 min
γ = 7.1 sec⁻¹
1.5 % Polox in
Water

Fig. 23

Network Models of Concentrated Polymer Solutions Derived from the Yamamoto Network Theory

by

G. G. Fuller and L. G. Leal
Department of Chemical Engineering
California Institute of Technology
Pasadena, California 91125

Abstract

Several choices of the functions describing the creation and destruction processes of entanglement junctions in the Yamamoto network theory of concentrated polymer solutions have been examined. These choices are simple functions of the extension of the network segments bridging the entanglement points and it is demonstrated that the moments of the distribution function describing the network conformation can be solved for analytically. This has been done for a wide range of two dimensional flows and for both the steady state and transient problem. the macroscopic stress tensor and flow birefringence are calculated and a variety of nonlinear effects result and are discussed.

I. Introduction

The traditional model of a concentrated polymer solution views the system as a three dimensional network formed from intermolecular entanglements of long chain macromolecules in close proximity. The resulting complex structure is simplified by envisioning this network as composed of elastic strands joined through temporary junctions, a notion which was motivated by the successful application of statistical mechanics to the description of rubber elasticity. Whereas the junctions in a rubber may be formed from permanent crosslinks, the network theory of concentrated solutions allows the junctions to be temporary and constantly undergoing creation and destruction processes. This model originated with the papers of Yamamoto (1956,1957,1958) and Lodge (1956) and can successfully describe many important macroscopic properties. The model proposed by Lodge, being linear, yields analytical results and has received a great deal of attention. A number of authors have subsequently modified it (Kaye (1966), Bird and Carreau (1968)) in an attempt to improve its predictive capability but these efforts have been largely empirical and do not offer a great deal of insight into the behavior of the network model. The model formulated by Yamamoto (1956, 1957), however, is of a more

general form which, though incapable of yielding analytical results without specification of certain molecular variables, does offer the possibility of providing this additional insight. This paper presents the results of several physically realistic choices for these molecular variables and demonstrates that simple, analytical results can be obtained which are capable of describing a variety of nonlinear phenomena.

II. Development of the Model

Figure 1 depicts the physical representation of the concentrated polymer solution as envisioned by Yamamoto. The state of the network is described through a distribution function $f(\underline{x},N,t)$, defined such that fd^3x is the number of elastic segments in the network with end to end vector in the range from $\underline{x}$ to $\underline{x}+d\underline{x}$ at a time t, which is composed of N statistical subunits. The objective in constructing the model is to relate macroscopic quantities such as stress and birefringence to the number, orientation and deformation of the network segments averaged over all possible conformations. The distribution function f obeys a continuity equation

$$\frac{\partial f}{\partial t} + \nabla\cdot(\dot{\underline{x}}f) = G(\underline{x},N) - \beta(\underline{x},N)\,f \qquad (1)$$

in which $\dot{\underline{x}}$ is the rate of change of the segment end to end vector. The function $G(\underline{x},N)$ governs the rate of entanglement creation and is defined such that $G(\underline{x},N)d^3\underline{x}dt$ is the number of segments formed with N subunits and end to end vector $\underline{x}$ in the time interval dt. The destruction of entanglement junctions is assumed to occur at a rate $\beta(\underline{x},N)$ which in general is a function of the conformation of the segments.

We shall consider the response of the network structure, as defined by the distribution function f, when the solution as a whole undergoes a general, linear motion

$$\underline{u} = \underline{\underline{\Gamma}} \cdot \underline{R} \qquad (2)$$

which is described via a velocity gradient tensor, $\underline{\underline{\Gamma}}$. Here $\underline{R}$ is a position vector of a material point defined from some arbitrary origin. If a polymer segment bridges two entanglement points with position vectors $\underline{R}_1$ and $\underline{R}_2$, the end to end vector of the segment is defined as $\underline{x} = (\underline{R}_2 - \underline{R}_1)$.

The most common assumption is that the junctions forming the network move affinely with the imposed velocity field so that $\dot{\underline{x}} = \underline{\underline{\Gamma}} \cdot \underline{x}$. In order to relax this assumption, Phan-Thien and Tanner (1977) have introduced an empirical

"slip tensor" which causes the network junctions to depart from a purely affine motion and have further assumed this tensor to be a linear function of the rate of deformation tensor $\underline{\underline{D}}(\underline{\underline{\Gamma}}+\underline{\underline{\Gamma}}^{+})/2$. Following this example, we shall take

$$\dot{\underline{x}} = (\underline{\underline{\Gamma}} - \xi\underline{\underline{D}}) \cdot \underline{x} \tag{3}$$

in which the parameter ξ is the slip coefficient. The effect of the slip mechanism used here, therefore, is to have the network deform affinely as if it were subjected to an "effective" velocity gradient tensor $\overset{*}{\underline{\underline{\Gamma}}} = (\underline{\underline{\Gamma}} - \xi\underline{\underline{D}})$.

A similar approach has also been used by Gordon et al (1971-77) in a series of papers for bead and spring models used to describe dilute polymer solutions. Equations (1) and (3) combine to produce

$$\frac{\partial f}{\partial t} + \nabla(\underline{\underline{\Gamma}} - \xi\underline{\underline{D}}) \cdot \underline{x}f = G(\underline{x},N) - \beta(\underline{x},N)f \tag{4}$$

Equation (4) is identical (with ξ=0) to that originally derived by Yamamoto and forms the starting point for several variations of the Yamamoto model (Phan-Thien and Tanner (1977), Wiegel (1969)). Since it is a first order parabolic differential equation, the method of characteristics can be used to solve equation (4) exactly for any choice of the functions G and β (although the resulting integrations may

be difficult to carry out). In the following sections, we shall present results for several ad hoc, though physically realistic, choices of G and β. For the purpose of example we shall consider a two dimensional linear flow in which

$$\underline{\underline{\Gamma}} = \frac{\gamma}{2} \begin{pmatrix} (1+\lambda) & (1-\lambda) & 0 \\ -(1-\lambda) & -(1+\lambda) & 0 \\ 0 & 0 & 0 \end{pmatrix} \tag{5}$$

where γ is the magnitude of the local velocity gradient. The parameter λ specifies the particular type of two dimensional flow and varies between ± 1. This type of motion was chosen because it offers the possibility of examining the important effects which occur with variations in the amount of vorticity in the flow and because it can be realized experimentally in a four roll mill. Flow birefringence experiments utilizing such a flow device have been conducted in this laboratory for concentrated polymer solutions and the detailed results of this work can be found elsewhere (Fuller and Leal (1980a)). Figure 2 shows the range of flows described by the velocity gradient tensor of equation (5) as λ is varied. The ratio of vorticity to the rate of extension which exists in this flow is

$$W_o = \frac{(1-\lambda)}{(1+\lambda)} \tag{6}$$

In order to proceed with the solution of equation (4) it is convenient to diagonalize the tensor $\underline{\underline{\Gamma}}^* = (\underline{\underline{\Gamma}} - \xi \underline{\underline{D}})$ by introducing a tensor $\underline{\underline{T}}$ such that $\underline{\underline{T}}^{-1} \cdot \underline{\underline{E}}\, \underline{\underline{T}} = \underline{\underline{V}}$ where $\underline{\underline{V}}$ is diagonal. Furthermore we transform the coordinates to a new frame $\underline{\rho} = (\underline{\rho}, \eta, z)$ such that $\underline{x} = \underline{\underline{T}} \cdot \rho$. The tensor $\underline{\underline{T}}$ is

$$\underline{\underline{T}} = \begin{pmatrix} \sqrt{U^+} & \sqrt{U^-} & 0 \\ -\sqrt{U^-} & \sqrt{U^+} & 0 \\ 0 & 0 & 0 \end{pmatrix} \tag{7}$$

where $$U^{\pm} = \{[(1-\xi)(1+\lambda) \pm \sqrt{V}]/2(1-\xi)(1+\lambda)\}^{1/2} \tag{8a}$$

$$V = (1-\xi)^2(1+\lambda)^2 - (1-\lambda)^2 \tag{8b}$$

The diagonalized tensor $\underline{\underline{V}}$ is then

$$\underline{\underline{V}} = \frac{\gamma}{2} \begin{pmatrix} \sqrt{V} & 0 & 0 \\ 0 & -\sqrt{V} & 0 \\ 0 & 0 & 0 \end{pmatrix} \tag{9}$$

and the continuity equation becomes

$$\frac{\alpha f}{\alpha t} + \frac{\gamma}{2} \sqrt{V} \frac{\alpha f}{\alpha t} - \frac{\gamma}{2} \sqrt{V} \frac{\alpha f}{\alpha \eta} = \hat{G}(\underline{\rho}, N) - \hat{\beta}(\underline{\rho}, N) f \tag{10}$$

where $\hat{G}(\underline{\rho}, N) = G(\underline{\underline{T}}\rho, N)$ and $\hat{\beta}(\underline{\rho}, N) = \beta(\underline{\underline{T}} \cdot \underline{\rho})$. The forms chosen for G and β at the rest state will be assumed to depend only on

the magnitude of the square of the end to end vector $(\underline{x}\cdot\underline{x}) = (\underline{\rho}\ (\underline{\underline{T}}^{+}\cdot\underline{\underline{T}})\underline{\rho})$. It is convenient at this point to write out the transformed value of this scalar quantity

$$x^2 + y^2 + z^2 = \rho^2 - 2w\rho\eta + \eta^2 + z^2 \tag{11}$$

where

$$w = (1 - \lambda)/(1 - \xi)(1 + \lambda) \tag{12}$$

When ξ is zero (affine deformation) w is precisely the ratio of vorticity to the rate of extension and the ρ and η axes are the principle axes of strain for the flow field defined by equation (5). In order to calculate macroscopic properties, it is necessary to determine the moments $\langle x^2 \rangle$, $\langle y^2 \rangle$, $\langle xy \rangle$, $\langle z^2 \rangle$ and $n=\langle 1 \rangle$. The quantity n is identified as the concentration of junctions existing in the network at any given time. These moments are related to the moments of the transformed frame by the multiplicative factor of $\det(\underline{\underline{T}}) = (1-w^2)^{1/2}$.

The characteristics of equation (10), expressed in terms of the coordinates (ρ, η, z) are

$$\rho = \rho_o e^{\sqrt{\frac{v}{2}}\,\gamma t}$$

$$\eta = \eta_o e^{-\sqrt{\frac{v}{2}}\,\gamma t} \qquad (13)$$

$$z = z_o$$

and the solution of equation (10), obtained by the method of characteristics is

$$f(\rho,\eta,z,t) = f_o(\rho_o,\eta_o,z_o)e^{-\int_o^t dt'\hat{\beta}(\rho_o e^{\frac{\gamma}{2}\sqrt{vt}'},\eta_o e^{-\frac{\gamma}{2}\sqrt{vt}'},z,N)}$$

$$+ \int_o^t dt'\hat{G}(\rho_o e^{\frac{\gamma}{2}\sqrt{vt}},\eta_o e^{-\frac{\gamma}{2}\sqrt{vt}},z_o,N)e^{-\int_t^t dt''\hat{\beta}(\rho_o e^{\frac{\gamma}{2}\sqrt{vt}''},\eta_o e^{-\frac{\gamma}{2}\sqrt{vt}''},z_o,N)} \qquad (14)$$

where $f_o(\rho_o,\eta_o,z_o)$ is the value of the segment distribution function at time t=0. For the case of no flow (γ=0), the relaxation of f with time is given by

$$f(\rho,\eta,z,t) = f_o(\rho,\eta,z)e^{-\hat{\beta}(\rho,\eta,z,N)t} + \frac{\hat{G}(\rho,\eta,z,N)}{\hat{\beta}(\rho,\eta,z,N)}\left(1-e^{-\hat{\beta}(\rho,\eta,z,N)t}\right) \qquad (15)$$

For the case of non zero γ, the most important time dependent problem is the evolution of f when the solution

starts from rest with a flow of the type defined by equation (5). The initial distribution for this case is given by taking the time in equation (15) to infinity giving

$$f_o(\rho,\eta,z) = \frac{\hat{G}(\rho,\eta,z,N)}{\hat{\beta}(\rho,\eta,z,N)} \tag{16}$$

For a given function $g(\rho,\eta,z)$, its average can be found immediately by integrating against the distribution function, f, over the coordinates (ρ,η,z). In carrying this out it is convenient to make a change in the variables of integration in equation (14) from t' and t'' to $\rho' = \rho_o e^{\frac{\gamma}{2}\sqrt{vt'}}$ and $\rho''=\rho_o e^{\frac{\gamma}{2}\sqrt{vt''}}$. The average of the function g is then

$$\langle g\rangle = \sqrt{1-w^2}\int_{-\infty}^{\infty}\iiint d\rho d\eta dz\, g(\rho,\eta,z) f_o\left(\rho e^{-\frac{\gamma}{2}\sqrt{vt}}, \eta e^{\frac{\gamma}{2}\sqrt{vt}}, z\right)$$

$$\times \exp\left[-\frac{2}{\sqrt{v\gamma}}\int_{\rho e}^{\rho} -\frac{\gamma}{2}\sqrt{vt}\,\frac{d\rho'}{\rho'}\hat{\beta}\left(\rho',\frac{\rho\eta}{\rho'},z,N\right)\right] \tag{17}$$

$$+\sqrt{1-w^2}\,\frac{2}{\sqrt{v\gamma}}\int_{-\infty}^{\infty}\iiint d\rho d\eta dz\, g(\rho,\eta,z)\int_{\rho e}^{\rho} -\frac{\gamma}{2}\sqrt{vt}\,\frac{d\rho'}{\rho'}\hat{G}\left(\rho',\frac{\rho\eta}{\rho'},z,N\right)$$

$$\times \exp\left[-\frac{2}{\sqrt{v\gamma}}\int_{\rho'}^{\rho}\frac{d\rho''}{\rho''}\,\hat{\beta}\left(\rho'',\frac{\eta\rho}{\rho''},z\right)\right]$$

Further changes in the variables of integration in the second integral in equation (17) from η, ρ', ρ'' to $\bar{\eta}=\frac{\rho\eta}{\rho'}$ and $\rho'=T\bar{\rho}+\rho e^{-\frac{\gamma}{2}\sqrt{vt}}$ where $T=(1-e^{-\frac{\gamma}{2}\sqrt{vt}})$ are made. Using the spherical symmetry of $G(\underline{x},N)$, the order of integration in the second integral of equation (17) is reversed and a further

change of variables of $\theta=\rho/\overline{\rho}$ and $\theta'=\rho''/\overline{\rho}$ shall be made. This leads to (after dropping the overbars on ρ and η)

$$\langle g\rangle = \sqrt{1-w^2}\int_{-\infty}^{\infty}\int\int d\rho d\eta dz\, g(\rho,\eta,z) f_o(\rho e^{-\frac{\gamma}{2}\sqrt{vt}}, e^{\frac{\gamma}{2}\sqrt{vt}}, z)$$

$$+ \frac{2T}{\sqrt{v\gamma}}\int_{-\infty}^{\infty}\int\int d\rho d\eta dz \int_1^{\infty}\frac{d\theta}{\theta}\, g(\rho\theta, \frac{T+\theta e^{-\frac{\gamma}{2}\sqrt{vt}}}{\theta}\eta, z)\hat{G}([T+\theta e^{-\frac{\gamma}{2}\sqrt{vt}}]\rho,\eta,z,N) \qquad (18)$$

$$\times \exp\left[-\frac{2}{\sqrt{v\gamma}}\int_{T+\theta\epsilon}^{\theta} -\frac{\gamma}{2}\sqrt{vt}\,\frac{d\theta'}{\theta'}\hat{\beta}(\rho\theta', \frac{T+\theta e^{-\sqrt{\frac{v}{2}}\gamma t}}{\theta'}\eta, z)\right]$$

Equation (18) is the time dependent generalization of the result obtained by Yamamoto (1957). In order to proceed further, it is necessary to specify the forms of G and β. Except where otherwise stated, the "Gaussian approximation" for the distribution $G(\underline{x},N)$ (Lodge (1968)) will be taken. In employing this assumption, the N subunits forming the segments are taken to be statistically independent and undergoing a random walk in space and it is further assumed that the mean extension of a segment never approaches the maximum possible end to end distance of Na where a is the length of a single subunit. This allows the spring function for the segments to be approximated as linear. In order to allow for the possibility that the segments might approach a nearly fully extended state it would be necessary to use a nonlinear spring function which ensured finite extensibility in much the same way that a nonlinear spring function is used in the description of dilute polymer solutions (Peterlin (1961)). If the end to end distance is made nondimensional with respect to the maximum end to end

distance, the function G is

$$G(\underline{x},N) = L\left(\frac{3N}{2}\right)^{\frac{3}{2}} e^{-\frac{3N}{2}(x^2+y^2+z^2)} \tag{19}$$

where L is assumed to be independent of the conformation for all the models considered here with the exception of the model of Phan-Thien and Tanner (1977) who assumed L to be proportional to $\langle r^2 \rangle$.

Yamamoto (1956) has calculated the stress tensor of the Gaussian network by determining the forces related to changes in the free energy of the system undergoing a virtual deformation. Using this approach he was able to show that

$$\underline{\underline{\tau}} = 3NRT \langle \underline{x}\,\underline{x} \rangle \tag{20}$$

where kT is the Boltzmann temperature.

The stresses which are most commonly measured are the shear stress and normal stress differences in simple shear flow, and the normal stress difference in purely extensional flow. For the case of simple shear flow, (λ=0), it should be noted that the (x,y,z) frame used in equation (5) is rotated 45° in the (x,y) plane from that normally used. If

$\hat{\underline{\underline{\tau}}}$ is the stress tensor in the plane rotated by 45° in the clockwise direction in the (x,y) plane, the shear stress in simple shear flow is

$$S \equiv \hat{\tau}_{\hat{x}\hat{y}} = \frac{3N\dot{k}T}{\zeta} (< x^2-y^2 >) \tag{21}$$

while the first and second normal stress differences are

$$N_1 \equiv \hat{\tau}_{\hat{x}\hat{y}} - \hat{\tau}_{\hat{x}\hat{y}} = 3N\dot{k}T < xy > \tag{22a}$$

$$N_2 \equiv \hat{\tau}_{\hat{y}\hat{y}} - \hat{\tau}_{\hat{z}\hat{z}} = 3N\dot{k}T(\tfrac{1}{2}< x^2+2xy+y^2 > - < z^2 >) \tag{22b}$$

For purely extensional flow, $\lambda = 1$ in equation 5, the normal stress difference of interest is

$$N_1' \equiv \tau_{xx} - \tau_{yy} = 3N\dot{k}T < x^2-y^2 > \tag{23}$$

In addition to the stress tensor, the birefringence resulting from the deformed system can be calculated. The birefringence results from the anisotropy of the polarizability tensor of the deformed network. The polarizability tensor of the segment can be related to the end to end vector for a segment by averaging over the contributions to the polarizability tensor of the individual backbone elements of the chain. This has been done for the Gaussian chain by Kuhn and Grun (1942). Their derivation

leads to the following polarizibility tensor for the segments (Yamakawa (1971))

$$\underline{\underline{\mu}} = N(p-q)\underline{\underline{I}} + 3(Na)^2 q < \underline{x}\,\underline{x} > \tag{24}$$

where p and q are constants independent of the segment conformation. Birefringence measured in the (x,y) plane is proportional to the difference in the major and minor principal axes of the polarizibility tensor. Therefore, the birefringence is simply proportional to the difference of the eigenvalves of the tensor $< \underline{x}\,\underline{x} >$ with the third column and row omitted giving

$$\Delta n = A\left\{(< x^2 > - < y^2 >)^2 + 4< xy >^2\right\}^{\frac{1}{2}} \tag{25}$$

where A is a constant of proportionality.

In what follows, several choices for the destruction function β will be examined and the corresponding stresses and birefringence calculated for simple flows of the type defined in equation (5).

III. Specific Network Models

A. Constant Breakage Function

Let us first consider the case in which β is taken to be a constant, i.e. $\beta = \beta_o$. In this case, the integrations involved in equation (18) can be easily carried out for the moments $n=\langle 1\rangle$, $\langle \rho^2\rangle$, $\langle \eta^2\rangle$, $\langle \rho\eta\rangle$ and $\langle z^2\rangle$. The results are

$$n = L/\beta_o \tag{26a}$$

$$\langle \rho^2 \rangle = \frac{L}{\beta_o} \cdot \frac{1}{3N} \frac{1-\sqrt{v}\alpha e^{-(1-\sqrt{v}\alpha t)}}{(1-w^2)(1-\sqrt{v}\alpha)} \tag{26b}$$

$$\langle \eta^2 \rangle = \frac{L}{\beta_o} \frac{1}{3N} \frac{1+\sqrt{v}\alpha e^{-(1+\sqrt{v}\alpha)t}}{(1-w^2)(1+\sqrt{v}\alpha)} \tag{26c}$$

$$\langle \eta\rho \rangle = \frac{L}{\beta_o} \frac{1}{3N} \frac{w}{1-w^2} \tag{26d}$$

$$\langle z^2 \rangle = \frac{L}{\beta_o} \frac{1}{3N} \tag{26e}$$

where $\alpha=\gamma/\beta_o$ is the dimensionless velocity gradient and time has been made nondimensional through multiplication by β_o. The moments $\langle x^2\rangle$, $\langle y^2\rangle$ and $\langle xy\rangle$ are then calculated by the relation $\langle \underline{x}\,\underline{x}\rangle = \langle \underline{\rho}\,\underline{\underline{T}}\;\;\underline{\underline{T}}\,\underline{\rho}\rangle$ and are

$$\langle xy \rangle = -\frac{L}{\beta_o} \frac{1}{3N} \frac{(1-\lambda)(1-\xi)}{(1-v\alpha^2)} \left[\alpha^2+2\alpha \frac{\sinh \sqrt{v}\alpha t}{\sqrt{v}} e^{-t} + 2\alpha^2 \cosh \sqrt{v}\alpha t\, e^{-t}\right] \tag{27a}$$

$$\left.\begin{matrix} <x^2> \\ <y^2> \end{matrix}\right\} = \frac{L}{\beta_o}\frac{1}{3N}\frac{(1-\xi)(1-\lambda)}{(1-v\alpha^2)}\left[\frac{1\pm(1-\xi)(1+\lambda)\alpha+(1-\lambda^2\alpha^2}{(1-\xi)(1+\lambda)}\right] \qquad (27b)$$

$$-[1\pm(1-\xi)(1+\lambda)\alpha]\alpha\cosh\sqrt{v}\alpha t\cdot e^{-t}+\left\{(1-\xi)(1+\lambda)\pm\sqrt{v}\alpha\right\}\frac{\alpha\sinh\sqrt{v}\alpha t e^{-t}}{\sqrt{v}}$$

where the upper sign in (27 b) is used for $<x^2>$ and the lower sign is used for $<y^2>$.

The constant destruction model leads to results which are precisely equivalent to the linear spring dumbbell used to model dilute solutions of macromolecules (Bird et al (1977)). The concentration of entanglement junctions, n, is a constant and remains at its rest state level L/β_o regardless of the flow strength. Since this concentration is constant, the network can be pictured as a solution of independent spring segments at a concentration of L/β_o and is therefore identical to the linear dumbbell model.

From the moments of equation (27), the stress functions and birefringence can be calculated. An extensive treatment of this model, in the context of dilute solutions of macromolecules, may be found in a series of papers by Gordon et al (1971-77). When $\xi=0$, the model predicts a shear rate independent viscosity and a zero second normal stress

difference. The growth of macroscopic properties from rest is monotonic for all flow types when the parameter v in equation 8 is positive. When ξ is nonzero, on the other hand, the model produces a shear thinning viscosity and a ratio of normal stress differences $N_2/N_1 = -\xi/2$ in simple shear flow. Examination of equation (27) shows that the growth in the moments can become oscillatory when ξ and λ are such that the parameter v in equation (8) is negative. It is interesting to note that the model, for finite values of ξ also predicts a maximum in the shear stress with respect to the velocity gradient in simple shear flow at $\alpha = 1/\sqrt{-v}$.

As pointed out by Lodge (1968), the constant destruction function model is equivalent to the Lodge network model with a single relaxation time. Several authors have modified the Lodge model in order to remove the deficiencies of a constant viscosity and zero second normal stress difference when $\xi = 0$. These include Kaye (1966) who related the creation and destruction functions to the local level of stress and Bird and Carreau (1968) who assumed that the creation and destruction processes are both linked to the second invariant of the rate of deformation tensor $\sqrt{\underline{\underline{D}}:\underline{\underline{D}}/2}$.

As in the case of the linear spring dumbbell, the

network model with a constant destruction function, is singular at a value of the dimensionless velocity gradient equal to

$$\alpha = 1/\sqrt{v} \tag{28}$$

With the linear dumbbell model, this singularity is removed by introducing a nonlinear spring function which forces finite extensibility (Peterlin (1961)). For a network model, it seems more likely that the singularity is removed by breaking of segment junctions as the structure is deformed. This can be accommodated in the present network model by making the destruction function, β , depend on the segment conformation. Since the function β is proportional to the probability that a given entanglement junction will break and leave the network, β should increase as the segments deform and the junctions support more tension. In the remaining models of this section physically plausible choices for the function β will be examined.

B. Quadratic Destruction Model

As the segments deform and the entanglement junctions support more tension, the probability of destruction should increase, as suggested in the preceding section. The destruction function should also be spherically symmetric in

the rest state. The simplest choice for β which has these properties and which admits largely analytical results is the following quadratic dependence on the end to end distance

$$\beta = \beta_o(1+\sigma(x^2+y^2+z^2)) \tag{29}$$

where σ is the square of the ratio of the maximum end to end distance to the length scale over which β changes. This form for the destruction function is very similar to that used by Phan-Thien and Tanner (1977) except that they introduced a preaveraging approximation in their calculations. A discussion of their model will be presented in the next section.

In treating the time dependent problem which has an initial distribution $G(\underline{x},N)/\beta(\underline{x})$, it is necessary to assume that σ is in the range $N>>\sigma>>1$. The requirement that σ not approach unity allows the use of linear springs in the segments, while the assumption that σ is much less than N permits the initial distribution to be approximated by $G(\underline{x},N)/\beta_o$ and the integrations in space to be carried out analytically. These requirements are both physically realistic and, in any case, the second requirement is actually not necessary for the case of steady state. The

moments in the (x,y,z) space are

$$n = L/\beta_o Q(t)\cdot e^{-t} + \frac{L}{\beta_o}\int_o^t dt' e^{-t'} Q(t') \tag{30a}$$

$$\langle x^2 \rangle = \frac{L}{\beta_o}\frac{e^{-t}}{3N}\frac{Q(t)A^+(t)}{C(t)} + \frac{L}{\beta_o}\frac{1}{3N}\int_0^t dt' e^{-t'}\frac{Q(t')A^+(t')}{C(t')} \tag{30b}$$

$$\langle y^2 \rangle = \frac{L}{\beta_o}\frac{e^{-t}}{3N}\frac{Q(t)A^-(t)}{C(t)} + \frac{L}{\beta_o}\frac{1}{3N}\int_0^t dt' e^{-t'}\frac{Q(t')A^-(t')}{C(t')} \tag{30c}$$

$$\langle xy \rangle = \frac{L}{\beta_o}\frac{e^{-t}}{3N}\frac{Q(t)\,B(t)}{C(t)} + \frac{L}{\beta_o}\frac{1}{3N}\int_0^t dt' e^{-t'}\frac{Q(t')\,B(t')}{C(t')} \tag{30d}$$

$$\langle z^2 \rangle = \frac{L}{\beta_o}\frac{e^{-t}}{3N}\frac{Q(t)}{Z(t)} + \frac{L}{\beta_o}\frac{1}{3N}\int_o^t dt' e^{-t'}\frac{Q(t')}{Z(t')} \tag{30e}$$

where

$$Q(t)=[(1-w^2)/C(t)Z(t)]^{1/2} \tag{31a}$$

$$A^{\pm}(t)=[\{(1-\xi)(1+\lambda)\mp\frac{\epsilon}{a}\}\cosh\sqrt{v}at + [(1-\xi)(1+\lambda)\mp v]\frac{\sinh\sqrt{v}at}{\sqrt{v}} + \frac{\epsilon}{a}(1-\lambda)wZ(t)]/(1-\xi)(1+\lambda) \tag{31b}$$

$$B(t)=[(1-\xi)(1+\lambda)wZ(t)-(1-\lambda)\{\cosh\sqrt{v}at + \frac{\epsilon}{\sqrt{v}a}\sinh\sqrt{v}at\}]/(1-\xi)(1+\lambda) \tag{31c}$$

$$C(t)=1 + 2\frac{\epsilon}{\sqrt{v}a}\sinh\sqrt{v}at + 2\frac{\epsilon^2}{va^2}(\cosh\sqrt{v}at - 1) - w^2Z^2(t) \tag{31d}$$

$$Z(t)=1 + \epsilon t \tag{31e}$$

$$\epsilon = 2\sigma/3N \tag{31f}$$

The use of the destruction function as defined in equation (29) removes the singularity of the constant breakage model and it is a simple matter to show that the maximum steady state value which a moment may attain is $(3N\epsilon/2)$. The conformation dependent destruction function also causes the entanglement junction density n to decrease from its rest state value L/β_o as the network is deformed. This decrease results from the increased probability of junction breakage as the segments joining the junctions stretch and supply increased tension on the entanglement points.

Figure 3 shows the normalized junction concentration $(\beta_o n/L)$ plotted against the velocity gradient for purely extensional flow and for simple shear flow. Since purely extensional flow will always be a "stronger" flow than simple shear at any given value of the velocity gradient, the junction concentration will decrease at a faster rate for pure extension than for simple shear as shown in figure 3.

The effect of the slip mechanism in purely extensional flow is simply to scale the velocity gradient by a factor of $(1-\xi)$ and therefore it is only necessary to consider the

case of $\xi=0$ in order to obtain the qualitative behavior of the moments of the distribution for this flow type. For flows with a finite amount of vorticity, the effect of the slip mechanism, as already noted, is to cause the network to behave as though it were deforming affinely with an effective velocity gradient tensor $\underline{\underline{\Gamma}}^{*}=(\underline{\underline{\Gamma}}-\xi\underline{\underline{D}})$. This effect is demonstrated in figure 3 where ξ is varied form 0 to 0.2 for the case of a simple shear flow ($\lambda=0$). As ξ is increased above zero, the decrease of the junction concentration is suppressed greatly and in fact can be shown to remain constant at the rest state value for all velocity gradients as ξ approaches unity.

The stress tensor can be calculated from equations (20) and (30). Figures 4-6 show the shear viscosity $\eta=S/\alpha$ and the normal stress coefficients $\Psi_i=N_i/\alpha^2$ plotted against the velocity gradient for several values of ξ. The conformation dependent destruction function of equation (29) produces a shear rate dependence for both the viscosity and normal stress coefficients for $\xi=0$ (whereas these functions were only shear rate dependent for nonzero ξ in the constant breakage model). As ξ is increased above zero, these functions drop off at a faster rate with the velocity gradient. As is demonstrated by figure 6, the absolute magnitude of the second normal stress difference is finite

for $\xi=0$ and increases with ξ. The ratio N_2/N_1 is still well approximated by $-\xi/2$ (as in the case of the constant breakage model) although this simple relation breaks down as ξ goes to zero since N_2 has a finite magnitude for this model when $\xi=0$ in contrast to the constant breakage model.

The dependence of the normal stress difference on the velocity gradient for purely extensional flow is shown in figure 7. The dimensionless stress difference $N_1'/2kT$ asymptotes to a value of ϵ^{-1} as the velocity gradient goes to infinity. The elongational viscosity N_1'/α is plotted in figure 8 and is predicted by the model to first increase with the velocity gradient which reflects the abrupt increase in the tension of the segments in the direction of the principal axis of strain as the critical point $\alpha=.5$ is surpassed. The elongational viscosity eventually passes an extremum and decreases at a rate inversely proportional to the velocity gradient as the gradient tends to infinity. This decrease is a consequence of the decrease in entanglement junction concentration with deformation which eventually overtakes the effect of increased tension in the remaining segments of the network. The magnitude of the extremum is controlled by the magnitude of ϵ in the model. As ϵ is decreased, this maximum will increase and will become infinite as ξ goes to zero and the model passes over

to the constant breakage model which possesses a singularity at $\alpha = .5$.

The initial increase in the elongational viscosity is supported by the majority of experimental data in extensional flows and in fact a maximum with respect to the velocity gradient has recently been reported by Munstedt and Laun (1979). A maximum in the elongational viscosity is also predicted in the molecular model of Aceirno et al (1976) where the authors built structure dependent relaxation times into the network. The recent model of Doi and Edwards (1979) which is based on the reptation concept of Edwards (1977) and de Gennes (1971), however, predicts a monotonically decreasing elongational viscosity.

The response of the quadratic law model to a start up flow can also be determined. Figures 9-11 show the growth of shear stress and normal stress differences for the inception of simple shear flow. The basic trend is qualitatively the same for each of these stresses with an overshoot occurring for large enough values of the velocity gradient. As in the case of the constant breakage model, the growth of the stresses becomes oscillatory when the parameter ν of equation (8) is less than zero. Figure 9 also shows the fact that the shear stress, for finite values

of ξ , possesses an extremum with respect to the velocity gradient. As already mentioned, an extremum also appears in the constant breakage model. A maximum exists as well in the model of Phan-Thien and Tanner (1977) as can be seen in their figure 2. As pointed out by Doi and Edwards (1979), the existence of a maximum in the stress with the velocity gradient leads to an instability in the flow at velocity gradients which surpass the extremum point. The presence of the oscillatory nature and the maximum, however, will be smoothed out and in fact may disappear in highly polydisperse samples where a spectrum of relaxation times will have to be included. It would be important, therefore, to consider the molecular weight distribution of polymer samples used in experimental investigations of these particular model predictions.

There is a great deal of experimental evidence which supports the existence of an overshoot in the stresses in the start up of simple shear flow (Huppler et al (1967), Osaki et al (1976)). These experiments are, however, difficult to carry out and care must be taken to account for experimental artifact when mechanical means are used to measure the transient stresses (Lockyer and Walters (1976)). Recently, however, Osaki et al (1979) have conducted experiments using the technique of flow

birefringence to measure the level of stress by appeal to the stress optical law (Philippoff (1963)). These experiments avoid the inherent problems associated with the inertia of mechanical components and do in fact show an overshoot for both the shear stress and the first normal stress difference. There have been reported cases of an undershoot following the initial overshoot (Huppler et al (1967)) but more recent measurements (Osaki et al (1976) have failed to demonstrate this effect.

The prediction of overshoot for this model results from the combined action of segmental deformation and the reduction of the entanglement junction density as the network responds to the imposed flow. As the time scale of the deformation process (which scales as γ) becomes sufficiently short relative to the time scale of the destruction process (β_o^{-1}), the first response of the network to an imposed flow is a significant level of segment deformation, and the network thus supports a large level of stress. Eventually, however, the destruction process takes over and the number of segments available to support the stress is reduced so that the stress drops off. Other molecular models which also predict an overshoot of stresses in shear flow include the models of Bird and Carreau (1968), Acierno et al (1976), Phan-Thien and Tanner (1977) and Doi

and Edwards (1979). The model of Doi and Edwards, however, while predicting overshoot in the shear stress and the second normal stress difference, produces a monotonic response for the first normal stress difference.

Figure 12 shows the response of the normal stress difference to the start up of purely extensional flow. There is also an overshoot of the stress for this situation when the velocity gradient is sufficiently large. This overshoot is again a direct result of the combined effects of segmental tension followed by a drop in entanglement junction concentration. Due to the difficulty of producing extensional flows experimentally, there is not a great deal of data on transient elongational stresses. Meissner (1971) has measured the elongational stress produced by the drawing of a low density polyethylene melt and although a sharp upturn of the stress was observed with time, a steady state was not achieved before the drawn filaments failed. Recently, however, Munstedt and Laun (1979) were able to achieve steady state levels of the stress in an extensional flow and a pronounced overshoot of the elongational viscosity was observed when low density polyethylene melts were subjected to elongational flows produced by two different apparatuses. The overshoot was observed only after the imposed strain rate was increased above a certain

level. We have also performed start up experiments in purely extensional flows generated in a four roll mill. These experiments, which are reported in detail in Fuller and Leal (1980a), used flow birefringence to measure the response of concentrated polyethylene oxide/water solutions and concentrated polyethylene/tricresyl phosphate solutions to the inception of extensional flow. Overshoot was observed in the birefringence for both systems which would suggest that the stresses overshoot as well.

Stress overshoot in extensional flow is also predicted by the model of Acierno et al and is directly related to the decrease in their structure parameter (which is related to the entanglement junction concentration) as the network deforms. The model of Wagner (1976), which is a modified Lodge model of a rubber-like liquid using a strain dependent memory function, also predicts an overshoot in the elongational stress and was shown to produce good fits to the data of Meissner (1971). The model of Phan-Thien and Tanner shows a monotonic rise in the stress for this flow but this is a consequence of the preaveraging approximation which they used as will be demonstrated in the next section. The model of Doi and Edwards, which has a constant density of junctions, shows a monotonic increase of the stresses with time in a purely extensional flow. This is

also true of the variations of the Lodge model proposed by Kaye (1966) and Bird and Carreau (1968).

Using equation (25), the birefringence resulting from the deformed network can also be calculated. Figure 13 shows the function $\Delta n/A$ plotted against the eigenvalue of the velocity gradient tensor $\sqrt{\lambda}\alpha$ for several values of λ and ξ. This figure demonstrates that the birefringence (or any invariant of the tensor $\langle \underline{x}\ \underline{x} \rangle$) scales with $\sqrt{\lambda}\alpha$ for a wide range of λ as long as ξ does not become too large. The reason that this correlation exists can be understood by appeal to a linear stability analysis of equation (4). Such an analysis has been carried out for the case of the dumbbell model by Tanner (1976) and more recently for a more general model of deformable systems by Olbricht et al (1980) for general linear flows. The results of such a study indicate that the strength of the flow with the slip mechanism in effect is dictated completely by the eigenvalue of the effective velocity gradient tensor $\underline{\underline{\Gamma}}^{*} = (\underline{\underline{\Gamma}} - \xi \underline{\underline{D}})$. The criterion for uncontrolled growth of the linearized model is given by equation (28) and the quantity $\sqrt{v}\alpha$ therefore controls the degree of deformation in the system. When ξ is equal to zero (affine motion) the group $\sqrt{v}\alpha$ becomes $2\sqrt{v}\alpha$ which is exactly twice the eigenvalue of the velocity gradient tensor of equation (5). For this reason one would

expect the birefringence to be well correlated against $\sqrt{\lambda}\alpha$ as long as ξ does not become too large. The situation becomes more complex when Brownian forces (which are included in the model through the creation function G) become important as in the case of weak flows ($\sqrt{v}\alpha<1$). The effect of Brownian motion is to force the segments to maintain a finite length even when the flows are weak. For this reason there will be a finite amount of deformation and birefringence even as $\alpha\sqrt{v}\Rightarrow 0$. It is evident that the correlation with $\sqrt{\lambda}\alpha$ must break down when v=0 which provides an estimate of the range of λ for a given value of ξ over which the correlation will hold. Setting v to zero, this estimate of the relationship between ξ, and the minimum value of λ for the correlation to hold is

$$\lambda^{*} = \xi/(2-\xi) \qquad (32)$$

The exact results in figure 13 provide a test of the validity of (32). For example, when ξ is 0.2, the correlation can be seen to break down when λ is 0.1 and this is below the lower bound of 0.11 set by equation (32). When ξ is increased to 0.3, the predicted lower bound on λ is 0.176, and the correlation can be seen to break down when λ approaches 0.2. These results suggest that experiments in which birefringence measurements are obtained for the

flow field considered here could be used to determine the smallest value of λ where the data correlate with $\sqrt{\lambda}\alpha$, and thus to place an upper bound on the magnitude of ξ. Such experiments have in fact been performed in this laboratory (Fuller and Leal (1980a)) using a four roll mill and the measured flow birefringence in concentrated solutions of polyethylene oxide in water. In this case the degree of birefringence was found to be well correlated with $\sqrt{\lambda}\alpha$ over the entire range of λ accessible to the apparatus which was $1 >> \lambda >> 0.16$. This suggests that ξ must be lower than approximately 0.27 for this particular system. This bound on ξ is consistent with the value estimated using the relation $N_2/N_1 = -\xi/2$ where the accepted range of the ratio of normal stresses is from -0.1 to -0.4 (Graessley (1974), Tanner (1973)).

C. Phan-Thien - Tanner Model

Equation (4) is the starting point for the model of Phan-Thien and Tanner (1977). In this model the Gaussian assumption is used for the creation function G. The destruction function β and L are both taken to have a simple quadratic dependence on the end to end distance. However, a preaveraging approximation is used such that

$$\beta = \beta_o(1 + \sigma\langle x^2 + y^2 + z^2\rangle) \tag{33a}$$

$$L = L_o(1 + \sigma\langle x^2 + y^2 + z^2\rangle) \tag{33b}$$

where the constants h_o and g_o which appear in the original paper are directly related to the constants β_o and L_o used here. Phan-Thien and Tanner further use the equality $\langle x^2+y^2+z^2\rangle = tr(\underline{\tau})/3NkT$ in order to construct a constitutive equation. It has been demonstrated that the resulting model is capable of fitting rheological data very well for a variety of conditions (Phan-Thien (1978), Dealy et al (1979)), but it would be of interest to examine the same model without recourse to the preaveraging approximation. This can be done in a straightfoward manner and follows along the same lines as the quadratic law model. One point worth mentioning is that because the function L has the same functional dependence as the destruction function, it is not necessary to assume anything about the magnitude of σ in order to obtain analytical results for the time dependent problem. The relevant averages in the (ρ,η,z) frame are

$$n=\frac{L\sqrt{(1-w^2)}}{\beta_o}\left[\ e^{-t}/\{(ac-b^2)d\}^{1/2}\right.$$
$$\left.+\int_o^t dt'\, e^{-t'}\{1+\frac{\epsilon}{2}[\frac{(c+a)-2wb}{ac-b^2}+\frac{1}{d}]\}/\{(ac-b^2)d\}^{\frac{1}{2}}\right] \tag{34a}$$

$$\langle\rho^2\rangle=\frac{L\sqrt{(1-w)}}{\beta_o 3N}\left[\ e^{-t}c/\{(ac-b^2)d\}^{1/2}(ac-b^2)\right.$$
$$\left.+\int_o^t dt'\, e^{-t'}\{1+\frac{\epsilon}{2}[\frac{3c-6wb}{ac-b^2}+\frac{ac-b^2}{c(ac-b^2)}+1]\}c/(ac-b^2)\{(ac-b^2)d\}^{\frac{1}{2}}\right] \tag{34b}$$

$$\langle \eta^2 \rangle = \frac{L}{\beta_o}\left(\frac{1-w}{3N}\right)^{\frac{1}{2}}\left[e^{-t} a \Big/ \{(ac-b^2)d\}^{\frac{1}{2}}(ac-b^2) \right.$$

$$\left. + \int_o^t dt'\, e^{-t'} \{1+\frac{\epsilon}{2}[\frac{3a-6wb}{ac-b^2} + \frac{(ac-b^2)}{a(ac-b^2)} + \frac{1}{d}]\} a \Big/ (ac-b^2)\{(ac-b^2)d\}^{\frac{1}{2}}\right] \qquad (34c)$$

$$\langle \rho\eta \rangle = \frac{L}{\beta_o}\left(\frac{1-w}{3N}\right)^{\frac{1}{2}}\left[e^{-t} b \Big/ \{(ac-b^2)d\}^{\frac{1}{2}}(ac-b^2) \right.$$

$$\left. + \int_o^t dt'\, e^{-t'} \{1+\frac{\epsilon}{2}[\frac{3(a+c)}{ac-b^2} - \frac{2w(ac-2b^2)}{b(ac-b^2)} + \frac{1}{b}]\} b \Big/ (ac-b^2)\{(ac-b^2)d\}^{\frac{1}{2}}\right] \qquad (34d)$$

$$\langle z^2 \rangle = \frac{L}{\beta_o}\left(\frac{1-w^2}{3N}\right)^{\frac{1}{2}}\left[e^{-t} \Big/ \{(ac-b^2)d\}^{\frac{1}{2}}d \right.$$

$$\left. + \int_o^t dt'\, e^{-t'} \{1+\frac{\epsilon}{2}[\frac{c+a-2wb}{ac-b^2} + \frac{3}{d}]\} \Big/ \{(ac-b^2)d\}^{\frac{1}{2}}d\right] \qquad (34e)$$

where

$$a = e^{-\sqrt{\nu\alpha}t} + \frac{\epsilon}{\sqrt{\nu\alpha}}(1 - e^{-\sqrt{\nu\alpha}t}) \qquad (35a)$$

$$b = w(1 + \epsilon t) \qquad (35b)$$

$$c = e^{\sqrt{\nu\alpha}t}[1 + \frac{\epsilon}{\sqrt{\nu\alpha}}(1-e^{-\sqrt{\nu\alpha}t})] \qquad (35c)$$

$$d = 1 + \epsilon t \qquad (35d)$$

From these averages, the stresses and the birefringence can be calculated as before. The predictions for this model are qualitatively very similar to the quadratic law model and for this reason it is not necessary to present figures describing the results. It is important to note that this

model does predict an overshoot in the birefringence and normal stress difference when purely extensional flow is started from rest. This is in contrast to the conclusions of Phan-Thien and Tanner and the difference is a consequence of the preaveraging approximation they used. The preaveraging approximation cannot be used successfully for this network model because the distribution function never becomes a strongly peaked function in strong flows as they assumed. Rather, the distribution function becomes a broad function with its maximum remaining at the origin. This is not the case for the nonlinear dumbbell model of dilute solutions where the preaveraging can be successfully used (Hinch (1977), Peterlin (1961), Fuller and Leal (1980b)). In this case the use of the nonlinear spring forces the probability mass of the dumbbell to remain confined to a finite region of space causing the distribution function to become strongly peaked in strong flows. In the case of the network model with a destruction function given by equation (29), there is no such constraint on the probability flux.

D. Square Well Model

Yamamoto (1956) originally proposed the following form for the destruction function

$$\beta = \begin{cases} \beta_o: & x^2 + y^2 + z^2 < R^2 \\ \infty: & x^2 + y^2 + z^2 \geq R^2 \end{cases} \qquad (36)$$

where R is a length scale which has been nondimensionalized by the maximum end to end distance and will be assumed to be in the range $N^{-1/2} << R << 1$. Using this model, Yamamoto demonstrated that a shear thinning viscosity in simple shear flow could be predicted, as well as an extensional viscosity with the same general trends as shown in figure 8. It is difficult, however, to carry out the integrations involved and Yamamoto was not able to arrive at explicit expressions for the stresses. For the flow field given by equation (5), a useful approximation can be used, however, which makes it possible to arrive at largely analytical results. This approximation is based on the observation that the probability mass governed by equation (1) will exit primarily out on the ρ axis with the η axis being an axis of compression. This suggests that the problem can be simplified by assuming the destruction function to be a function solely of ρ. That is

$$\beta = \begin{cases} \beta_o: & |\rho| < R \\ \infty: & |\rho| > R \end{cases} \qquad (37)$$

This approximation is strictly valid only when $w<<1$ (equation (12)) since the ρ and η axes become coincident when $w \Rightarrow 1$.. For this reason the results obtained using (37) are only useful for flows which are almost purely extensional and cannot be used for the case of simple shear flow. Using equation (18), the appropriate moments in the (ρ,η,z) frame are

$$n = \frac{L}{\beta_o}(1-w^2)^{1/2}\{e^{-t}E(t) + \int_o^t dt' e^{-t'}E(t')\} \tag{38a}$$

$$\langle \rho^2 \rangle = \frac{L}{\beta_o}\frac{2}{3N}[\exp\{-(1-\sqrt{v}\alpha)t'\}D(t') + \int_o^t dt' \exp\{-(1-\sqrt{v}\alpha)t\}D(t)]/(1-w^2) \tag{38b}$$

$$\langle \eta^2 \rangle = \frac{L}{3N\beta_o}\exp\{-(1+\sqrt{v}\alpha)t\}[E(t)+2w^2 D(t)/(1-w^2)] + \frac{L}{3N\beta_o}\int_o^t dt' \exp\{-(1+\sqrt{v}\alpha)t'\}[E(t')+2w^2 D(t')/(1-w^2)] \tag{38c}$$

$$\langle \rho^2 \rangle = \frac{L}{\beta_o} 2w\ [e^{-t}D(t) + \int_o^t dt' e^{-t'}D(t')]/(1-w^2) \tag{38d}$$

$$\langle Z^2 \rangle = n/3N \tag{38e}$$

$$E(t) = \mathrm{erf}(\chi(1-w^2)^{1/2}e^{-\sqrt{v}\alpha t/2}) \tag{38f}$$

$$D(t) = [E(t) - (\chi(1-w^2)^{1/2}e^{-\frac{\sqrt{v}\alpha t}{2}}\ e^{-\chi^2(1-w^2)e^{-\sqrt{v}\alpha t}}]/2 \tag{38g}$$

$$\chi = \sqrt{\frac{3N}{2}}\,R \tag{38h}$$

The steady state elongational stress in purely extensional flow is shown in figure 14. The effect of the

square well model for the destruction function β is to remove all segments from the network with end to end distances greater than R and this produces a maximum in the stress as a function of the velocity gradient. The reason for the extremum is that, as the network becomes greatly deformed and all existing segments achieve an end to end distance of R, the junction density begins to drop off rapidly, reducing the amount of stress that the network as a whole can support. In the quadratic law model, although the stress attains a saturation value (as seen in figure 7), the individual segments remaining in the network can extend indefinitely. That is, even though the average segmental end to end distance is limited to a maximum possible value of $(3N\epsilon/2\bar{})^{1}$, the end to end distance of the segments remaining in the network which is $\langle x^2+y^2+z^2\rangle/n$ can increase without bound. In the square well model, however, the quantity $\langle x^2+y^2+z^2\rangle/n$ is limited to a value of $O(R^2)$.

Doi and Edwards (1979), have pointed out that an extremum in the stress represents a point of neutral stability and flows at a higher velocity gradient will be unstable. Indeed, the flow birefringence experiments in purely extensional flows using a four roll mill (Fuller and Leal (1980a)) did show a flow instability at sufficiently high velocity gradients and this instability was directly

attributable to the viscoelasticity of the polymer solutions in which it was observed.

The square well model does predict a good correlation between birefringence and the eigenvalue of the velocity gradient tensor, as well as an overshoot in both the stress and birefringence as purely extensional flow is started from rest.

IV. Relaxation

From equation (15), the relaxation of the moments of the distribution function can be calculated immediately, given the form of the distribution function at the instant the flow is arrested. This is a straightforward calculation for all the choices of the destruction function considered here. For the purpose of illustration, the results for the quadratic law model are presented below,

$$n = \frac{L}{\beta_o}\{H(t) + e^{-t}\int_o^\infty dt'\, e^{-t'}\hat{Q}(t',t)\} \tag{39a}$$

$$\langle x^2\rangle = \frac{L}{\beta_o}\{H(t) + e^{-t}\int_o^\infty dt'\, e^{-t'}\hat{Q}(t',t)\hat{A}(t',t)/\hat{C}(t',t)\}/3N \tag{39b}$$

$$\langle y^2\rangle = \frac{L}{\beta_o}\{H(t) + e^{-t}\int_o^\infty dt'\, e^{-t'}\hat{Q}(t',t)\hat{A}(t',t)/\hat{C}(t',t)\}/3N \tag{39c}$$

$$\langle xy \rangle = \frac{L}{\beta_o} \; e^{-t}\int_o^\infty dt' \; \bar{e}^{t}\hat{Q}(t',t)B\,(t'\;)/\hat{C}(t',t)/3N \tag{39d}$$

$$\langle z^2 \rangle = \frac{L}{\beta_o} \; \{H(t) + e^{-t}\int_o^\infty dt' \; \bar{e}^{t'}\hat{Q}(t',t)/Z(t' + t)\}/3N \tag{39e}$$

where

$$\hat{Q}(t',t) = \{(1-w^2)^{\frac{1}{2}}/\hat{C}(t',t)A(t + t')\}^{\frac{1}{2}} \tag{40a}$$

$$\hat{A}^{\pm}(t',t) = A^{\pm}(t') + v\epsilon t/(1-\xi)^2\,(1+\lambda)^2 \tag{40b}$$

$$H(t) = 1-\bar{e}^{t}/(1 + \epsilon t)^{\frac{3}{2}} \tag{40c}$$

$$\hat{C}(t',t) = C(t') + (\epsilon t)^2 + 2\epsilon t \cosh\sqrt{v}\alpha t' + 2\epsilon\frac{t\epsilon}{\sqrt{v}\alpha}\sinh\sqrt{v}\alpha t' - w^2(Z^2(t' + t) - Z\,(t')^2) \tag{40d}$$

and all other variables are defined in equation (31).

The predictions for relaxation of the shear stress and first normal stress difference after a simple shear flow is suddenly stopped are shown in figure 15. As the velocity gradient increases, the time scale for decay of the stresses decreases, and this is in general agreement with experiment (Huppler et al (1967), Osaki et al (1979)). The predictions

do differ from experiment, however, in that the shear stress is predicted to relax slightly slower than the first normal stress difference whereas the measured data indicate the opposite trend (Huppler et al (1967)). It is generally agreed, however, that the measurement of normal stresses is not nearly as precise as the shear stress measurement and further confirmation of this point is required (Huppler et al (1967)). The effect of the slip mechanism does not influence the general trends already noted and the results for finite values of ξ are not reproduced here. Also the same qualitative results would be predicted by the other models presented here with different choices for G and β.

V. Conclusions

We have examined the behavior of the network model of Yamamoto for several choices for the creation and destruction functions which describe the dynamics of entanglement loss and creation in a concentrated solution. In particular, it is demonstrated that the model can predict a variety of nonlinear effects which are supported by experimental data if the destruction function is allowed to depend on the end to end distance of the segments which bridge the entanglements. If the destruction function is simply a constant and independent of segmental conformation,

the model is precisely the same as the linear dumbbell model of dilute solution theory.

The principal consequence of making the destruction function depend on the segmental conformation is that the number of entanglement junctions per unit volume, n, will decrease as the network deforms under the action of an imposed flow. This "loosening" of the structure causes the variety of nonlinear phenomena which can be predicted by the model such as shear rate dependent stress functions and the overshoot of stress and birefringence for start-up flows. The detailed response of the model is controlled by two parameters, ξ , the slip parameter which prescribes the degree to which the network will deform affinely, and ϵ (or χ for the square well model), which is related to the segment length scale over which the destruction function increases. This paper has dealt primarily with the qualitative features of the Yamamoto network model and does not address the question of how well the the model can produce a quantitative fit to experimental data. This must of course be the final objective of the modelling and is the focus of current research in this laboratory.

ACKNOWLEDGEMENT

This research was supported by the Office of Naval Research. One of us (G.G.F.) is indebted to the National Research Council of Canada for fellowship support.

References

Acierno, D., La Mantia, F. P., Marrucci, G., Rizzo, G. and Titomanlio, G., J. Non-Newt. Fluid Mech. 1,125(1976).

Bird, R. B. and Carreau, P. J., Chem. Eng. Sci. 23,427(1968).

Bird, R. B., Armstrong, R. C. and Hassager, O., Dynamics of Polymeric Liquids, Volume II: Kinetic Theory, Wiley, 1977.

de Gennes, P., J. Chem. Phys. 15,572(1971).

Dealy, J. M. and Tsang, W., Time Scales for Reentanglement in Molten Polymers, Paper presented at the Golden Jubilee Meeting of the Society of Rheology, Boston, Oct. 1979.

Doi, M. and Edwards, S. F., J.C.S. Faraday II 75,38(1979).

Edwards, S. F., Polymer 6,143(1977).

Fuller, G. G. and Leal, L. G., Flow Birefringence of Concentrated Polymer Solutions in Two Dimensional Flows, forthcoming publication (1980a).

Fuller, G. G. and Leal, L. G., Dynamics of Flowing Polymer Molecules in Dilute Solution, forthcoming publication (1980b).

Gordon, R. J. and Schowalter, W. R., Trans. Soc. Rheol. 16,79 (1972); Gordon, R. J. and Everage, A. E., J. Appl. Polym. Sci. 15,1903(1971); Everage, A. E. and Gordon, R. J., ibid 16,1967 (1972); Everage, A. E. and Gordon, R. J., A.I.C.H.E. J. 17,1257(1971); Everage, A. E. and Gordon, R. J., J. Appl.

Polym. Sci. 18,3137(1974); Everage, A. E. and Gordon, R. J., ibid 21,1421(1977).

Graessley, Adv. Polymer Sci. 16,1(1974).

Hinch, E. J., Phys. Fluids 20,S22(1977).

Huppler, D., Macdonald, I. F., Ashare E., Spriggs, T. W., Bird, R. B., and Holmes, L. A., Trans. Soc. Rheol. 11,181(1967).

Kaye, A., Brit. J. Appl. Phys. 17,803(1966).

Kuhn ,W. and Grun, F., Kolloid Z. 101,248(1942).

Lockyer, M. A., and Walters, K., Rheol. Acta 15,179(1976).

Lodge, A. S., Rheol. Acta. 7,379(1968).

Lodge, A. S., Trans. Faraday Soc. 52,120(1956).

Meissner, J., Rheol. Acta 10,230(1971).

Munstedt, H. and Laun, H. M., Rheol. Acta 18, 492(1979).

Olbricht, W. L., Rallison, J. M. and Leal, L. G., A Criterion for Strong Flows Based on Microstructure Deformation, forthcoming publication, (1980); also presented at the 2nd Joint Meeting of the American and Japanese Societies of Rheology, Kana, Hawaii, April 1979.

Osaki, K., Ohta, S., Fukuda, M. and Kurata, M. J., Polym. Sci. 14,1701(1976).

Osaki K., Bessho, N., Kojimoto, T. and Kurata, M., J. Rheol. 23,457(1979).

Peterlin, A., Polymer 2,257(1961).

Phan-Thien, N., J. Rheol. 22,259(1978).

Phan-Thien, N. and Tanner, R. I., J. Non-Newt. Fluid Mech. 2,353(1977).

Philippoff, W., in: E. H. Lee (ed.), Proc. IV Intern. Congr. Rheol., Providence 1963, Vol. 2, p 343, Interscience Publ. (N. Y. 1965)

Schowalter, W. R., Mechanics of Non-Newtonian Fluids, Pergamon Press, 1978.

Tanner, R. I., (1973).

Tanner, R. I., AICHE J. 22,910(1976).

Wagner, M. H., Rheol. Acta 15,136(1976).

Wiegel, F. M., Physica 42, 156(1969).

Yamakawa, H., Modern Theory of Polymer Solutions, Harper and Row Publ. (N. Y. 1971).

Yamamoto, M, J. Phys. Soc. Japan 11,413(1956).

Yamamoto, M, J. Phys. Soc. Japan 12,1148(1957).

Yamamoto, M, J. Phys. Soc. Japan 13,1200(1958).

Figure Captions

Figure 1. Network representation of a concentrated polymer solution.

Figure 2. Range of flows represented by equation (5) and simulated in the four roll mill.

Figure 3. Normalized entanglement junction concentration versus α.

Figure 4. Normalized shear viscosity versus α.

Figure 5. Normalized first normal stress coefficient versus α.

Figure 6. Normalized second normal stress coefficient versus α.

Figure 7. Normalized elongational stress difference versus α.

Figure 8. Normalized elongational viscosity versus α.

Figure 9. Transient normalized shear stress versus time (in units of β_o^{-1}).

Figure 10. Transient normalized first normal stress coefficient versus time (in units of β_o^{-1}).

Figure 11. Transient normalized second normal stress coefficient versus time (in units of β_o^{-1}).

Figure 12. Transient normalized elongational stress versus time (in units of β_o^{-1}).

Figure 13. Normalized birefringence $\Delta n / A$ versus $\sqrt{\lambda}\,\alpha$.

Figure 14. Normalized elongational stress versus α . (Square Well Model)

Figure 15. Relaxation of shear stress (- - - -) and first normal stress difference (———) with time (in units of β_o^{-1}). The stresses have been normalized with respect to their values at t=0.

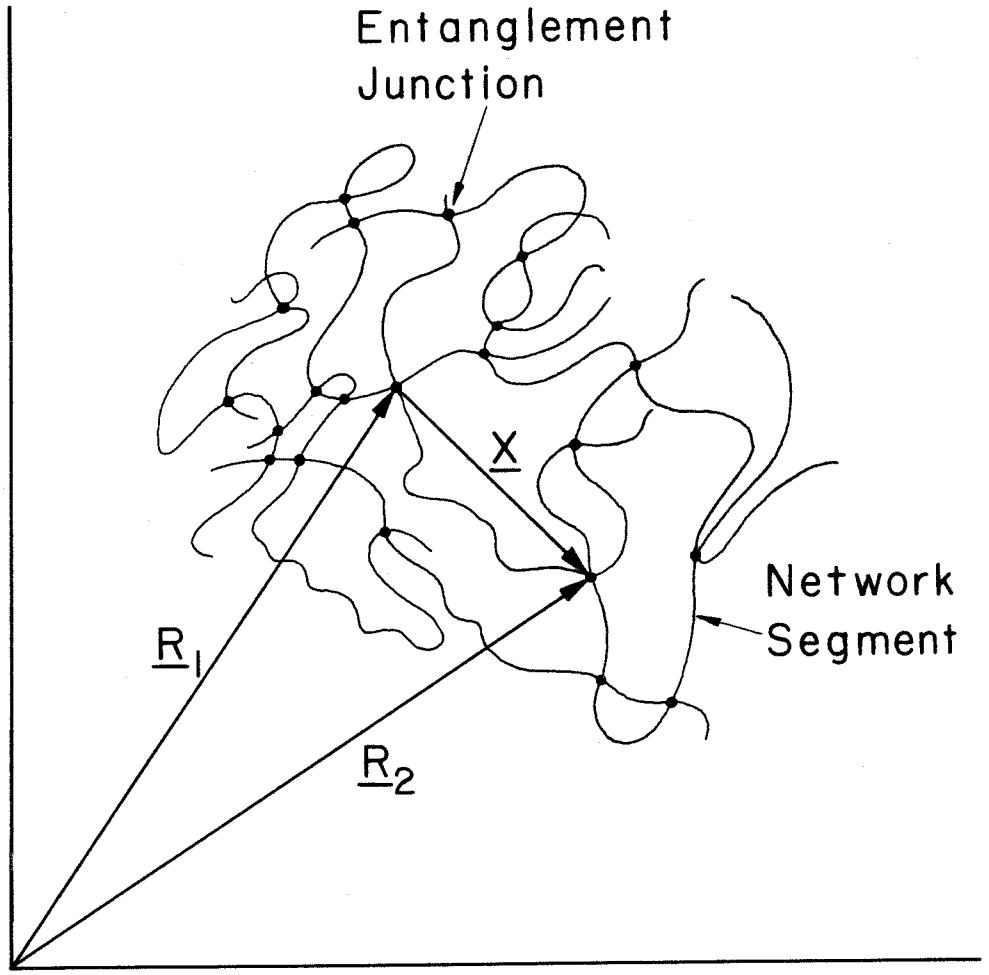

Fig. 1

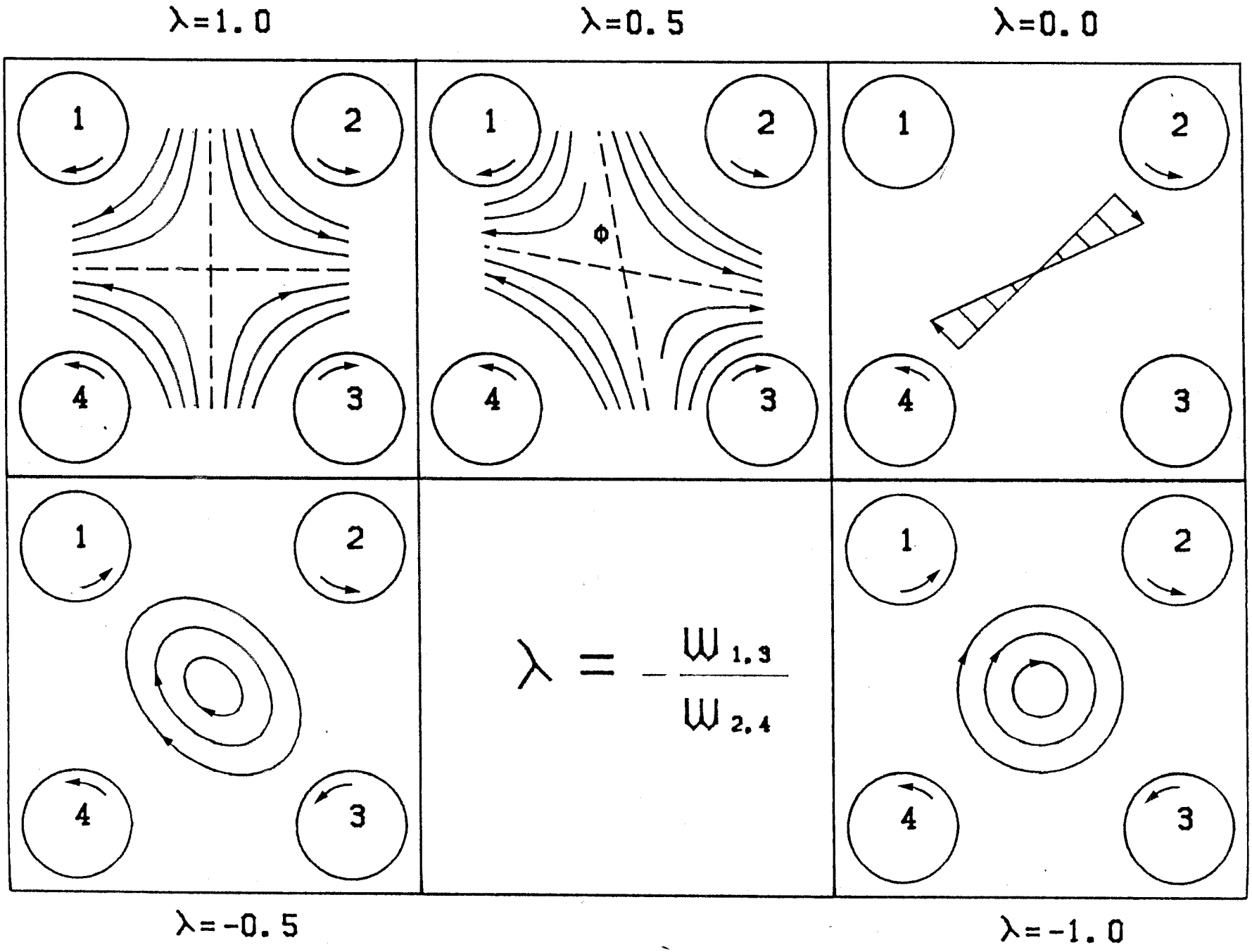

Fig. 2

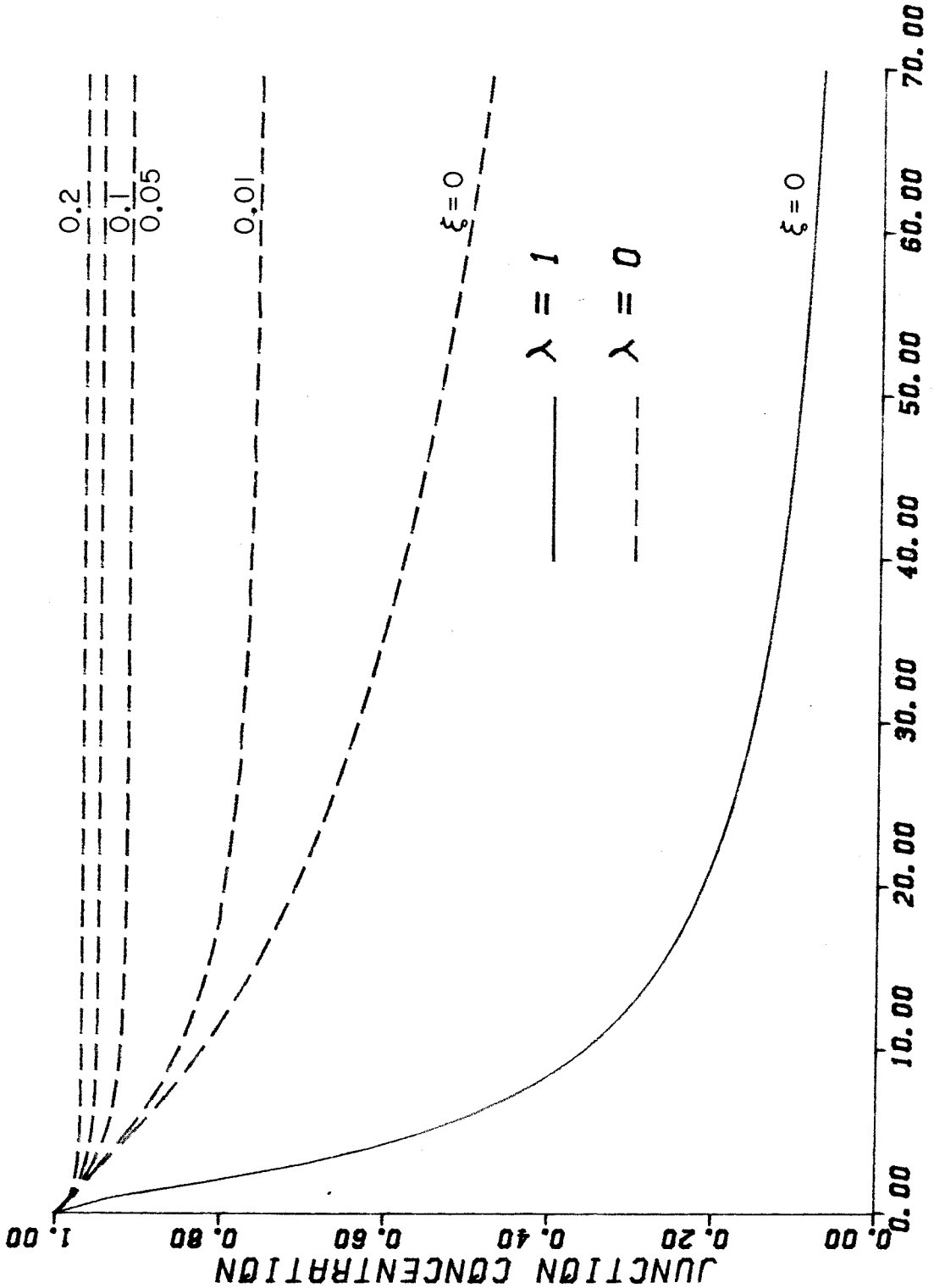
JUNCTION CONCENTRATION
0.00
0.20
0.40
0.60
0.80
1.00
0.00
10.00
20.00
30.00
40.00
50.00
60.00
70.00
α
λ = 1
λ = 0
ξ = 0
ξ = 0
0.2
0.1
0.05
0.01

Fig. 3

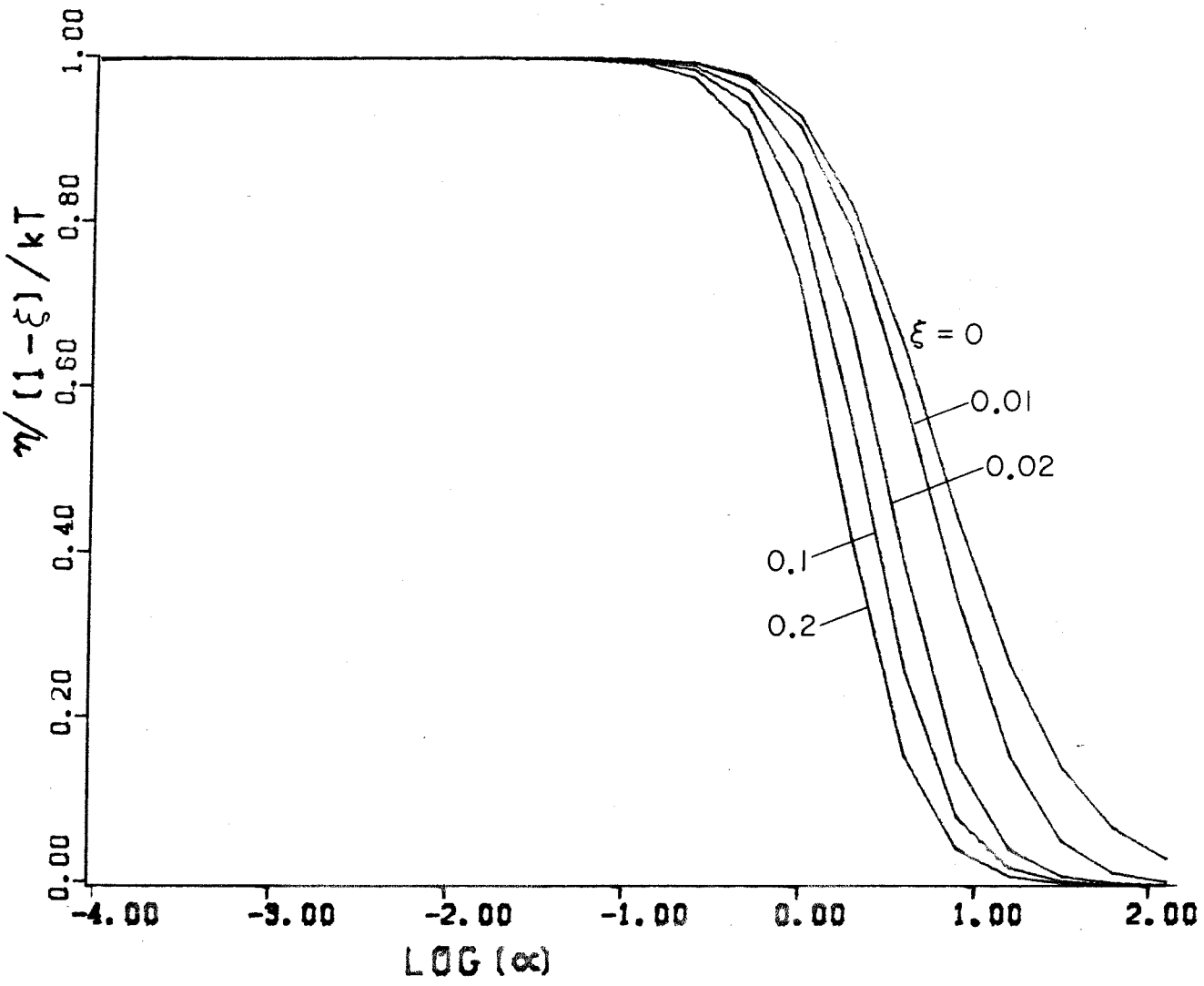
η/(1-ξ)/kT
1.00
0.80
0.60
0.40
0.20
0.00
-4.00
-3.00
-2.00
-1.00
0.00
1.00
2.00
LOG (α)
ξ = 0
0.01
0.02
0.1
0.2

Fig. 4

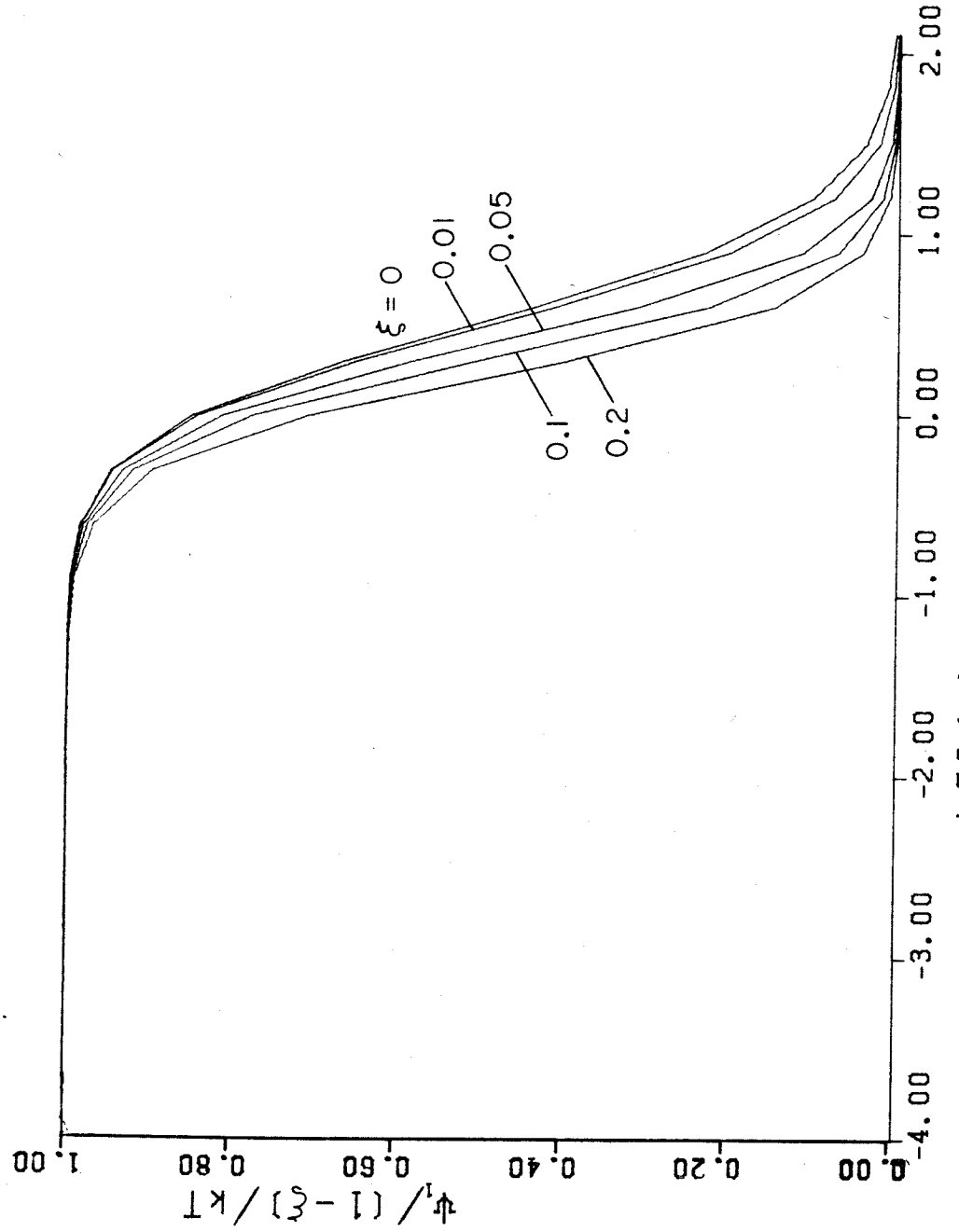
ψ1/(1-ξ)/kT
0.00
0.20
0.40
0.60
0.80
1.00
-4.00
-3.00
-2.00
-1.00
0.00
1.00
2.00
LOG(α)
ξ = 0
0.01
0.05
0.1
0.2

Fig. 5

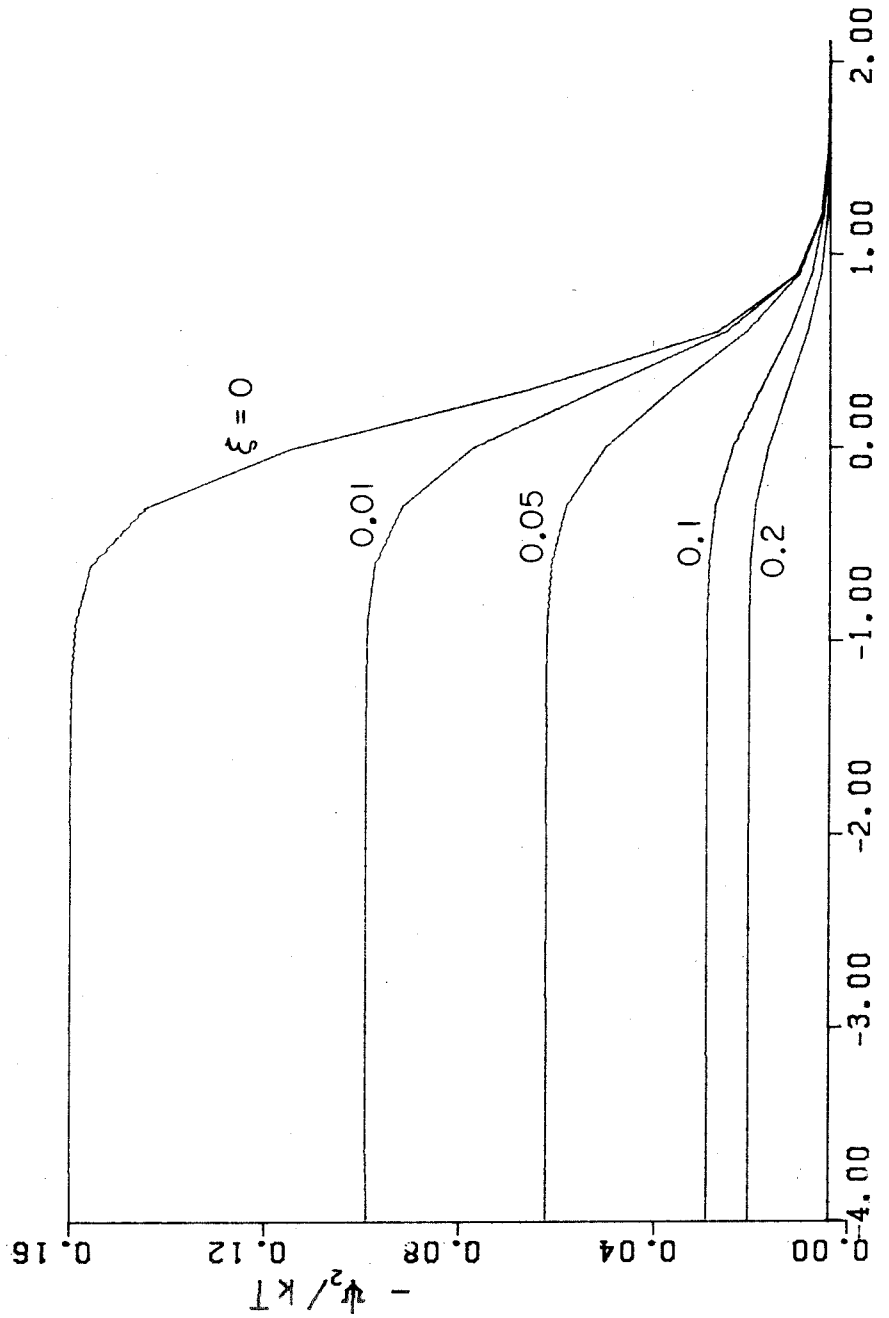
$\xi = 0$
0.01
0.05
0.1
0.2
$-\psi_2/kT$
0.00
0.04
0.08
0.12
0.16
LOG (α)
-4.00
-3.00
-2.00
-1.00
0.00
1.00
2.00

Fig. 6

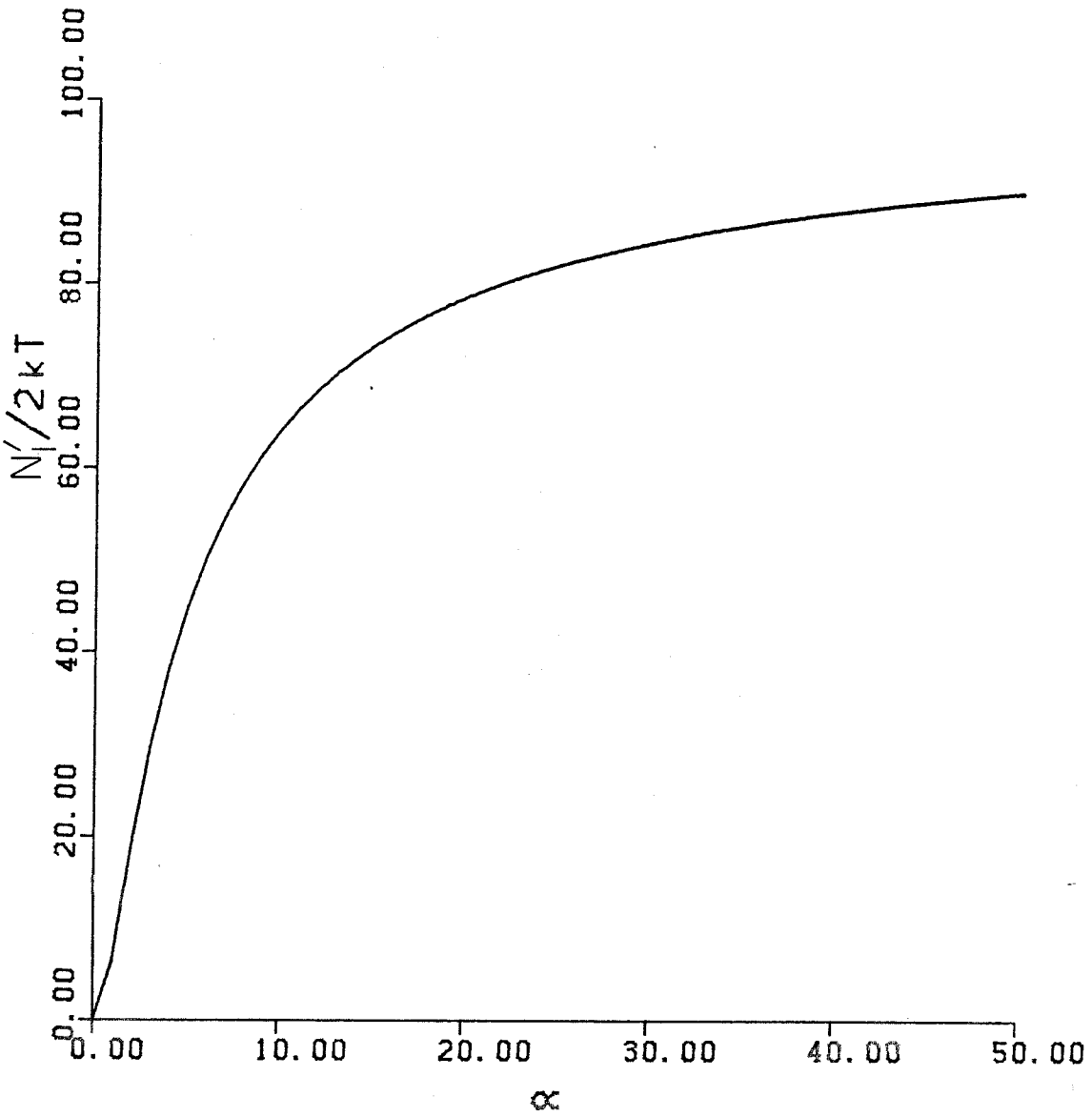
100.00
80.00
60.00
40.00
20.00
0.00
$N_i'/2kT$
0.00
10.00
20.00
30.00
40.00
50.00
α

Fig. 7

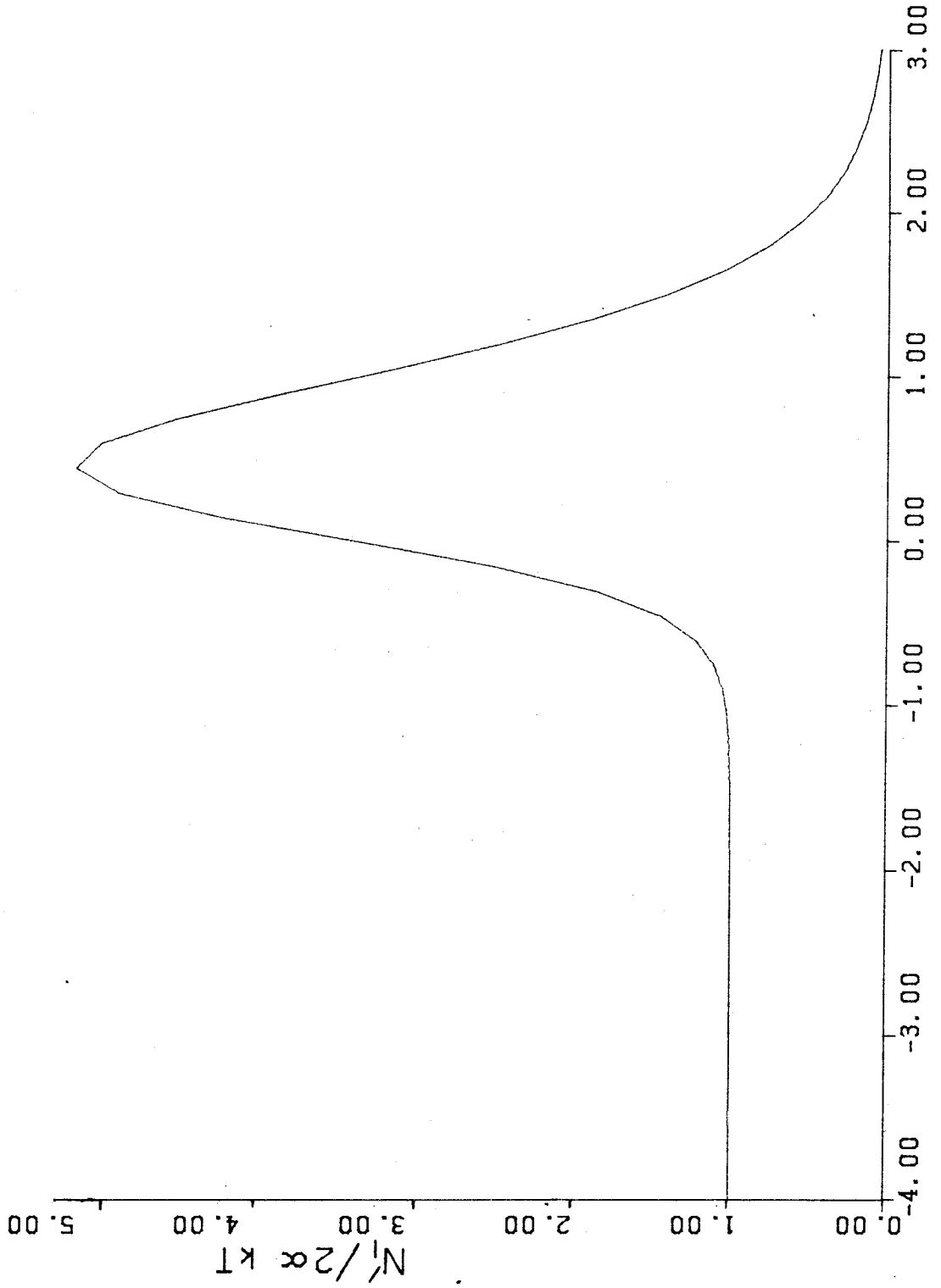
0.00
1.00
2.00
3.00
4.00
5.00
N'i/2α kT
-4.00
-3.00
-2.00
-1.00
0.00
1.00
2.00
3.00
LOG (α)

Fig. 8

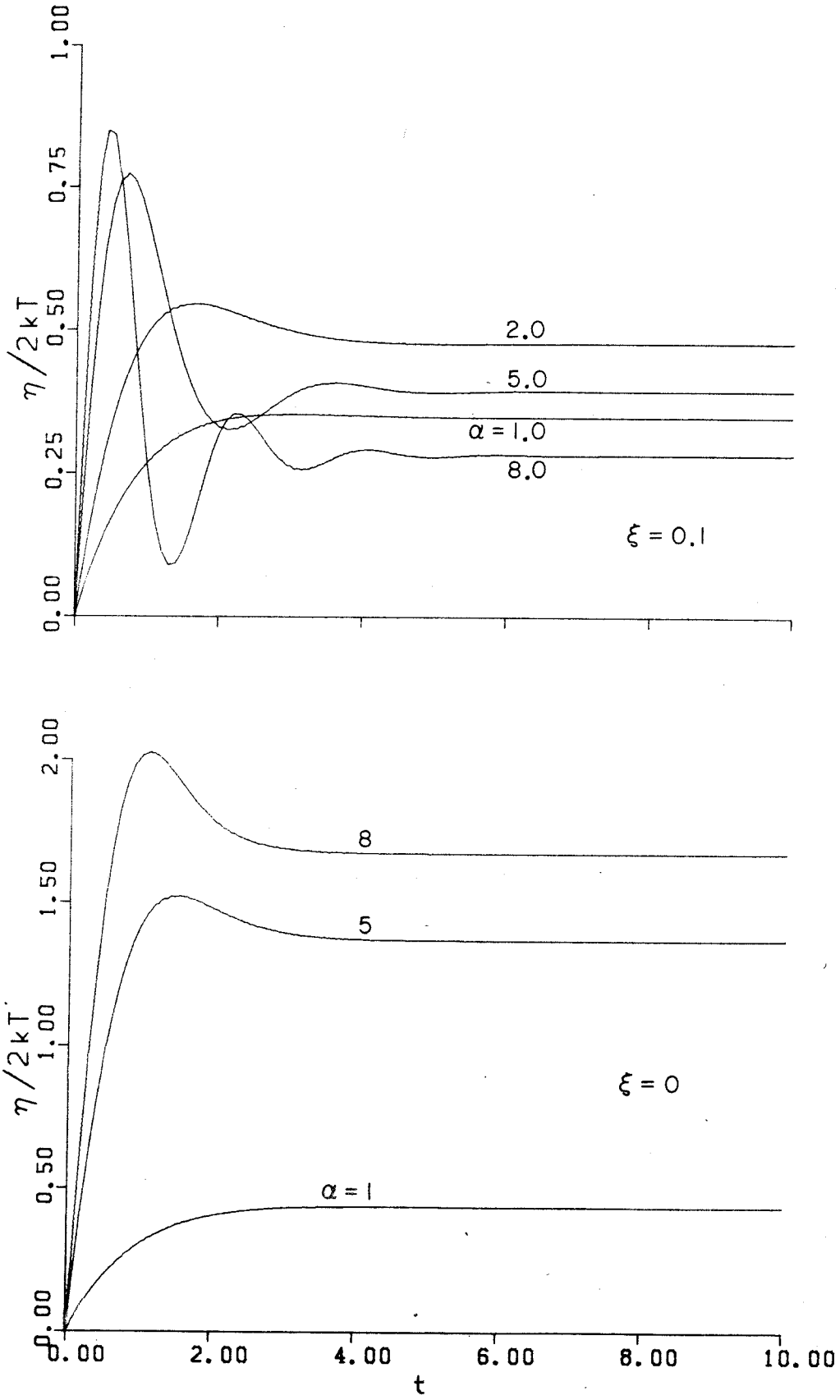
η/2kT
1.00
0.75
0.50
0.25
0.00
2.0
5.0
α = 1.0
8.0
ξ = 0.1
η/2kT
2.00
1.50
1.00
0.50
0.00
8
5
ξ = 0
α = 1
0.00
2.00
4.00
6.00
8.00
10.00
t

Fig. 9

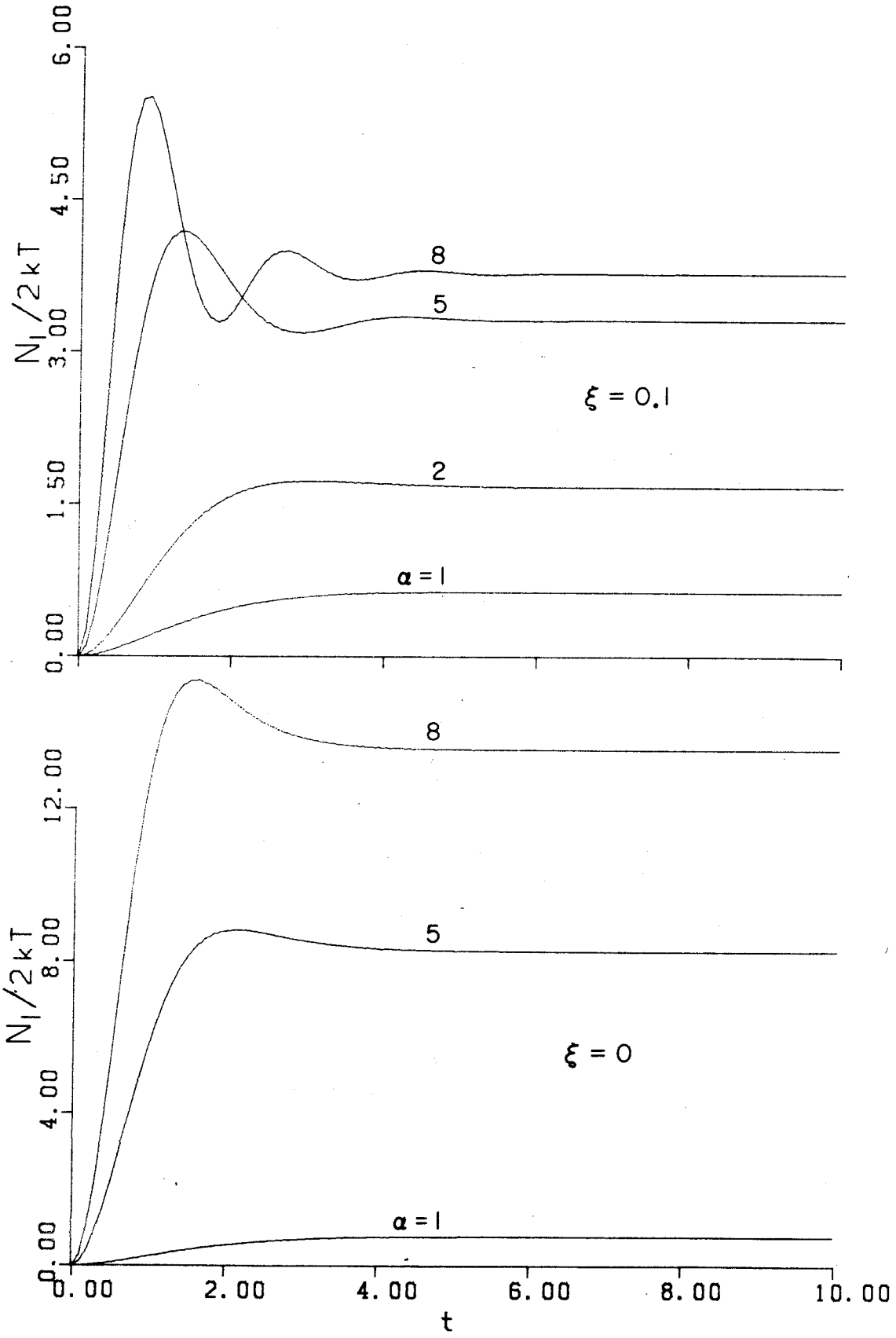
6.00
4.50
3.00
1.50
0.00
$N_l/2kT$
8
5
2
α = 1
ξ = 0.1
12.00
8.00
4.00
0.00
$N_l/2kT$
8
5
α = 1
ξ = 0
0.00
2.00
4.00
6.00
8.00
10.00
t

Fig. 10

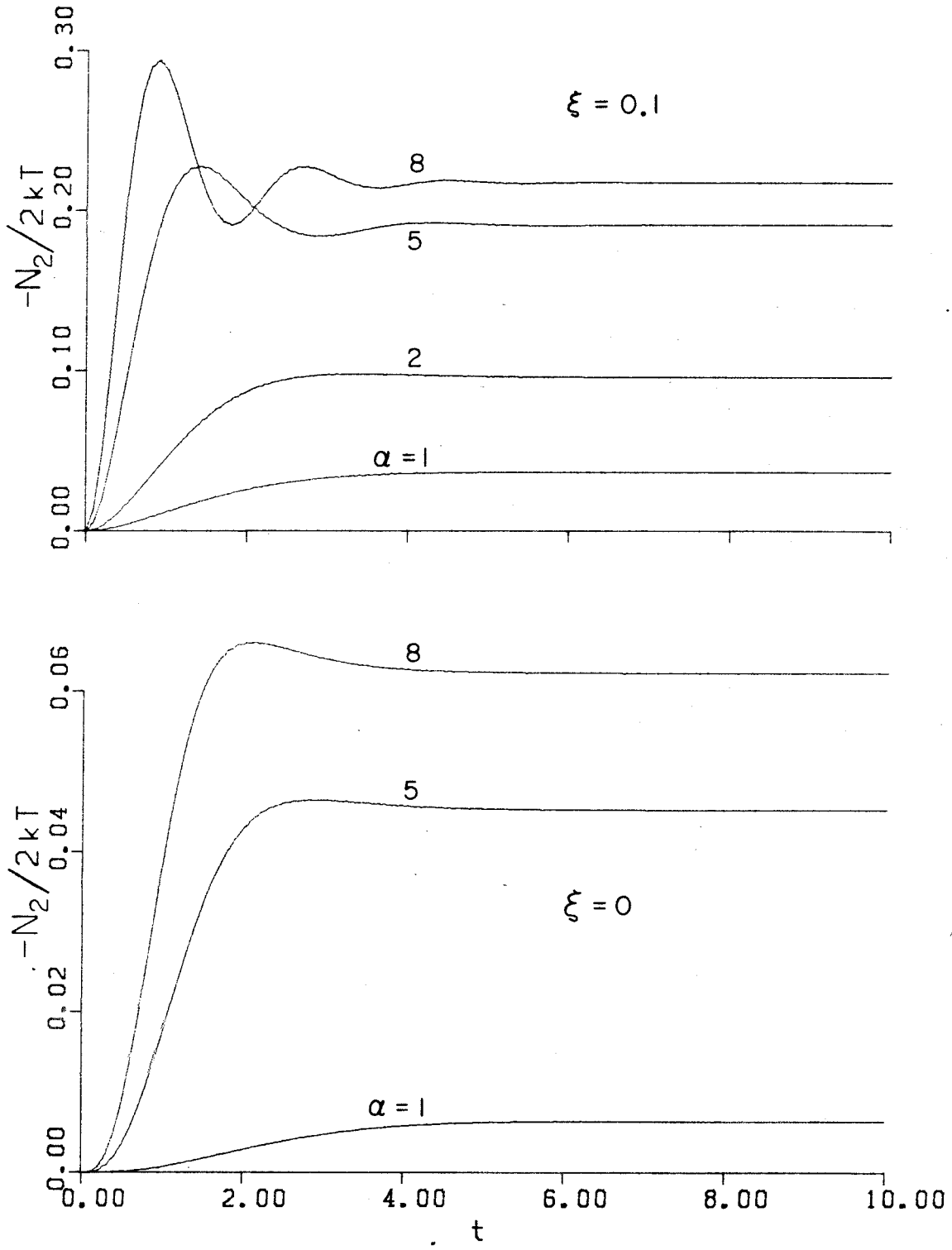
$-N_2/2kT$
0.30
0.20
0.10
0.00
$\xi = 0.1$
8
5
2
$\alpha = 1$
$-N_2/2kT$
0.06
0.04
0.02
0.00
8
5
$\xi = 0$
$\alpha = 1$
0.00
2.00
4.00
6.00
8.00
10.00
t

Fig. 11

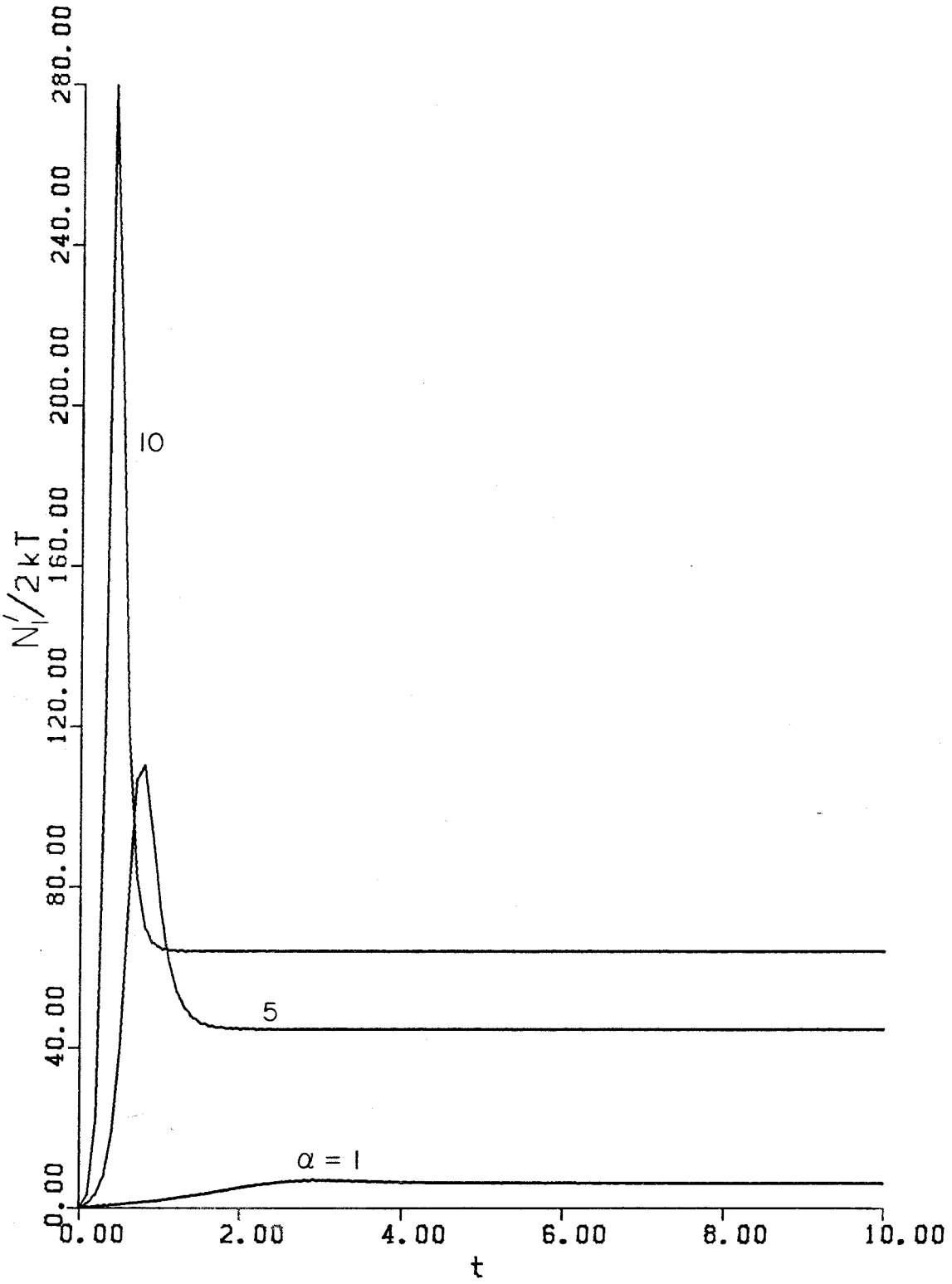
280.00
240.00
200.00
160.00
120.00
80.00
40.00
0.00
$N_1'/2kT$
10
5
α = 1
0.00
2.00
4.00
6.00
8.00
10.00
t

Fig. 12

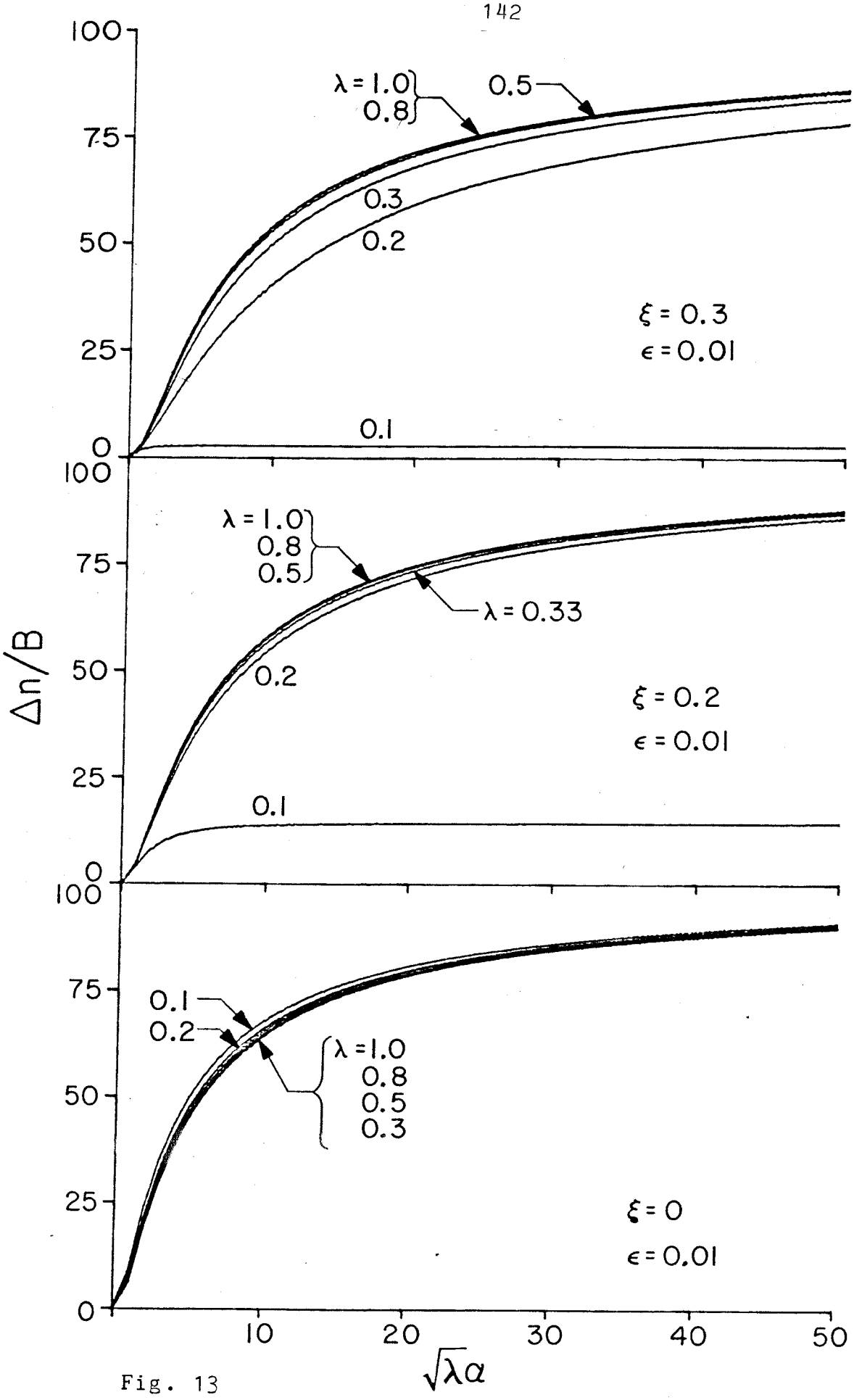
100
75
50
25
0
λ = 1.0
0.8
0.5
0.3
0.2
0.1
ξ = 0.3
ϵ = 0.01
λ = 1.0
0.8
0.5
λ = 0.33
0.2
0.1
ξ = 0.2
ϵ = 0.01
0.1
0.2
λ = 1.0
0.8
0.5
0.3
ξ = 0
ϵ = 0.01
Δn/B
10
20
30
40
50
√λα

Fig. 13

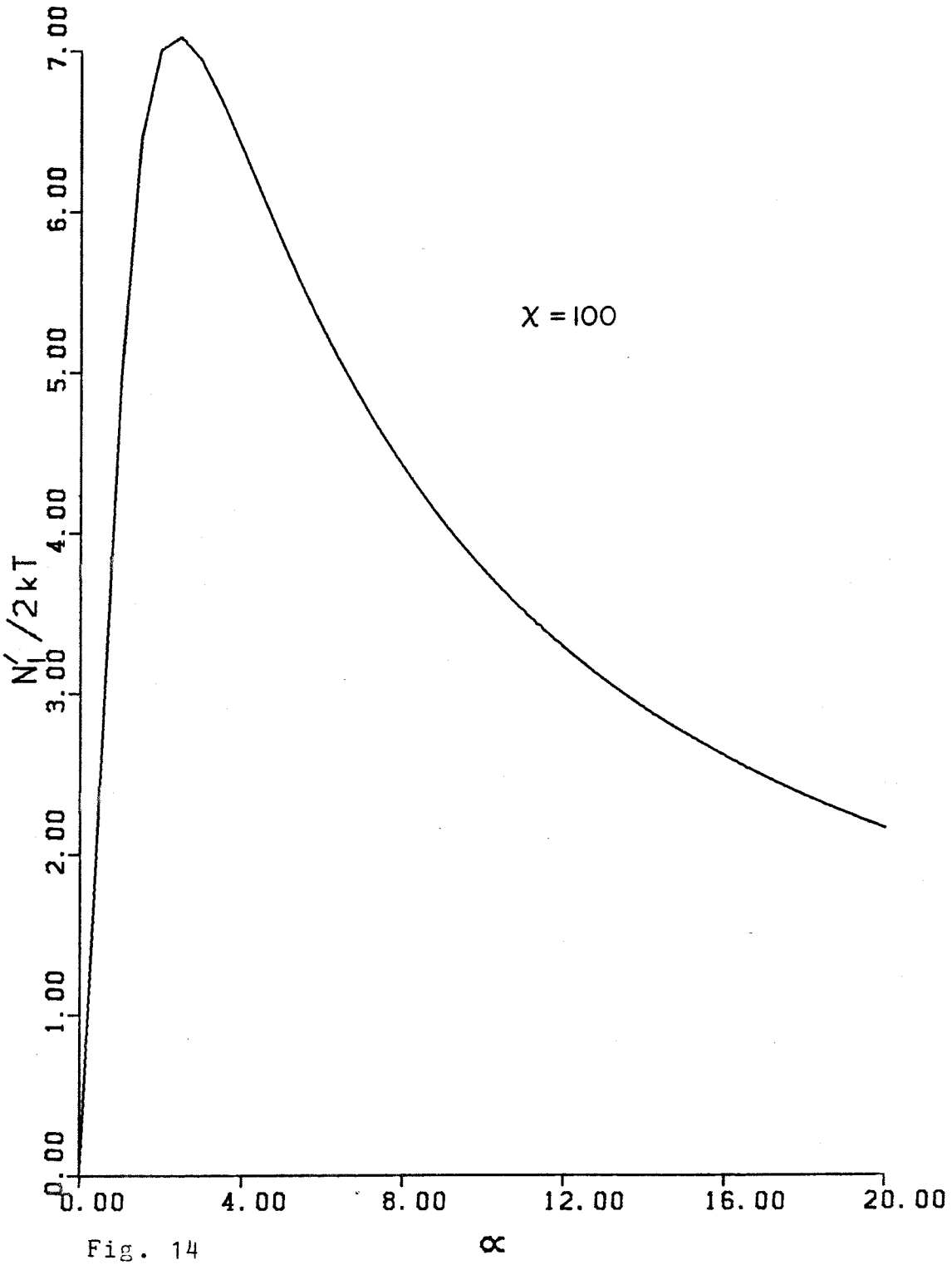
7.00
6.00
5.00
4.00
3.00
2.00
1.00
0.00
$N_1'/2kT$
χ = 100
0.00
4.00
8.00
12.00
16.00
20.00
α

Fig. 14

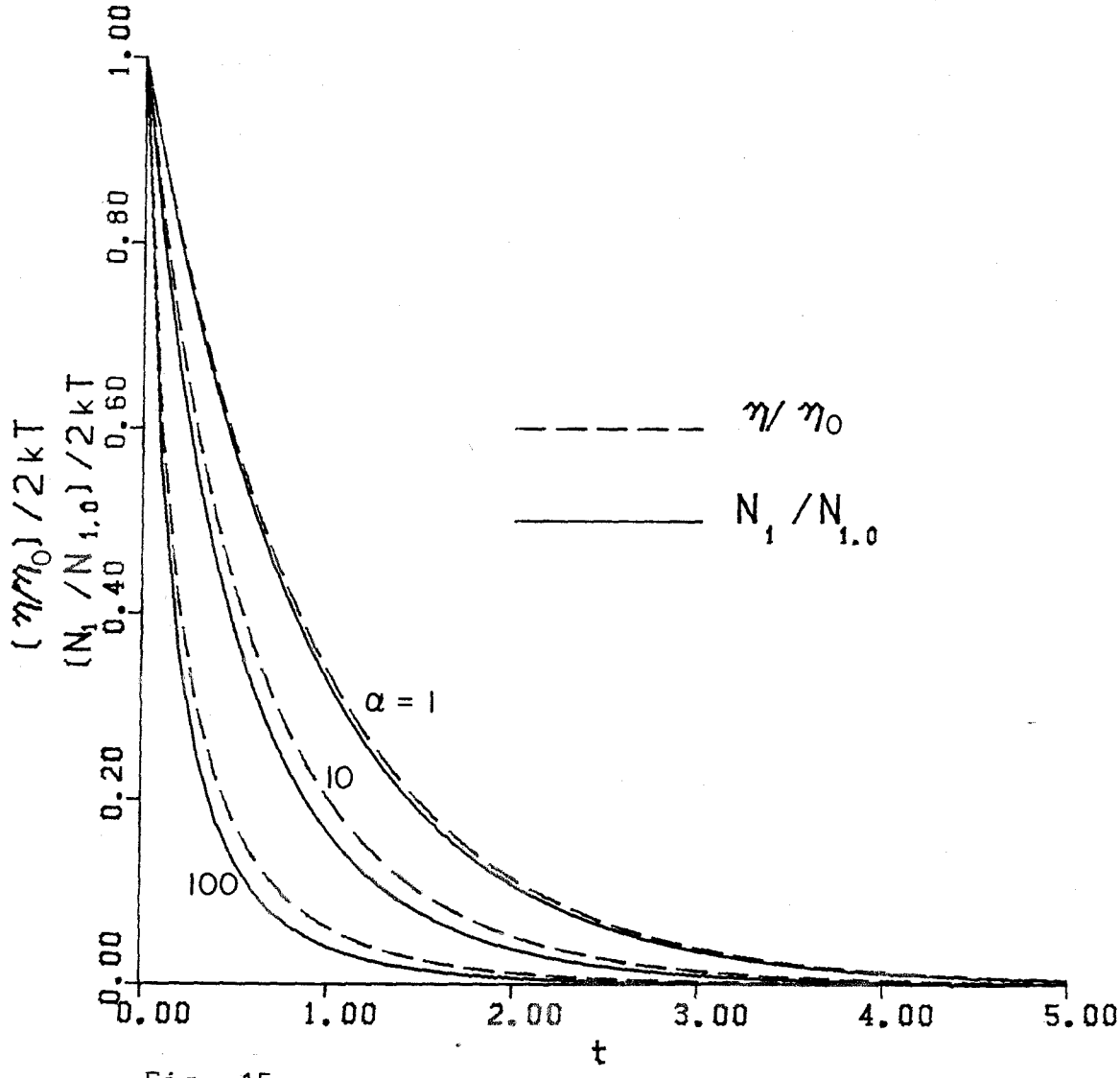
1.00
0.80
0.60
0.40
0.20
0.00
0.00
1.00
2.00
3.00
4.00
5.00
t
[η/η0] /2kT
[N1 /N1.0] /2kT
η/ η0
N1 /N1.0
α = 1
10
100

Fig. 15

Flow Birefringence of Dilute Polymer Solutions in Two-Dimensional Flows

by

G. G. Fuller and L. G. Leal

Department of Chemical Engineering
California Institute of Technology
Pasadena, California 91125

Abstract

Flow birefringence measurements have been obtained on three molecular weight samples ($2\text{-}8\times10^6$ MW, $M_W/M_N = 1.14\text{-}1.3$) of polystyrene in dilute solution (50-100ppm) in a viscous polychorinated biphenyl solvent. The flows were generated using a four roll mill which could simulate a wide range of two dimensional flows in which the flow type (i.e. the ratio of the rate of rotation to the rate of strain) could be varied independently of the velocity gradient. The normalized birefringence, corrected for concentration, ($\Delta n/nc$), was observed to approach a saturation value at high velocity gradients in purely extensional flow. This saturation value was independent of both the molecular weight and the concentration c, in agreement with theory. In addition, the magnitude of the saturation value is consistent with nearly fully extended chains and suggests extensions in the range of 20-50 times the rest state size. The data of the birefringence over a wide range of flows were found to be well correlated against the eigenvalue of the velocity gradient tensor in agreement with the results of the "strong/weak" flow theories of Tanner (1976) and Olbricht et al (1980).

The experiments are compared with a simple dumbbell

model which incorporates the effects of a nonlinear spring, variable hydrodynamic friction, and internal viscosity. It is shown that this simple model can simulate the experimental results surprisingly well if the effects of molecular weight distribution and finite transit times in the flow device are taken into account.

I. Introduction

When subjected to a flow field, a macromolecule in solution will respond to the hydrodynamic forces imposed on it by altering its conformation through reorientation and deformation. It is this change in the conformation of the microstructure which gives rise to the non-Newtonian flow properties which are characteristic of such systems. It is known, for example, that even minute concentrations of macromolecules can cause a substantial decrease in the drag in turbulent shear flows (Toms phenomena) and increased drag in flows through porous media. These phenomena are thought to result from flow-induced stretching of the macromolecules (cf. Hinch (1977), Dreher and Gogarty (1979)).

There has, of course, been a substantial effort to describe the dynamics of macromolecular motions in very dilute solutions using a variety of molecular models (Bird et al (1977)) and these studies have contributed considerable understanding of the mechanisms and nature of flow-induced conformation changes in macromolecules. However, it must always be kept in mind that these are model studies, and there is a critical need for direct experimental determination of the conformational response to flow, from which the various models can be systematically

evaluated and improved. The acquisition of data which can address this issue is the focus of current research in this laboratory. To this end we are employing optical techniques which probe polymer solutions subjected to a variety of flow conditions in order to determine the extent of deformation and orientation of the macromolecules as well as the kinematics of the flow.

This paper reports the results of studies of dilute solutions (50 to 100 ppm) of high molecular weight polystyrene dissolved in a viscous solvent (polychlorinated biphenyl). Flow birefringence was used in order to measure the extent of macromolecular deformation in a wide range of two dimensional flows which are produced in a four roll mill. The experimental apparatus used in this study has also been used to study polymer solutions of higher concentration where intermolecular interactions play a dominant role and the results of that work have been reported elsewhere (Fuller and Leal (1980a)).

Previous investigations using the technique of flow birefringence of dilute polymer solutions have been restricted to the use of either simple shear flow (Philippoff (1963)) in which fluid elements rotate at a rate identical to the rate at which they deform, or purely

extensional flows (Pope and Keller (1978)) where there is no rotation of fluid elements. Consideration of the role of flow type (which can be characterized by the ratio of vorticity to the rate of strain in the two dimensional flows to be considered here) has therefore not been fully addressed. The consequences of flow type have been studied theoretically and criteria governing the onset of large scale deformations in the microstructure have been established based upon several simple models of deformable micro-elements (i.e. either particles of macromolecules) (Tanner (1976), Olbricht et al (1980)). In addition, it may be noted that an understanding of the role of flow type on macromolecular extension is particularly important in the problem of turbulent drag reduction (c.f. Leal, Fuller and Olbricht (1980)). Since it is the flow type combined with the magnitude of the velocity gradient which prescribes the strength of the flow, and the corresponding degree of polymer deformation, it is important that this point be explored experimentally. The four roll mill used in the present experiments made it possible to systematically vary the flow type over a wide range of two dimensional flows, from purely extensional flows to flows which are purely rotational. The study reported here in fact considered flows ranging from pure extension to flows which approach a simple shearing flow.

Prior experiments have also not systematically examined the role of molecular weight or the distribution of the molecular weights in the deformation process. In the experiments discussed here, three samples were studied, varying in molecular weight from 2×10^6 to 8.42×10^6. We also present the results of simple molecular model calculations in order to investigate the degree to which the experimental results can be simulated. The dumbbell model which we use provides a relatively crude representation of a real macromolecule, but does incorporate such effects as internal viscosity, a nonlinear entropic spring and conformation dependent hydrodynamic friction. It is demonstrated that this simple model can fit the data reasonably well if the molecular weight distribution and response time of a macromolecule reacting to the flow are properly accounted for.

II. Theoretical Developments

Important qualitative insight into the dynamic and steady state response of a polymer chain to flow can be obtained using the elastic dumbbell model introduced by Kuhn (1934). In contrast to the "many bead and spring" models of Rouse (1953) and Zimm (1956) where the positions

of many points along the polymer chain are considered, the dumbbell model focuses only on the response of the end to end vector $\underline{r}'$ joining the end points of the chain. Thus, only the principal mode of relaxation is considered and the chain is pictured as a spring joining two points in space (figure 1). Since it is only the relatively slow, long wavelength motions of the macromolecule which are considered, acceleration terms can be neglected and the dynamical equation governing conformation changes in the macromolecule is obtained by noting that the sum of all forces acting on the dumbbell should be zero, i.e.

$$\underline{F}_s + \underline{F}_f + \underline{F}_B + \underline{F}_{iv} = 0 \qquad (1)$$

The forces which appear in equation (1) are:

(1) $F_s = -3NkT\,\xi(r'/R)\underline{r}'/R^2$; the spring force arising from entropy considerations. Here, kT is the Boltzmann temperature and N is the number of statistical subunits making up the chain. The quantity N is proportional to the molecular weight and can be thought of as being equal to the ratio, N_m/n, of the total number of monomer units, N_m, in the chain to the minimum number of monomer units, n, that is required in order that a subunit obey

Gaussian statistics. The function $\mathcal{E}(r'/R)$ is, in general, nonlinear and dependent upon the end to end distance of the macromolecule. Indeed, as $\underline{r}' \to R$, where $R=Na$ is the total possible chain length and a is the length of a subunit, $\mathcal{E}(\underline{r}'/R) \to \infty$. The form for (r'/R) which will be used here is the so called Warner spring (Warner (1972)) in which $\mathcal{E}(r'/R)=1/(1-(r'/R)^2)$.

(2) $F_f = \zeta(r'/R)(\underline{v}-\dot{\underline{r}}')$; the hydrodynamic friction force arising from the relative motion of the solvent and the "beads" of the dumbbell. The parameter ζ is the external friction factor of the entire chain and in general will be a function of the conformation of the chain (Hinch (1974), de Gennes (1974)). The dependence of ζ on r reflects the fact that hydrodynamic interaction between different elements of the chain will change as the polymer is distorted. Indeed, hydrodynamic considerations (Batchelor (1970), Cox (1970)) suggest that the friction factor ζ should increase roughly in proportion to the length scale of the chain. We shall therefore use the form $\zeta=\zeta_o Q(r'/R)$ where $Q(r'/R)=\sqrt{N}r'/R$. In adopting this linear dependence of the friction factor on

the end to end separation distance in the dumbbell we are neglecting a correction factor of the form $\log(r'/\sqrt{N}a)$ which should not alter the qualitative results of the model.

(3) $F_B = kT\nabla \ln(\psi)$; a stochastic Brownian force which acts on the beads of the dumbbell, and arises from the random forces between the solvent molecules and the polymer chain. Here, the probability distribution function for the end to end vector is denoted as ψ .

(4) $F_{iv} = -\zeta_i(\dot{\underline{r}}' - \underline{\Omega} \wedge \underline{r}')$; the force due to "internal viscosity" in the macromolecule which is proportional to its rate of deformation, here assumed to be the difference between the rate of change of r and the rate of rotation of $\underline{r}'$. The angular velocity of the polymer chain is denoted as $\underline{\Omega}$ and ζ_i is known as the internal viscosity coefficient. The notion of an internal viscosity mechanism is introduced in an attempt to account for the effects of local constraints on the dynamics of chain conformation (Cerf (1969), de Gennes (1977)). In general, $\underline{\Omega}$ will be a function of the conformation of the chain. For example,

when there is little deformation and the chain is highly coiled, the polymer will rotate much like a rigid sphere. When it becomes highly deformed, on the other hand, the rotation will lag behind that of a sphere.

An equation of motion for the end-to-end vector of the dumbbell can be obtained by solving equation (1) for $\dot{\underline{r}}'$, and this can be solved (at least in principle) once the bulk velocity field is specified. In the present paper, we consider the general, two-dimensional linear flow

$$\underline{v} = \gamma \underline{\underline{\Gamma}} \cdot \underline{r}' \tag{2}$$

where

$$\underline{\underline{\Gamma}} = \frac{1}{2}\begin{pmatrix} (1+\lambda) & (1-\lambda) & 0 \\ -(1-\lambda) & -(1+\lambda) & 0 \\ 0 & 0 & 0 \end{pmatrix} \tag{3}$$

We have demonstrated earlier (Fuller and Leal (1980a)) that this flow can be simulated using the four roll mill which is described in the experimental section of the paper. The four roll mill consists of four cylinders, the centers of which form a square. The flow of interest is

created in the center region of the square by the rotation of the rollers. Figure 2 illustrates how the flow field, specified by equations (2) and (3) is simulated using the four roll mill. The flow type parameter λ is determined by the relative rates and direction of rotation of rollers 1 and 3 with respect to rollers 2 and 4 and varies between plus and minus one. When λ =1 the flow is purely extensional (also called hyperbolic flow in this two dimensional case) and as λ is decreased, vorticity is systematically added to the flow until, at λ =-1, the flow is purely rotational. The case of simple shear flow is simulated when λ =0. The magnitude of the local velocity gradient, γ , is determined by the rate of rotation of the fastest pair of rollers (rollers 2 and 4).

Using equations (1) and (2), the equation of motion for the dumbbell is obtained by solving for $\dot{\underline{r}}'$. Once this is obtained, it can be combined with the equation of continuity for the probability distribution function

$$\frac{\partial \psi}{\partial t} + \nabla(\dot{\underline{r}}'\psi) = 0 \qquad (4)$$

Following this procedure, the conformation-space diffusion (or Fokker-Planck) equation for ψ is obtained

$$\frac{\partial\psi}{\partial t} + \alpha\nabla\frac{\underline{\underline{\Gamma}}\cdot\underline{r}}{1+\varepsilon/Q}\,\psi - \frac{1}{2}\nabla\frac{1}{1+\varepsilon/Q}\frac{\xi}{Q}\,\psi + \alpha\nabla\frac{\varepsilon/Q}{1+\varepsilon/Q}\,w\hat{\underline{z}}\wedge\underline{r}\psi$$

$$- \frac{1}{6N}\,\nabla\,\frac{1}{1+\varepsilon/Q}\,\frac{1}{Q}\,\nabla\psi \qquad (5)$$

where $\alpha = \gamma\theta$ and $\theta = \zeta_o R^2/6NkT$ is the intrinsic relaxation time for the dumbbell. In equation (4) $\underline{r}=\underline{r}'/R$, $w = \Omega/\gamma$, $\varepsilon = \zeta_i/\zeta$ and $\hat{\underline{z}}$ is a unit vector in the z direction.

The equations for the evolution of the moments of the distribution $\langle x_i x_j\rangle$ can be calculated by multiplying equation (5) by $x_i x_j$ and integrating over the coordinates (x,y,z). However, since the functions $\xi(r)$, $Q(r)$ and w all depend on the conformation of the dumbbell, the resulting terms involving these functions cannot be evaluated explicitly without first solving for the distribution function ψ. Since the coefficients appearing in equation (5) are nonlinear, solution for ψ will in general not be possible. In order to proceed further, we therefore follow the example of Peterlin (1961) and Cerf (1969) and replace ξ, Q and w by their appropriate averaged values. This type of approximation has also been used by Tanner (1977), Hinch (1977) and Phan-Thien et al. (1978). Although this pre-averaging approach is clearly "ad hoc" and approximate, we believe that it will yield reasonable results over a wide range of flow strengths. When the flows are weak and the

dumbbell is not greatly distorted, the nonlinear coefficients in equation (5) are slowly varying functions and do not depart much from their rest state values. On the other hand, when the flows are strong, producing significant distortion of the dumbbell, the probability distribution function becomes strongly peaked and, in fact, can be approximated as a delta function in space. This occurs as a consequence of the typically large values of N that are associated with a macromolecule and the fact that the Warner spring causes the probability mass of the dumbbell to be confined to a space bounded by a sphere of finite radius R. As the dumbbell becomes greatly distorted, the flux of probability mass is reflected off this boundary and ψ becomes strongly peaked in the neighborhood of the boundary. With the functions ξ, Q and w expressed in pre-averaged form, the governing equations for the moments of the distribution are then

$$\frac{d\langle x^2\rangle}{dt} = \frac{1}{1+\varepsilon/Q}\left\{-(\xi/Q)\langle x^2\rangle + \alpha(1+\lambda)\langle x^2\rangle + 2\alpha\left[\frac{(1-\lambda)}{2} + \frac{\varepsilon w}{Q}\right]\langle xy\rangle + \frac{1}{3NQ}\right\} \tag{6a}$$

$$\frac{d\langle y^2\rangle}{dt} = \frac{1}{1+\varepsilon/Q}\left\{-(\xi/Q)\langle y^2\rangle - \alpha(1+\lambda)\langle y^2\rangle - 2\alpha\left[\frac{(1-\lambda)}{2} + \frac{\varepsilon w}{Q}\right]\langle xy\rangle + \frac{1}{3NQ}\right\} \tag{6b}$$

$$\frac{d\langle xy\rangle}{dt} = \frac{1}{1+\varepsilon/Q}\left\{-(\xi/Q)\langle xy\rangle + \alpha\left[\frac{(1-\lambda)}{2} + \frac{\varepsilon w}{Q}\right]\langle y^2\rangle - \alpha\left[\frac{(1-\lambda)}{2} + \frac{\varepsilon w}{Q}\right]\langle x^2\rangle\right\} \tag{6c}$$

$$\frac{d}{dt}\langle z^2\rangle = \frac{1}{1+\varepsilon/Q}\{-(\ /Q)\langle z^2\rangle + \frac{1}{3}\frac{1}{NQ}\} \tag{6d}$$

where

$$\zeta = 1/(1-\langle r^2\rangle) \tag{7a}$$

$$Q = \sqrt{N}\langle r^2\rangle^{\frac{1}{2}} \tag{7b}$$

$$w = \frac{\frac{1}{2}(1-\lambda)\langle x^2+y^2\rangle + (1+\lambda)\langle xy\rangle}{\langle x^2+y^2\rangle} \tag{7c}$$

The equation for w given in equation (7) is derived in Fuller and Leal (1980b) and comes directly from the equation of motion for the rate of change of the end to end vector $\underline{\dot{r}}$.

The moments of the distribution can be obtained by solving the four coupled equations in equation (6) for any given initial condition. The most important initial value problem is when the system starts from rest and the moments

at t=0 are $\langle x^2\rangle=\langle y^2\rangle=\langle z^2\rangle=1/(N+1)$ and $\langle xy\rangle=0$. Given the moments of the distribution function, such macroscopic properties of the polymer solution as the stress tensor and birefringence can be calculated. In particular, Peterlin (1961) has shown that the birefringence is given by

$$\Delta n/nc = 2\pi\{(n^2 + 2)/3n\}^2 (N_A/M) N(\mu_1 - \mu_2) \\ [(\langle x^2\rangle - \langle y^2\rangle)^2 + 4\langle xy\rangle]^{\frac{1}{2}} \qquad (8)$$

where Δn is the birefringence, n is the refractive index of the solution, c is the concentration in g/cm^3, N is Avogadro's number and M is the molecular weight. μ_1 and μ_2 are the polarizabilities of a subunit parallel and normal to the chain axis respectively. The polarizability difference $(\mu_1-\mu_2)$ can be determined by independent measurements in simple shear flow and data for a number of polymer/solvent systems exist in the literature (Polymer Handbook (1965)). The physical constants in equation (8) can therefore be evaluated and measurements of Δn can provide a measure of polymer deformation. In particular, as the polymer becomes highly extended and anisotropic, the birefringence is essentially proportional to the square of the largest dimension of the polymer. As will be pointed out later, the orientation of the distorted polymer can also be determined from birefringence experiments.

In using equation (8) for the birefringence we are only considering the intrinsic birefringence and neglecting any contributions due to form birefringence (Peterlin (1976)). The form birefringence is proportional to the square of the difference of the refractive index for the polymer and the solvent, respectively. In the polymer/solvent system studied experimentally (polystyrene/polychlorinated biphenyl), this difference is very small and this, combined with the large intrinsic segmental polarizability difference of polystyrene (Polymer Handbook (1965)), makes the neglect of form birefringence a reasonable approximation. Given equation (8), Peterlin showed that the birefringence tends to the following saturation value when the polymer reaches its maximum extension:

$$\frac{\Delta n}{nc} = 2\pi\{(n^2 + 2)/3n\}^2 (N_A/M)(\mu_1 - \mu_2)N \qquad (9)$$

Figure 3 shows the predicted steady state value for the root mean square end to end distance in the dumbbell $\langle r^2 \rangle^{\frac{1}{2}}$ for a value of N=2500 and ε =0, plotted as a function of the velocity gradient for several different flow types. The most striking feature which is brought out by this figure is the existence of multiple steady state solutions, which

presumably will lead to a hysteresis loop in $\langle r^2 \rangle^{\frac{1}{2}}$ in an experiment where α is first increased above some critical value and then decreased. For example, if we consider the case of $\lambda = 1.0$, it is suggested in figure 3 that a molecule starting from the rest state subjected to velocity gradients in the range between zero and the critical value $\alpha_1 = 0.275$ (where the slope $(\partial \langle r^2 \rangle^{\frac{1}{2}} / \partial \alpha)$ becomes infinite) will achieve steady states which represent only a small departure from the rest state configuration. On the other hand macromolecules residing in a hyperbolic flow with a velocity gradient greater than α_1 will become greatly extended at steady state. Furthermore, if α is decreased from this larger value after the molecules have had time to become fully extended, the large extension will persist for all velocity gradients greater than $\alpha_2 = 0.026$ where again the slope in the curve is infinite. Only in very weak flows ($\alpha < \alpha_2$) will the macromolecules collapse back to a near rest state configuration if they are highly extended in their initial configuration. As illustrated in figure 3, the existence of multiple steady states appears over a wide range of flow types down to a value of $\lambda = 3 \times 10^{-4}$.

The hysteresis which appears in these model calculations is a consequence of the conformation dependence of the external friction factor. This leads to a pronounced

increase in the frictional grip of the solvent on the polymer chain as it unravels, and since its dimension increases by a factor of $O(\sqrt{N})$ from the coiled rest state to highly extended states. Therefore, even though a critical value of the velocity gradient of α_1 is required to induce the transition to a highly stretched state, it is predicted (or suggested) that a much weaker gradient α_2 is capable of maintaining the large deformation of the chain. This hysteresis was first predicted by de Gennes (1974) and Hinch (1974), and Tanner (1975) later obtained quantitative results showing this effect using a model similar to the one used here for a single value of N and for uniaxial extensional flow. The existence of the hysteresis depends on both the molecular weight (through the parameter N) and the flow type, and a detailed discussion of this dependency is presented in Fuller and Leal (1980b). The steady state birefringence will have qualitatively the same dependence on the velocity gradient as does $\langle r^2 \rangle$ and in fact becomes very close to $\langle r^2 \rangle$ in a quantitative sense for large extensions.

Besides the steady state conformation of the dumbbell, the transient response of the moments of the distribution can also be determined from equation (6). In particular, the time which is required to reach steady state from the

rest state configuration can be calculated. This is of critical importance for the experiments to be described in the next section where the polymer molecules are only subjected to strong flows for a finite period of time. Figure 4 shows the required time (in units of θ) as a function of the velocity gradient for the dumbbell to achieve 90% of the steady state extension for the case N=1000 and purely extensional flow (i.e. λ =1.0). It will be noted that there is a pronounced maximum in the time required to approach steady state for velocity gradients near the critical value, α_1 . In this domain, the hydrodynamic friction forces are too weak to overcome the entropic "spring" except when the dumbbell is highly extended. Once a dumbbell becomes highly extended, the friction forces can maintain it in an extended state, but the only mechanism which can lead to a sufficiently extended state is diffusion and the times required to achieve a statistical steady state are therefore predicted to be very long. As the velocity gradient is increased, the amount of extension which is required for the friction forces to overcome the spring decreases, and the time required to approach steady state drops off rapidly. Eventually, the friction forces become dominant for any configuration near equilibrium, and the time required for extension scales as γ^{-1}.

In order to properly analyze the experiments described in the next section it is necessary to consider the transit times of the polymer chains in the flow device and compare those times with the time required for the polymer configuration to approach steady state. The flows generated in the four roll mill used in the experiments were characterized using flow visualization techniques and homodyne light scattering spectroscopy. Detailed accounts of the procedures and results are reported in Fuller and Leal (1980a) and Fuller et al (1980). It was found that the flow device was capable of simulating the velocity field described by equation (3) as long as the magnitude of the flow type parameter λ was greater than approximately 0.1. Using equation (3), the trajectory of a particle starting at (x_o, y_o) at time zero is therefore

$$x = x_o \frac{(1 + \lambda)}{2\sqrt{\lambda}} \sinh\sqrt{\lambda}\gamma t + x_o \cosh\sqrt{\lambda}\gamma t + y_o \frac{(1 - \lambda)}{2} \sinh\sqrt{\lambda}\gamma t \qquad (10a)$$

$$y = -x_o \frac{(1 - \lambda)}{2\sqrt{\lambda}} \sinh\sqrt{\lambda}\gamma t - y_o \frac{(1 + \lambda)}{2\sqrt{\lambda}} \sinh\sqrt{\lambda}\gamma t + y_o \cosh\sqrt{\lambda}\gamma t \qquad (10b)$$

The birefringence experiments were performed by sending a laser beam of radius ℓ along the z axis through the

stagnation point of the four roller flow. The macromolecules within this sample region will have been subjected to a range of transit times depending on the particular streamline the molecule is travelling on. In principle, a molecule could reside at the stagnation point indefinitely while molecules entering the test region at the point $(x,y)=(\ell/\sqrt{2},\ell/\sqrt{2})$ will have spent the least amount of time in the flow. Therefore, a conservative estimate of the time available to molecules within the test domain to respond to the flow can be obtained by calculating the time required for a particle to reach the point $(x,y)=(\ell/\sqrt{2},\ell/\sqrt{2})$ on the sample region boundary if it starts from a radial distance D away from the stagnation point at time zero (see figure 5). In particular, for a particle which reaches the point $(x,y)=(\ell/\sqrt{2},\ell/\sqrt{2})$ starting from $(D\cos\phi, D\sin\phi)$, the transit time and the angle ϕ can be found using equation (10). The solution for the transit time is a straightforward calculation and yields

$$t = \frac{1}{\sqrt{\lambda}\gamma} \sinh^{-1}\left[\frac{\lambda}{1+\lambda}\left(\left(\frac{D}{\ell}\right)^2 - 1\right)\right]^{\frac{1}{2}} \qquad (11)$$

Examination of the two limits of $\lambda = 1$ and $\lambda = 0$ leads to

$$t_1 = \frac{\log(\sqrt{2}\ D/\ell)}{\gamma} \tag{12}$$

and

$$t_o = \frac{\sqrt{(D/\ell)^2 - 1}}{\gamma} \tag{13}$$

respectively, as expected.

The transit time for molecules in the four roll mill and the required time for a molecule to achieve 90% of steady state extension can now be compared for a given value of the velocity gradient in order to estimate the range of steady states that can actually be realized experimentally. Figure 4 shows this comparison for the case of purely extensional flow and for two values of the ratio (ℓ/D) which are in the range used in the experiment. The results shown in figure 4 suggest that steady state levels of extension will not be achieved for velocity gradients near the critical value, α_1 , due to the finite transit times of the molecules in the four roll mill and the long diffusion controlled growth times for the molecules. On either side of the critical point, however, the experiment is capable of attaining steady state levels of deformation.

The realizable degree of extension is shown by the dashed curves in figure 3. These curves were computed for λ =1.0 and λ =0.1, for two different values of ℓ/D, by

calculating the extension achieved by a macromolecule starting from rest and subjected to the flow field for a duration of time given by equation (11). As the ratio ℓ/D increases, the range of transit times is decreased and the observed transition in α from the coiled rest state to full extension is predicted to become more gradual as would be expected.

Another important consideration which must be accounted for in comparing experimental data to theoretical predictions is the molecular weight distribution of the polymer sample. Our calculations up to this point have all considered monodisperse distributions where the ratio of the weight averaged molecular weight M_w and the number averaged molecular weight M_n is unity. In general, however, commercial polymer samples will be characterized by a ratio of M_w/M_n which is greater than unity, and by the presence of a high molecular weight tail. If the distribution of molecular weight is given by $P(M/M_o)$, where M_o is the most probable molecular weight of the distribution, any measured quantity which depends on molecular weight will be an average over this distribution. For example, the measured birefringence will be

$$\langle \Delta n \rangle / n \langle c \rangle = \frac{B \int_0^\infty dNP(N/N_o) N \left[(\langle x^2 \rangle - \langle y^2 \rangle)^2 + 4\langle xy \rangle^2 \right]^{\frac{1}{2}}}{\int_0^\infty dNP(N/N_o) N} \qquad (14)$$

where $B=2\pi\{(n^2+2)/3n\}^2 (\mu_1-\mu_2)N_A$.

In carrying out this integration it must be remembered that the molecular weight enters into the birefringence not only through the parameter N, but also through the relaxation time θ which appears implicitly in the dimensionless velocity gradient α. From the definition for θ following equation (5) and the fact that the friction factor in the rest state is proportional to the rest state chain radius, $\sqrt{N}a$, the relaxation time will scale as $\theta \sim N^{3/2}$ for this Gaussian model.

A simple distribution which possesses a high molecular weight tail and which depends only on the two parameters M_w and M_n (which are usually all that are available from standard analysis of commercial samples) is the log-normal distribution (Billmeyer (1962)):

$$P(M/M_o) = e^{-\sigma^2/2} e^{-\log^2(M/M_o)/2\sigma^2} \qquad (15)$$

$$\sigma^2 = \log(M_w/M_n)$$

$$M_o = M_n e^{-\sigma^2/2}$$

Using this distribution and equation (14), we have calculated the average birefringence for N =2500 and M_w/M_n=1.17 which were typical values for the experiments. The effect of the finite transit time of the polymer molecules was taken into account using the same procedure as described above in connection with the dashed curves in figure 3. In evaluating (14) we have assumed that the chains are Gaussian so that the relaxation time θ scales with the molecular weight as $\theta \sim M^{3/2}$. The results are found in figure 6 where the birefringence which is predicted as observable in the four roll mill is plotted against the eigenvalue of the velocity gradient tensor of equation 3, $\sqrt{\lambda}\,\alpha$. We have considered a wide range of the flow type parameter λ and several values of the ratio $\varepsilon = (\zeta_i/\zeta)$ which specifies the magnitude of the internal viscosity effect.

Figure 6 demonstrates that the curves of "observable" birefringence (as well as any invariant of the tensor of moments $\langle \underline{x}\ \underline{x} \rangle$) should fall close to one another over a wide range of the parameter λ when plotted against $\sqrt{\lambda}\,\alpha$. The range of λ over which this correlation exists depends upon the magnitude of the internal viscosity effect and in fact the correlation breaks down when ε becomes too large (as in

the case of $\varepsilon = 0.5$ in figure 6). An analogous situation was also found for a series of network models used to describe concentrated solutions (Fuller and Leal (1980a)) where it was predicted that the birefringence could be correlated against $\sqrt{\lambda}\alpha$ over a wide range of λ provided that the effects of nonaffine deformation were not too pronounced.

The correlation illustrated in figure 6 for the case of $\lambda = 0$ results from the fact that the eigenvalue of the velocity gradient tensor prescribes the strength of the flow and therefore the extent of macromolecular deformation. This latter fact can also be demonstrated by a simple linear stability analysis of the equations of motion of the moments listed in (6). Neglecting Brownian motion, such an analysis (Tanner (1976), Olbricht et al (1980)) predicts that the dumbbell will undergo unbounded growth whenever $\sqrt{\lambda}\alpha > 1/2$. This simple calculation, although sufficient to reveal the flow strength is not capable of predicting steady state results and leads to either infinite growth or complete collapse of the end to end vector depending on the magnitude of $\sqrt{\lambda}\alpha$. Inclusion of Brownian motion causes the end to end vector to have a finite size even when the flow is weak ($\sqrt{\lambda}\alpha < 1/2$) and for that reason the correlation of the birefringence with $\sqrt{\lambda}\alpha$ will break down as $\lambda \to 0$. This is the reason for the departure of the $\lambda = 0.1$ curve for $\varepsilon = 0$ from

the correlation in figure 6.

Internal viscosity affects this situation in two ways. As can be seen from equation (6) the internal viscosity increases the time scale of the dynamics of the dumbbell by a factor of $(1+\varepsilon/Q)$ regardless of the flow type. Thus, in spite of the fact that internal viscosity will not affect the actual steady state end to end extension in irrotational flows, the finite transit times inherent in the experiment and the increased time scale for the dumbbell's response will cause the birefringence to rise more slowly with α as ε is increased. This effect will carry over to all flow types. When the flow contains a rotational component the internal viscosity additionally affects the steady state conformation of the dumbbell. In particular, for a given value of $\sqrt{\lambda}\alpha$, an increase in internal viscosity will cause a decrease in the end to end separation in the dumbbell and a consequent decrease in the birefringence whenever the flow contains vorticity (i.e. the term $\varepsilon w/Q$ in equation is nonzero). Furthermore, the magnitude of the decrease in birefringence will increase as the flow becomes increasingly rotational (i.e. as λ is decreased). Therefore as the internal viscosity is increased, the range of λ over which the correlation of birefringence with $\sqrt{\lambda}\alpha$ holds will be reduced. This point is brought out in figure 6

and suggests that measurements of birefringence as a function of flow type may provide an estimate of the magnitude of the internal viscosity parameter ε for a given polymer/solvent system.

Figure 6 also demonstrates the importance of the influence of the molecular weight distribution. If the sample is monodisperse, the model predicts a sharp transition from the rest state configuration to a highly stretched state at a critical value of the velocity gradient. As shown by figure 3 this transition is quite abrupt even when the effect of finite transit times in an actual experiment is considered. However, the distribution of molecular weights can markedly broaden this transition due to the strong dependence on the molecular weight of the critical value of the velocity gradient at which the transition occurs.

III. Experimental

A. Description and Characterization of the Materials and Apparatus

Measurements were performed using three different molecular weight samples of polystyrene dissolved in a

polychlorinated biphenyl solvent. The physical properties of the polymer samples are listed in table 1. The 8.42×10^6 and 4.48×10^6 molecular weight samples were purchased from Toyo Soda Manufacturing Co. and the 2×10^6 molecular weight sample was purchased from Pressure Chemical Co.. The PCB solvent was obtained from Prodelec Co. (France) which produced this product under the name Pyralene 4000. All of the experiments were run at a temperature of 20° C at which the viscosity of the solvent is 454 cp and its refractive index is 1.630.

Polymer solutions of 100 ppm were made by first dissolving the required amount of polymer in a small volume of a volatile solvent (dichloromethane). After dissolution for a period of one day this solution was mixed with the PCB solvent and the entire mixture was allowed to sit heated from below to about 50-60° C for several days. This provided a gentle mixing of the constituents by thermal convection. The solution was then placed under a vacuum for one day in order to draw off the dichloromethane. Solutions of polymer at lower concentration were prepared by dilution of the 100ppm solutions. The final solutions were then passed through a 1 micron teflon filter.

The experimental apparatus was described in detail in

Fuller and Leal (1980a) and a simple schematic of the arrangement used for the birefringence measurements is seen in figure 7. The orientation of the various vectors of polarization, the principal axes of the refractive index tensor of the deformed sample and the orientation of the four roll mill are shown in figure 8. If I_o is the intensity of the incident light beam, the intensity of the light passing through the analyzer polarizer can be shown to be

$$I = I_o \sin^2 2\theta \sin^2 \frac{\delta}{2} \qquad (16)$$

where θ is the orientation angle defining the principal axis of the sample refractive index tensor and $\delta = 2\pi d(n_{\parallel} - n_{\perp})/\lambda$. Here $\Delta n = (n_{\parallel} - n_{\perp})$, λ is the wavelength of the light and d is the path length of the sample. The procedure which was followed in measuring the birefringence is to first rotate the flow device and determine the angle χ (see figure 7) at which the intensity measured at the photodetector is at a maximum. This maximum occurs when the orientation angle of the deformed polymer θ is ± 45 . At this orientation the intensity was recorded and the birefringence was calculated using equation 16. In using equation 16 the path length d was assumed to be the total depth of the flow device. This approximation neglects the

fact that the velocity fields in the flow device are not truly two dimensional due to the boundaries at the top and bottom of the four roll mill. It is evident that the velocity gradients in the (x,y) plane will, in fact, vary along the z axis and go to zero at the boundaries. Therefore the birefringence measurements reported here, for a given value of the velocity gradient at the centerplane of the four roll mill, will slightly underestimate the level of birefringence which would occur if the centerplane flow existed throughout the measurement path (i.e. for all z).

Flow visualization studies as well as homodyne light scattering spectroscopy experiments were performed in order to characterize the flows in the four roll mill and the results of these studies are reported in detail in Fuller and Leal (1980a) and Fuller et al (1980). In particular it was found that the four roll mill could closely simulate the velocity field of equation 3 for all $|\lambda| > 0.1$. Furthermore, the velocity gradients were found to depend linearly on the angular velocities of the fastest pair of rollers, ω, according to

$$\gamma = 0.678\omega$$

where ω is measured in radians/sec. This linear

relationship was found to hold over the entire range of roller velocities accessible in this device (0-35 sec^{-1}).

The homodyne light scattering experiments reported in Fuller et al (1980) were performed on a Newtonian liquid (glycerin) and were repeated here for the polymer solutions. Since the experimental arrangement (and corresponding theoretical analysis) of the experiment is reported in Fuller et al (1980), only a brief summary will be given here. The homodyne scattering technique involves measurement of the autocorrelation function of the light scattered from particles in the flowing solution. The autocorrelation function, in turn, contains information regarding the motion of the particles which contribute to the scattered light spectrum. The principal advantage of this method (in contrast to other optical techniques such as laser doppler velocimetry) is that the mean motion of the particles does not influence the measurements and it is the variations in the particle velocities arising from velocity gradients which dominate the autocorrelation function. This makes it possible to determine local velocity gradients directly with a single measurement thereby avoiding the inherent difficulties of taking point by point velocity measurements and differentiating experimental data to determine the velocity gradients. One important drawback of

this method, however, is that the correlation function depends strongly on the spatial distribution of incident light intensity used to induce the scattered light. Since this distribution is very difficult to measure, absolute determination of velocity gradients is not an easy task. However, if one is only interested in relative measurements of velocity gradients (i.e. the dependence of the velocity gradient on the roller speed or velocity gradients as a function of position), the procedure for accomplishing this is straightforward and outlined in detail in Fuller et al (1980).

Figures 9 and 10 show the results of such measurements for the 8.42×10^6 and 4.48×10^6 molecular weight solutions at 100 ppm where the measured velocity gradient ($\partial v_x/\partial x$) in arbitary units is plotted against the angular velocity of the rollers. These measurements were taken at the center stagnation point in the flow device. In both cases the velocity gradient is seen to be linear in the roller velocities over the entire range of roller speeds which were used in the birefringence experiments.

B. Results of Flow Birefringence Measurements

The polymer/solvent system investigated here was

studied previously by Philippoff (1963) who measured the flow birefringence from solutions of 9×10^6 MW polystyrene in Arochlor 1248 subjected to simple shear flow. These experiments were performed at 25°C where the solvent viscosity was 250 cp and over a concentration range from 500 ppm to 1%. These experiments demonstrated that the PCB solvent is itself birefringent and that data taken on polymer solutions using this solvent must be adjusted in order to account for this effect. Figure 11 shows the birefingence measured for the solvent subjected to a variety of flow types in the four roller device. The angle χ at which the birefringence intensity was a maximum was independent of the flow type and equal to 0° which is an expected result. The birefringence of the solvent for the extensional flows measured here was considerably higher than that reported by Philippoff for the case of simple shear flow. In particular the case of $\lambda = 1.0$ produced birefringence which was 20 times greater than the measurements of Philippoff at comparable velocity gradients which reflects the greater effectiveness of purely extensional flow over simple shear flow in orientation of anisotropic particles for a given velocity gradient.

Both the polymer and solvent will contribute to the birefringence of the solution and the effect of the solvent

must be subtracted out. If Δn_o and Δn_1 are the birefringence of the solvent and solution respectively and β is the angle between the principal axes of the solvent and solution refractive index tensors, Philippoff (1963) showed that the birefringence Δn_2 arising from the polymer alone is given by

$$\Delta n_2 = \left[\Delta n_o^2 + \Delta n_1^2 - 2\Delta n_1 \Delta n_2 \sin\beta\right]^{\frac{1}{2}} \qquad (17)$$

This simple relationship is derived by assuming that the effects of the solvent and polymer can be linearly superimposed and that the polarizability tensors of the solvent and polymer are additive.

Figure 12 shows photographs of the birefringence pattern resulting when a 100 ppm solution of the 2×10^6 molecular weight sample is subjected to various flow types and velocity gradients. The region of visible birefringence is extremely narrow and was, in fact, determined to be roughly 0.01 to 0.02 inches in thickness. This localization of the birefringence and therefore of the region containing significantly deformed polymer is typical of extensional flows (Crowley et al (1976), Pope and Keller (1978)) and results from the fact that the polymer chains require a finite amount of time in order to respond to the flow. This

is demonstrated in figure 4 where very small ratios of ℓ/D in the experiment are required in order that the majority of molecules in the sample region approach steady state extensions. In all of the photographs the orientation of the camera was kept constant relative to the four roll mill and the photographs indicate qualitatively that the birefringence curves coincide with the exit streamlines which emanate from the stagnation point of the flow. Assuming this to be true, the parameter λ associated with the flow can be estimated from the angle at which the birefringence curve departs from the horizontal. For the velocity gradient tensor of equation (3) it is a simple matter to show that if this angle is ϕ the parameter λ is

$$\lambda = [\tan(45^\circ - \phi)]^2 \tag{18}$$

For the case of $\lambda = 0.333$ (as determined by the roller speeds), for example, an angle of 16° is measured from the photographs of figure 12, and this yields a value of $\lambda = 0.31$ from equation (18). Similarly, the $\lambda = 0.2$ photograph yields an angle of $\phi = 22$ which leads to a value of λ of 0.18 from equation (18).

Using equation (17), the birefringence measured for the polystyrene solutions was adjusted in order to obtain the

contribution due to the polymer alone. The results for 100 ppm solutions for all three molecular weights and for several different flow types are shown in figures 13-15. It is important to note that the birefringence of the polystyrene is of the opposite sign to that of the solvent and this arises from the fact that $(\mu_1-\mu_2)$ is a negative quantity for this polymer. The absolute magnitude of the polymer birefringence is an order of magnitude higher than the solvent birefringence for this concentration of polymer. This is in contrast to the results of Philippoff where the birefringence from the polymer subjected to simple shear flow was only a small fraction of the solvent birefringence for solutions of even higher concentration (500 ppm). Indeed, when adjusted for concentration, the birefringence measured in this work from the 8.42×10^6 molecular weight polystyrene subjected to purely extensional flow was over three orders of magnitude greater than that reported by Philippoff of a 9×10^6 molecular weight sample in simple shear flow at comparable velocity gradients. This point underscores the relative strength of extensional flows over simple shear flow and the much greater deformation (or stretching) of the macromolecules which this implies.

The important role that flow type plays in the deformation of the macromolecules and the effect of

molecular weight on this process are both demonstrated by the data in figures 13-15. As vorticity is added to the flows by decreasing the parameter λ, the polymer chains will tend to rotate continuously into and away from the principal axes of strain of the flow and will therefore be alternatively extended and compressed leading to a decrease in the overall distortion of the molecule. The effect of molecular weight is principally to alter the relaxation time of the polymer. As molecular weight is increased the relaxation time increases as well and for any given value of the velocity gradient the amount of deformation (and therefore birefringence) will be greater for larger molecular weights. In the dumbbell model presented in the previous section this effect enters through the fact that the dimensionless velocity gradient, α, being scaled by the relaxation time, will increase with the molecular weight thereby leading to higher deformations.

Solutions of 50 ppm for the the 8.42×10^6 and 4.48×10^6 polystyrene were also studied. Figure 16 compares the birefringence from the 50 and 100 ppm solutions for the case of purely extensional flow and indicates that the birefringence is linearly proportional to the concentration in the range from 50-100 ppm. This suggests strongly that the polymer molecules are behaving in a largely independent

fashion. Linearity of the birefringence with concentration was also reported by Philippoff (1963) from about 500-1500 ppm for a 9×10^6 polystyrene subjected to simple shear flow and by Pope and Keller (1978) for 2×10^6 molecular weight polystyrene in the range of 300-5000 ppm for a uniaxial extensional flow.

An estimate of the range of concentration over which the flow birefringence should be a linear function of the concentration can be obtained by considering the volume fraction of the constituent polymer molecules in the flowing solution. The appropriate length scale to use when estimating the volume fraction is the hydrodynamic radius of the polymer chain (Hinch (1977)) which is roughly the largest length scale of the molecule. If ν^* represents the volume fraction of polymer above which dilutedness can no longer be assumed and interactions begin to become important, this would be equal to

$$\nu^* = \frac{4\pi}{3} r^3 \frac{c^*}{M} N_A$$

where r is the largest length scale of the polymer and c^* is the weight concentration. The maximum value of r occurs when the chain is fully extended and is proportional to the

molecular weight M. Therefore the lower bound on the concentration c* above which interactions become important will scale as $c \sim M^{-2}$. Using this simple scaling rule, the concentration range of 300-5000 ppm over which the birefringence was reported to be linear for the 2×10^6 MW sample studied by Pope and Keller is compatible with the range of 50-100 ppm for the 4.48 and 8.42×10^6 samples presented here. The much higher concentration range reported by Philippoff for a 9×10^6 MW sample can be understood by realizing that in simple shear flow the hydrodynamic radius would never depart greatly from the highly coiled rest state over the range of velocity gradients he studied.

As discussed previously, it is of interest to plot the birefringence data collected for various flow types against the eigenvalue of the velocity gradient tensor $\sqrt{\lambda}\,\alpha$ in order to see the range of λ over which the birefringence can be correlated against this group. This is done in figure 17 for all three molecular weight samples at 100 ppm and it appears that the correlation holds in all three cases over the entire range of λ studied ($1.0 \geq \lambda \geq 0.2$). From the dumbbell model of the previous section this would suggest that the role of internal viscosity is relatively minor and that the parameter ε is 0.3 or less. This estimate was

arrived at through simple qualitative comparisons of the data and model curves of the type shown in figure 6.

It is important to note that the birefringence for both the 8.42×10^6 and 4.48×10^6 molecular weight samples achieve the same asymptote at high velocity gradients to within about 6%. The fact that this asymptote is independent of molecular weight is in agreement with equation (9) and it is possible to estimate the degree to which the polymer molecules in the experiments achieved full extension from this saturation value. In the case of the 8.42×10^6 molecular weight sample, for example, if it is assumed that the minimum number of monomer units which are required in order to form a Gaussian subunit is n=10, the parameter N is 7874. Using equation (9), the saturation value of $\Delta n_\infty/nc$ is calculated to be 0.045. This value, when compared to the measured asymptote of 0.015 would suggest that the polymer chains in the experiment are very near to full extension. Since the birefingence at high chain extensions is roughly proportional to the square of the largest length scale of the chain, a value of $\Delta n_\infty/nc$ of 0.015 would suggest that the polymer molecules have achieved about 60% of their maximum possible extension. These estimates, however, do strongly depend on the value chosen for the parameter n from which N is calculated and for that reason should be treated only as

rough approximations. This value for $\Delta n_\infty/nc$ is also in the same neighborhood as the value of 0.04 that was reported by Pope and Keller. Alternatively, using equation (9), the experimentally determined asymptote can be used to estimate the parameter N associated with the macromolecules studied. For example, values of 2500, 1330 and 594 are computed for the 8.42×10^6, 4.48×10^6 and 2×10^6 samples respectively. Based on the number of monomer units for each polymer sample (for example the number of monomer units for the 8.42×10^6 MW sample is 78740) these estimates for N lead to a value of n, the number of monomer units required to make a Gaussian subunit, equal to 30. For the simple Gaussian model used here, the ratio of the maximum extension length to the rest state end to end distance is equal to $\sqrt{N}$ which would suggest that the 2.0, 4.48 and 8.42×10^6 MW samples have been extended by factors of 24, 36 and 50 respectively.

It is also of interest to see how closely the simple dumbbell model can predict the qualitative features of the experimental results. In order to obtain a comparison it is necessary to estimate the relaxation times of the polymer molecules and to this end we have used the results of dynamic light scattering experiments performed in this laboratory (Sankur (1976)) for samples of 4.1×10^6 polystyrene in cyclohexane at theta conditions. From this

work it was found that the relaxation time of the polymer was 97×10^{-6} seconds. Adjusting this value for temperature and solvent viscosity and assuming Gaussian statistics (i.e. $\theta \sim M^{3/2}$), the birefringence was calculated for the physical characteristics (i.e. M_w/M_n, n, $(\mu_1 - \mu_2)$) listed in table 1 and for the experimental estimates N corresponding to each respective molecular weight listed above . The effect of finite transit times in the test region of the four roller device were also taken into account using the same method by which the dashed curves in figure 3 were calculated. This was done assuming $\varepsilon = 0$ and for $\lambda = 1.0$. In carrying out this calculation using the simple dumbbell model it is necessary to adjust the relaxation time by a factor of 2.214 as pointed out by Peterlin (1963) due to the fact that the dumbbell model overestimates the relaxation time by this amount relative to the more realistic predictions of the bead and spring model of Zimm (1956) which includes the effects of hydrodynamic interaction. The model predictions are shown in figure 17 as the solid curves. The qualitative agreement between the model and the data is quite satisfactory considering the relative simplicity of the model and the ad hoc choices for the forms of the friction factor and spring functions.

The close resemblance between the model predictions and the

experimental data demonstrates the importance of considering the finite transit times in the flow device and the distribution of molecular weights in the sample. Both of these effects contribute to smoothing out the transition from the highly coiled rest state to highly extended states which would occur abruptly for a monomolecular system at a critical value of the velocity gradient. Comparison of the model curves to the data in figure 17 also shows that the relaxation time of the polymer samples studied here scales roughly with the molecular weight as $M^{3/2}$.

IV. Conclusions

We have reported the results of flow birefringence experiments on dilute concentrations of polystyrene of high molecular weight dissolved in a viscous solvent. In particular the important consequences of the flow type and molecular weight are systematically considered. The experimental results have been complemented by calculations using a simple dumbbell model, and the comparison between theory and experiment brings out many important features which must be considered in analyzing the data. Among these are the effects of transit times in the experiment, molecular weight distributions and internal viscosity.

The experimental apparatus used in this investigation is not without limitations and efforts are being directed in this laboratory to overcome several shortcomings. One refinement which can be made in the four roll mill used here would be to increase the aspect ratio of the rollers (i.e. the ratio of the length to radius) which would improve the simulation of purely two dimensional flows and make the assumption of constant birefringence/length along the sample path which is used in equation(16) more valid. Another restriction of the four roll mill used here is the range of flow types ($|\lambda|<0.1$) which can be investigated. This limitation is probably inherent to the basic design of the four roll mill and is a reflection of its inability to simulate simple shear flow although the simulation of highly rotational flows or highly extensional flows is quite satisfactory. However, the variation of flow type in the neighborhood of that of simple shear flow is desirable, especially with regard to the investigation of the importance of the internal viscosity mechanism. Current research efforts are being made in this laboratory to design flow devices which would be capable of achieving this goal.

Another restriction which results from the practicalities of the design of the four roll mill is that the device is typically quite large and the dimension of the

diagonal spacing between the rollers is typically on the order of one centimeter. This places a restriction on the choice of solvents which one can use when studying dilute polymer solutions, as the solution viscosity must be sufficiently large in order to avoid large values of the Reynolds number over the range of velocity gradients which are of interest. For this reason, the effect of the polymer/solvent interaction cannot be readily investigated and flow devices of much small length scale such as the sucking jet (Pope and Keller (1978)) would be preferred in order to study such effects.

One area of interest which can be studied with the present experimental arrangement is the effect of the molecular architecture of the polymer (side chain branching, rigidity etc.) and the influence of electroviscous effects in ionic polymer/solvent systems. These effects have not been systematically investigated in the past and are the focus of current research efforts in this laboratory.

ACKNOWLEDGEMENT

This research was supported by the Office of Naval Research. One of us (G.G.F.) is indebted to the National Research Council of Canada for fellowship support.

The authors would like to thank Mr. P. N. Dunlap for supplying the photographs for figure 12.

References

Batchelor, G. K., J. Fluid Mech. 44,479(1970).

Billmeyer, F., Textbook of Polymer Science, Interscience Publ. (1962).

Bird, R. B., Armstrong, R. C. and Hassager, O., Dynamics of Polymeric Liquids, Volume II: Kinetic Theory, Wiley, (1977).

Cerf, R., J. Chim. Phys. 66,479(1969).

Cox, R. G., J. Fluid Mech. 44,791(1970).

Crowley, P. G., Frank, F. C., Mackely, M. R. and Stephenson, R. G., J. Polym. Sci. Polym. Phys. Ed. 14,1111(1976).

de Gennes, P. G., J. Chem. Phys., 60,5030(1974).

de Gennes, P. G., J. Chem. Phys., 66,5825(1977).

Dreher, K. D. and Gogarty, W. B., J. Rheol. 23,208(1979).

Fuller, G. G. and Leal, L. G., Flow Birefringence of Concentrated Polymer Solutions in Two Dimensional Flows, forthcoming publication (1980a).

Fuller, G. G. and Leal, L. G., Dynamics of Polymer Molecules in Dilute Solution, forthcoming publication (1980b).

Fuller, G. G., Rallison, J. M., Schmidt, R. L. and Leal, L. G., The Measurement of Velocity Gradients by Homodyne Light Scattering Spectroscopy, forthcoming publication (1980).

Hinch, E. J., Proc. Symp. Polym. Lubtification, Brest (1974).

Hinch, E. J., Phys. Fluids 20,522(1977).

Kuhn, W. and Kuhn, H., Helv. Chim. Acta. 28,1533(1945).

Leal, L. G., Fuller, G. G. and Olbricht, W. L., Studies of the Flow-Induced Stretching of a Macromolecule in a Dilute Solution, forthcoming publication (1980); also presented at the Viscous Drag Reduction Symposium, Dallas, Texas, Nov. 7-8, 1979.

Olbricht, W. L., Rallison, J. M. and Leal, L. G., A Criterion for Strong Flow Based on Microstructure Deformation, forthcoming publication, (1980).

Peterlin, A., J. Chem. Phys. 21,1272(1963).

Peterlin, A., Polymer 2,257(1961).

Peterlin, A., Ann. Rev. Fluid Mech. 8,35(1976).

Philippoff, W., in: E. H. Lee (ed.), Proc. IV Intern. Congr. (1963) Rheol., Providence 1963, Vol. 2, p 343, Interscience Publ. (N. Y. 1965).

Phan-Thien, N, Atkinson, J. D. and Tanner, R. I., J. Non-Newt. Fluid Mech. 3,309(1978).

Polymer Handbook, Eds. Brandrup, J. and Immergut, E. H., John Wiley and Sons Publ. (1965).

Pope, D. P. and Keller, A., Colloid and Polym. Sci. 255,633(1977).

Pope, D. P. and Keller, A., ibid 256,751(1978).

Rouse, P. E. Jr., J. Chem. Phys. 21,1272(1953).

Sankur, V. D., Phd. Thesis, California Institute of Technology (1976)

Tanner, R. I., Trans. Soc. Rheol. 19,557(1975).

Tanner, R. I., AICHE J. 22,910(1976).

Warner, H. R., Ind. Eng. Chem. Fund. 11,375(1972).

Zimm, B. H., J. Chem. Phys. 24,269(1956).

Table 1

Sample	Molecular Weight	$\frac{M_w}{M_n}$	n_p †	$(\nu_1 - \nu_2)$†
1	2×10^6	1.3	1.6	$-145 \times 10^{-25} cm^3$
2	4.48×10^6	1.14	"	"
3	8.42×10^6	1.17	"	"

†Polymer Handbook (1965).

Figure Captions

Figure 1. The dumbbell model

Figure 2. Flow fields described by equation (3) and simulated using the four roll mill.

Figure 3. Steady state end to end distance $\langle r^2 \rangle^{1/2}$ versus the velocity gradient α. The dashed curves represent the end to end distance achieved by dumbbells residing in the flow for a duration of time specified by equation (11) for ℓ/D = 0.002 and 0.003.

Figure 4. Time to reach 90% of steady state in units of for N=1000 and purely extensional flow and the transit times for molecules entering the sample region for ℓ/D = 0.002 and 0.003.

Figure 5. Trajectories of molecules in the four roll mill. The molecules are assumed to be in a near rest state configuration upon entering the large dashed circle of radius D. The sample region is represented by the small solid circle in the center of the figure.

Figure 6. Normalized birefringence $\langle n \rangle / n \langle c \rangle B$ versus the eigenvalue of the velocity gradient tensor of equation (3) $\sqrt{\lambda}\alpha$, M_w/M_n=1.17

Figure 7. Schematic diagram of the flow birefringence experiment.

Figure 8. Relative orientations of the polarization vectors and and the sample refractive index tensor and the .

flow device.

Figure 9. Velocity gradient in arbitrary units versus the angular velocity of the rollers for the 100 ppm solution of 8.42×10^6 polystyrene. Measurements were taken at the center stagnation point at a scattering angle of approximately 50 degrees.

Figure 10. Velocity gradient in arbitrary units versus the angular velocity of the rollers for the 100 ppm solution of 4.48×10^6 polystyrene. Measurements were taken for the same conditions specified in figure 9.

Figure 11. Birefringence versus the velocity gradient for the PCB solvent. ⊙-λ=1., Δ-λ=0.75, +-λ=0.5, X-λ=0.25

Figure 12. Photographs of the birefringence pattern for the 2x10 molecular weight polystyrene of 100 ppm. A λ=1.0, γ=17.7 sec^{-1}; B λ=0.8, γ=23.6 sec^{-1}; C λ=0.5, γ=9.5 sec^{-1}; D λ=0.33, γ=11.8 sec^{-1}; E λ=0.2, γ=23.6 sec^{-1}

Figure 13. Birefringence versus the velocity gradient for the 2.00×10^6 molecular weight polystyrene at 100 ppm concentration. ⊙ λ=1.0, Δ λ=0.8, + λ=0.5, X λ=0.33, ◇ λ=0.2

Figure 14. Birefringence versus the velocity gradient for the 4.48×10^6 molecular weight polystyrene at 100 ppm concentration. ⊙ λ=1.0, Δ λ=0.8, + λ=0.5,

X λ=0.33, ◇ λ=0.2

Figure 15. Birefringence versus the velocity gradient for the 8.42×10^6 molecular weight polystyrene at 100 ppm concentration. O λ=1.0, Δ λ=0.8, + λ=0.5, X λ=0.33, ◇ λ=0.25

Figure 16. Birefringence versus the velocity gradient for the 8.42^6 and $4.48^6 \times 10$ molecular weight polystyrene at 100 and 50 ppm concentration. ● MW=8.42×10^6, c=100 ppm; Δ MW=4.48×10^6, c=100 ppm + MW=8.42×10^6, c=50 ppm; X MW=4.48×10^6, c=50 ppm

Figure 17. Birefringence versus the eigenvalue of the velocity gradient tensor for all three molecular weight samples. The symbols are defined in figures 14-16 for each respective molecular weight sample. The solid curves are the results of the model calculations using the log-normal distribution of molecular weights and taking into account finite transit times in the flow device with $\ell/D = 0.003$.

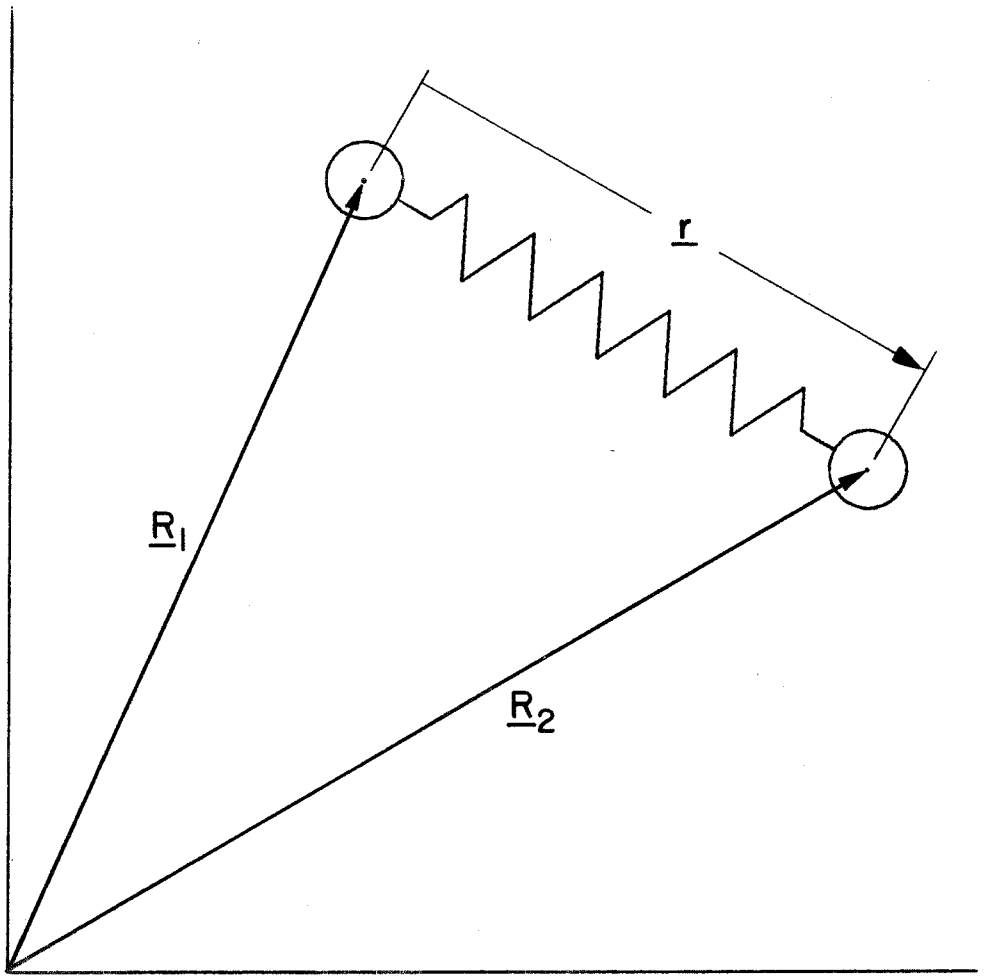

Fig. 1

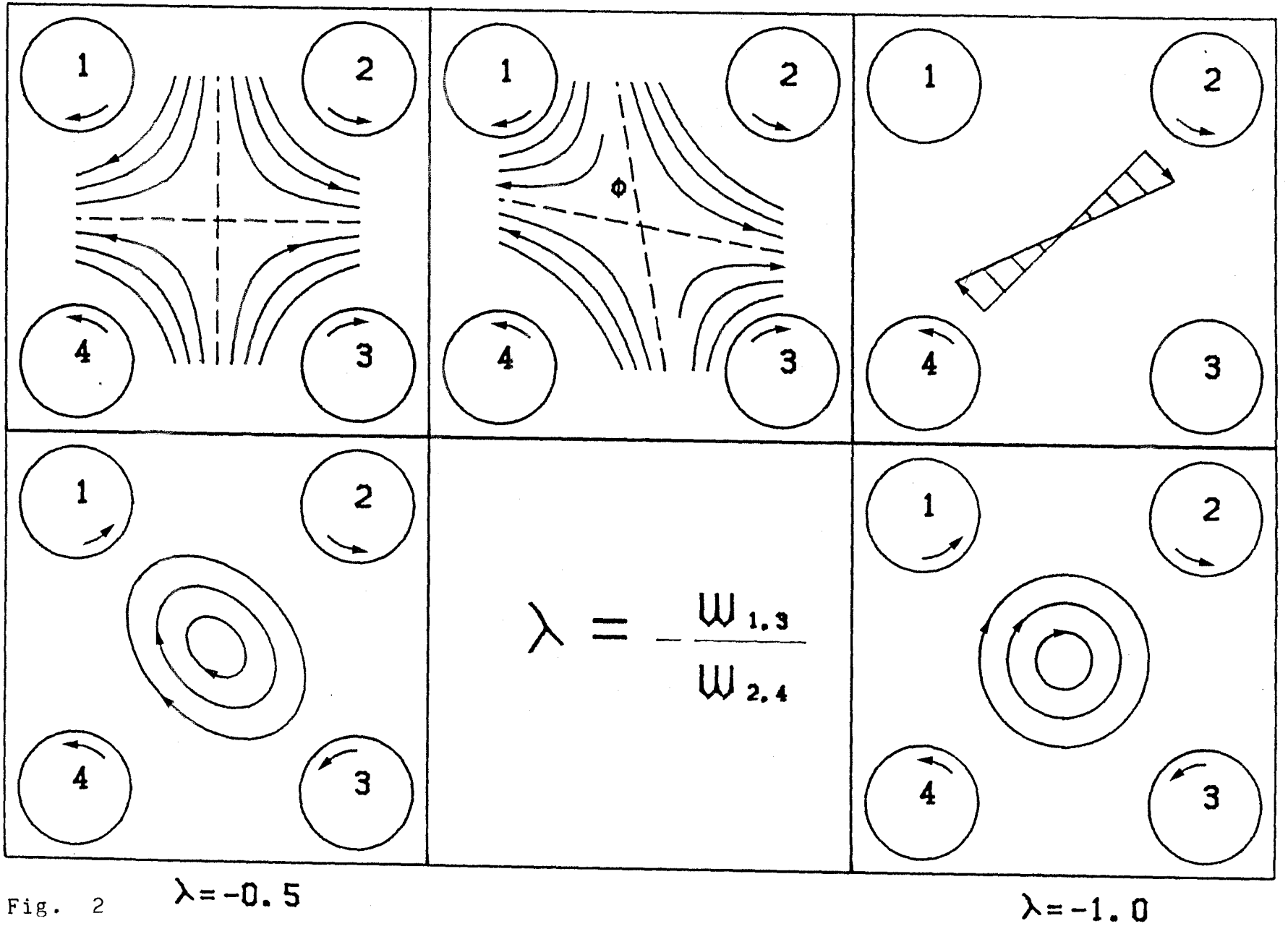

Fig. 2

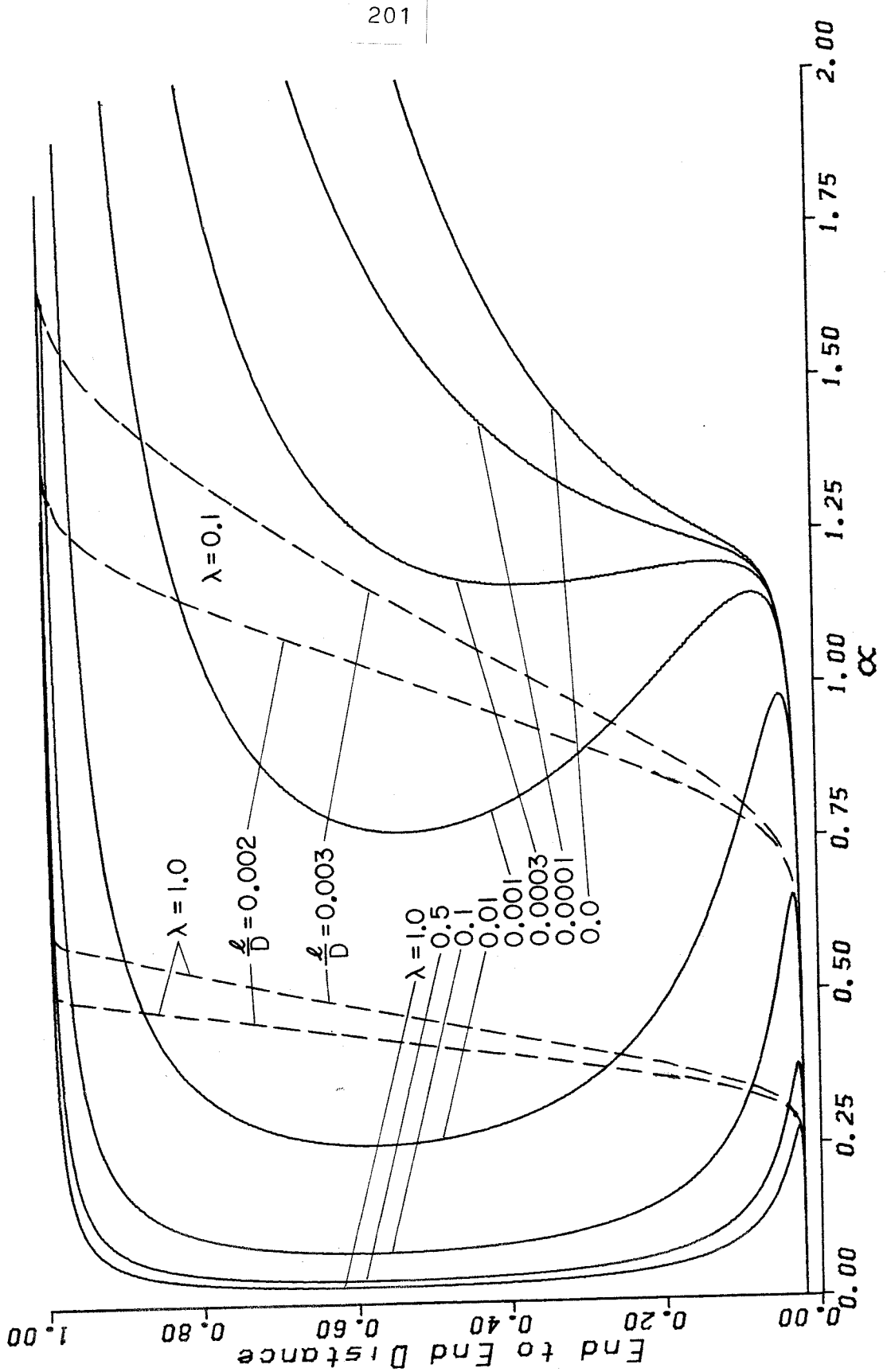
End to End Distance
0.00
0.20
0.40
0.60
0.80
1.00
0.00
0.25
0.50
0.75
1.00
1.25
1.50
1.75
2.00
α
λ = 0.1
λ = 1.0
ℓ/D = 0.002
ℓ/D = 0.003
λ = 1.0
0.5
0.1
0.01
0.001
0.0003
0.0001
0.0

Fig. 3

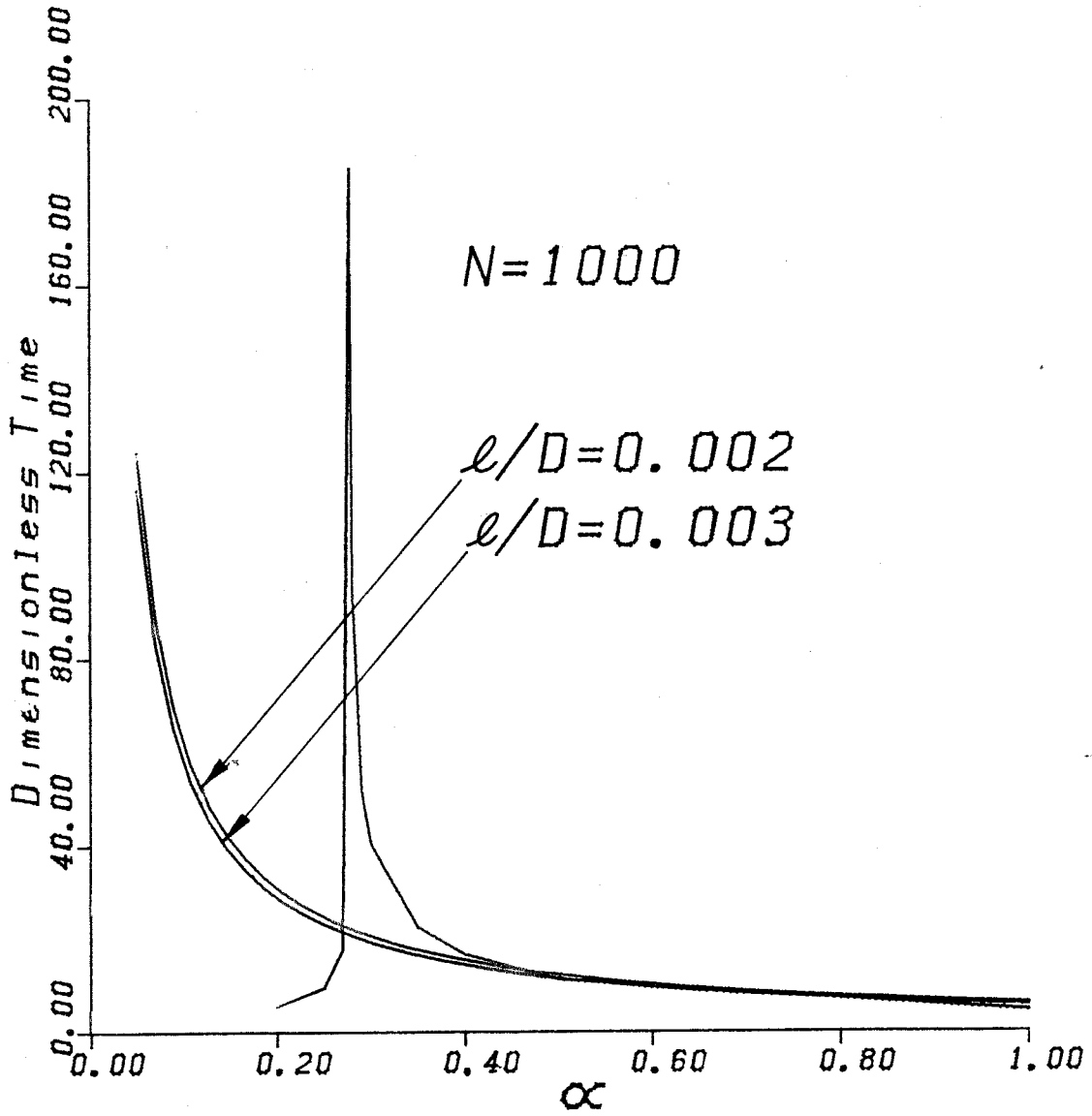
N=1000
ℓ/D=0.002
ℓ/D=0.003
Dimensionless Time
0.00
40.00
80.00
120.00
160.00
200.00
0.00
0.20
0.40
0.60
0.80
1.00
α

Fig. 4

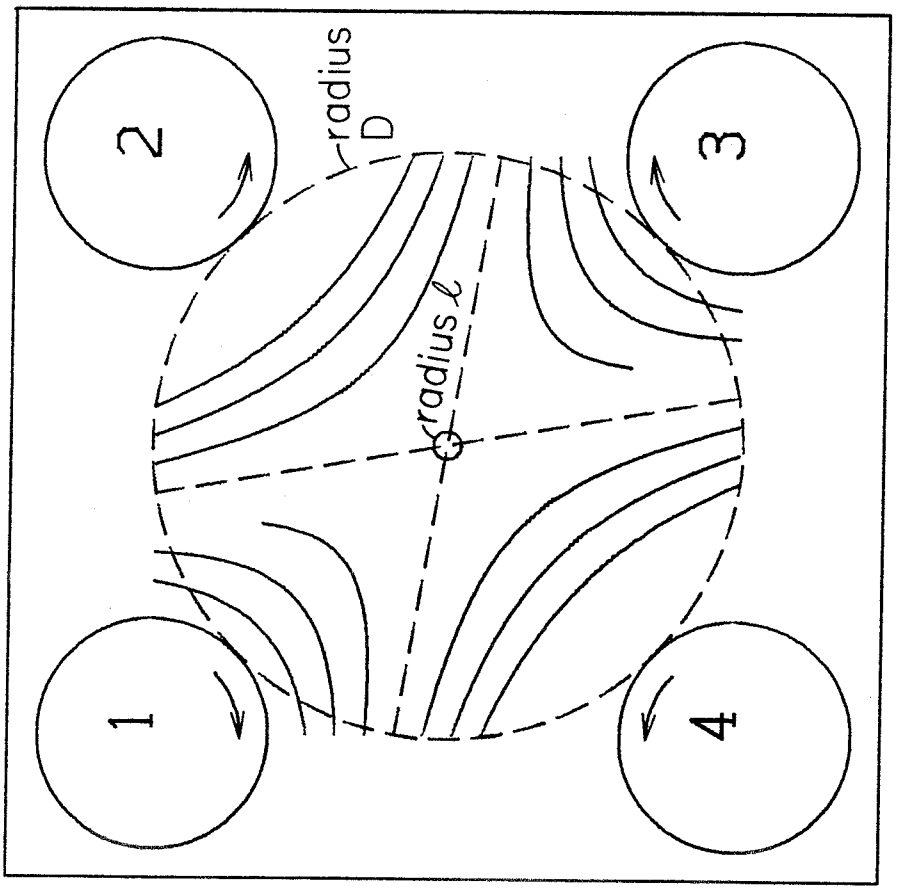

Fig. 5

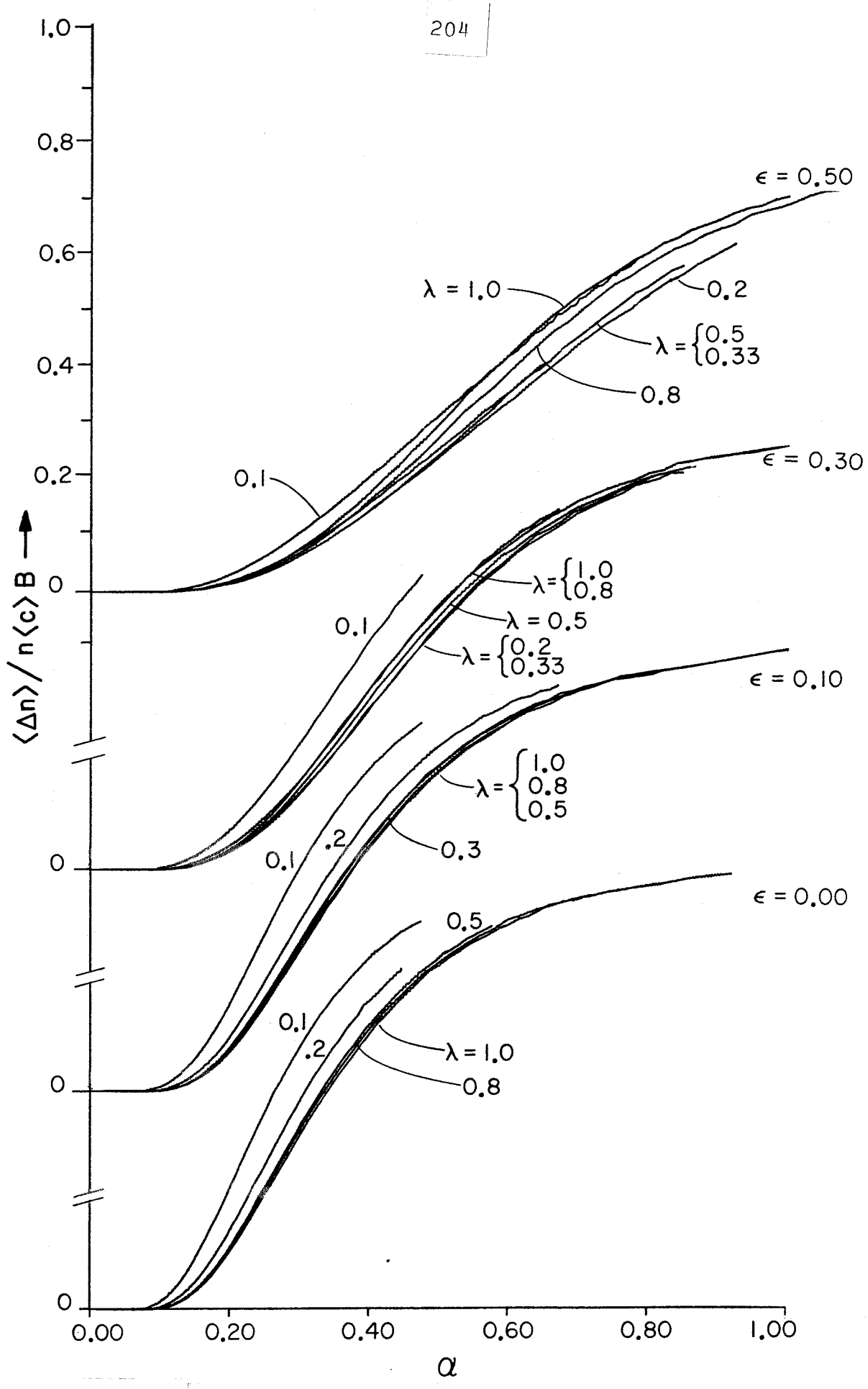
1.0
0.8
0.6
0.4
0.2
0
0
0
0
⟨Δn⟩ / n⟨c⟩B
ϵ = 0.50
λ = 1.0
0.2
λ = {0.5 / 0.33
0.8
0.1
ϵ = 0.30
λ = {1.0 / 0.8
λ = 0.5
λ = {0.2 / 0.33
0.1
ϵ = 0.10
λ = {1.0 / 0.8 / 0.5
0.1
.2
0.3
ϵ = 0.00
0.5
0.1
.2
λ = 1.0
0.8
0.00
0.20
0.40
0.60
0.80
1.00
α

Fig. 6

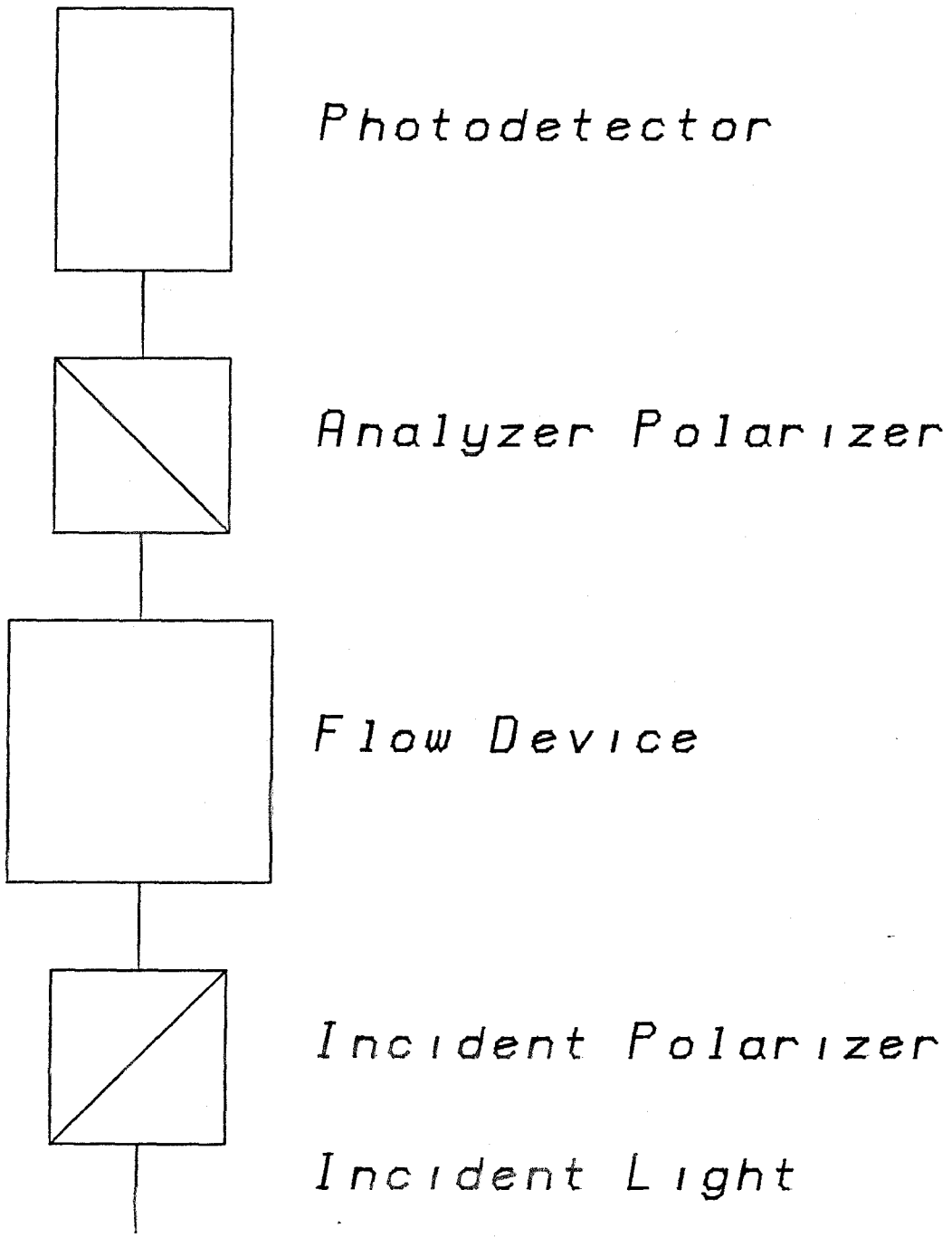
Photodetector
Analyzer Polarizer
Flow Device
Incident Polarizer
Incident Light

Fig. 7

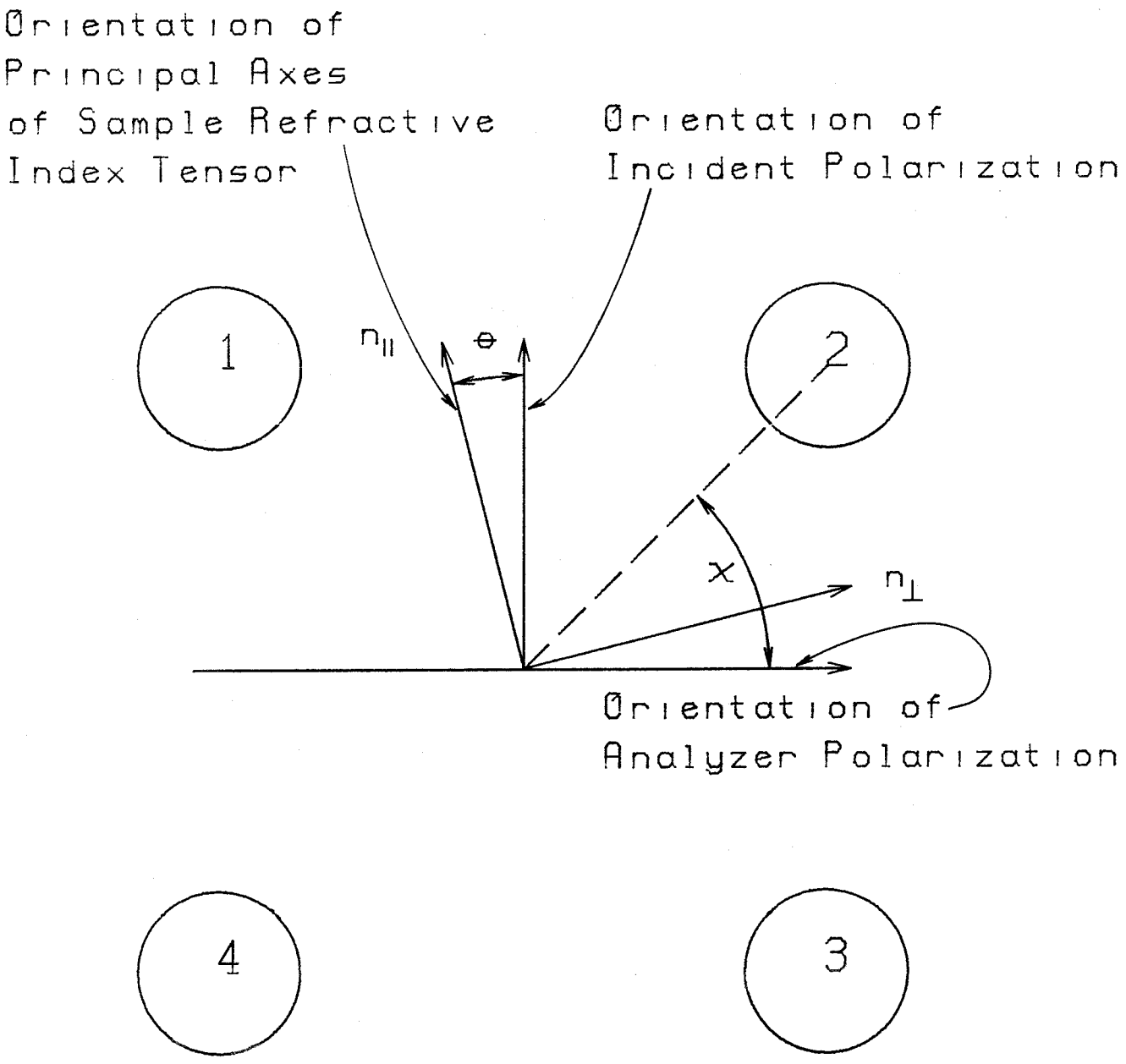
Orientation of
Principal Axes
of Sample Refractive
Index Tensor
Orientation of
Incident Polarization
1
2
$n_{\parallel}$
θ
χ
$n_{\perp}$
Orientation of
Analyzer Polarization
4
3

Fig. 8

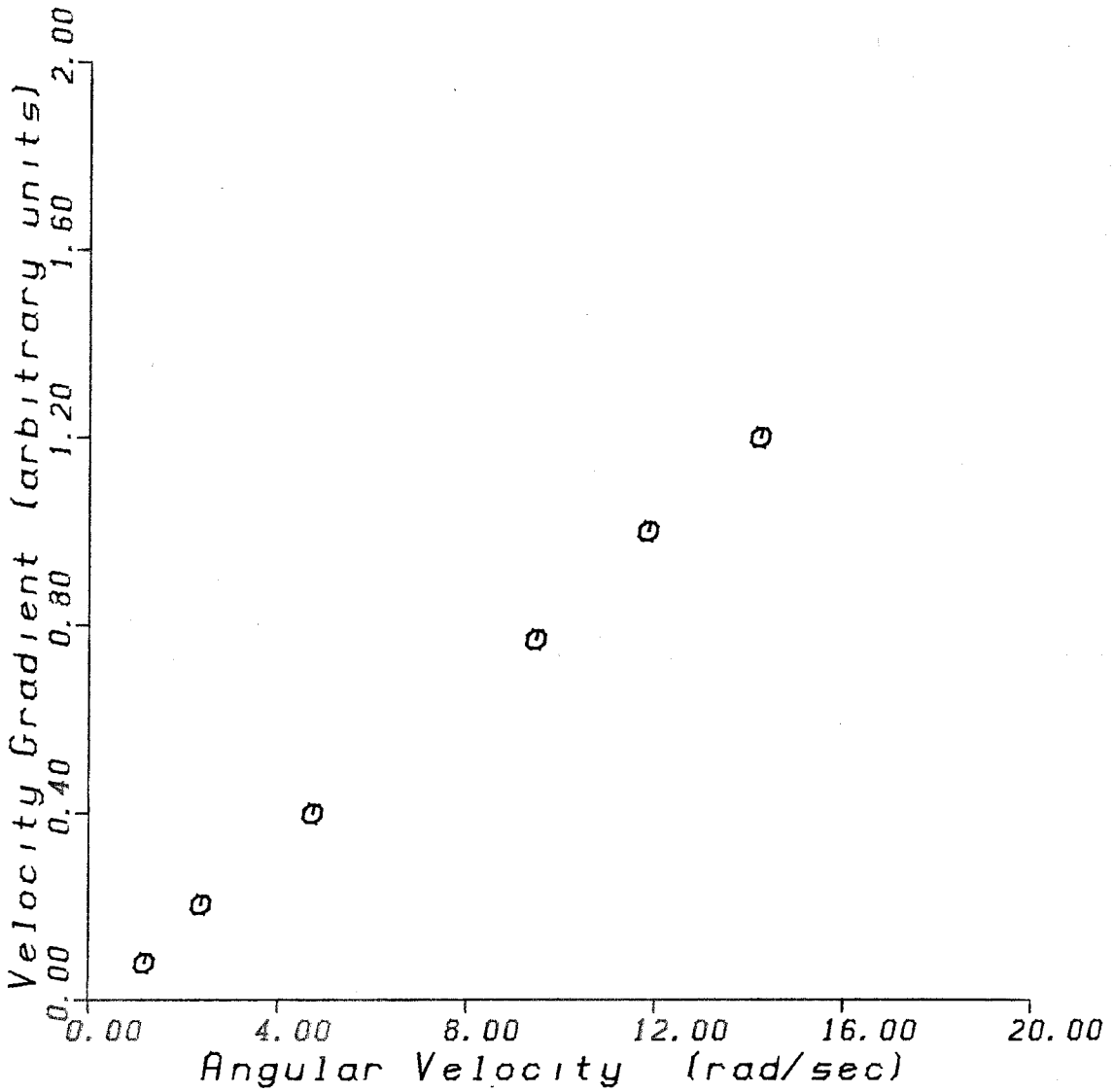
Velocity Gradient (arbitrary units)
0.00
0.40
0.80
1.20
1.60
2.00
0.00
4.00
8.00
12.00
16.00
20.00
Angular Velocity (rad/sec)

Fig. 9

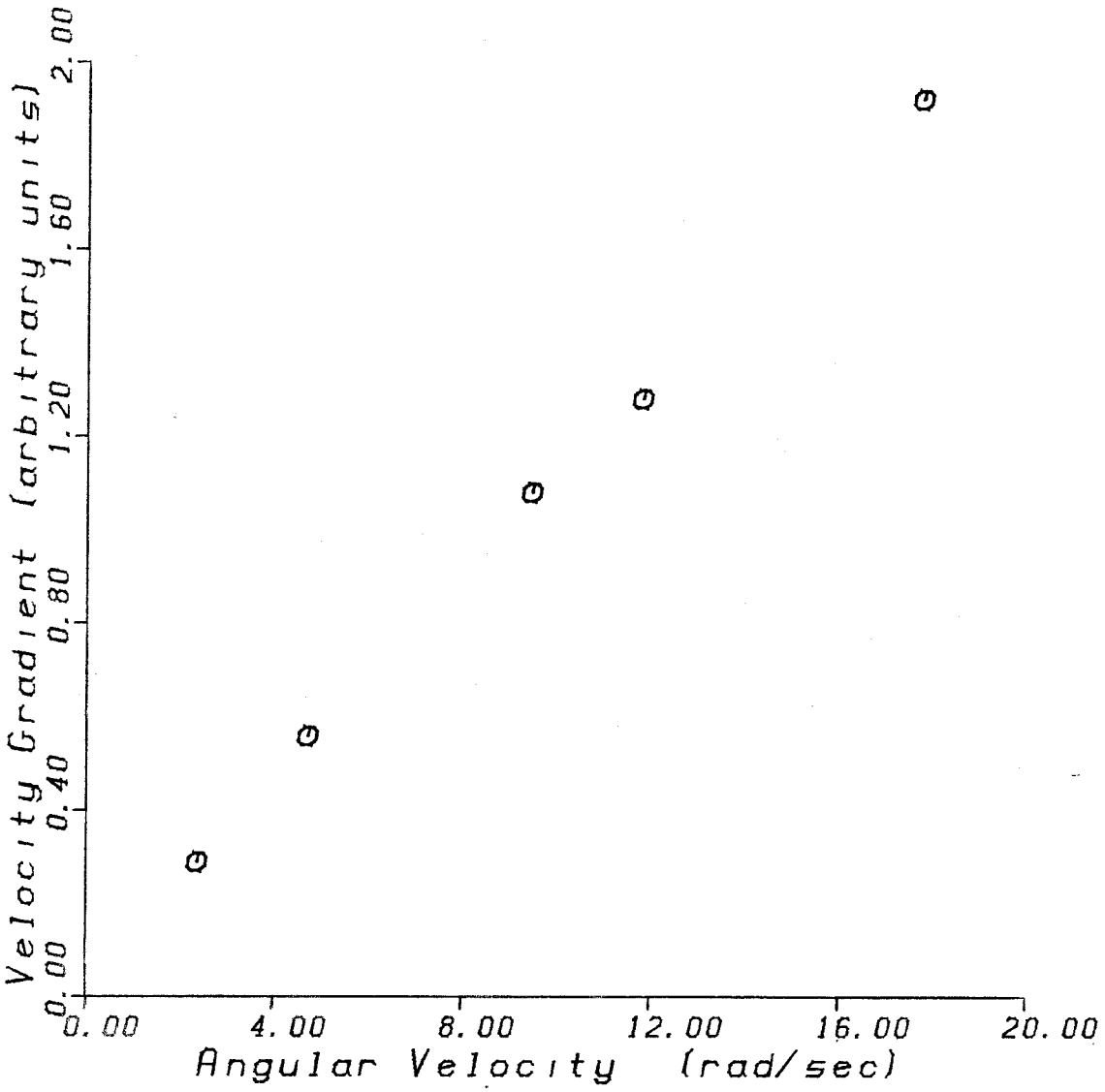
Velocity Gradient (arbitrary units)
0.00
0.40
0.80
1.20
1.60
2.00
0.00
4.00
8.00
12.00
16.00
20.00
Angular Velocity (rad/sec)

Fig. 10

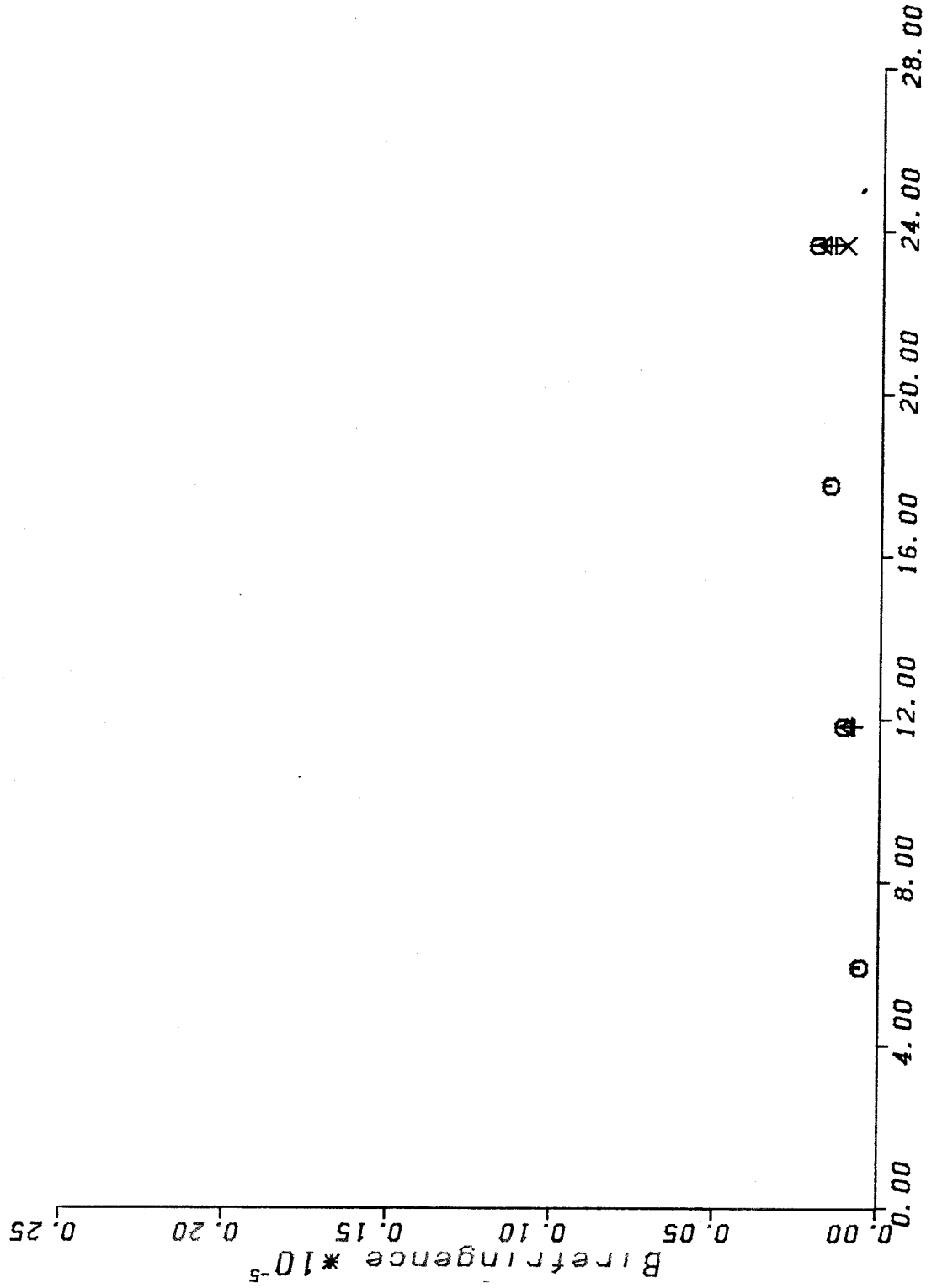
Birefringence *10-5
0.00
0.05
0.10
0.15
0.20
0.25
0.00
4.00
8.00
12.00
16.00
20.00
24.00
28.00
γ (/sec)

Fig. 11

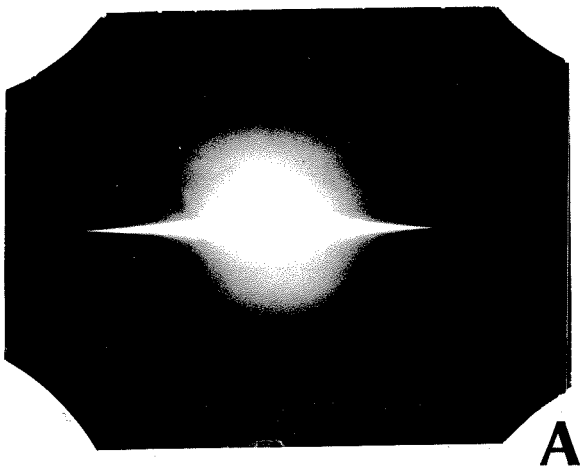

A

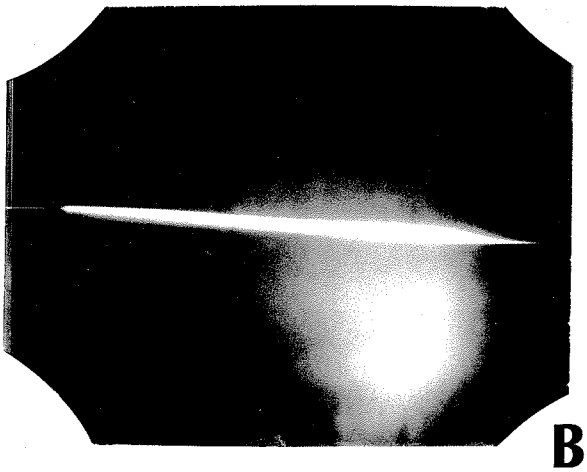

B

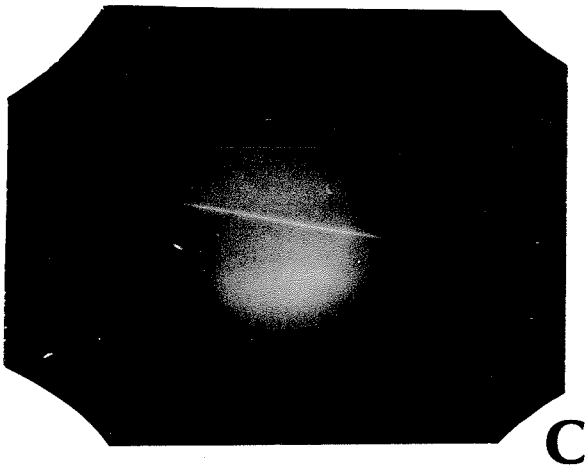

C

D

E

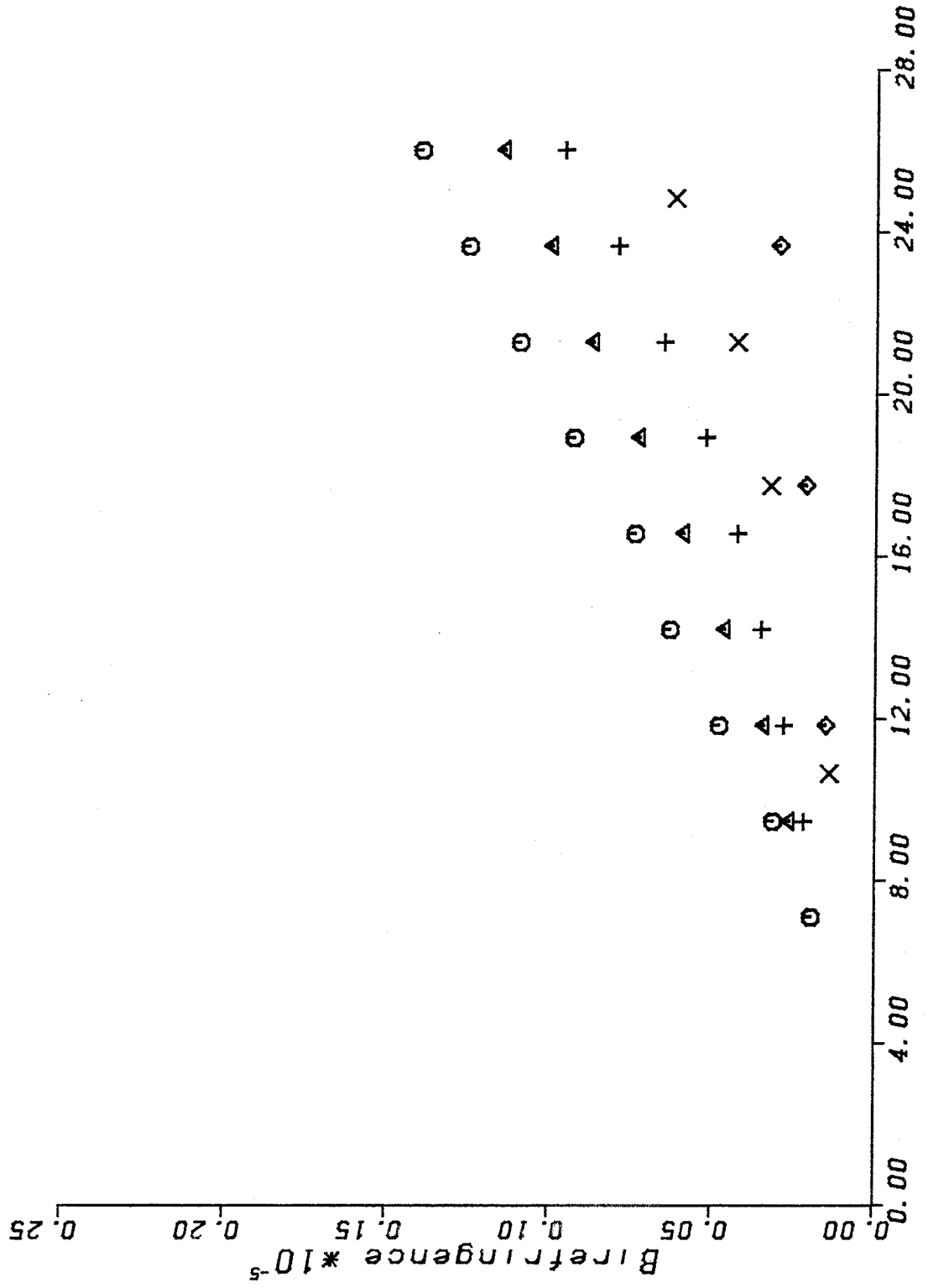
Birefringence *10-5
0.00
0.05
0.10
0.15
0.20
0.25
0.00
4.00
8.00
12.00
16.00
20.00
24.00
28.00
γ (/sec)

Fig. 13

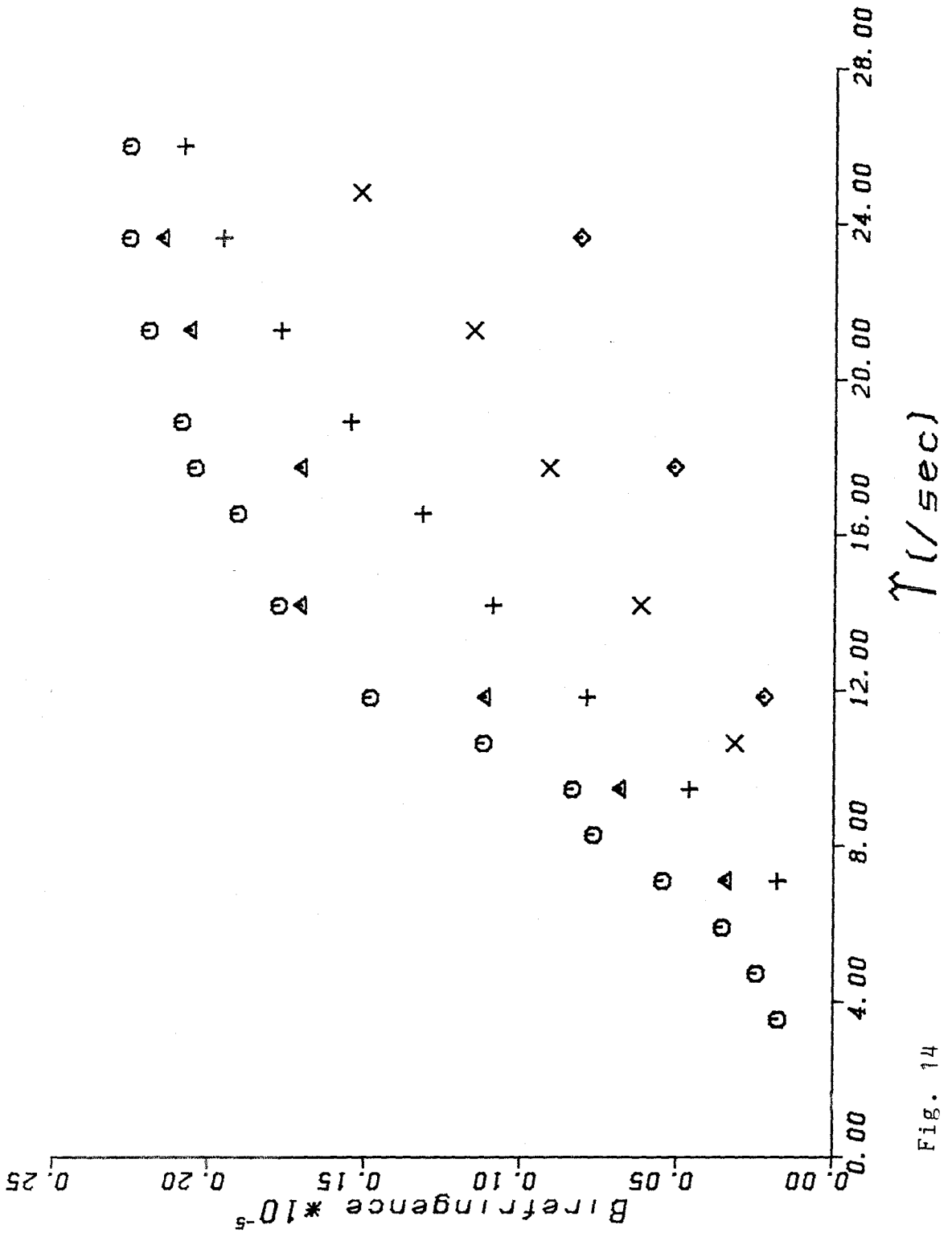
Birefringence *10-5
0.00
0.05
0.10
0.15
0.20
0.25
0.00
4.00
8.00
12.00
16.00
20.00
24.00
28.00
τ (/sec)

Fig. 14

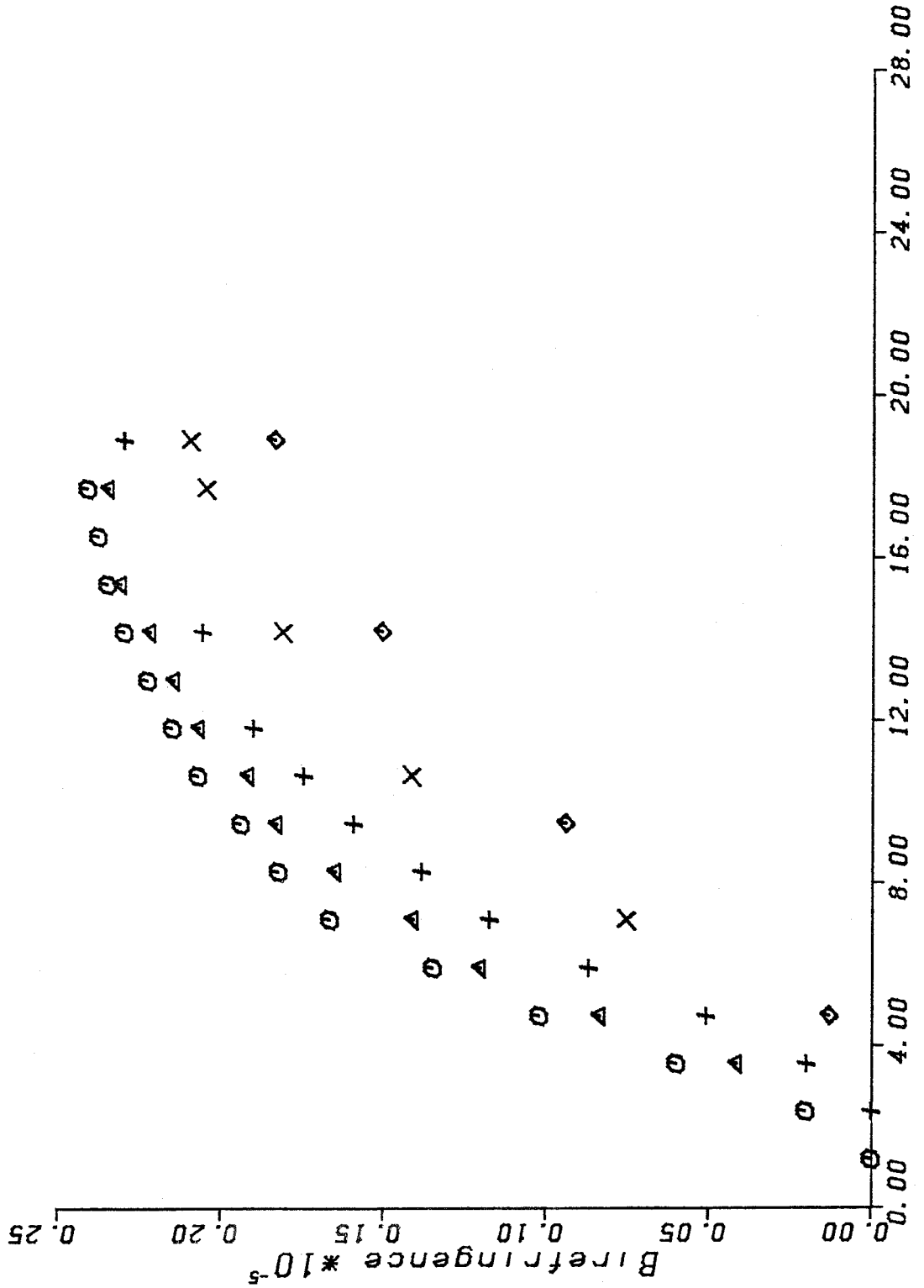
Birefringence *10^-5
0.00
0.05
0.10
0.15
0.20
0.25
0.00
4.00
8.00
12.00
16.00
20.00
24.00
28.00
γ (/sec)

Fig. 15

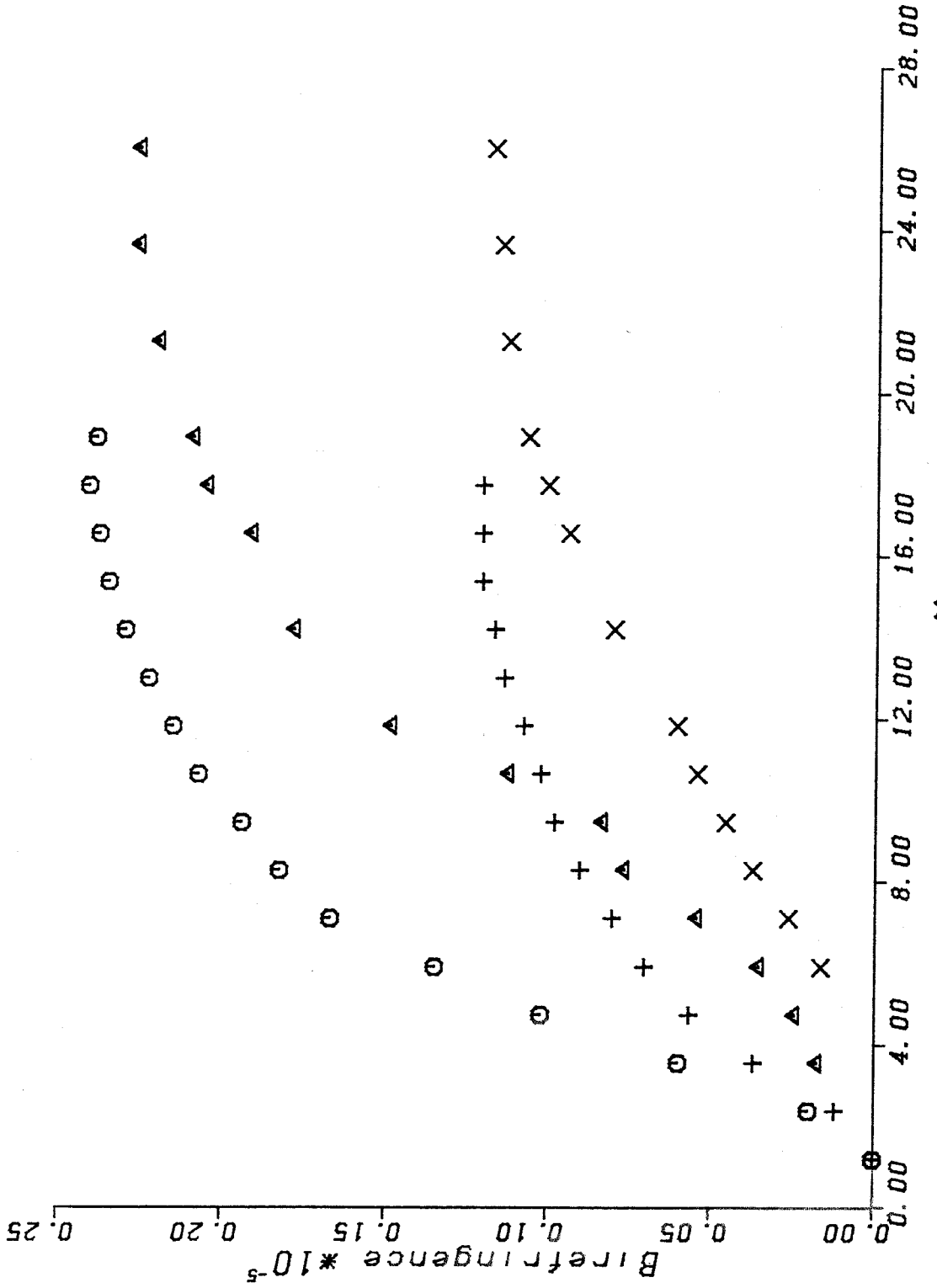
Birefringence *10-5
0.00
0.05
0.10
0.15
0.20
0.25
0.00
4.00
8.00
12.00
16.00
20.00
24.00
28.00
γ (/sec)

Fig. 16

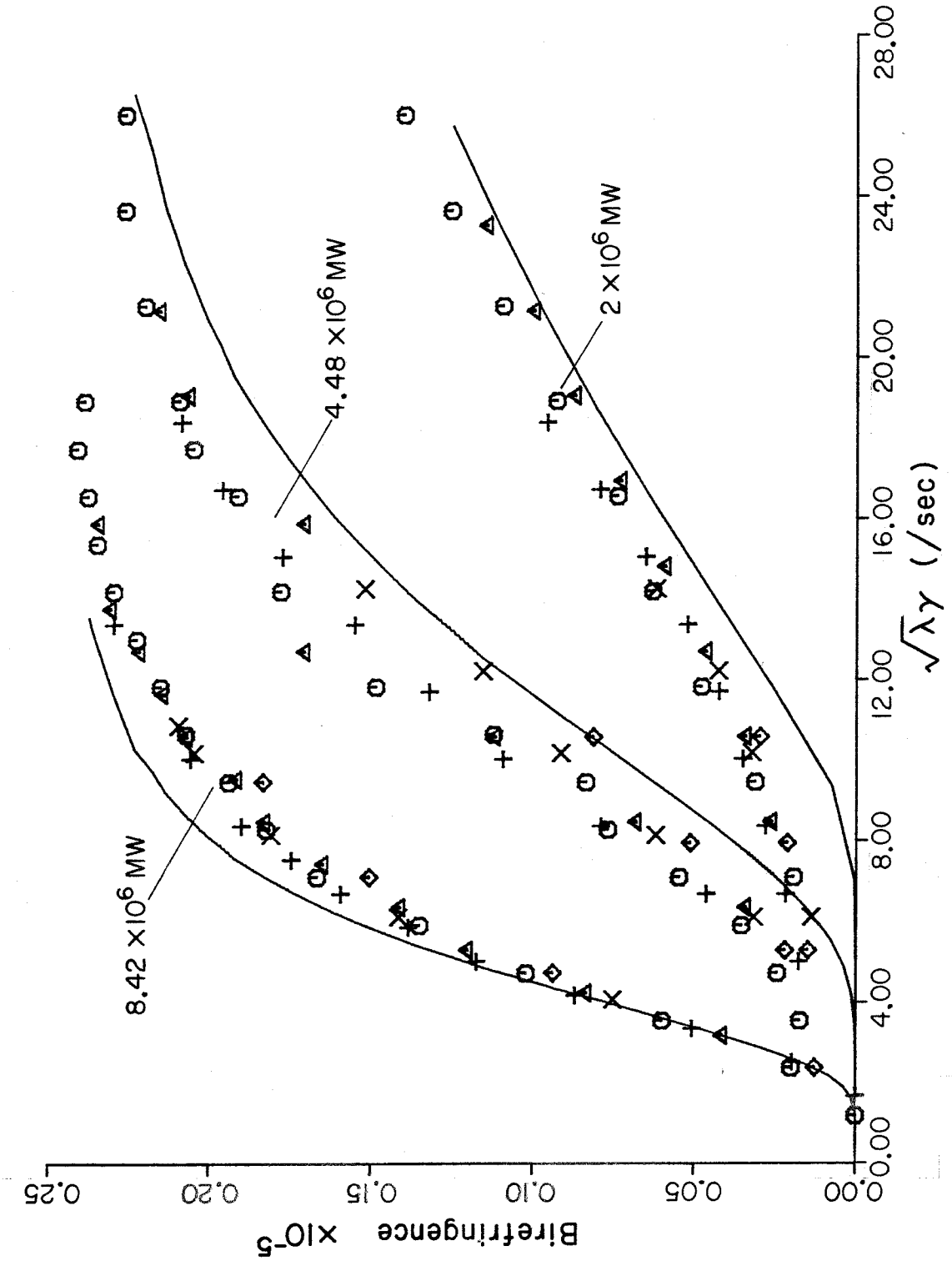
Birefringence ×10⁻⁵
0.00
0.05
0.10
0.15
0.20
0.25
0.00
4.00
8.00
12.00
16.00
20.00
24.00
28.00
√λγ (/sec)
8.42 ×10⁶ MW
4.48 ×10⁶ MW
2 ×10⁶ MW

Fig. 17

Dynamics of Flowing Polymer Molecules in Dilute Solution

by

G. G. Fuller and L. G. Leal

Department of Chemical Engineering
California Institute of Technology
Pasadena, California 91125

Abstract

The properties of a nonlinear spring, variable hydrodynamic friction and internal viscosity used in the dumbbell model of dilute polymer solutions are examined in detail for a general two-dimensional flow. Both steady and transient start up flows are investigated and the response of the bulk stress is calculated. It is found that the existence hysteresis in the steady states of the dumbbell model arising from the variable friction factor is strongly dependent on both the flow type (i.e. the ratio of vorticity to the rate of strain) and the molecular weight. Two methods of solution for the dumbbell with internal viscosity are presented. The first method uses a perturbation expansion valid for small values of the internal viscosity and leads to largely analytical results. The second technique uses the preaveraging approximation of Cerf (1969). Both methods are shown to yield qualitatively the same trends for both the steady and transient flows which are considered.

Introduction

Efforts to model the flow properties of dilute polymer solutions using the dumbbell model are numerous and the results of investigations towards this end are well documented (Bird et al.(1977) Williams (1975)). The use of this model, which was first proposed by Kuhn (1934), is principally motivated by the mathematical tractability resulting from its inherent simplicity and its success at describing a surprisingly large number of physical observations. The complexity of the dumbbell model has evolved along with the measurement of new nonlinear flow properties of polymer solutions and a number of increasingly exotic features have been attributed to the dumbbell in order to account for these experimental realities.

In particular, these features include a nonlinear spring connector, internal viscosity and conformation dependent hydrodynamic friction. While the origin of these effects can be argued to have a molecular basis, it must be remembered that their precise relationship to molecular properties is somewhat tenuous. Nontheless, a main advantage of the dumbbell model is the ability to systematically vary the parameters associated with these effects and thereby uncover the role of each particular

mechanism in the dynamic response of the dumbbell. This can be done in a way which is largely free of empirical assumptions in the basic structure of the model and can therefore provide some insight into the possible molecular significance of observed phenomena.

In adopting the dumbbell model to describe mechanical and optical properties of dilute polymer solutions, we are neglecting any of the fine structure of the polymer chain. Instead we restrict our attention to the response of a single variable, the end to end vector $\underline{r}'$, the orientation and magnitude of which are assumed to describe the conformation of the polymer. This simplification is justified in studying most flow situations for the reason that it is the relatively long wave length motions associated with the end to end vector which will largely determine how the macromolecule responds to the imposed flow. Oscillatory flows of ultra high frequency are an exception and in such a case the dynamics of local structure (monomer groups, side chains etc.) will dominate the relaxation spectra (Lodge et al (1979)). In this regime the correct model must incorporate some semblance of the fine structure of the chain which the simple dumbbell obviously cannot accommodate. Most flows of practical importance, however, will not possess such high frequency components and

the dumbbell can successfully account for most of the qualitative observations in dilute solutions.

The purpose of this paper is to present the results of model calculations which examine the consequences of the three properties of the dumbbell previously mentioned in a variety of bulk flows. In particular, the effect of flow type (specifically the ratio of the vorticity to the rate of strain in the flow) is examined and several new results are presented. This work is presented in two parts. First, we consider the effect of the nonlinear spring and of variable hydrodynamic friction. In the second half of the paper, the role of internal viscosity is discussed.

I. Part One: Nonlinear Spring and Variable Hydrodynamic Friction

I.I Development of the Model

The standard approach to analyzing the response of the dumbbell model to flow, which we follow here, is to first write down a balance of the forces acting on the dumbbell which is pictured in figure 1. For the model considered here this balance is

$$\underline{F}_f + \underline{F}_s + \underline{F}_B = 0 \qquad (1)$$

where $\underline{F}_f$, $\underline{F}_s$ and $\underline{F}_B$ are the forces due to hydrodynamic friction, the spring connector and Brownian motion respectively.

The hydrodynamic friction force arises from relative motion between the dumbbell and the solvent and is assumed to take the form

$$\underline{F}_f = -\zeta(\underline{r}')(\dot{\underline{r}}' - \underline{\underline{\Gamma}} \cdot \underline{r}') \qquad (2)$$

Here $\dot{\underline{r}}$ is the rate of change of the end to end vector of the dumbbell, while $\underline{\underline{\Gamma}} \cdot \underline{r}'$ is the relative undisturbed velocity of the fluid at the two ends of the dumbbell. The velocity gradient tensor of the undisturbed flow is denoted as $\underline{\underline{\Gamma}}$, and it is evident from the form of (2) that the undisturbed velocity has been assumed to vary only linearly with spatial position. The hydrodynamic friction factor between the solvent and the polymer, which has been denoted as ζ, will, in general, be dependent on the end to end distance $\underline{r}'$. The origin of this conformation dependence of

ζ comes from consideration of the hydrodynamic interactions existing within the chain. When the chain is in its near rest state configuration, its highly coiled conformation will cause most of the interior chain elements to be shielded from the flow and the friction factor ζ will be proportional to the coiled dimension $\sqrt{N}a$ where N is the number of subunits of length "a" comprising the chain. As the polymer is distorted by the flow, more and more of the chain elements will be exposed to the flow and contribute to the hydrodynamic friction. From hydrodynamic considerations (Hinch (1974), de Gennes (1974))) the fiction factor ζ should increase roughly in proportion to the length scale of the chain as it is distorted.

The proper way in which to account for this effect would be to use a model with sufficient structure to include intramolecular hydrodynamic interaction such as the bead and spring model (Zimm (1956)) or perhaps an extensible, flexible thread (Hinch (1976a, 1976b)). In order to include this effect in the dumbbell model, the friction factor ζ, which is assigned to the molecule as a whole, is allowed to depend on the end to end distance r'. We shall therefore take

$$\zeta = \zeta_0 Q(r') \qquad (3)$$

in which ζ_o is the friction factor in the rest state and $Q(r')$ is assumed to be equal to $r'/\sqrt{N}a$. This is the same choice adopted by Hinch (1977) but differs from the form used by Tanner (1975b) and Phan-Thien et al. (1978) which was $Q=1+r'/\sqrt{N}a$. We prefer the choice of Hinch because in the rest state where $\langle r'^2 \rangle = \sqrt{N}a$, the friction factor becomes ζ_o whereas Tanner's choice leads to $2\zeta_o$. Slender body theory calculations for low Reynolds number flows suggest that this linear form for Q neglects an additional logarithmic contribution to the friction factor which is proportional to $\ln(r/\sqrt{N}a)$. It may also be noted that the friction factor for a highly distorted chain should not be a scalar quantity as assumed by (3) but rather a second-order tensor. Accounting for these additional refinements will not significantly affect the stretching process of the dumbbell and for that reason will not be accounted for.

The spring connector force, $\underline{F}_s$ is a consequence of the action of the entropy of the chain which opposes deformation of the polymer and tends to restore the chain to the randomly coiled rest state. As the chain becomes highly distorted and approaches the maximum extension length $R=Na$, the entropic spring force becomes infinite which forces the chain to be finitely extensible. The polymer will then be restricted in its extensibility to the maximum value of its

chain length. The form for $\underline{F}_s$ will be taken as

$$\underline{F}_s = -\frac{3NkT}{R^2}\xi(r'/R)\,\underline{r}' \tag{4}$$

where kT is the Boltzmann temperature and $\xi(r'/R)$ is a nonlinear function of the end to end vector which becomes infinite when $r' \to R$. There have been a number of choices for the form of ξ (Langevin spring (Peterlin (1961), Warner spring (Warner (1972), linear locked spring (Tanner (1971, 1975a)) and while it can be argued that the Langevin spring has some fundamental basis we shall take the simpler Warner spring in which

$$\xi(r'/R) = \frac{1}{1-(r'/R)^2} \tag{5}$$

The precise form for ξ will not affect the general trend of the model predictions and all of the above mentioned spring laws share the features of a singularity at $r' \to Na$ and a constant limit in the neighborhood of zero deformation.

The Brownian motion force is caused by random thermal agitation of the solvent molecules onto the polymer chain. This will be taken to be the following effective entropic force:

$$\underline{F}_B = -kT \nabla \log \psi \qquad (6)$$

where ψ is the distribution function of the dumbbell conformation. Brownian forces, then, affect the dumbbell in two ways. In the first instance, they lead to the elastic spring connector which arises from maximizing the number of configurations available to the dumbbell (which leads to a maximum entropy) and secondly, stochastic forces drive the dumbbell conformation through all possible realizations.

In general, a polymer chain will have a finite axis ratio. It is here that the dumbbell model considered here, with an infinite aspect ratio, is the most limited. As shown by Bretherton (1962), a rigid axisymmetric particle with its symmetry axis oriented along the unit vector $\underline{q}$ will have the following rotation

$$\dot{\underline{q}} = \underline{\underline{\Omega}} \cdot \underline{q} + G(\underline{\underline{D}} \cdot \underline{q} - (\underline{q} \cdot \underline{\underline{D}} \cdot \underline{q})\underline{q})$$

where G is a constant which is specified by the geometry of the particle and $\underline{\underline{\Omega}}$ and $\underline{\underline{D}}$ are the vorticity and rate of strain tensors of the flow respectively. The constant G, therefore determines the efficiency of the rate of strain

tensor in rotating the particle. The dumbbell model, as do all particles of infinite aspect ratio, has a value of G=1 and therefore both $\underline{\underline{D}}$ and $\underline{\underline{\Omega}}$ will be equally effective in rotating the dumbbell. A real polymer chain, however, with a finite aspect ratio will in general be characterized by a different value of G and it has been suggested by Hinch (1977) that this parameter should be in fact a function of the chain conformation and less than unity. The case of a conformation independent value for G for the dumbbell model has been investigated in detail by Gordon et al (1972). Throughout this paper, however, it will be assumed that G is unity.

For the purpose of example we shall consider a two dimensional linear flow in which

$$\underline{\underline{\Gamma}} = \gamma \underline{\underline{\Delta}} = \gamma \begin{pmatrix} 0 & 1 & 0 \\ \lambda & 0 & 0 \\ 0 & 0 & 0 \end{pmatrix} \qquad (7)$$

where γ is the magnitude of the local velocity gradient. The parameter λ specifies the particular type of two dimensional flow and varies between ± 1. This type of motion was chosen because it offers the possibility of examining the important effects which occur with variations in the amount of vorticity in the flow and because it can be realized.

experimentally in a four roll mill. Flow birefringence experiments utilizing such a flow device have been conducted in this laboratory for dilute solutions (50 - 100 ppm) of high molecular weight polystyrene in a viscous solvent and the detailed results of this work can be found elsewhere (Fuller and Leal (1980)). Figure 2 shows the range of flows described by the velocity gradient tensor of equation (7) as λ is varied. The ratio of vorticity to the rate of extension in this flow is

$$\omega = \frac{1-\lambda}{1+\lambda} \tag{8}$$

Combining equations (1-6) the equation of motion for the dumbbell end to end distance is

$$\dot{\underline{r}} = \underline{\underline{\Gamma}} \cdot \underline{r}' - \frac{3NkT}{R^2\zeta} \underline{\underline{\xi}} \cdot \underline{r}' - \frac{kT}{\zeta} \nabla \log \psi \tag{9}$$

which when multiplied by ψ gives the flux of probability mass in configuration space. This probability mass is conserved so that the following continuity equation can written

$$\frac{\partial \psi}{\partial t} + \alpha \nabla \cdot \underline{\underline{\Lambda}} \cdot \underline{r} \psi - \frac{1}{2} \nabla \frac{\underline{\xi}}{Q} \underline{r} \psi - \frac{1}{6N} \nabla \frac{1}{Q} \nabla \psi = 0 \qquad (10)$$

where $\underline{r} = r'/Na$, $\alpha = \gamma\theta$ and $\theta = \zeta_0 R^2/6NkT$ is the rest state relaxation time of the dumbbell.

From the moments of the distribution function, $\langle x_i x_j \rangle$, the macroscopic properties of the solution may be computed. The evolution equation for these moments can be obtained by multiplying equation (10) by $x_i x_j$ and averaging over the distribution function. The terms involving ξ and Q, however, being nonlinear, cannot be evaluated without first solving for ψ which, in general, will not be possible due to the presence of Q and ξ in equation (10). This problem can be circumvented by using the preaveraging approximation of Peterlin (1961) in which the functions Q and ξ at each instant are replaced by their values at the mean square end-to-end distance, $\langle r^2 \rangle^{1/2}$, which exist at that moment. This approach has also been used by Hinch (1977), Tanner (1975b), and Phan-Thien et al. (1978) in related problems. Although this pre-averaging approach is clearly "ad hoc" and approximate, we believe that it will yield reasonable results over a wide range of flow strengths. When the flows

are weak and the dumbbell is not greatly distorted, the nonlinear coefficients in equation (10) are slowly varying functions and do not depart much from their rest state values. On the other hand, when the flows are strong, producing significant distortion of the dumbbell, the probability distribution function becomes strongly peaked and, in fact, can be approximated as a delta function in space. This occurs as a consequence of the typically large values of N that are associated with a macromolecule and the fact that the Warner spring causes the probability mass of the dumbbell to be confined to a space bounded by a sphere of finite radius R. As the dumbbell becomes greatly distorted, the flux of probability mass is reflected off this boundary and ψ becomes strongly peaked in the neighborhood of the boundary. With the functions ξ and Q expressed in pre-averaged form, the governing equations for the moments of the distribution are then

$$\frac{d}{dt}\langle x^2\rangle = -\xi(\langle r^2\rangle^{1/2})\langle x^2\rangle + 2\alpha\langle xy\rangle + \frac{1}{3NQ(\langle r^2\rangle^{1/2})}$$

$$\frac{d}{dt}\langle y^2\rangle = -\xi(\langle r^2\rangle^{1/2})\langle y^2\rangle + 2\lambda\alpha\langle xy\rangle + \frac{1}{3NQ(\langle r^2\rangle^{1/2})}$$

$$\frac{d}{dt}\langle xy\rangle = -\xi(\langle r^2\rangle^{1/2})\langle xy\rangle + \alpha\langle y^2\rangle + \alpha\lambda\langle x^2\rangle \qquad (11)$$

$$\frac{d}{dt}\langle z^2\rangle = -\xi\left(\langle r^2\rangle^{1/2}\right)\langle z^2\rangle + \frac{1}{3NQ\left(\langle r^2\rangle^{1/2}\right)}$$

in which

$$\xi = \frac{1}{1-\langle r^2\rangle} \qquad (12)$$

$$Q = \sqrt{N}\,\langle r^2\rangle^{1/2} \qquad (13)$$

The coupled differential equations (11) can be solved in conjunction with equations (12) and (13) for any given initial conditions. The most important initial value problem is that in which the system starts from rest in which $\langle x_i x_j\rangle = \delta_{ij}/3(N+1)$ (or $\langle x_i x_j\rangle = \delta_{ij}/3N$ for the linear spring, ξ and $Q=1$).

The relationship between the moments which appear in equation (11) and the macroscopic stress tensor for the solution can be calculated from the following expression due to Kramers (1944) (see also Bird et al (1977))

$$\underset{\approx}{\tau} = \langle \underline{r}'\underline{F}_c'\rangle \qquad (14)$$

where $\underline{F}_c$ is the force acting along the end to end vector. For the present model, this is the spring tension $\underline{F}_s$. Equation (14) neglects an isotropic contribution (Bird et al (1977)) which can be added to the pressure term of the overall stress tensor. Using equations (4) and (12), the stress is then

$$\underline{\underline{\tau}} = 3NkT\,\xi_0(\langle r^2\rangle)\langle \underline{r}\underline{r}\rangle \tag{15}$$

In particular, for simple shear flow, the shear stress is

$$S \equiv \tau_{xy} = 3NkT\,\xi_0\langle xy\rangle \tag{16}$$

and the shear viscosity is $\eta = S/\alpha$.

The first and second normal stress differences are

$$N_1 \equiv \tau_{xx} - \tau_{yy} = 3NkT\,\xi_0\left[\langle x^2\rangle - \langle y^2\rangle\right] \tag{17}$$

$$N_2 \equiv \tau_{yy} - \tau_{zz} = 3NkT\,\xi_0\left[\langle y^2\rangle - \langle z^2\rangle\right] \tag{18}$$

and the normal stress difference coefficients are $\Psi_1 = N_1/\alpha^2$ and $\Psi_2 = N_2/\alpha^2$.

When using equation (15) for purely extensional flow, ($\lambda=1$), it must be remembered that the velocity gradient tensor in equation (7) is rotated by 45° in the (x,y) plane from the frame usually used for this flow type. If $(\hat{x},\hat{y})$ is the frame rotated 45° in the counterclockwise direction in the (x,y) plane, the elongational stress for $\lambda=1$ is

$$N_1' \equiv \left(\tau_{\hat{x}\hat{x}} - \tau_{\hat{y}\hat{y}}\right) = 3NkT\xi_p\langle xy\rangle \qquad (19)$$

In addition to the stress tensor, the birefringence resulting from the deformed dumbbell can also be calculated. This birefringence is a consequence of the anisotropy of the polarizability tensor of the deformed dumbbell. The polarizability tensor of the dumbbell can be related to the end to end vector by averaging over the contributions to the polarizability tensor from the individual backbone elements of the chain. This has been done for the Gaussian chain by Kuhn and Grun (1942). Their derivation leads to the following polarizability tensor for the dumbbell (Yamakawa (1971))

$$\underline{\underline{\mu}} = N(p-q)\underline{\underline{I}} + 3R^2q\langle \underline{r}\,\underline{r}\rangle \qquad (20)$$

where p and q are constants independent of the dumbbell conformation. Birefringence measured in the (x,y) plane is

proportional to the difference in the major and minor principal axes of the polarizability tensor. Therefore, the birefringence is simply proportional to the difference of the eigenvalues of the tensor $\langle x_i x_j \rangle$ with the third column and row omitted giving (Peterlin (1961))

$$\frac{\Delta n}{nc} = 2\pi\left\{(n^2+2)/3N\right\}^2(\mu_1-\mu_2)(N_A/M)N\cdot\left[(\langle x^2\rangle-\langle y^2\rangle)^2+4\langle xy\rangle^2\right] \qquad (21)$$

where Δn is the birefringence, n is the refractive index of the solution, c is the concentration in g/cm^3, N_A is Avogadro's number and M is the molecular weight. μ_1 and μ_2 are the polarizabilities of a subunit parallel and normal to the chain axis respectively.

I.II Results

Let us now turn to the calculated results obtained by solving for the moments in equations (11)-(13). The predicted steady-state values in the end to end distance are shown in the sequence of curves in figure 3 for the three basic variations of the present model; namely, linear spring and constant friction factor, non-linear spring and non-linear spring with conformation dependent friction factor. calculations shown in figure 3 were performed for a

single value of N equal to 2500 and for λ in the range from $0 \leqslant \lambda \ll 1$. The negative range of λ is largely uninteresting since the corresponding flow types are incapable of inducing significant extension.

The response of the dumbbell with a simple linear spring is characterized by the presence of a singularity at a critical value of the velocity gradient. At this critical point the hydrodynamic friction forces exactly balance the restoring force which the entropic spring can supply. It is a simple matter to show that the critical value of the dimensional velocity gradient α is

$$\alpha = \frac{1}{2\sqrt{\lambda}} \qquad (22)$$

The flow type therefore appears to play a critical role in determining the strength of a particular flow as measured by its ability to induce extension of the macromolecule. The quantity $\sqrt{\lambda}\alpha$ is the eigenvalue of the velocity gradient tensor of equation (7). It is well known from previous theoretical investigations into the role of flow type in determining the strength of flows (Tanner (1976), Olbricht et al (1980)) that it is the eigenvalue of the velocity gradient tensor which is the important parameter. From equation (22) it is readily seen that simple shear flow

(λ=0) represents a neutral case in which no singularity exists for finite values of α.

The existence of a flow induced singularity for the linear dumbbell model was first pointed out by Takserman-Krozer (1963). The addition of a nonlinear spring to the model was first considered by Peterlin (1961), who used the Langevin spring function. The nonlinear spring insures the finite extensibility of the dumbbell and thereby removes the singularity. However, it can be seen in part (B) of figure 3 that a fairly sharp transition still exists from the coiled configuration to stretched states as α surpasses the critical values specified by equation (22). The sharpness of this transition is controlled by the magnitude of N (becoming sharper as N is increased).

The addition of a conformation dependent friction factor profoundly affects the steady state solution structure, as is evident in figure 3C. One new feature is the existence of multiple steady states in the end to end distance for all but the smallest values of λ. This leads to a hysteresis in the predicted conformation of a polymer chain subjected to "extensional" flows. For example, tracing along the λ=1.0 curve in figure 3C it is evident that a dumbbell which starts from the rest state will remain

in a nearly undeformed state for all flows in which $\alpha < \alpha_1 = 0.277$, where the slope $\partial \langle r^2 \rangle^{1/2} / \partial \alpha$ becomes infinite. Once the gradient surpasses α_1, however, the steady states are highly extended (this has been called the coil-stretch transition by de Gennes (1974, 1979)). On the other hand, tracing along the upper branch of the solution curve for =1, it can be seen that a dumbbell which starts in a highly extended state can be sustained by much lower values of than were necessary to induce the extension in the first place. In fact, for $\lambda = 1$, high extensions can be sustained down to a velocity gradient of $\alpha_2 = 0.026$ at which the slope $\partial \langle r^2 \rangle^{1/2} / \partial \alpha$ again becomes infinite for this particular value of N. The fact that $\alpha_2 < \alpha_1$ is a direct consequence of the greatly enhanced friction factor which exists in the extended state (increased by $O(\sqrt{N})$ over its rest state value). This hysteresis was first discussed by deGennes (1974) and Hinch (1974). Tanner (1975b) and more recently Phan-Thien et al. (1978) also investigated this problem and obtained quantitative predictions of the hysteresis effect for uniaxial extensional flow. However, none of the work done to date fully addresses the important effects of molecular weight and flow type on the hysterisis.

The size of the hysteresis loop (i.e. the difference

($\alpha_1 - \alpha_2$)) depends on both the type of flow, and the molecular weight of the polymer (characterized here by the parameter N). Figure 3C demonstrates the effect of flow type, and it is seen that for this particular value of N = 2500 that the hysteresis effect persists down to a value of $\lambda = 3 \times 10^{-4}$. This is an important prediction and suggests that flows which are only a slight perturbation from simple shear flow can induce hysteresis in the steady state extension of macromolecules.

In order to expose the influence of molecular weight on the magnitude of the hysteresis loop we have calculated the critical velocity gradients α_1 and α_2 for the case of $\lambda = 1.0$ as the parameter N was varied over several orders of magnitude. The results are illustrated in figure 4. It is evident that the difference ($\alpha_1 - \alpha_2$) increases with N, and is in fact, nonexistent if N becomes too small even for $\lambda = 1$. As N increases to large values, the critical value eventually becomes proportional to $\alpha_1 / \sqrt{N}$. Similar calculations were carried out holding N constant while varying the flow type parameter λ. The calculated values of α_1 and α_2 as functions of λ are shown in figure 5 for two values of N. The range of λ over which the hysteresis loop exists increases with N, but is always bounded between $0 < \lambda \leq 1$.

From equation (21) it is clear that the response of the birefringence to the flow will qualitatively look very similar to the curves for $\langle r^2 \rangle$. In particular, the curves of birefringence will be characterized by critical velocity gradients and hysteresis loops in the same way depicted by figure 3 for $\langle r^2 \rangle^{1/2}$. For the large values of N typical of macromolecules and for large deformations, the birefringence will be essentially proportional to the square of the largest length scale of the dumbbell.

Besides steady state calculations, the time dependent problem outlined earlier can also be solved. This problem was also investigated for a uniaxial extensional flow by Tanner (1975b), who noted that extremely long time scales were required for the variable friction factor dumbbell to approach steady state when started from rest in flows with velocity gradients in the neighborhood of $\alpha = \alpha_1$. This effect was investigated in somewhat more detail in the present work, by determining the time (in units of θ) required for the dumbbell to achieve 90% of the steady state conformation. The results for the three variations of the dumbbell model cited earlier in connection with figure 3 are shown in figure 6 for λ=1.0. All three variants of the model show a pronounced maximum in the time scale for stretching in the vicinity of the respective critical values

of the velocity gradient. This results from a balancing of the hydrodynamic friction and entropic spring forces at the critical point. When this occurs, the only mechanism for initial growth is Brownian diffusion, in which $\langle r^2 \rangle$ increases algebraically with time. For the linear spring model this growth continues indefinitely. On the other hand, when the nonlinear spring is introduced, the steady state value of $\langle r^2 \rangle$ is greatly restricted, and the steady state is reached in a finite time. The incorporation of a variable friction factor, and the resulting coil-stretch transition lead to a much larger steady state value for $\langle r^2 \rangle$ and the diffusion mechanism remains operative for a longer period of time. As the dumbbell extends and the friction factor increases, the rate of deformation eventually picks up. This causes the friction forces to eventually dominate but the resulting time scale to reach steady state is very long (about 180θ for N=1000).

Rheological predictions for the model can be calculated from equation (15). Figures 7 and 8 show the steady state shear stress and shear viscosity for simple shear flow with, and without, the conformation dependent friction factor for two different values of N. The use of a nonlinear spring admits the possibility of a shear rate dependent viscosity (the linear spring dumbbell predicts a constant viscosity)

and the magnitude of N controls the rate at which the viscosity drops off with increasing α. The use of a conformation dependent friction factor causes an increase in the shear viscosity with increasing shear rate in the neighborhood of $\lambda=1$. The viscosity eventually becomes shear thinning at high velocity gradients and the viscosity therefore possesses an extremum (the magnitude of which increases with N). This prediction of shear thickening was first pointed out by Tanner (1975b) and later in more detail by Phan-Thien et al. (1978).

This shear thickening prediction is in direct contrast to the available rheological data on dilute solutions of polyacrylamide in water (Baird and Metzner (1977), Tsai and Darby (1978), Argumedo et al (1978)) in which the shear viscosity was found to decrease monotonically over the entire range of velocity gradients investigated. It should be noted that for truly dilute solutions the contribution of the polymer to the shear viscosity will be small. The ratio of the polymer contribution to the viscosity of the solvent viscosity is $c[\eta]$ where c is the weight concentration and $[\eta]$ is the intrinsic viscosity. For polystyrene of 4×10^6 MW, for example, with an intrinsic viscosity of 152 cm^3/g in cyclohexane at theta conditions, the contribution of the polymer at 100 ppm would only be 1.5% of the solution

viscosity. This would mean that if N is in the neighborhood of 10^3 for this polymer (where figure 8 shows an order of magnitude increase in the shear viscosity), shear thickening of about 15% is predicted by the model which should be measurable. Phan-Thien et al. (1978) have suggested that this inconsistency in the model could be removed by using a conformation dependent friction factor only for strong flows ($\sqrt{\lambda}\dot{\alpha} > 1/2$ for the velocity gradient tensor studied here), while using the constant friction factor for weak flows. While this would solve the problem from a purely operational point of view, the incorporation of the conformation dependent friction factor is still not fully satisfactory. The origin of this discrepency in predicting the rheology in simple shear may be due to the infinite aspect ratio of the dumbbell and incorporation of a conformation dependent parameter G which controls the rotation of the particle may alleviate this problem. Indeed, Hinch (1977), who built this effect into a dumbbell model which also had a variable friction factor, reported a shear thinning viscosity.

The first normal stress difference in simple shear is shown in figure 9. The effect of the nonlinear spring is to cause N_1 to increase with $\dot{\alpha}$ at a rate less than the simple quadratic dependence in $\dot{\alpha}$ predicted by the linear spring

model. The first normal stress coefficient N_1/α^2, therefore, would be a monotonically decreasing function of α in much the same way as the shear viscosity. Introduction of the variable friction factor produces an extremum in N_1/α^2, which is again in contrast to the experimental evidence of Baird and Metzner (1977). The second normal stress difference N_2 is predicted to be identically zero for the present model with or without a conformation dependent friction factor. Unfortunately, there is a lack of data on the second normal stress difference for dilute solutions but it is generally thought that N_2/N_1 should be in the range from -.1 to -.4 (Graessley (1974), Tanner (1973)).

Although the dumbbell model with variable hydrodynamic friction fails to predict the correct qualitative response of the rheological functions in simple shear flow, flow birefringence measurements by Fuller and Leal (1980) on dilute polystyrene solutions indicated that the use of a variable friction factor was necessary in order to properly simulate the data using the dumbbell model. The flows in these experiments were generated using a four roll mill where λ was varied between $0.2 \leq \lambda \leq 1.0$ and were, therefore, largely extensional in nature. For that reason those results agree with the conclusions of Phan-Thien et al.

that use of the variable friction factor as done for the present model, although producing apparently incorrect rheological predictions for simple shear, will be satisfactory for extensional flows.

Figure 10 shows the elongational viscosity N_1'/α plotted against α for two values of N. The elongational viscosity undergoes a pronounced increase when the critical velocity gradient is surpassed and levels off as $\alpha \to \infty$. The asymptote is proportional to $N^{3/2}$ for the constant friction factor model and proportional to $N^{1/2}$ when the friction factor varies with the end to end distance. The existence of a constant asymptote for large α is a consequence of the nonlinear spring which constrains the dumbbell to a finite end to end distance. Unfortunately, it is extremely difficult to produce steady state elongational flows for dilute polymer solutions, and there is therefore a total lack of experimental data with which to compare the model predictions.

The transient shear stress and first normal stress difference when a shear flow is started from rest are shown in figures 11 and 12. As the velocity gradient is increased, there is an overshoot in the stresses which is supported by the recent experiments of Argumedo et al

(1979). The overshoot in the first normal stress difference results from the fact that the end to end distance in the nonlinear spring dumbbell is also predicted to overshoot at high velocity gradients. The overshoot in the shear stress is also caused in part by the overshoot in the end to end distance, but also results from the simultaneous action of extension and rotation of the dumbbell. In low velocity gradients where the dumbbell does not extend greatly, the distortion of the dumbbell continues simultaneously with the rotation until a steady state conformation is reached. At large velocity gradients, where the effect of the nonlinear spring becomes important, the dumbbell extension is retarded and reaches its maximum before the rotation stops. As the dumbbell continues to rotate toward the x axis, the moment $\langle xy \rangle$ decreases and the shear stress drops resulting in an overshoot of the stress. The overshoots in S and N_1, are also predicted by the models of Tanner (1975a, 1975b) and Phan-Thien *et al.* (1978).

Figure 13 shows the transient response of the elongational stress to start up of the two-dimensional extensional flow. At values of α which are lower than the critical points for both the constant and variable friction factor models, the time scales to reach steady state levels of stress are short. In the vicinity of the critical

velocity gradients for each model, the time required to reach steady state greatly increases, as pointed out earlier by figure 6. Once the critical velocity gradient is surpassed, the time scale for each model to achieve steady state decreases, and eventually scales as α'.

I.III Discussion

The dumbbell model which has been discussed so far is essentially equivalent to the model used by Tanner (1975b) with the exception of the different choice of the variable friction factor. This, however, does not alter the qualitative predictions of the model and the results presented here, although more detailed, are very close to the results which he obtained. However, the effects of flow type, and molecular weight, have been examined here in some detail, with specific emphasis on the existence and magnitude of the hysterisis loop associated with the inclusion of the variable friction factor. It was found that the multiple steady states existed for a wide range of flow types from purely extensional flows to flows which are only slightly less rotational than simple shear flow. It was also found that the range of flow types where the hysterisis was present increased with the molecular weight. In part II, the additional mechanism of an internal

viscosity is explored, and several interesting predictions are presented and discussed.

Part II. Internal Viscosity

The notion of an internal viscosity mechanism in polymer chains is motivated by a desire to cast the effects of local structural constraints on the dynamics of the chain conformation into a simple form. This is achieved through the addition of a force proportional to the rate of deformation of the end to end vector, $\dot{\underline{r}}'_{def}$, of the dumbbell with the constant of proportionality being called the internal viscosity coefficient ζ_i. Although there is some conflict with regard to the precise molecular origin of the internal viscosity coefficient (in particular its dependence upon the molecular weight and the solvent viscosity), use of the internal viscosity model has led to successful fitting of experimental data in flowing polymer solutions. Direct measurement of such internal friction forces is difficult. Traditionally, experiments to investigate the magnitude of the internal viscosity effect have involved measurement of nonlinear flow effects such as non-Newtonian viscosity, first and second normal stress differences and the frequency dependence of the complex viscosity. These measurements have been performed almost exclusively in steady and

oscillatory simple shear flows. It is the ability of the internal viscosity models to fit certain features of this data and its simplicity which makes it an attractive concept. Recent experiments reported by Fuller and Leal (1980) have demonstrated that the magnitude of the internal viscosity contribution to the dynamics of polymers in flowing solution can also be extracted by measurement of flow birefringence as a function of the flow type (i.e. the ratio of the vorticity to the rate of strain in the two dimensional flows which are studied here).

This section further examines the consequences of the internal viscosity mechanism in a variety of flow situations. In particular, the response of polymer conformation to start up flows is investigated for the velocity gradient tensor of equation (7). The effect of internal viscosity combined with finite extensibility by use of the nonlinear Warner spring is also examined. Two methods of solution are examined. The first method, valid for small values of the internal viscosity parameter, uses the perturbation scheme first introduced by Booij and van Wiechen (1968) and it is shown that largely analytical results can be obtained. The second method uses an approximation procedure developed by Cerf (1969) to calculate the conformation for arbitrary values of ξ_i.

II.I Development of the Model

The introduction of the internal viscosity mechanism leads to an additional contribution to the force balance of equation (1) which is now rewritten as

$$\underline{F}_f + \underline{F}_S + \underline{F}_B + \underline{F}_{IV} = 0 \tag{23}$$

where the internal viscosity force is taken as

$$F_{IV} = \zeta_i \dot{\underline{r}}'_{def} \tag{24}$$

As before, the equation of motion for the dumbbell is obtained by solving for the time rate of change of the end to end vector of the dumbbell $\dot{\underline{r}}'$. Before doing this however, the form of the rate of deformation $\dot{\underline{r}}'_{def}$ must be specified. Two prescriptions have been used in the past; that proposed by Kuhn and Kuhn (1945) in which

$$\dot{\underline{r}}'_{def} = \frac{\dot{\underline{r}}' \cdot \underline{r}'}{r^2} \underline{r} \tag{25}$$

and the definition used by Cerf (1957) which is

$$\dot{\underline{r}}'_{def} = \dot{\underline{r}}' - \underline{\underline{L}} \cdot \underline{r}' \tag{26}$$

where $\underline{\omega}$ is the angular velocity of the dumbbell which must be determined.

Both definitions for the rate of deformation lead to the same results. The angular velocity, $\underline{\omega}$ can be determined directly from the evolution equation for $\underline{r}'$ which is obtained from (23) using equation (25) for the rate of deformation. As will be brought out later, however, it is often convenient to choose one form over the other depending on the magnitude of the ratio of the internal viscosity coefficient to the external friction factor ζ_i/ζ which will be denoted as ϵ. It will be shown that for small values of ϵ largely analytical results can be obtained for the time dependent response of the dumbbell using the definition (25) while for larger values of ϵ, the definition (26) is more useful and accommodates an approximation technique from which model predictions can be obtained for arbitrary values of ϵ.

II.II Perturbation Solution for $\epsilon \ll 1$, $\xi(r)=1$ (Linear Spring), $Q(r)=1$ (Constant Friction Factor)

Let us first consider the development of an asymptotic solution for the dumbbell with a linear spring and constant

hydrodynamic friction factor and small values of the internal viscosity, $\epsilon << 1$. Taking equation (25) as the definition for the rate of deformation, the equation of motion for the dumbbell in this case is

$$\dot{\underline{r}} = \alpha \underline{\underline{\Delta}} \cdot \underline{r} - \frac{1}{2}\underline{r} - \frac{1}{6N}\nabla \log \psi + \frac{\epsilon}{1+\epsilon}\underline{r}\left\{\frac{1}{2} - \alpha\left(\underline{r}\cdot\underline{\underline{\Delta}}\cdot\underline{r}\right)\right. \tag{27}$$

$$\left. + \frac{1}{6Nr^2}(\underline{r}\cdot\nabla)\log\psi\right\}$$

In writing equation (27) we have nondimensionalized time by the dumbbell relaxation time, and scaled the end to end vector by R=Na. The continuity equation for ψ becomes

$$\frac{\partial \psi}{\partial t} + \alpha \nabla\cdot\underline{\underline{\Delta}}\cdot\underline{r}\psi - \frac{1}{2}\nabla\cdot\underline{r}\psi - \frac{1}{6N}\nabla^2\psi \tag{28}$$

$$+ \frac{\epsilon}{1+\epsilon}\nabla\cdot\underline{r}\left\{\frac{1}{2} - \alpha\frac{\left(\underline{r}\cdot\underline{\underline{\Delta}}\cdot\underline{r}\right)}{r^2} + \frac{1}{6Nr^2}(\underline{r}\cdot\nabla)\right\}\psi = 0$$

Equation (28) has been studied by Booij and van Wiechen (1968) who solved it for steady simple shear flow and for small values of the parameter ϵ. Booij and van Wiechen were able to calculate various moments of the distribution function as functions of the velocity gradient, but did not arrive at analytical results and only solved for the moments of the distribution numerically. We will show that it is possible to obtain largely analytical results for the more general velocity gradient tensor, given by equation (7), for both the steady state and transient start-up problems.

Following Booij et al we shall seek a perturbation solution for the distribution function in the form of

$$\Psi(\underline{r},t) = \Psi^{\circ}(\underline{r},t) + \frac{\epsilon}{1+\epsilon}\Psi'(\underline{r},t) + \cdots \tag{29}$$

and rewrite equation (28) in the form of

$$\frac{\partial \Psi}{\partial t} + \mathcal{L}_{\circ}\Psi + \frac{\epsilon}{1+\epsilon}\mathcal{L}_{1}\Psi + \cdots \tag{30}$$

subject to the initial condition $\Psi(\underline{r},0)=g(x,y,z)$

The operators $\mathcal{L}_{\circ}$ and $\mathcal{L}_{1}$, are then defined as

$$\begin{aligned}\mathcal{L}_{\circ} &= \alpha\nabla\underline{\underline{\Lambda}}\cdot\underline{r} - \tfrac{1}{2}\nabla\underline{r} - \frac{1}{6N}\nabla^{2} \\ \mathcal{L}_{1} &= \nabla\cdot\underline{r}\left\{\tfrac{1}{2} + \frac{1}{6Nr^{2}}(\underline{r}\cdot\nabla) - \frac{\alpha}{r^{2}}(\underline{r}\cdot\underline{\underline{\Lambda}}\cdot\underline{r})\right\}\end{aligned} \tag{31}$$

Combining equations (29) and (30), the following equations emerge

$$\frac{\partial \Psi^{\circ}}{\partial t} + \mathcal{L}_{\circ}\Psi^{\circ} = 0 \quad ; \quad \Psi^{\circ}(\underline{r},0) = g(\underline{r}) \tag{32a}$$

$$\frac{\partial \Psi'}{\partial t} + \mathcal{L}_{1}\Psi' = -\mathcal{L}_{1}\Psi^{\circ}; \quad \Psi'(\underline{r},0) = 0 \tag{32b}$$

Equations (32a) and (32b) can be solved by introducing the Green's function $G(\underline{r}, \underline{r}'; t)$ defined by

$$\frac{\partial G}{\partial t} + \mathcal{L}_0 G = 0 \; ; \quad G(\underline{r}, \underline{r}'; 0) = \delta(x-x')\delta(y-y')\delta(z-z') \tag{33}$$

where $\delta(\;)$ is the Dirac delta function. Once the solution for $G(\underline{r}, \underline{r}'; t)$ is obtained, the solutions to equations (32a) and (32b) can be simply expressed in the form

$$\psi^0(\underline{r}, t) = \iiint_{-\infty}^{\infty} dx'dy'dz' G(\underline{r}, \underline{r}'; t) g(\underline{r}')$$

$$\psi'(\underline{r}, t) = -\int_0^t d\tau \iiint_{-\infty}^{\infty} dx'dy'dz' G(\underline{r}, \underline{r}'; t-\tau) \mathcal{L}_1(\underline{r}') \psi^0(\underline{r}', \tau) \tag{34}$$

Given ψ^0 and ψ' it is now possible to calculate the moments of the distribution function as

$$\langle x_i x_j \rangle = \langle x_i x_j \rangle^0 + \frac{\epsilon}{1+\epsilon} \langle x_i x_j \rangle' + \cdots \tag{35}$$

where $x_i = (x, w, z)$ and $\langle x_i x_j \rangle^p = \iiint_{-\infty}^{\infty} dx dy dz \; x_i x_j \psi^p(x, y, z; t)$. It is a simple matter to show that the equation of motion for the moment $\langle x_i x_j \rangle$ is

$$\frac{d}{dt} \langle x_i x_j \rangle' = -\langle x_i x_j \mathcal{L}_1 \rangle^0 - \langle x_i x_j \mathcal{L}_0 \rangle' \tag{36}$$

Using the definitions of $\mathcal{L}_0$ and $\mathcal{L}_1$ and integrating by

parts, equation (36) becomes

$$\frac{d}{dt}\langle x_i x_j\rangle' + \langle x_i x_j\rangle' - \alpha\langle x_j \Lambda_{iR} x_k\rangle' - \alpha\langle x_i \Lambda_{jR} x_k\rangle'$$

$$= \langle x_i x_j\rangle^\circ - \left\langle \frac{1}{N}\frac{x_i x_j}{r^2} + 2\alpha^2 \frac{(\underline{r}\cdot\underline{\underline{\Lambda}}\cdot\underline{r})}{r^2} x_i x_j \right\rangle^\circ \qquad (37)$$

In general, equation (37) represents a set of six coupled equations from which the moments $\langle x_i x_j\rangle'$ can be calculated. For the special case of the "4 roller" flow of equation (7), equation (37) leads to

$$\frac{d}{dt}\langle x^2\rangle' + \langle x^2\rangle' - 2\alpha\langle xy\rangle' = \langle x^2\rangle^\circ - \left\langle \frac{1}{N}\frac{x^2}{r^2} + 2\alpha\frac{x^3 y}{r^2}\right\rangle^\circ$$

$$\frac{d}{dt}\langle y^2\rangle' + \langle y^2\rangle' - 2\lambda\alpha\langle xy\rangle' = \langle y^2\rangle^\circ - \left\langle \frac{1}{N}\frac{y^2}{r^2} + 2\alpha\frac{y^3 x}{r^2}\right\rangle^\circ$$

$$\frac{d}{dt}\langle xy\rangle' + \langle xy\rangle' - \alpha\langle x^2\rangle' - \lambda\alpha\langle y^2\rangle' = \langle xy\rangle^\circ - \left\langle \frac{1}{N}xy + 2\alpha\frac{x^2 y^2}{r^2}\right\rangle^\circ \qquad (38)$$

$$\frac{d}{dt}\langle z^2\rangle' + \langle z^2\rangle' = \langle z^2\rangle^\circ - \left\langle \frac{1}{N}\frac{z^2}{r^2} + 2\alpha\frac{xyz^2}{r^2}\right\rangle^\circ$$

To proceed further it is necessary to solve for the Green's function defined in equation (33). This can be done

in a straightforward manner by first introducing the spatial Fourier transform for G and then solving the resulting quasilinear first order partial differential equation by the method of characteristics. For the case where the initial condition is that of a fluid at rest, the distribution function is

$$g(x,y,z) = \left(\frac{3N}{2\pi}\right)^{3/2} e^{-\frac{3N}{2}\left(x^2+y^2+z^2\right)} \tag{39}$$

Following the method outlined above, the distribution function Ψ° is found to be

$$\Psi^\circ(\underline{r},t) = \left(\frac{3N}{2\pi}\right)^{3/2} \sqrt{ac-b^2}\; e^{-\frac{3N}{2}\left(a(t)x^2 - 2b(t)xy + c(t)y^2 + z^2\right)} \tag{40}$$

where

$$a(t) = 2\lambda\left[(1+\lambda)\left\{1-\beta\sinh(\beta t)\cdot e^{-t} - \beta^2\cosh(\beta t)\cdot e^{-t}\right\} + (1-\lambda)(1-\beta^2)\right]/D$$

$$b(t) = \frac{\beta^2}{\alpha}(1-\lambda)\left[1-\cosh(\beta t)\cdot e^{-t} - \beta\sinh(\beta t)\cdot e^{-t}\right]/D$$

$$c(t) = 2\left[(1+\lambda)\left\{1-\beta\sinh(\beta t)\cdot e^{-t} - \beta^2\cosh(\beta t)\cdot e^{-t}\right\} - (1-\lambda)(1-\beta^2)\right]/D \tag{41}$$

$$D = (1+\lambda)^2\left[1 - 2\beta\sinh(\beta t)\,e^{-t} - \beta^2 e^{-2t} - (1-\lambda)^2(1-\beta^2)\right]$$

$$\beta = 2\sqrt{\lambda}\,\alpha$$

Using this expression for ψ°, the averages required in equations (38) can be shown to be

$$\langle x^2\rangle^\circ = c/3N(ac-b^2)$$

$$\langle y^2\rangle^\circ = a/3N(ac-b^2)$$

$$\langle z^2\rangle^\circ = 1/3N$$

$$\langle xy\rangle^\circ = b/3N(ac-b^2)$$

$$\left\langle \frac{x^2}{r^2}\right\rangle^\circ = \frac{cI_1}{4\sqrt{ac-b^2}} - \frac{(ac-2b^2-c^2)(2-\sqrt{ac-b^2}\,I_2)}{2\left[(a+c)^2-4(ac-b^2)\right]} \qquad (42)$$

$$\left\langle \frac{y^2}{r^2}\right\rangle^\circ = \text{the same as } \left\langle \frac{x^2}{r^2}\right\rangle^\circ \text{ with } a \text{ and } c \text{ interchanged}$$

$$\left\langle \frac{xy}{r^2}\right\rangle^\circ = \frac{bI_1}{4\sqrt{ac-b^2}} - \frac{(a+c)b(2-\sqrt{ac-b^2}\,I_2)}{2\left[(a+c)^2-4(ac-b^2)\right]}$$

$$\left\langle \frac{x^3y}{r^2}\right\rangle^\circ = \frac{3cbI_3}{16(ac-b^2)^{3/2}} + \frac{(b^2+c^2)b\,(4/3-\sqrt{ac-b^2}\,I_4)}{\left[(a+c)^2-4(ac-b^2)\right]2(ac-b^2)} + \frac{b\left[c^2(a+c)^2-4ac(ac-b^2)\right]I_5}{4c\left[(a+c)^2-4(ac-b^2)\right]}$$

$$\left\langle \frac{xy^3}{r^2}\right\rangle^\circ = \text{the same as } \left\langle \frac{x^3y}{r^2}\right\rangle^\circ \text{ with } a \text{ and } c \text{ interchanged.}$$

$$\left\langle \frac{x^2y^2}{r^2}\right\rangle^\circ = \frac{(ac+2b^2)I_3}{16(ac-b^2)^{3/2}} + \frac{b^2(c+a)(4/3-\sqrt{ac-b^2}\,I_4)}{2(ac-b^2)\left[(a+c)^2-4(ac-b^2)\right]} + \frac{2(a^2+c^2)b^2-ac(c-\ )^2 I_5}{4\left[(a+c)^2-4(ac-b^2)\right]}$$

$$\langle z^2\rangle^\circ - \left\langle \frac{1}{N}\frac{z^2}{r^2} + 2\alpha\frac{xyz^2}{r^2}\right\rangle^\circ = 0$$

where

$$I_1 = \int_{-1}^{1} dx\,(1-x^2)/Q(x)$$

$$I_2 = \int_{-1}^{1} dx\left[x^2 + \frac{(1-x^2)(c+a)}{2(ac-b^2)}\right]/Q(x)$$

$$I_3 = \int_{-1}^{1} dx\,(1-x^2)^2/Q(x)$$

$$I_4 = \int_{-1}^{1} dx\,(1-x^2)\left[x^2 + \frac{(c+a)(1-x^2)}{2(ac-b^2)}\right]/Q(x)$$

$$I_5 = \int_{-1}^{1} dx\left[\left\{x^2 + \frac{(c+a)(1-x^2)^2}{2(ac-b^2)}\right\} - Q(x)\right]^2/Q(x)$$

$$Q(x) = \left[1 + (a+c-2)x^2 - (a+c-2-2c+b^2)x^4\right]^{1/2}$$

The functions I_1 through I_2 are simple combinations of the following integrals which can be evaluated in terms of elliptic integrals

$$\int_{-1}^{1} dx/Q(x) = \frac{2\,F(\phi,s)}{(x_+^2+x_-^2)}$$

$$\int_{-1}^{1} dx\,x^2/Q(x) = 2\sqrt{x_+^2+x_-^2}\,E(\phi,s) - \frac{2x_-^2\,F(\phi,s)}{\sqrt{x_+^2+x_-^2}} - 2\sqrt{\frac{x_+^2-1}{x_-^2+1}}$$

(44)

$$\int_{-1}^{1} dx\,x^4/Q(x) = \frac{2}{3\sqrt{x_+^2+x_-^2}}\left[(2x_-^2-x_+^2)x_-^2\,F(\phi,s) - 2(x_-^4-x_+^4)E(\phi,s)\right]$$

$$-\frac{2}{3}(2x_+^2-x_-^2+1)\sqrt{\frac{x_+^2-1}{x_-^2+1}}$$

where

$$X_{\pm}^2 = \frac{\sqrt{(c+a)^2-4(ac-b^2)} \pm (c+a-2)}{2(c+a-1-ac+b^2)}$$

$$\phi = \sin^{-1}\left[\frac{X_+^2 + X_-^2}{X_+^2(X_-^2+1)}\right]^{1/2}$$

$$S = \sqrt{\frac{X_+^2}{X_+^2+X_-^2}}$$

where F and E are elliptic integrals of the first and second kind. It should be noted that at steady state, the above equations simplify considerably since $(c+a)=2$ and $x_+ = x_-$. It can be shown from equations (42), that there is no effect on the moment $\langle z^2 \rangle$ to first order in the internal viscosity parameter ϵ .

At steady state the moments can be calculated directly, and figure 14 displays results for $\langle x^2 \rangle'$, $\langle y^2 \rangle'$ and $\langle xy \rangle'$ in a simple shear flow as a function of the velocity gradient. Figure 15 illustrates the dependence of the internal viscosity effect on the flow type parameter λ for several values of the velocity gradient. It should be noted that in plotting figure 15, the velocity gradient was kept below the value of 1/2, as the linear spring dumbbell model is singular at that point. As expected, the contribution of internal viscosity effect on the moments is negative and therefore suppresses the flow induced deformation. There is

no effect on the steady state conformation in either purely extensional flows where the polymer does not rotate, or in purely rotational flows where no deformation is possible. The maximum effect of the internal viscosity can be seen to occur somewhere between simple shear flow and purely extensional flow, and to shift towards the purely extensional limit as the velocity gradient is increased. We have shown that the steady results can therefore be calculated directly from equations (38,41-44). This is in contrast to the method of Booij et al, who evaluated the triple integrations appearing in equations (38) numerically. For the time dependent case, it is still necessary to proceed to a numerical solution of the differential equations in (38) but this can be accomplished using straightforward techniques and the results are shown in figures 16-18, where the moments $\langle x^2 \rangle^1$, $\langle y^2 \rangle^1$ and $\langle xy \rangle^1$ are plotted as functions of time for several values of the velocity gradient and in a simple shear flow. The effect of internal viscosity is seen to be qualitatively the same for all three moments, with an undershoot followed by an approach to steady state. The transient effect upon the total moments $\langle x^2 \rangle$ (i.e. $\langle x^2 \rangle^0 + \frac{\epsilon}{1+\epsilon} \langle x^2 \rangle^1$) and $\langle xy \rangle$ is, however, largely uninteresting, since both moments undergo a monotonic rise to steady state as shown in figures 19 and 20 for a value of ϵ equal to 0.1. However, since the linear

dumbbell model predicts that the unperturbed moment $\langle y^2 \rangle^\circ$ will remain unchanged at the rest state value for all times in simple shear flow, the internal viscosity effect causes the total moment $\langle y^2 \rangle$ to undershoot its steady state value. This undershoot effect seems to be unique to the internal viscosity mechanism and does not occur when either the nonlinear spring or the variable friction factor is introduced without the presence of internal viscosity. This suggests that direct experimental evidence for the existence of internal viscosity could be achieved by a light scattering experiment (Cottrell et al. (1969) in which the total intensity of light scattered from the molecules is measured with the scattering vector aligned along the y axis as shown in figure 21. The appearance of a minimum in $\langle y^2 \rangle$ should show up as a maximum in the intensity of the scattered light.

Figure 22 shows the transient end to end distance of the dumbbell in a purely extensional flow ($\lambda = 1.0$) for a value of $\epsilon = 0.1$. When the flow is purely extensional, the internal viscosity only affects the transient response of the dumbbell and has no effect on the steady state.

Using equation (15), the stress tensor in simple shear flow can be expressed in the form

$$\frac{\underline{\underline{\tau}}}{3NkT} = \langle \underline{r}\underline{r} \rangle - \frac{2\epsilon}{1+\epsilon} \left\langle \underline{r}\,\underline{r} \left(\frac{1}{2} + \frac{1}{6N} \frac{\underline{r}\cdot\nabla \log\Psi}{r^2} - \alpha \frac{(\underline{r}\cdot\underline{\underline{\Delta}}\cdot\underline{r})}{r^2} \right) \right\rangle \qquad (45)$$

Retaining only terms up to first order in $\epsilon/(1+\epsilon)$ and using equation (38c), the shear stress is

$$\frac{S}{3NkT} = \langle xy \rangle^{\circ} + \frac{2\epsilon}{1+\epsilon} \left(\alpha \langle y^2 \rangle' - \frac{d}{dt} \langle xy \rangle' \right) \qquad (46)$$

Similarly, the first and second normal stress differences are

$$\frac{N_1}{3NkT} = \langle x^2 - y^2 \rangle^{\circ} + \frac{2\epsilon}{1+\epsilon} \left[2\alpha \langle xy \rangle' - \frac{d}{dt} \left(\langle x^2 \rangle' - \langle y^2 \rangle' \right) \right] \qquad (47)$$

$$\frac{N_2}{3NkT} = \langle y^2 - z^2 \rangle^{\circ} - \frac{\epsilon}{1+\epsilon} \frac{d}{dt} \langle y^2 \rangle' = - \frac{\epsilon}{1+\epsilon} \frac{d}{dt} \langle y^2 \rangle' \qquad (48)$$

The introduction of internal viscosity leads to a shear viscosity and first normal stress difference coefficient which are both shear thinning. This results from the decrease in the spring force contribution to the stress due to the suppressed deformation when internal viscosity is added. A portion of the lost stress contribution from the

spring is made up by the additional internal viscosity force but the net force in the dumbbell connector is decreased. The steady state second normal stress difference, however, is zero, in agreement with the predictions of Bazua and Williams (1974) for other internal viscosity models based on the many bead and spring model of Rouse (1953). The contribution to the second normal stress from the spring force which results in the finite, negative value of $(\langle y^2 \rangle - \langle z^2 \rangle)$ is exactly cancelled by a positive contribution from the internal viscosity force. The dumbbell model developed by Phan-Thien et al. (1978) in which the diffusion equation governing the conformation was derived starting from a Langevin equation (whereas we have used a conformation space approach) was reported to predict a finite, negative value of N_2 at the steady state.

Predictions for the transient response of the stresses in start up of simple shear flow are shown in figures 23-25. The internal viscosity causes the shear stress to start from a non-zero value of $-2\epsilon/(1+\epsilon)\frac{d}{dt}\langle xy \rangle'$ when dumbbell subjected to an instantaneous start up flow. This results from the fact that at t=0 the instantaneous rate of deformation applied to the system is nonzero and the internal viscosity force thus yields a finite contribution to the stress. The first and second normal stress

differences start from zero.

The model predicts that there is a nonzero second normal stress difference at finite times which is first positive and then slightly negative before decaying to zero as $t \to \infty$. The steady state second normal stress difference is zero due to the exact balancing of the spring contribution (which is negative) and a positive internal viscosity contribution arising from the rate of deformation. At finite times, these two effects do not exactly balance and initially, when the dumbbell just begins to respond, the rate of deformation is large and the internal viscosity effect dominates. This results in the positive values for N_2 for short times.

II.III Arbitrary Values of ϵ, $\xi_0 = 1$; The Cerf Model

The preceding analysis has investigated the effect of internal viscosity when the parameter ϵ is small. For cases where the parameter ϵ is large (or at least not small), the perturbation solution of the previous section is no longer valid, and an alternate method of solution must be used. Cerf has developed a technique which does accommodate arbitrarily large values of ϵ and has used it to analyze the internal viscosity model for steady state and

oscillatory shear flow. In this section, we use Cerf's method to examine the more general class of flow types described here by equation (7), for both transient and steady state conditions.

In order to implement Cerf's method of analysis, it is necessary to use equation (26) as the definition for the rate of deformation. In using this expression, the angular velocity must be specified, and it is here that some confusion has arisen in the past. Initial studies simply set $\underline{\underline{\Lambda}}$ equal to the angular velocity of the fluid, and the resulting stress tensors lacked the proper symmetry. Cerf corrected for this by choosing $\underline{\underline{\Lambda}}$ to ensure that there was no external torque on the dumbbell, and arrived at an expression for $\underline{\underline{\Lambda}}$ which was a function of the dumbbell conformation. The same procedure can be repeated for the dumbbell model here, but it is more straightforward to calculate $\underline{\underline{\Lambda}}$ directly from the equation of motion (27).

Given a general steady linear flow field, it is convenient to first rotate the coordinates so that the vorticity axis is parallel to the z axis. The velocity can then be written as

$$\underline{v} = (\underline{\underline{D}} + \underline{\underline{\Omega}}) \cdot \underline{r} \tag{49}$$

where $\underline{\underline{D}}=(\nabla\underline{v}+\nabla\underline{v}^{+})/2$ is the rate of strain tensor, and $\underline{\underline{\Omega}}=(\nabla\underline{v}-\nabla\underline{v}^{+})/2$ is the vorticity tensor. After the above prescribed rotation of the coordinates, $\underline{\underline{D}}$ and $\underline{\underline{\Omega}}$ can be written as

$$\underline{\underline{D}} = \begin{pmatrix} a & d & e \\ d & b & f \\ e & f & c \end{pmatrix}$$

$$\underline{\underline{\Omega}} = \begin{pmatrix} 0 & \ell & 0 \\ -\ell & 0 & 0 \\ 0 & 0 & 0 \end{pmatrix} \tag{50}$$

The rate of rotation of the dumbbell is

$$\dot{\underline{r}}_{rot} = \dot{\underline{r}} - \dot{\underline{r}}_{def} = \dot{\underline{r}} - \frac{\underline{r}\cdot\dot{\underline{r}}}{r^2}\underline{r} \tag{51}$$

which after using the equation of motion (27) is

$$\dot{\underline{r}}_{rot} = \left[(\underline{\underline{D}}+\underline{\underline{\Omega}})\cdot\underline{r} - \frac{\underline{r}\cdot(\underline{\underline{D}}+\underline{\underline{\Omega}})\cdot\underline{r}}{r^2}\underline{r}\right] - \frac{1}{6N}\left[\nabla\log\Psi - \frac{\underline{r}\cdot\nabla\log\Psi}{r^2}\underline{r}\right] \tag{52}$$

Since we are seeking the mean rotation of the dumbbell in the (x,y) plane, we can set z to zero in the above equation. The x and y components of the rotation in the xy plane are then

$$\dot{x}_{rot} = \left\{ -\frac{(d-\ell)x^2 + (d+\ell)y^2 - (b-a)xy}{x^2+y^2} - \frac{1}{6N}\left(\frac{1}{y}\frac{\partial}{\partial x}\log\Psi - \frac{x\frac{\partial}{\partial x}\log\Psi + y\frac{\partial}{\partial y}\log\Psi}{x^2+y^2}\frac{x}{y}\right)\right\} y$$

$$\dot{y}_{rot} = -\left\{ \frac{-(d-\ell)x^2 + (d+\ell)y^2 - (b-a)xy}{x^2+y^2} - \frac{1}{6N}\left(\frac{1}{x}\frac{\partial}{\partial y}\log\Psi - \frac{x\frac{\partial}{\partial x}\log\Psi + y\frac{\partial}{\partial y}\log\Psi}{x^2+y^2}\frac{y}{x}\right)\right\} x \qquad (53)$$

In this approximation, we shall use a preaveraged value of $\dot{\underline{L}}$. When the terms within the curly brackets of (54) are averaged over the distribution function, the Brownian motion terms drop out and the average angular velocity is

$$\left\langle \dot{\underline{L}} \right\rangle = \left\langle \frac{-(d-\ell)x^2 + (d+\ell)y^2 - (b-a)xy}{x^2+y^2} \right\rangle \hat{\underline{z}} \qquad (54)$$

where $\hat{z}$ is a unit vector in the z direction.

Following Cerf, we make the further approximation that

$\langle \underline{\underline{L}} x_i x_j \rangle = \langle \underline{\underline{L}} \rangle \langle x_i x_j \rangle$ which leads to

$$\langle \underline{L} \rangle = \frac{-(d-\ell)\langle x^2 \rangle + (d+\ell)\langle y^2 \rangle - (b-a)\langle xy \rangle}{\langle x^2 \rangle + \langle y^2 \rangle} \hat{\underline{\underline{z}}} \tag{55}$$

The above relation for $\langle \underline{\underline{L}} \rangle$ is equivalent to that which would be obtained by following Cerf, and determining $\langle \underline{\underline{L}} \rangle$ on the basis that the dumbbell be free of external torques. For the 4 roller flow field of equation (7), the average angular velocity is

$$\langle \underline{L} \rangle = \gamma w \hat{\underline{\underline{z}}} \tag{56}$$

where

$$w = \frac{\langle y^2 \rangle - \lambda \langle x^2 \rangle}{\langle x^2 \rangle + \langle y^2 \rangle} \tag{57}$$

The evolution equation for the end to end vector, r, of the dumbbell is now

$$\dot{\underline{r}} = \left(\alpha \underline{\underline{\Delta}} \cdot \underline{r} - \frac{1}{6N} \nabla \log \Psi - \frac{1}{2} \underline{r} + \alpha \epsilon w \hat{\underline{\underline{z}}} \wedge \underline{r} \right) / (1+\epsilon) \tag{58}$$

The diffusion equation is therefore found to be

$$\frac{\partial \Psi}{\partial \tau} + \alpha \nabla \underline{\underline{\Lambda}} \cdot \underline{r} \Psi - \frac{1}{2} \nabla \underline{r} \Psi - \frac{1}{6N} \nabla^2 \Psi + \epsilon \alpha \nabla W \underline{\underline{\hat{\epsilon}}} \times \underline{r} \Psi = 0 \tag{59}$$

where we have introduced a scaled time variable $\tau = t/(1+\epsilon)$. Using equation (59), equations for the moments of the distribution can be obtained by multiplying through by $\langle x_i x_j \rangle$, and averaging over Ψ. This leads to

$$\begin{aligned}
\frac{d}{d\tau}\langle x^2 \rangle &= -\langle x^2 \rangle + 2\alpha(1+\epsilon w)\langle xy \rangle + \frac{1}{3N} \\
\frac{d}{d\tau}\langle y^2 \rangle &= -\langle y^2 \rangle + 2\alpha(\lambda - \epsilon w)\langle xy \rangle + \frac{1}{3N} \\
\frac{d}{d\tau}\langle xy \rangle &= -\langle xy \rangle + \alpha(1+\epsilon w)\langle y^2 \rangle + \alpha(\lambda - \epsilon w)\langle xy \rangle \\
\frac{d}{d\tau}\langle z^2 \rangle &= -\langle z^2 \rangle + \frac{1}{3N}
\end{aligned} \tag{60}$$

One consequence of the preaveraging scheme is that the moments $\langle x^2 \rangle$, $\langle y^2 \rangle$, and $\langle xy \rangle$ have no dependence on the z coordinate. This results from the disappearance of the Brownian motion terms when calculating the average angular velocity in (55). From the results of the perturbation

solution where the internal viscosity had no effect on $\langle z \rangle$ to first order, this will probably not be very important.

The solution of (61) for the steady state moments is

$$\langle x^2 \rangle = \left\{ 1 + \frac{2\alpha^2(1+\lambda)(1+\epsilon w)}{1-4\alpha^2(1+\epsilon w)(\lambda-\epsilon w)} \right\} /3N$$

$$\langle y^2 \rangle = \left\{ 1 + \frac{2\alpha^2(1+\lambda)(\lambda-\epsilon w)}{1-4\alpha^2(1+\epsilon w)(\lambda-\epsilon w)} \right\} /3N$$

$$\langle xy \rangle = \frac{(1+\lambda)\alpha/3N}{1-4\alpha^2(1+\epsilon w)(\lambda-\epsilon w)} \qquad (61)$$

$$\langle z^2 \rangle = \frac{1}{3N}$$

Substituting the expressions for $\langle x^2 \rangle$ and $\langle y^2 \rangle$ into the definition for w, the following cubic equation is obtained

$$8\alpha^2\epsilon^2 w^3 + 4\alpha^2\epsilon(1+\lambda)(2-\epsilon)w^2 + 2\left[1-4\alpha^2\lambda+\alpha^2(1+\lambda)^2 \right. \qquad (62)$$

$$\left. -2\alpha^2\epsilon(1-\lambda)^2 + \alpha^2(1+\lambda)^2\epsilon \right] w - (1-\lambda)(1-4\lambda\alpha^2) = 0$$

Given values for α, λ and ϵ, this equation can be solved for the roots w which, in turn can be used in equation (61) to determine the steady state moments. Figure

14 shows the quantities $\langle x_i x_j \rangle' = \lim_{\epsilon \to 0} (\langle x_i x_j \rangle - \langle x_i x_j \rangle_{\epsilon=0})$ plotted against α for simple shear flow. Comparison between the results from the preaveraging method and the perturbation method indicates qualitative agreement over the entire range of α. Furthermore, for large values of α the results from the two methods are quantitatively close. The reason for the discrepancy at small values of α is that Brownian motion effects, which are neglected in the calculation of the angular velocity for the preaveraged model, become important for such weak flows. Figure 15 compares $\langle x^2 \rangle' + \langle y^2 \rangle'$ calculated with the preaveraged model with the same quantity resulting from the perturbation model as a function of the flow type parameter λ. Here the two models are again qualitatively similar, but since the maximum value of α considered must be smaller than 1/2, in order to avoid the singularity at $\lambda = 1$, the flows included in this figure are all weak flows and for that reason the two models are not quantitatively close. In spite of the detailed differences in the two sets of results, however, the relatively good qualitative agreement for weak flows, where the pre-averaging technique must clearly break down, indicates that both solution techniques are providing a reasonable approximation of the exact solution. Let us now consider the steady state solutions for finite ϵ where the perturbation technique is no longer valid. Coincidentally,

we note that the pre-averaging technique used to obtain these solutions is expected to provide a better approximation to the exact solution as ϵ is increased.

Figure 26 shows the results for the end to end distance plotted against the velocity gradient for several values of ϵ and $\lambda=0.2$. As pointed out in the previous section, and as can be clearly seen from equations (61), the linear dumbbell with no internal viscosity ($\epsilon=0$) contains a singularity in the moments when $\alpha=1/2\sqrt{\lambda}$. This corresponds to a value of $\alpha=1.118$ in figure 26. However, the addition of internal viscosity suppresses the moments, and if ϵ becomes large enough, the singularity is removed altogether. For the flow type of figure 26 this occurs when ϵ exceeds a value of 5.85. Above this critical value of ϵ, multiple steady states are possible as evidenced by the curves for $\epsilon=6$ and higher in figure 26. The detailed features of figure 26 require further explanation. For $\epsilon<\epsilon_{cr}=5.85$, a steady solution is seen to be possible only for $\alpha<\alpha_{cr}=1.118$ and this solution is unique. The steady state values for $\langle r^2\rangle^{1/2}$ are decreased by the presence of internal viscosity as ϵ is increased, but in every case the solution becomes singular as $\alpha\rightarrow\alpha_{cr}$ and the end to end distance becomes unbounded. Although internal viscosity can reduce the average degree of deformation, it cannot

influence the existence of, or conditions for, the singularity. The situation for $\epsilon > \epsilon_{cr}$ is, however, dramatically changed. In all cases, except for a very small range of ϵ exemplified by $\epsilon = 6$ in figure 26, there is one branch of solutions which exhibits only a very small degree of deformation (actually indistinguishable from $N\langle r^2\rangle^{1/2} = 1$ in figure 26) for arbitrary values of α including $\alpha > \alpha_{cr}$. The exceptional cases, for ϵ near ϵ_{cr}, exhibit a similar behavior but steady solutions only exist up to a finite value of α. This is the case for $\epsilon = 6$ in figure 26. A second branch of steady solutions is also evident for $\epsilon > \epsilon_{cr}$ and α greater the some value (which depends on) near to α_{cr}. Near α_{cr} this second solution branch exhibits two possible steady states. The upper portion corresponds to large extensions and represents stable solutions which we have indicated by a solid line in figure 26. The lower portion, on the other hand, (which we have indicated with a dashed line) represents unstable steady solutions which could not be realized. In summary, then, for $\epsilon > \epsilon_{cr}$, there is a unique stable steady solution in which the dumbbell hardly deformed at all, for almost all values of α, including $\alpha > \alpha_{cr}$. For $\alpha \sim \alpha_{cr}$, there is a second branch of stable solutions with larger values of $\langle r^2\rangle^{1/2}$.

Similar behavior also occurs for other values of λ in the range $0<\lambda<1$. An expression for ϵ_{cr} as a function of the flow type parameter λ can be derived from equation (62). In particular, we set α equal to its critical value of $1/2\sqrt{\lambda}$ and look for roots of the resulting cubic equation which lie in the region of interest between w=0 (corresponding to an infinitely stretched dumbbell) and w=(1-)/2 (the normalized rotation rate of a highly coiled dumbbell). The critical value ϵ_{cr} as a function of the flow type parameter λ is found to be

$$\epsilon_{cr} = \frac{(1+\lambda)^2}{(1-\lambda)^2-4\lambda} \qquad \lambda < 0.0171796$$

$$\epsilon_{cr} = \frac{8\lambda+4\sqrt{\lambda}(1+\lambda)}{(1-\lambda)^2} \qquad \lambda \geq 0.0171796 \tag{63}$$

When $\epsilon > \epsilon_{cr}$, there are three real roots of equation (62), one of which is w=0. Of the other two, only one root will lie in the region of interest $0<w<(1-\lambda)/2$. The parameter ϵ_{cr} is a rapidly rising function of and tends to infinity for purely extensional flow. For simple shear flow ($\lambda=0$) ϵ_{cr} is unity, a result previously found by Cerf. When ϵ is much greater than ϵ_{cr} the dumbbell behaves like a rigid particle with very little deformation,

and its rotation approaches the rotation of fluid elements.

The fact that internal viscosity alone can cause a linear dumbbell model of a macromolecule to remain in an essentially undeformed state is a potentially important theoretical result. It must be noted, however, that internal viscosity is competely ineffective in a purely extensional flow, except to alter the time scale for molecular deformation. Furthermore, the required magnitude of the internal viscosity parameter ϵ which is required to inhibit deformation over the whole range of α is quite large, $1 \leqslant \epsilon < \infty$, and it is not at all clear that values of this magnitude would be achieved in a real system. Thus, the practical significance of these results remains to be determined by comparison with experiment. Let us now turn briefly to the time-dependent start up problem for the linear dumbbell with finite internal viscosity.

The time dependent problem can be solved by standard numerical methods to integrate the moment equations (60). Figures 16-20,22 show the comparison between the results from the preaveraged model and from the perturbation solution, for simple shear ($\lambda = 0$) and extensional flows($\lambda = 1$). The two models predict qualitatively the same effects, and are even quantitatively quite similar for the

relatively large velocity gradients that were used in the figures. In particular, the preaveraged model predicts a minimum in the moment $\langle y^2 \rangle$ for the start up of simple shear flow as was also found using the perturbation model.

As in the case of steady state flows, the time dependent solutions reveal a transition in the response of the dumbbell conformation when the parameter ϵ exceeds its critical value. In particular, as the dumbbell becomes more rigid, the time scale for rotation shifts towards the rotation time of a fluid element, and the dumbbell experiences a tumbling motion in the start up of simple shear flow. The moments and the angular velocity for this case are plotted against time for different values of ϵ in figures 27 through 30. The tumbling action is most clearly evidenced in figure 29 where it can be seen that the moment $\langle xy \rangle$ continuously changes sign for $\epsilon > 1$ (the critical value for shear flow) as the dumbbell responds to the start up of the flow. The frequency of the oscillations associated with this tumbling motion increases with the velocity gradient as illustrated in figures 27 through 30 by comparing the cases of $\alpha = 10$ and $\alpha = 20$ for $\epsilon = 1.5$. This time dependent behavior is analogous to the motion of a viscous drop which also experiences this tumbling phenomenon when the ratio of the drop viscosity to the viscosity of the suspending fluid is

large enough. This effect has been predicted theoretically for the viscous fluid drop in simple shear flow, and has also been confirmed experimentally (Cox (1969), Torza et al (1972)).

Finally, let us briefly consider the predicted behavior of the bulk stresses for the linear dumbbell with internal viscosity. The stress tensor for the preaveraged model can be calculated using equation (15). For simple shear flow the shear stress and normal stress differences are

$$\frac{S}{3NKT} = \left[\langle xy\rangle + 2\alpha\epsilon w\langle x^2\rangle\right]/(1+\epsilon) \tag{64}$$

$$\frac{N_1}{3NKT} = \left[\langle x^2\rangle - \langle y^2\rangle + 2\alpha\epsilon(1-2w)\langle xy\rangle\right]/(1+\epsilon) \tag{65}$$

$$\frac{N_2}{3NKT} = \left[\langle y^2 - z^2\rangle + 2\alpha\epsilon w\langle xy\rangle\right]/(1+\epsilon)$$

$$= -\frac{d}{dt}\langle y^2\rangle \tag{66}$$

The shear stress and normal stress differences for small values of ϵ show qualitatively the same response with the preaveraged model as with the perturbation model as can be seen in figures 23-25 for the start up shear flow with

ϵ =0.1. In particular, both models show the same trends in the second normal stress difference which is predicted to first rise and then decay to zero in time.

As was stated previously, the viscosity and coefficient of the first normal stress difference, Ψ_1, become shear thinning when the internal viscosity is considered. This point has been brought out previously in detail by Bazua and Williams (1974). As ϵ exceeds its critical value of unity for simple shear flow, the stress functions begin to oscillate in time. This effect is displayed in figures 23 - 25 for the shear stress N_1 and N_2 and is a consequence of the "tumbling" action of the dumbbells.

II.IV Nonlinear Spring, Arbitrary Values of ϵ

In the preceding sub-section, we have considered the effect of internal viscosity (of arbitrary magnitude) on the behavior of the dumbbell model with a linear spring and a constant hydrodynamic friction factor. Let us now turn to the case for a nonlinear spring in the form given in equation (5) and internal viscosity. We have seen, in the previous sections, that the dumbbell with a linear spring possesses a singularity for $\alpha = 1/2\sqrt{\lambda}$, and this is still true when internal viscosity is included in the model unless

$\epsilon > \epsilon_{cr}$. This unrealistic singular behavior is removed by incorporating a nonlinear spring into the dumbbell. Using the Warner spring function, equations (60) become

$$\frac{d\langle x^2\rangle}{d\tau} = -\xi_e\langle x^2\rangle + 2\alpha(1+\epsilon w)\langle xy\rangle + \frac{1}{3N}$$

$$\frac{d\langle y^2\rangle}{d\tau} = -\xi\langle y^2\rangle + 2\alpha(\lambda-\epsilon w)\langle xy\rangle + \frac{1}{3N}$$

$$\frac{d\langle xy\rangle}{d\tau} = -\xi_e\langle xy\rangle + \alpha(1+\epsilon w)\langle y^2\rangle + \alpha(\lambda-\epsilon w)\langle x^2\rangle \qquad (67)$$

$$\frac{d\langle z^2\rangle}{d\tau} = -\xi_e\langle z^2\rangle + \frac{1}{3N}$$

Let us consider the solutions of these equations beginning with steady state conditions. In this case, the solutions (steady state) are easily shown to be

$$\langle x^2\rangle = \frac{1}{3N\xi_e}\left[1 + \frac{2\alpha^2(1+\lambda)(1+\epsilon w)}{\xi_e^2 - 4\alpha^2(1+\epsilon w)(\lambda-\epsilon w)}\right]$$

$$\langle y^2\rangle = \frac{1}{3N\xi_e}\left[1 + \frac{2\alpha^2(1+\lambda)(\lambda-\epsilon w)}{\xi_e^2 - 4\alpha^2(1+\epsilon w)(\lambda-\epsilon w)}\right] \qquad (68)$$

$$\langle xy\rangle = \frac{\alpha(1+\lambda)}{3N\xi_e\left[\xi_e^2 - 4\alpha^2(1+\epsilon w)(\lambda-\epsilon w)\right]}$$

$$\langle z^2\rangle = 1/3N\xi_e$$

Adding the equations in (68) to give the moment $\langle r^2 \rangle$ and substituting the expressions for $\langle x^2 \rangle$ and $\langle y^2 \rangle$ into the equation for w, we have two coupled equations, which when arranged are

$$3\left[\xi_0^2 - 4\alpha^2(1+\epsilon w)(\lambda-\epsilon w)\right](1-N\xi_0) + 2\alpha^2(1+\lambda)^2 = 0 \tag{69a}$$

$$\left[\xi_0^2 - 4\alpha^2(1+\epsilon w)(\lambda-\epsilon w)\right](1-\lambda-2w) - 2\alpha^2(1+\lambda)^2(1+\epsilon)w = 0 \tag{69b}$$

Using equation (12), $\langle r^2 \rangle$ can be eliminated from the above equations in favor of ξ_0. The equations (69) can then be combined to give the following expressions

$$w = (1-\lambda)\Big/\left[2 - 3(1+\epsilon)(1-N\xi_0)\right]$$

$$\alpha^2 = 3\xi_0^2(1-N\xi_0)\Big/\left[12(1+\epsilon w)(\lambda-\epsilon w)(1-N\xi_0) - (1+\lambda)^2\right] \tag{70}$$

Using these equations the steady state moments of the nonlinear dumbbell with internal viscosity can be calculated as a function of α for given values of λ and ϵ by first

choosing the value of the end to end vector which specifies ξ_e. From there w can be calculated directly, and α can then be determined. These values for $\lambda, \epsilon, \xi_e, \alpha$ and W can then be used in equation (70) to calculate the moments of the distribution. This procedure was carried out for ϵ=10 of 10 for several different flow types and the results are shown in figure 31. Since a value of 10 for is the critical value for λ=0.228, we can expect multiple steady states for flow types where λ is less than this value but unique steady solutions for larger values of λ. Figure 31 indicates that this is indeed the case. For λ >0.288, a single, unique steady solution exists, and the results are essentially identical to those calculated earlier for a dumbbell with a nonlinear spring, but no internal viscosity. For λ <0.288, on the other hand, one branch of stable steady solutions exists with $N\langle r^2\rangle^{1/2} \sim 1$ for all values of α, and a second branch of stable solutions exists for sufficiently large α which again is nearly identical to the results obtained without any internal viscosity in figure 3B. The lower portion of this upper branch of solutions, indicated in figure 31 with dashed lines, is unstable. It may be noted from figure 31 that the value of α at which multiple steady states start to appear tends to infinity as $\lambda \to 0$ (simple shear flow).

The effect of the nonlinear spring is then to allow two stable steady states to exist when both α and ϵ exceed their critical values for a given flow type. For flows between simple shear flow, and purely extensional flow, the dumbbell could either be in a highly extended state, or in an essentially undeformed conformation depending on its initial conditions and the values of ϵ and α.

All of the properties of the dumbbell with the nonlinear spring and internal viscosity such as the moments of the distribution and the stresses can be calculated as before. However, the qualitative features of the presence of both effects will essentially be a straightforward combination of the predictions already presented and for that reason detailed results will not be presented here. The salient points which deserve mention include the following:

1. The combination of internal viscosity and the nonlinear spring still produces the appearance of a minimum in $\langle y^2 \rangle$ as simple shear flow is started from rest. However, the magnitude of the minimum increases with increases in the internal viscosity parameter ϵ.

2. The second normal stress difference is still

zero at steady state but is finite (and initially positive) for the transient case of a start up shear flow.

3. The introduction of the nonlinear spring does not greatly influence the quantitative relationship between the values of $\alpha = \alpha_{cr}$ and $\epsilon = \epsilon_{cr}$ at which the dumbbell will have multiple steady states, and λ in flows where $0<\lambda<1$.

4. The "tumbling" action of the dumbbell still occurs with the introduction of the nonlinear spring when $\epsilon > \epsilon_{cr}$ and this leads again to oscillations in the macroscopic properties.

II.V Discussion

The influence of internal viscosity has been examined in detail using two calculation techniques for the problems of transient and steady two dimensional flows. The perturbation scheme was solved analytically and the moments of the distribution and the stresses were calculated. The internal viscosity effect was then shown to be strongly influenced by the flow type, having a maximum influence for flow types between that of simple shear flow and purely

extensional flow. Its effect on the transient response to simple shear flow when ϵ is small is most strongly seen in the moment $\langle y^2 \rangle$ which is predicted to experience a minimum in time. Using the perturbation solution, it was also demonstrated that the model predicts shear thinning in both the viscosity and first normal stress difference coefficient. The second normal stress difference is, however, zero at steady state although its transient response is nonzero and in fact is initially positive.

The preaveraged solution was shown to be in good qualitative agreement with the perturbation solution for small ϵ and is capable of predicting the model response when the internal viscosity becomes large. The most striking effect of large values of the internal viscosity parameter ϵ is the appearance of multiple steady states for flow types in the range of $0<\lambda<1$ and the removal of the singularity at $\alpha = 1/2\sqrt{\lambda}$. For the linear spring dumbbell, this occurs when ϵ exceeds a critical value which depends on the flow type. In the region where the multiple steady states exist, the dumbbell is characterized by either a largely distorted configuration in which the spring forces balance the viscous forces with a negligible contribution from internal viscosity or a highly coiled configuration where the internal viscosity forces are the primary

"restoring" forces. In the transient response to start up of flows where $\epsilon > \epsilon_{cr}$, the dumbbell conformation responds much like a viscous drop and experiences a tumbling action. When this occurs, the macroscopic properties of the dumbbell suspension oscillate in time until steady state is reached.

We have not presented results for the combination of the internal viscosity, nonlinear spring and variable friction. Calculations with all three effects combined have been performed but it was found that no significantly new predictions result and that the unique contributions of each effect combine in a straightforward fashion.

III. Conclusions

In this paper, we have examined the effects of three attributes which have been suggested for the dumbbell in order to model observed flow phenomena in dilute polymer solutions subjected to flow. In some instances the results presented here are basically reviews of several acknowledged predictions of the model (the rheological predictions of part one in particular), but other model predictions, the authors believe, are new. This is the case, in particular, for the predicted effects of flow type and molecular weight on the features of a dumbbell with a nonlinear spring and

variable friction factor.

The additional effects introduced by viscosity have also been explored via two methods of solution. These included a largely analytic perturbation solution to the time dependent problem (in contrast to prior solutions which were numerical and restricted to the steady state) and a second method based upon the preaveraging technique due to Cerf. Several interesting predictions were uncovered which include the transient response of the moments of the distribution and the stresses. At large values of the internal viscosity parameter, the solution structure was found to undergo profound changes which led to multiple steady states and oscillatory response of the moments and stresses.

While these predictions are interesting, the degree to which they are manifested in an experiment will be strongly affected by the molecular weight distribution of the actual polymer sample and the transit times experienced by the molecules in the region of the flow in which measurements are taken. The effect of finite transit times is especially important in extensional flows (i.e. $\lambda > 0$) which cannot be created over a finite domain. These two points are taken up in detail in Fuller and Leal (1980) which reports the results of flow birefringence experiments in a four roll mill.

ACKNOWLEDGEMENT

This research was supported by the Office of Naval Research. One of us (G.G.F.) is indebted to the National Research Council of Canada for fellowship support.

References

Argumedo, A, Tung, T. T. and Chang, K. I., J. Rheology 22,449(1978).

Baird, K. M. and Metzner, A. B., Trans. Soc. Rheol 21,237(1977).

Bazua, E. R. and Williams, M. C., J. Poly. Sci. 12,825(1974).

Bird, R. B., Armstrong, R. C. and Hassager, O., Dynamics of Polymeric Liquids Volume II: Kinetic Theory, Wiley, (1977).

Booij, H. C. and van Wiechen, P. H., J. Chem. Phys. 52,5056(1968)

Bretheron, F. P., J. Fluid Mech. 14,284(1962).

Cerf, R., J. Polym. Sci. 23,125(1957).

Cerf, R., J. Chim. Phys. 66,479(1969).

Cottrell, F. R., Merrill, E. W. and Smith, K. A., J. Polym. Sci. A-2,7,1415(1969).

Cox, R. G., J. Fluid Mech. 37,601(1969).

de Gennes, P. G., J. Chem. Phys., 60,5030(1974).

de Gennes, P. G., Scaling Concepts in Polymer Physics, Cornell Univ. Press (1979).

Fuller, G. G. and Leal, L. G., Flow Birefringence of Dilute Polymer Solutions in Two Dimensional Flows, forthcoming publication (1980).

Gordon, R. J. and Schowalter, W. R., Trans. Soc. Rheol. 16,79 (1972); Gordon, R. J. and Everage, A. E., J. Appl. Polym. Sci. 15,1903(1971); Everage, A. E. and Gordon, R. J. ibid 16,1967

(1972); Everage, A. E. and Gordon, R. J., A.I.C.H.E. J. 17,1257(1971); Everage, A. E. and Gordon, R. J., J. Appl. Polym. Sci. 18,3137(1974); Everage, A. E. and Gordon, R. J., ibid 21,1421(1977).

Graessley, Adv. Polymer Sci. 16,1(1974).

Hinch, E. J., Proc. Symp. Polym. Lubtification, Brest (1974).

Hinch, E. J., J. Fluid Mech. 74,317(1976a).

Hinch, E. J., J. Fluid Mech. 75,765(1976b).

Hinch, E. J., Phys. Fluids 20,S22(1977).

Kramers, H. A., Physica 11,1(1944).

Kuhn, W., Kolloid-Z. 68,2(1934).

Kuhn ,W. and Grun, F., Kolloid Z. 101,248(1942).

Kuhn, W. and Kuhn, H., Helv. Chim. Acta. 28,1533(1945).

Lodge, T. P., Soli, A. L., Miller, J. W. and Shrag, J. L., Paper presented at the Golden Jubilee Meeting of the Society of Rheology, Boston, Mass. (1979).

Olbricht, W. L., Rallison, J. M. and Leal, L. G., A Criterion for Strong Flow Based on Microstructure Deformation, forthcoming publication, (1980).

Peterlin, A., Polymer 2,257(1961).

Phan-Thien, N., Atkinson, J. D. and Tanner, R. I., J. Non-Newt. Fluid Mech. 3,309(1978)

Rouse, P. E. Jr., J. Chem. Phys. 21,1272(1953).

Takserman-Krozer, R., J. Polym. Sci. A1,2477(1963).

Tanner, R. I., Trans. Soc. Rheol. 17,365(1973).

Tanner, R. I., Trans. Soc. Rheol. 19,37(1975a).

Tanner, R. I., Trans. Soc. Rheol. 19,557(1975b).

Tanner, R. I., AICHE J. 22,910(1976).

Tanner, R. I. and Strehrenberger, W., J. Chem. Phys. 55,1958(1971).

Torza, S., Cox, R. G. and Mason, S. G., J. Colloid Int. Sci. 38,395(1972).

Tsai, C. F. and Darby, R., J. Rheol. 22,219(1978).

Warner, H. R., Ind. Eng. Chem. Fund. 11,375(1972).

Williams, M. C., AICHE J. 21,1(1975).

Yamakawa, H., Modern Theory of Polymer Solutions, Harper and Row Publ. (N. Y. 1971).

Zimm, B. H., J. Chem. Phys. 24,269(1956).

Figure Captions

Figure 1. The dumbbell model.

Figure 2. Flow field described by equation (7).

Figure 3. End to end distance of the dumbbell versus the velocity gradient. (A) Linear spring, constant friction factor, (B) Nonlinear spring, constant friction factor, C) Nonlinear spring, variable friction factor.

Figure 4. Hysteresis effect as a function of N.

Figure 5. Hysteresis effect as a function of λ.

Figure 6. Time to reach 90% of steady state (in units of θ) versus the velocity gradient.

Figure 7. Shear stress versus the velocity gradient.

Figure 8. Shear viscosity versus the velocity gradient.

Figure 9. First normal stress difference versus the velocity gradient.

Figure 10. Elongational viscosity versus the velocity gradient.

Figure 11. Shear stress versus time.

Figure 12. First normal stress difference versus time.

Figure 13. Elongational stress versus time.

Figure 14. $N\langle x_i x_j \rangle'$ versus the velocity gradient.

Figure 15. $N\langle r^2 \rangle'$ versus λ.

Figure 16. $N\langle x^2 \rangle'$ versus time, ——— perturbation solution, ----- preaveraged solution.

Figure 17. $N\langle y^2 \rangle'$ versus time, ——— perturbation solution, ----- preaveraged solution.

Figure 18. $N\langle xy\rangle^{1}$ versus time, ——— perturbation solution, ----- preaveraged solution.

Figure 19. $N\langle x^2\rangle$ versus time, ϵ=0.1, ----- perturbation solution, -·-·- preaveraged solution.

Figure 20. $N\langle xy\rangle$ versus time, ϵ=0.1, ----- perturbation solution, -·-·- preaveraged solution.

Figure 21. Total intensity light scattering experiment to measure the transient value of $\langle y^2\rangle$.

Figure 22. $N\langle r^2\rangle$ versus time, λ=1.0, ϵ=0.1, ----- perturbation solution -·-·- preaveraged solution.

Figure 23. Shear stress versus time. ----- perturbation solution, All other dashed curves are for the preaveraged solution.

Figure 24. First normal stress difference versus time. All other dashed curves are for the preaveraged solution.

Figure 25. Second normal stress difference versus time. All other dashed curves are for the preaveraged solution.

Figure 26. End to end distance versus the velocity gradient for λ=0.2. Unstable branches are denoted by dashed lines.

Figure 27. $N\langle x^2\rangle$ versus time. α=10 for the solid curves, α=20 for the dashed line.

Figure 28. $N\langle y^2\rangle$ versus time. α=10 for the solid curves, α=20 for the dashed line.

Figure 29. $N\langle xy\rangle$ versus time. α=10 for the solid curves, α=20 for the dashed lines.

Figure 30. w versus time. α=10 for the solid curves, α=20 for

the dashed line.

Figure 31. End to end distance versus the velocity gradient for $\epsilon = 10$. Unstable branches are denoted by dashed lines.

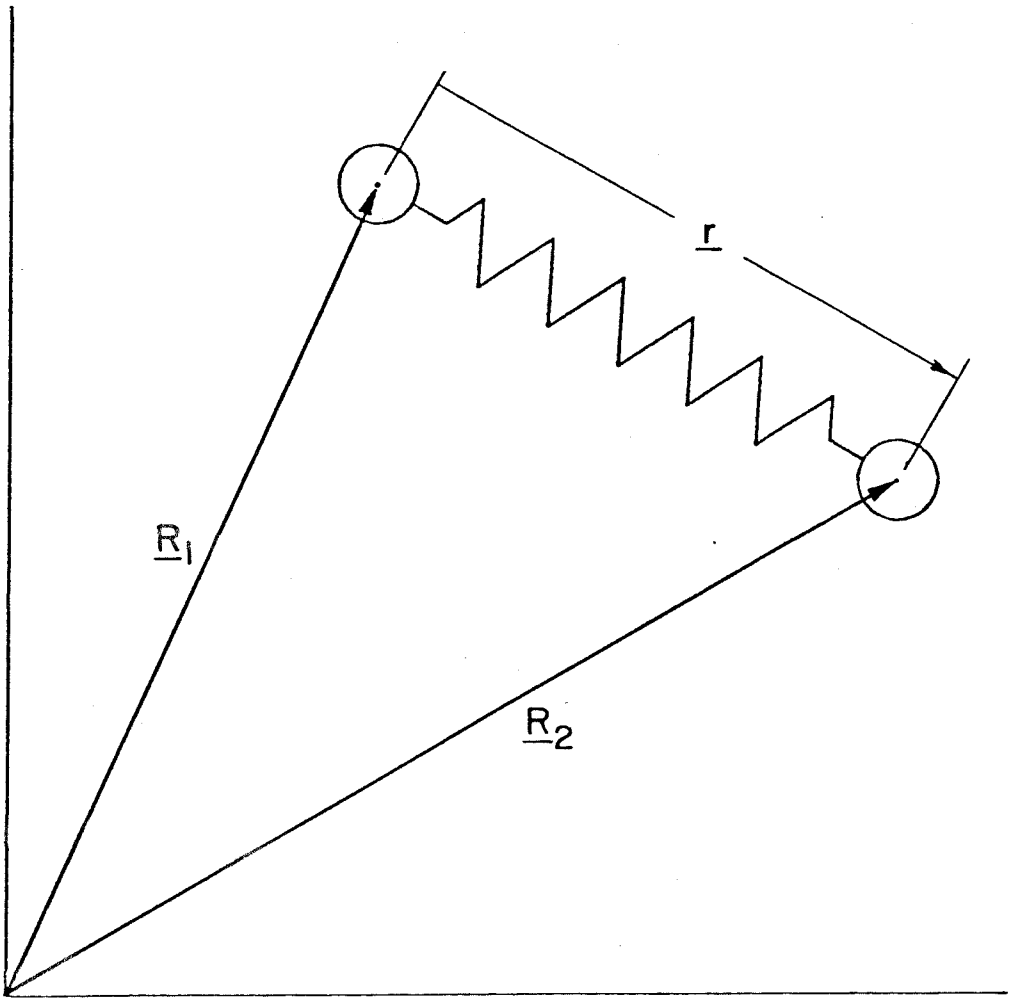

Fig. 1

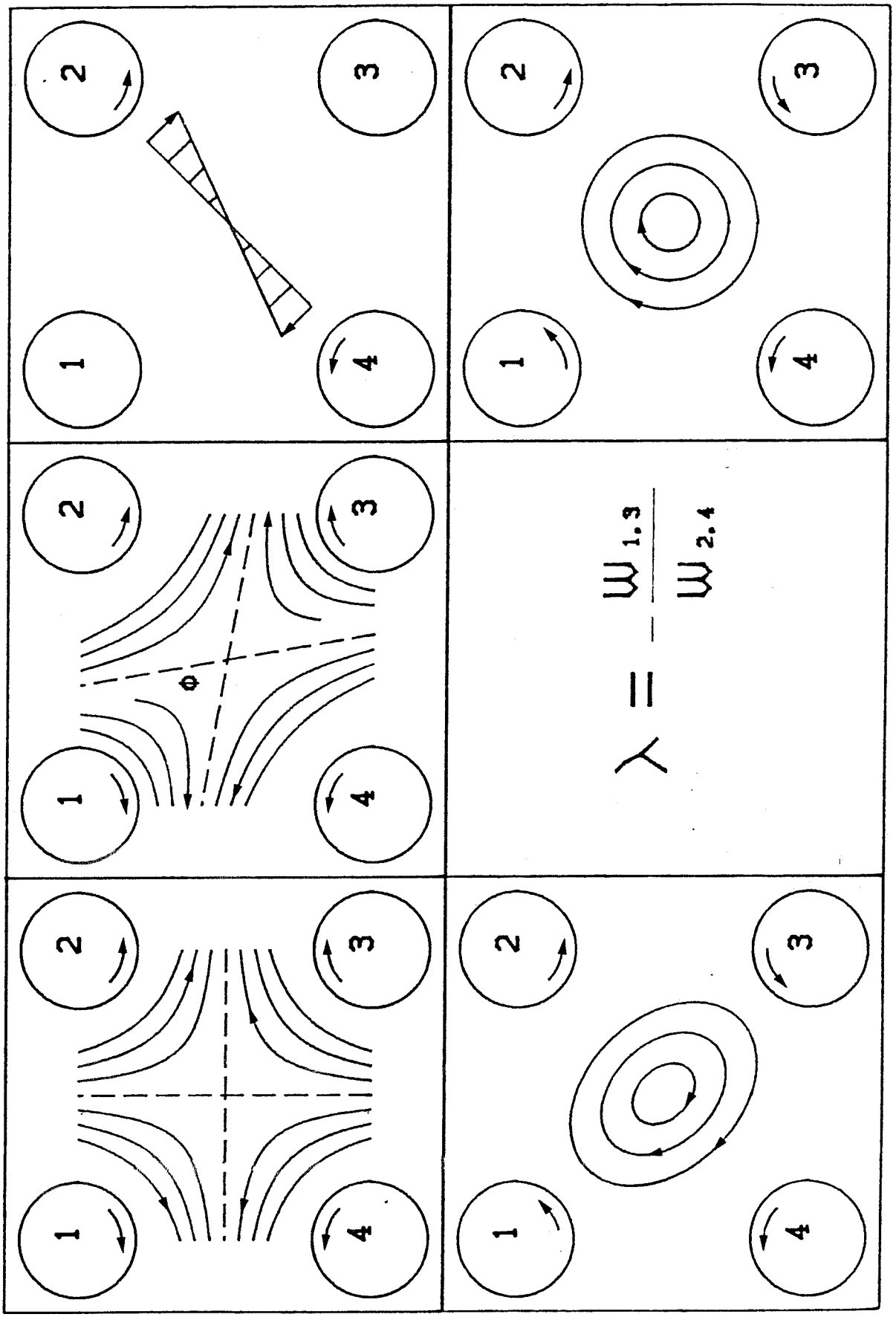

Fig. 2

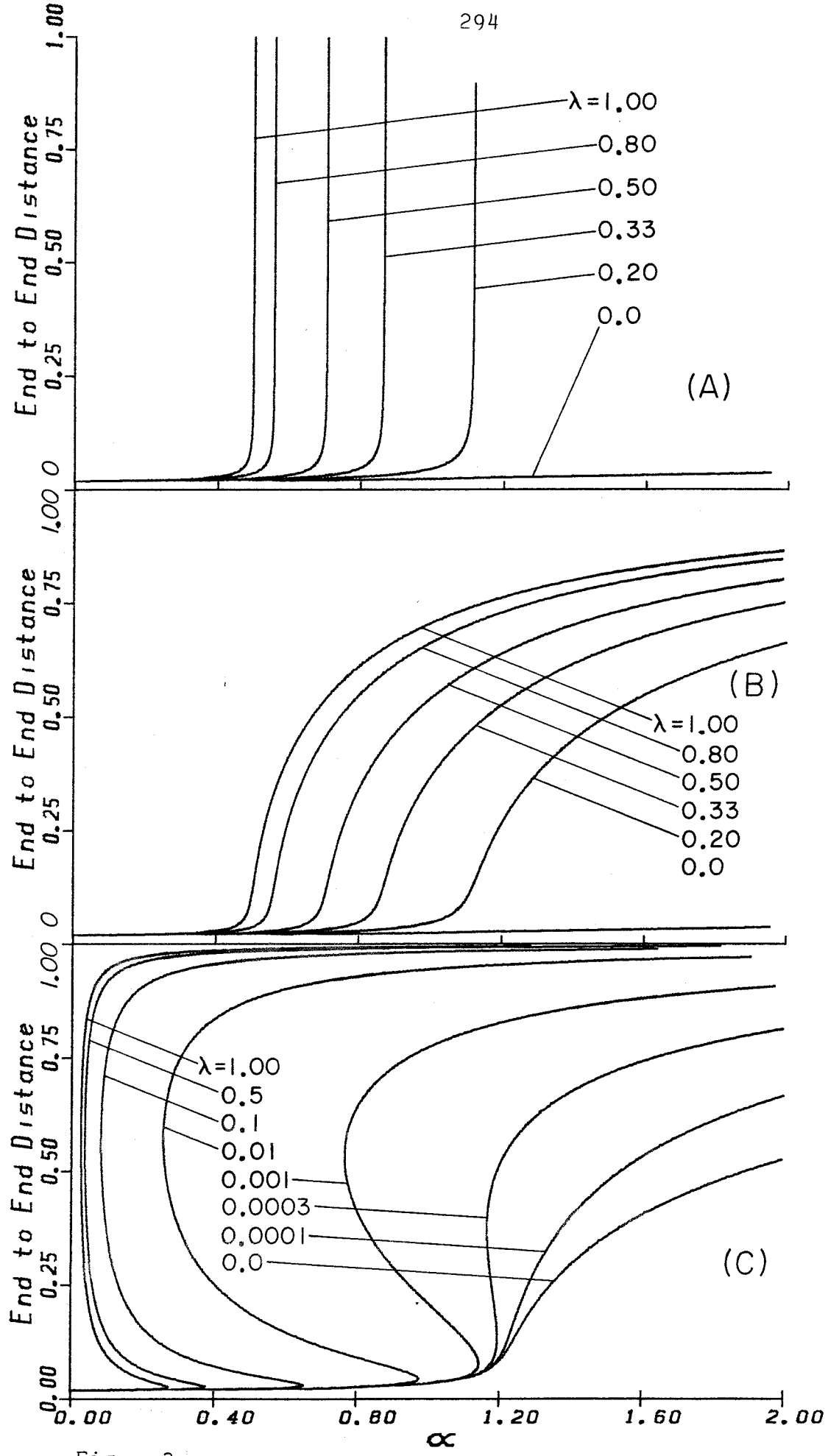
End to End Distance
1.00
0.75
0.50
0.25
0
λ=1.00
0.80
0.50
0.33
0.20
0.0
(A)
(B)
λ=1.00
0.80
0.50
0.33
0.20
0.0
λ=1.00
0.5
0.1
0.01
0.001
0.0003
0.0001
0.0
(C)
0.00
0.40
0.80
1.20
1.60
2.00
α

Fig. 3

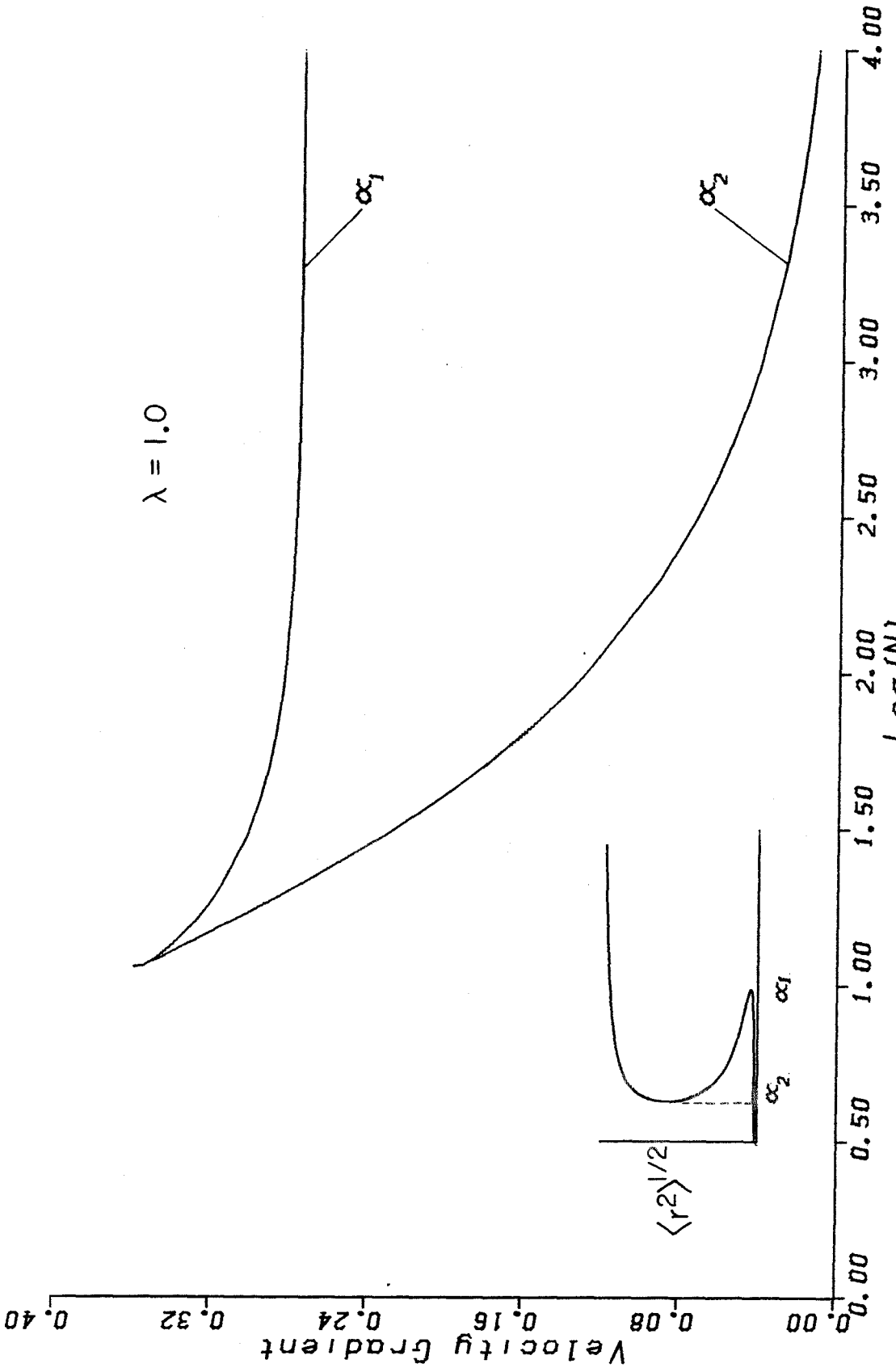
Velocity Gradient
0.00
0.08
0.16
0.24
0.32
0.40
0.00
0.50
1.00
1.50
2.00
2.50
3.00
3.50
4.00
Log (N)
λ = 1.0
α1
α2
⟨r²⟩^1/2

Fig. 4

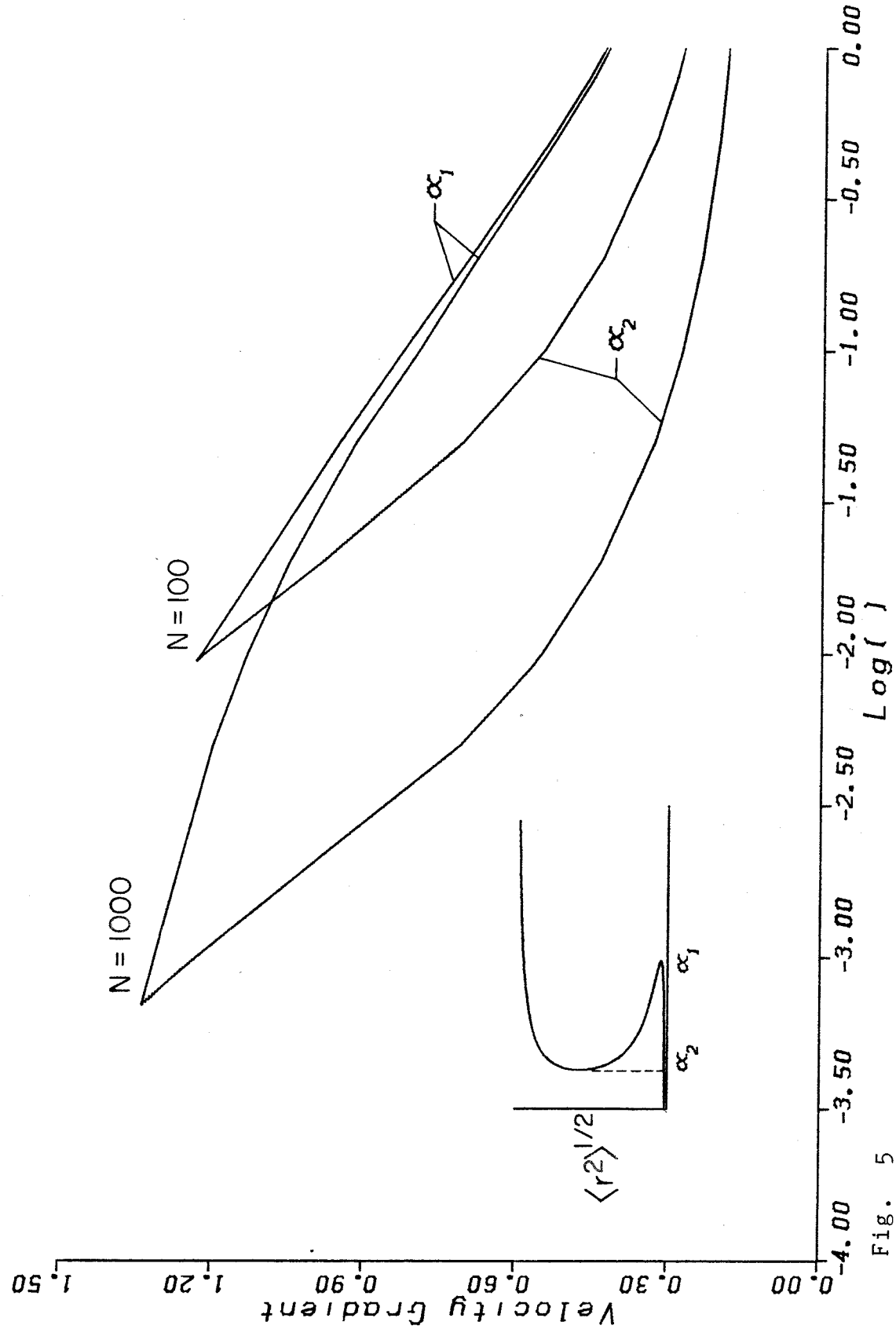
Velocity Gradient
0.00
0.30
0.60
0.90
1.20
1.50
-4.00
-3.50
-3.00
-2.50
-2.00
-1.50
-1.00
-0.50
0.00
Log( )
N = 1000
N = 100
α_1
α_2
$\langle r^2 \rangle^{1/2}$
α_1
α_2

Fig. 5

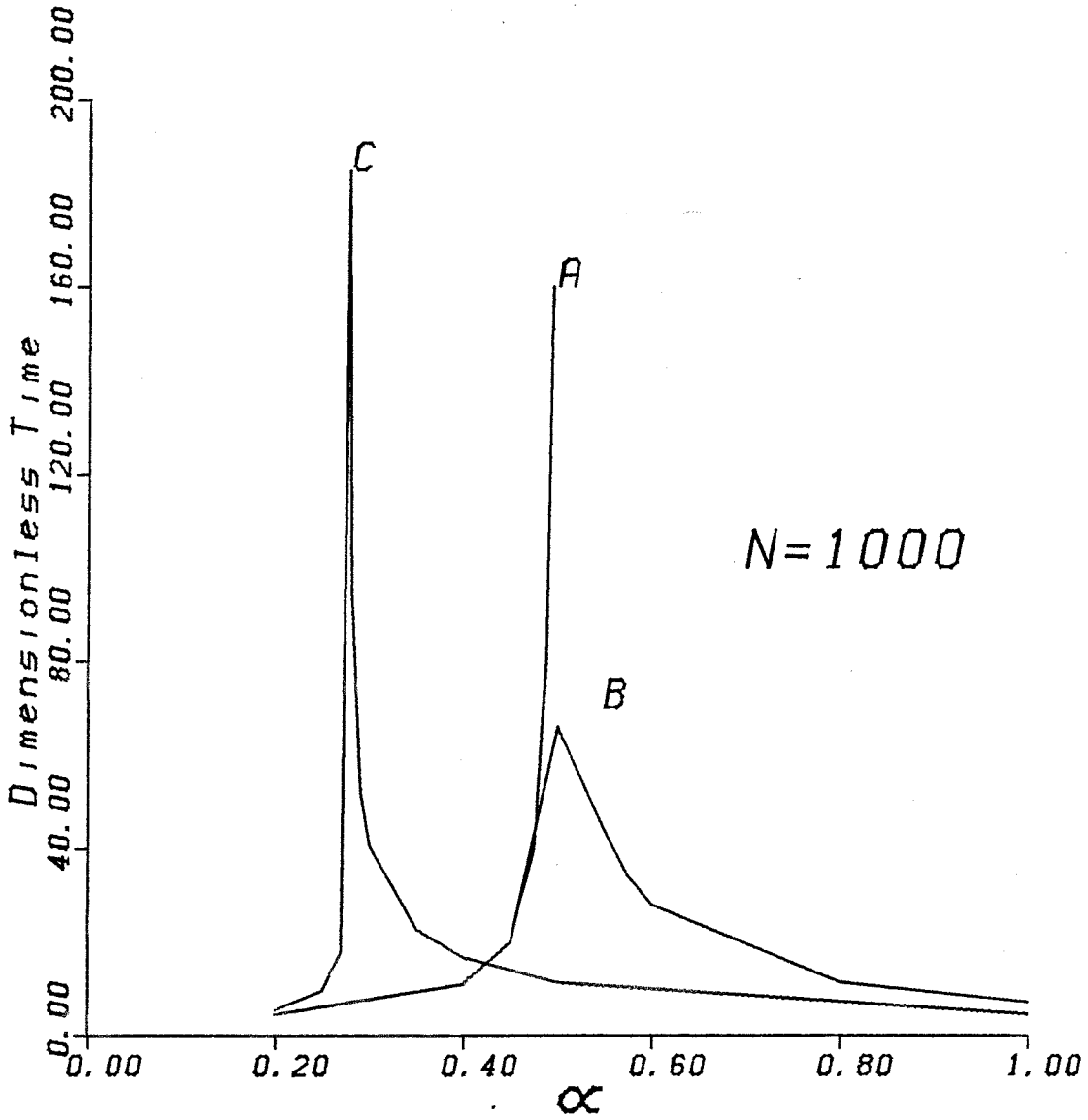
Dimensionless Time
200.00
160.00
120.00
80.00
40.00
0.00
0.00
0.20
0.40
0.60
0.80
1.00
α
C
A
B
N=1000

Fig. 6

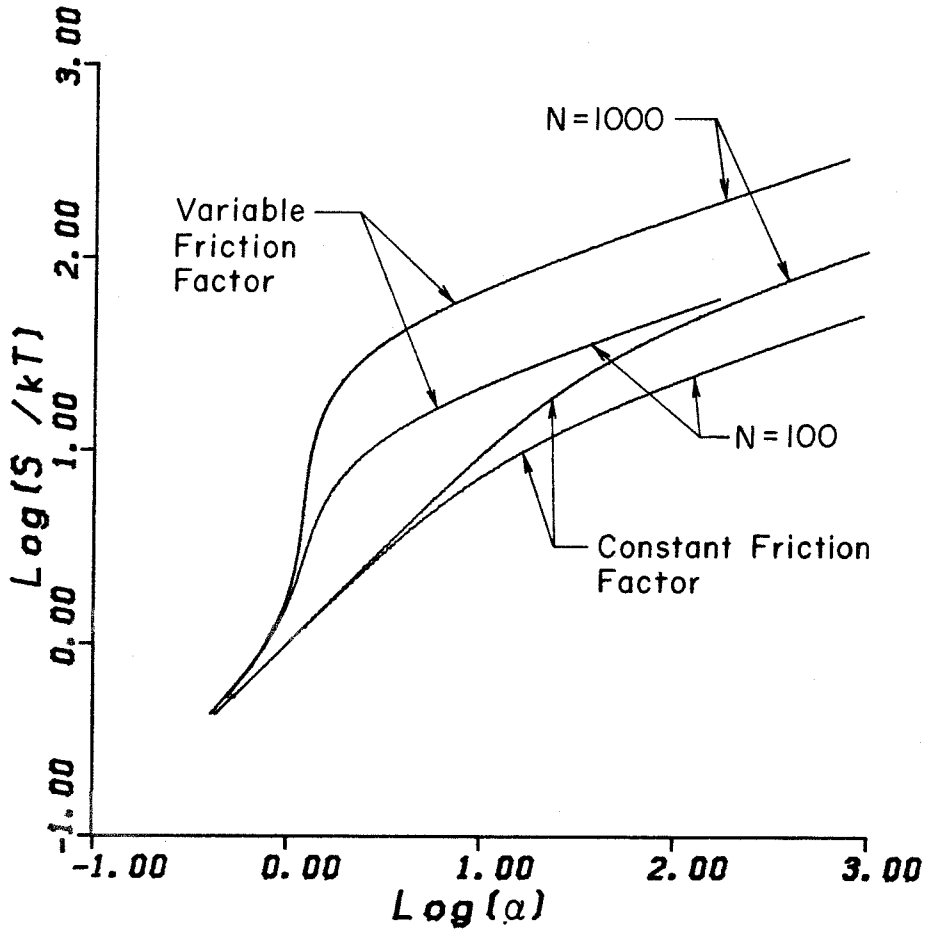
N=1000
Variable
Friction
Factor
N=100
Constant Friction
Factor
Log (S /kT)
3.00
2.00
1.00
0.00
-1.00
-1.00
0.00
1.00
2.00
3.00
Log (α)

Fig. 7

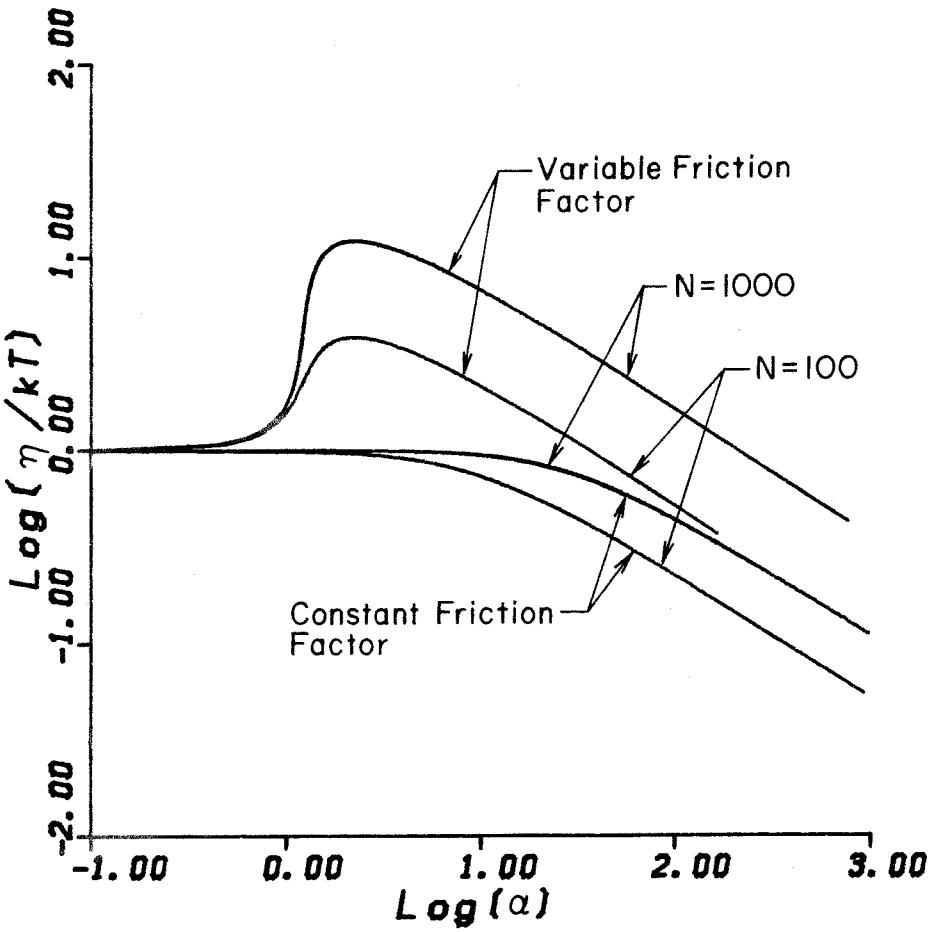
Variable Friction Factor
N=1000
N=100
Constant Friction Factor
Log (η/kT)
Log (α)
2.00
1.00
0.00
-1.00
-2.00
-1.00
0.00
1.00
2.00
3.00

Fig. 8

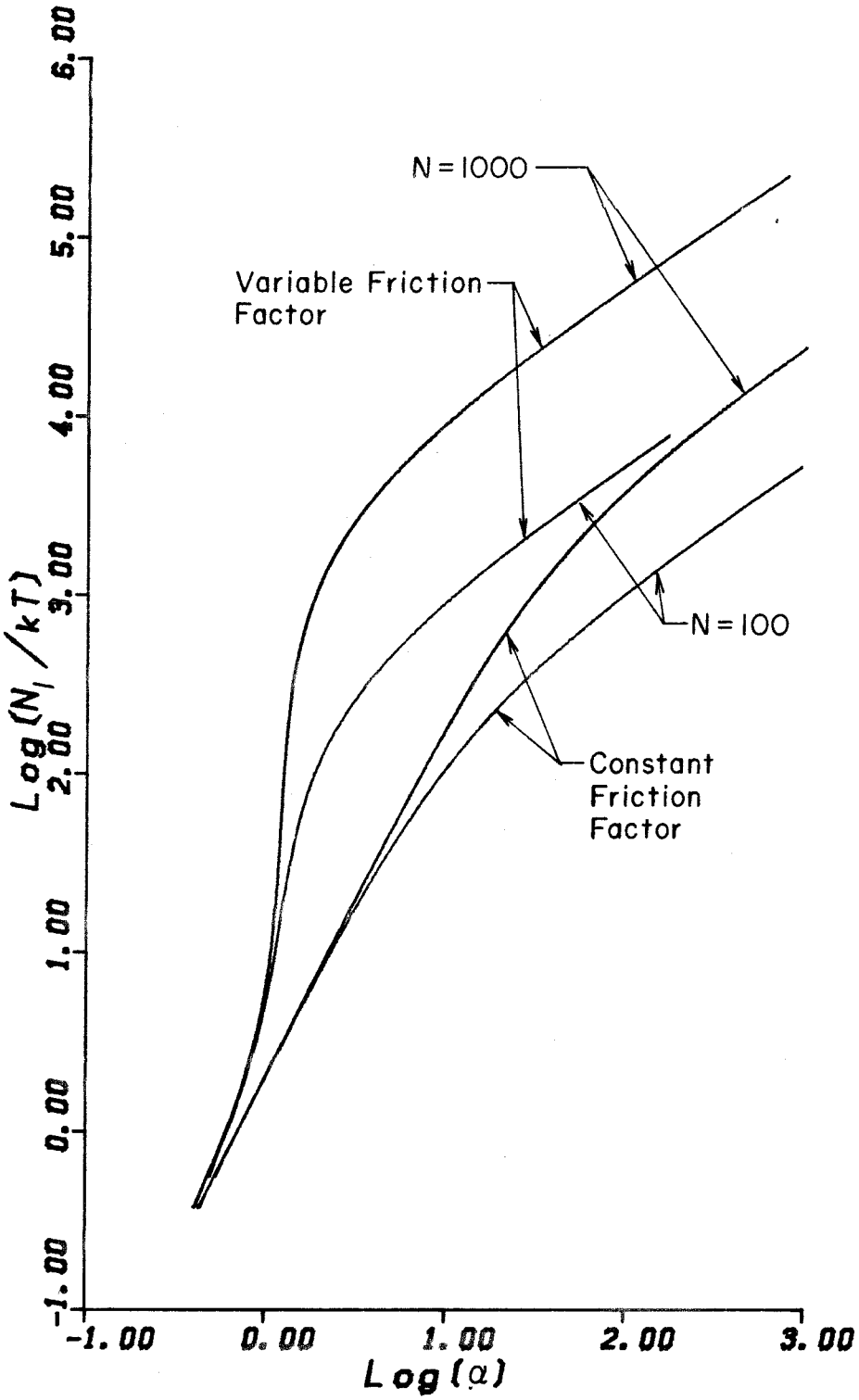
N = 1000
Variable Friction Factor
N = 100
Constant Friction Factor
Log (N_l / kT)
Log (α)
6.00
5.00
4.00
3.00
2.00
1.00
0.00
-1.00
-1.00
0.00
1.00
2.00
3.00

Fig. 9

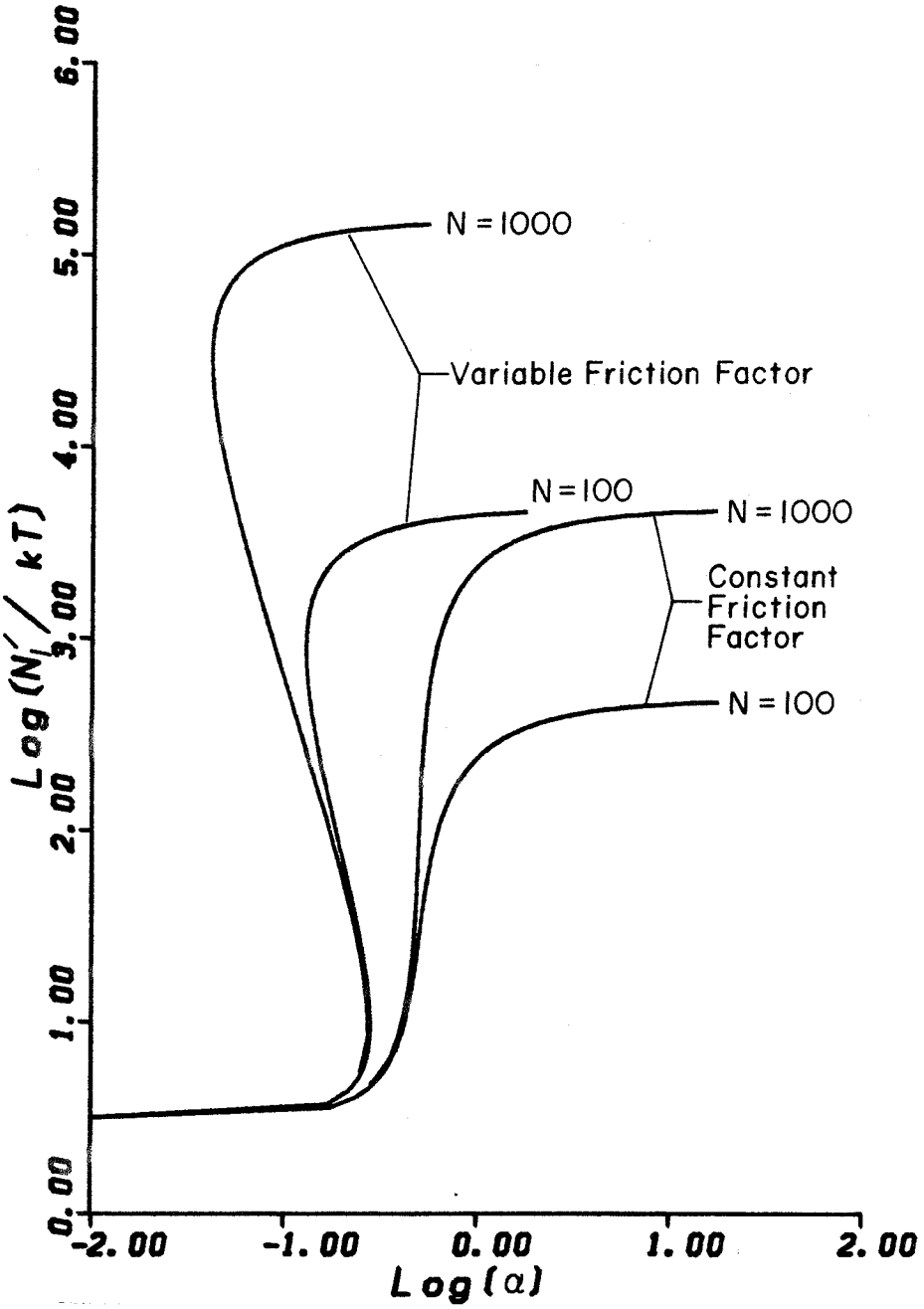
6.00
5.00
4.00
3.00
2.00
1.00
0.00
Log (N'i / kT)
N = 1000
Variable Friction Factor
N = 100
N = 1000
Constant
Friction
Factor
N = 100
-2.00
-1.00
0.00
1.00
2.00
Log (α)

Fig. 10

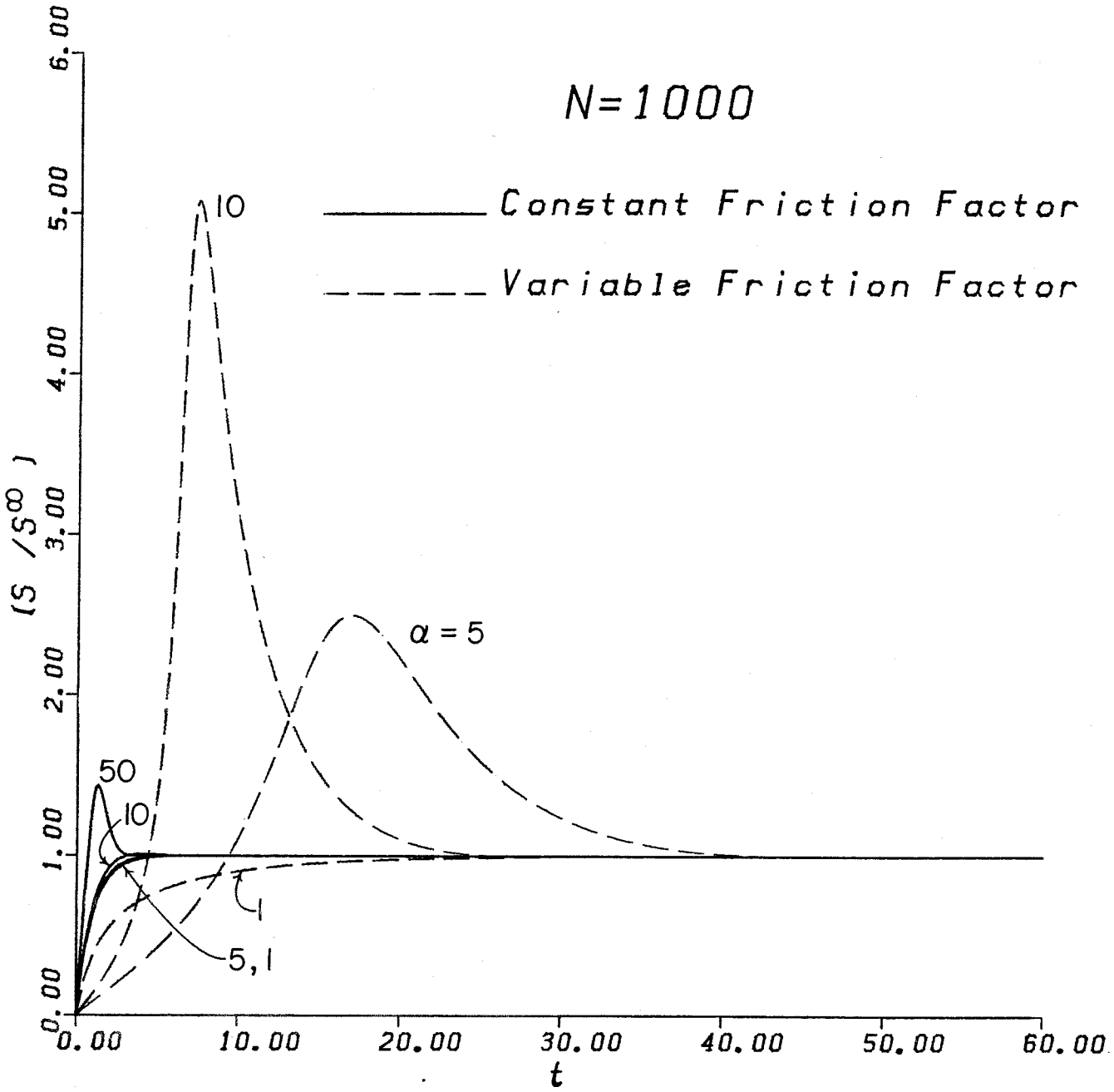
N=1000
Constant Friction Factor
Variable Friction Factor
10
α = 5
50
10
5,1
1
(S /S∞)
0.00
1.00
2.00
3.00
4.00
5.00
6.00
0.00
10.00
20.00
30.00
40.00
50.00
60.00
t

Fig. 11

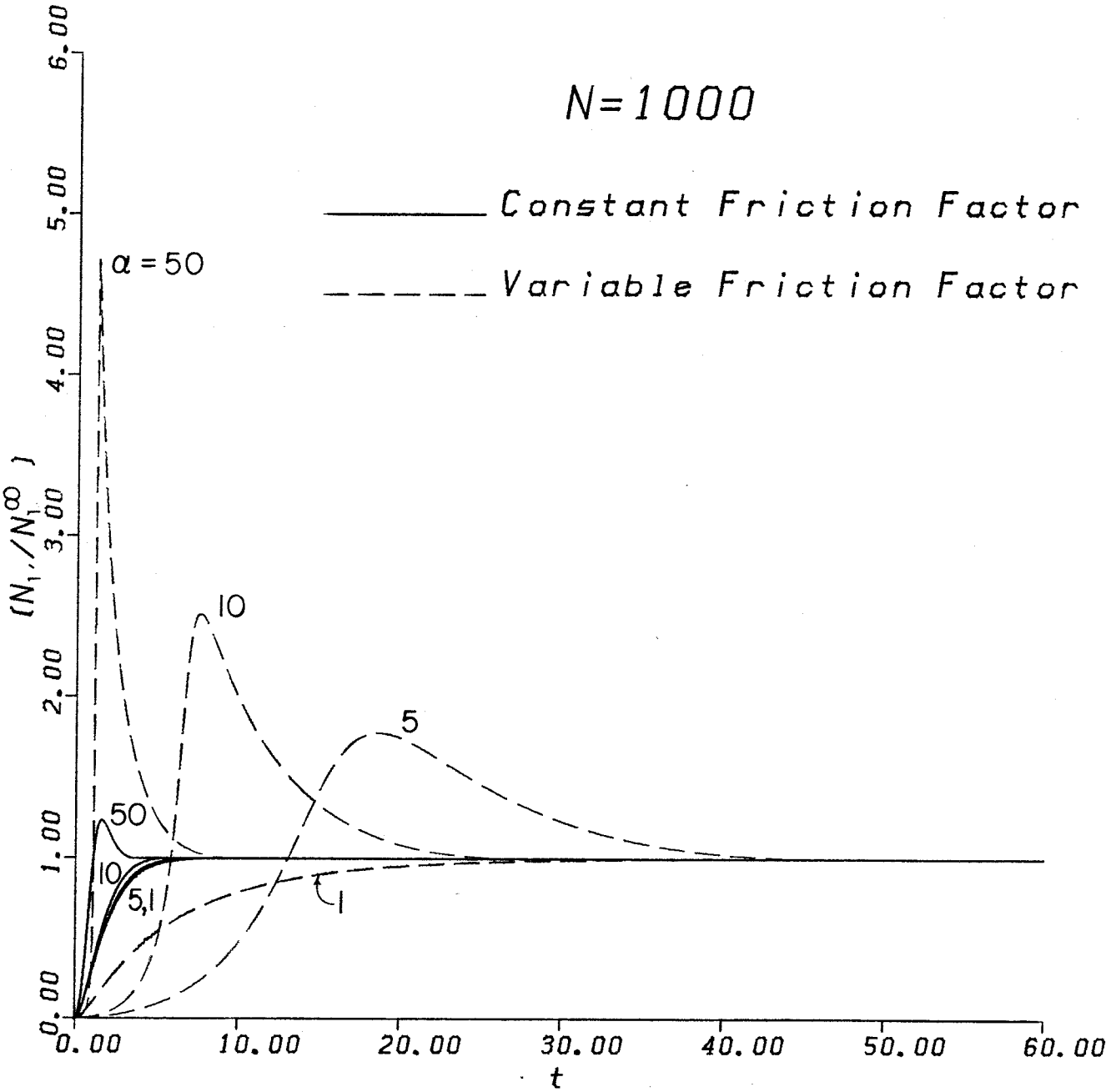
N=1000
Constant Friction Factor
Variable Friction Factor
α=50
10
5
50
10
5,1
1
(N1./N1∞)
t
0.00
1.00
2.00
3.00
4.00
5.00
6.00
0.00
10.00
20.00
30.00
40.00
50.00
60.00

Fig. 12

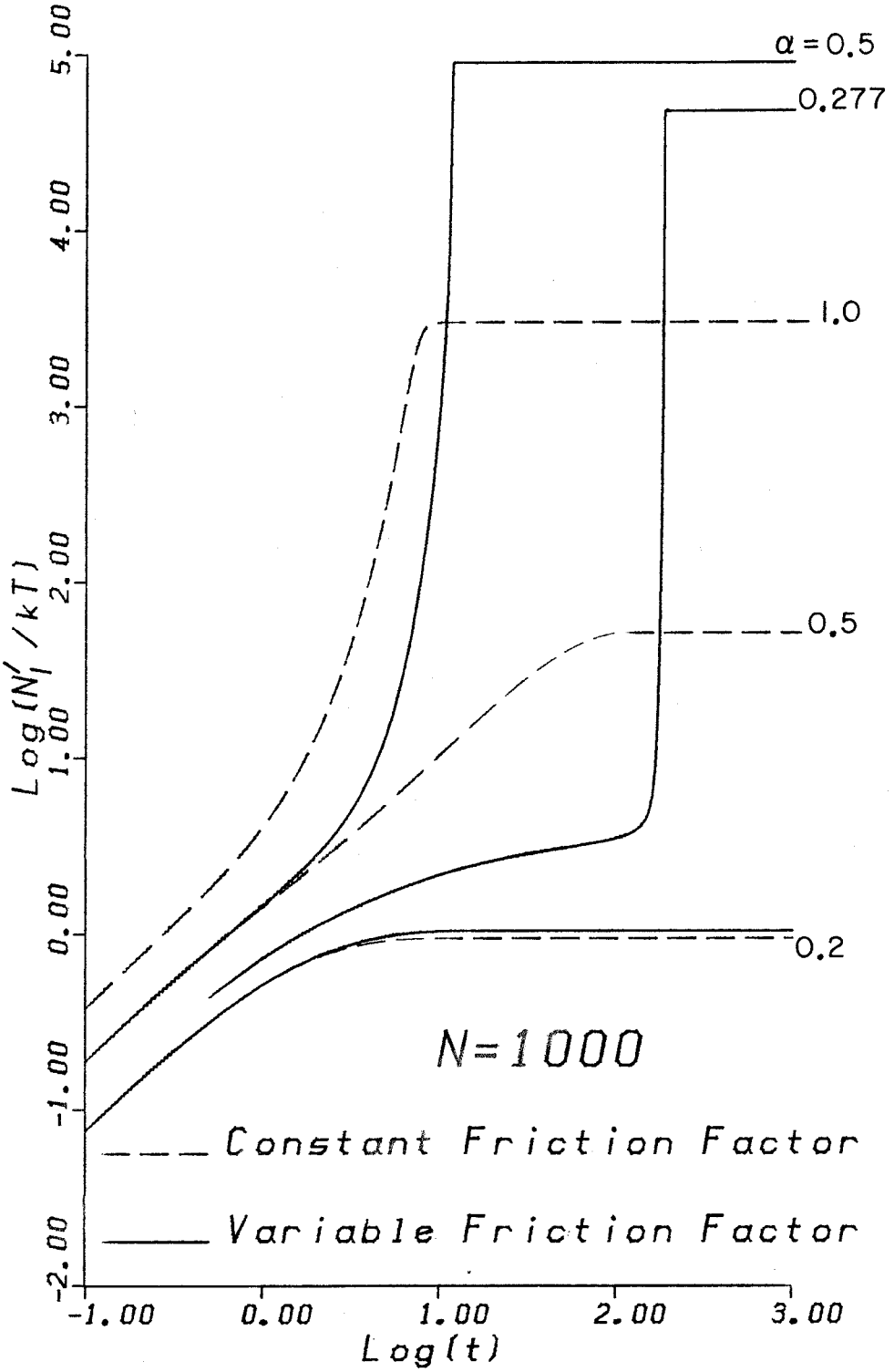
α = 0.5
0.277
1.0
0.5
0.2
N=1000
Constant Friction Factor
Variable Friction Factor
Log(N'l/kT)
Log(t)
5.00
4.00
3.00
2.00
1.00
0.00
-1.00
-2.00
-1.00
0.00
1.00
2.00
3.00

Fig. 13

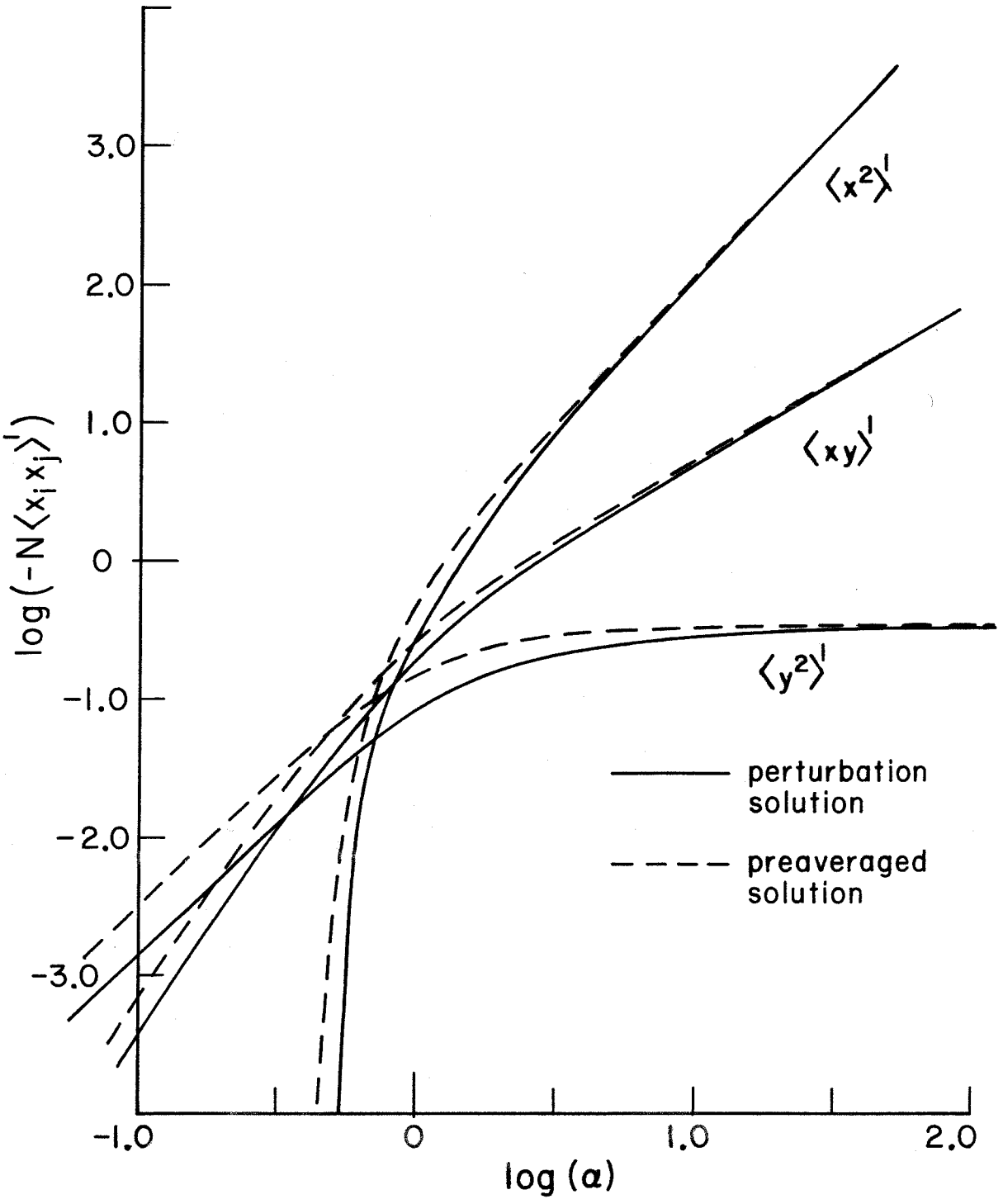
3.0
2.0
1.0
0
-1.0
-2.0
-3.0
log(-N⟨xᵢxⱼ⟩')
⟨x²⟩'
⟨xy⟩'
⟨y²⟩'
perturbation solution
preaveraged solution
-1.0
0
1.0
2.0
log (α)

Fig. 14

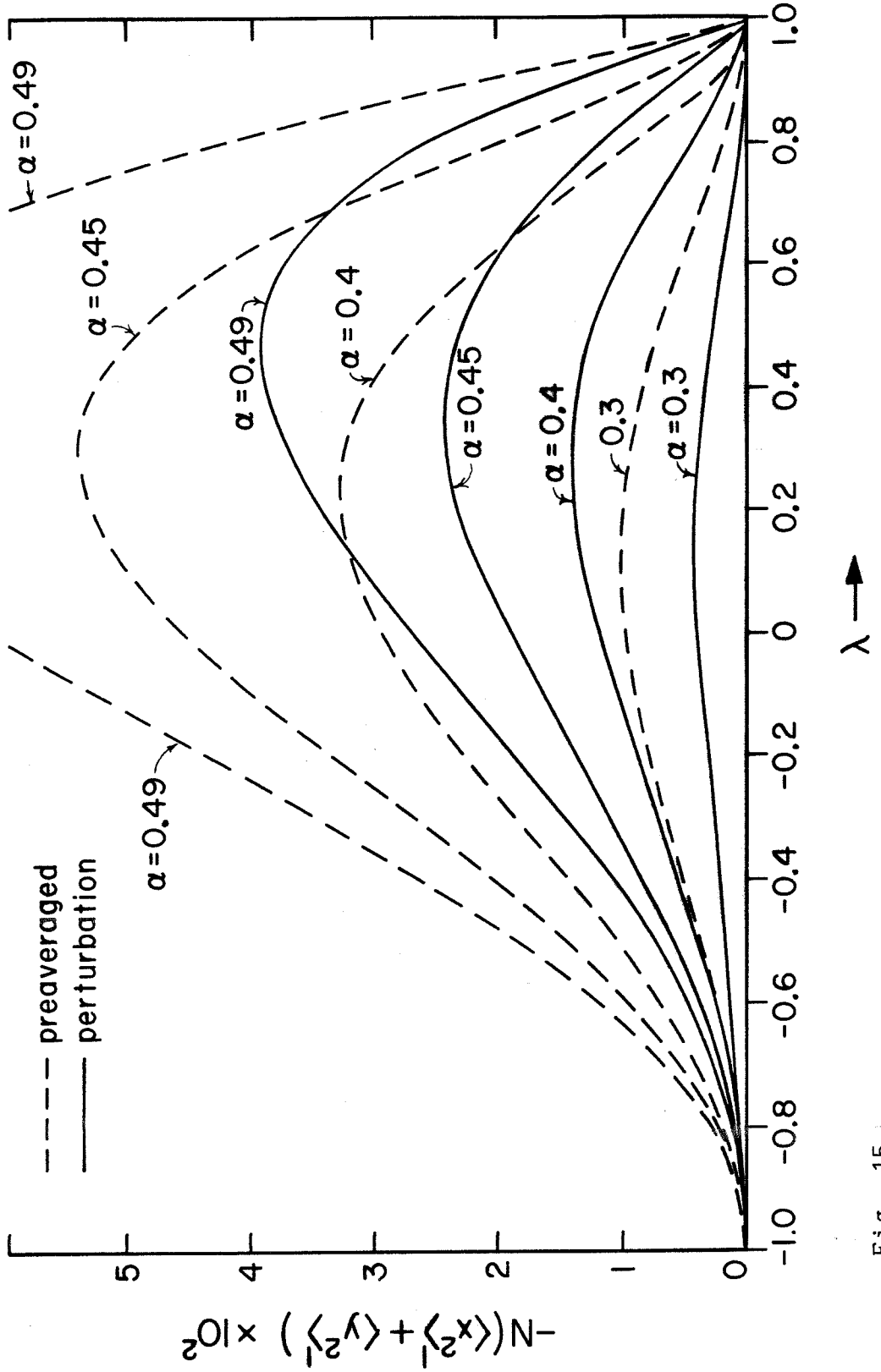
$-N(\langle x^2\rangle' + \langle y^2\rangle') \times 10^2$
5
4
3
2
1
0
-1.0
-0.8
-0.6
-0.4
-0.2
0
0.2
0.4
0.6
0.8
1.0
λ
preaveraged
perturbation
α=0.49
α=0.45
α=0.49
α=0.4
α=0.45
α=0.4
0.3
α=0.3
α=0.49

Fig. 15

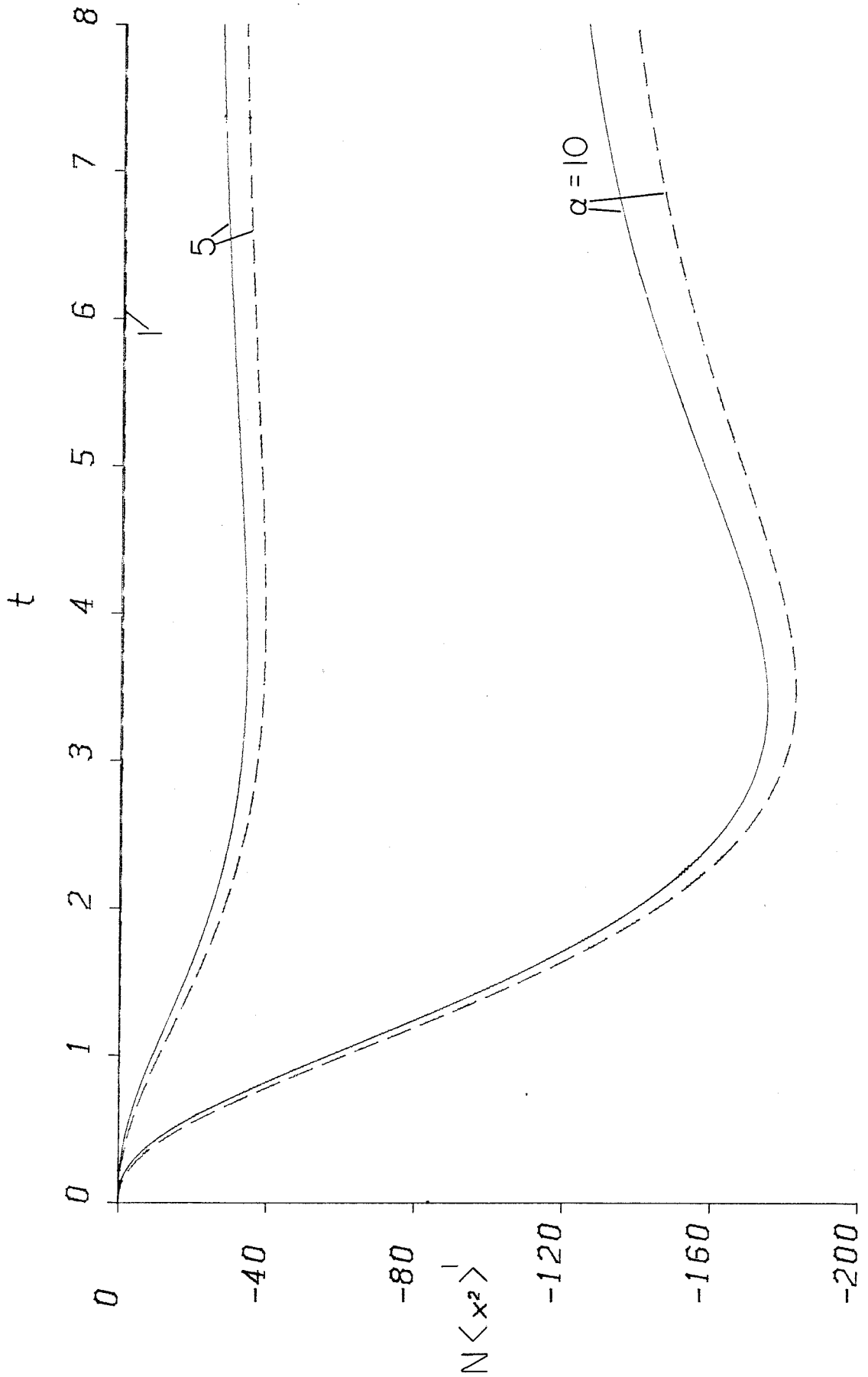

Fig. 16

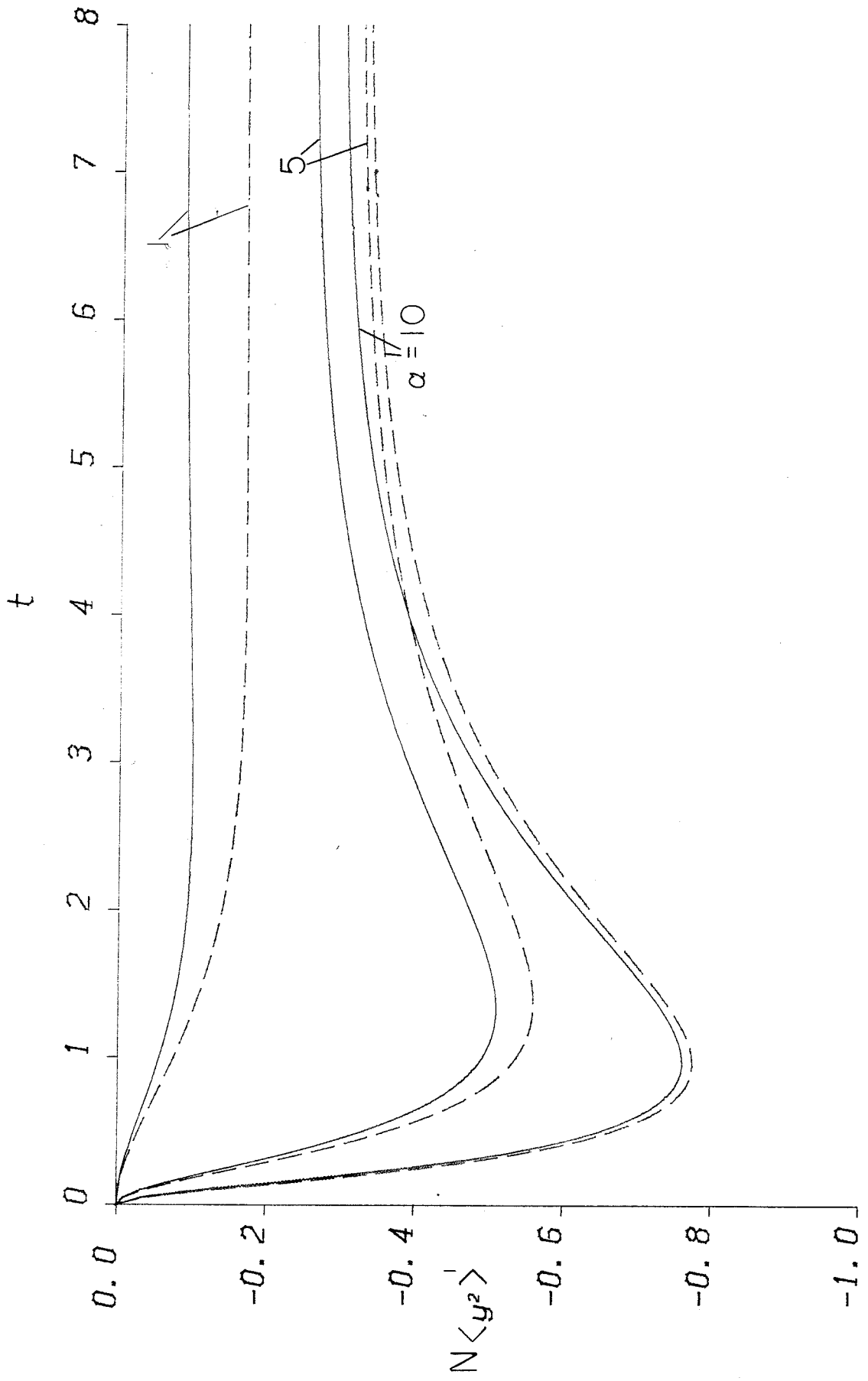

Fig. 17

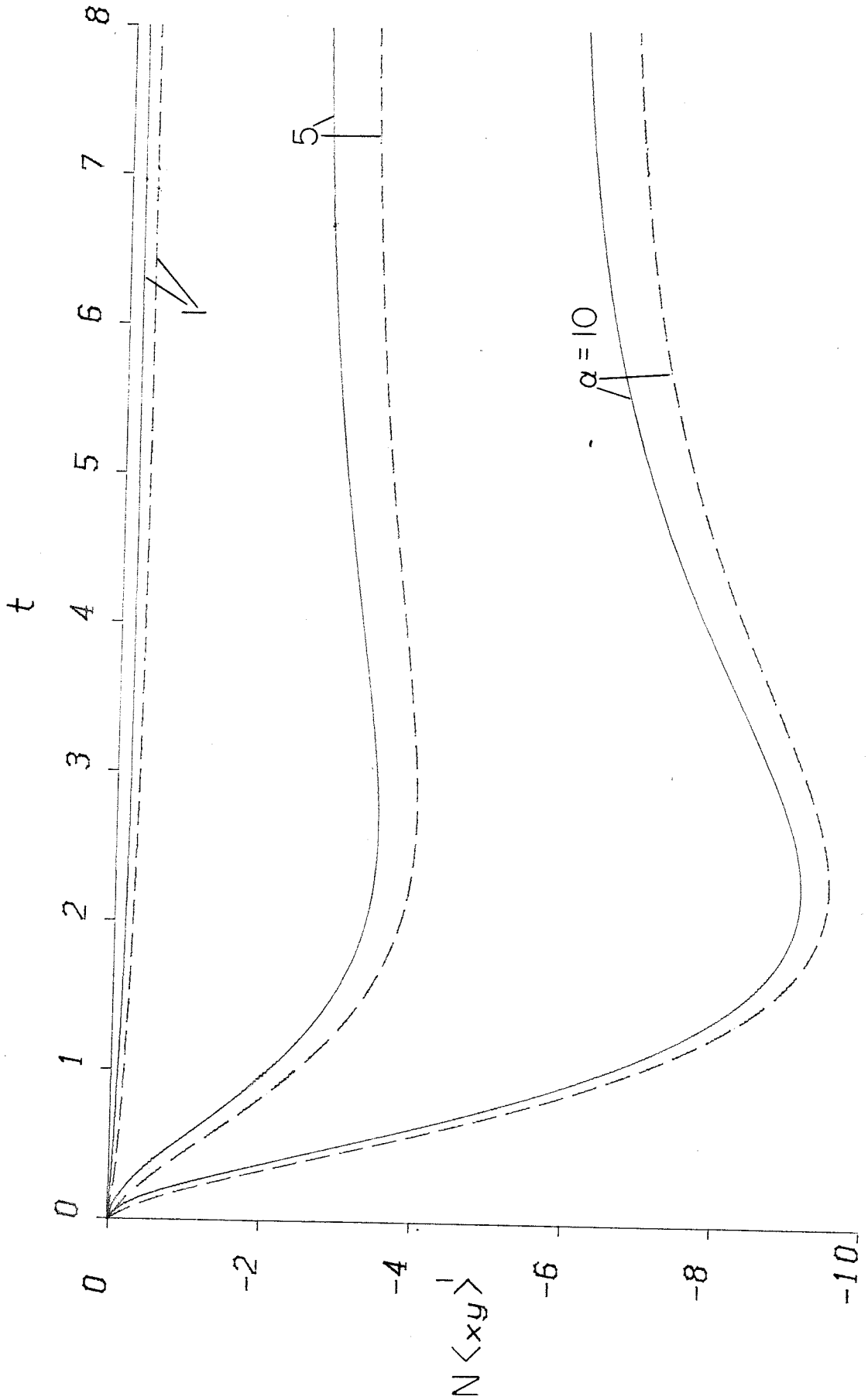

Fig. 18

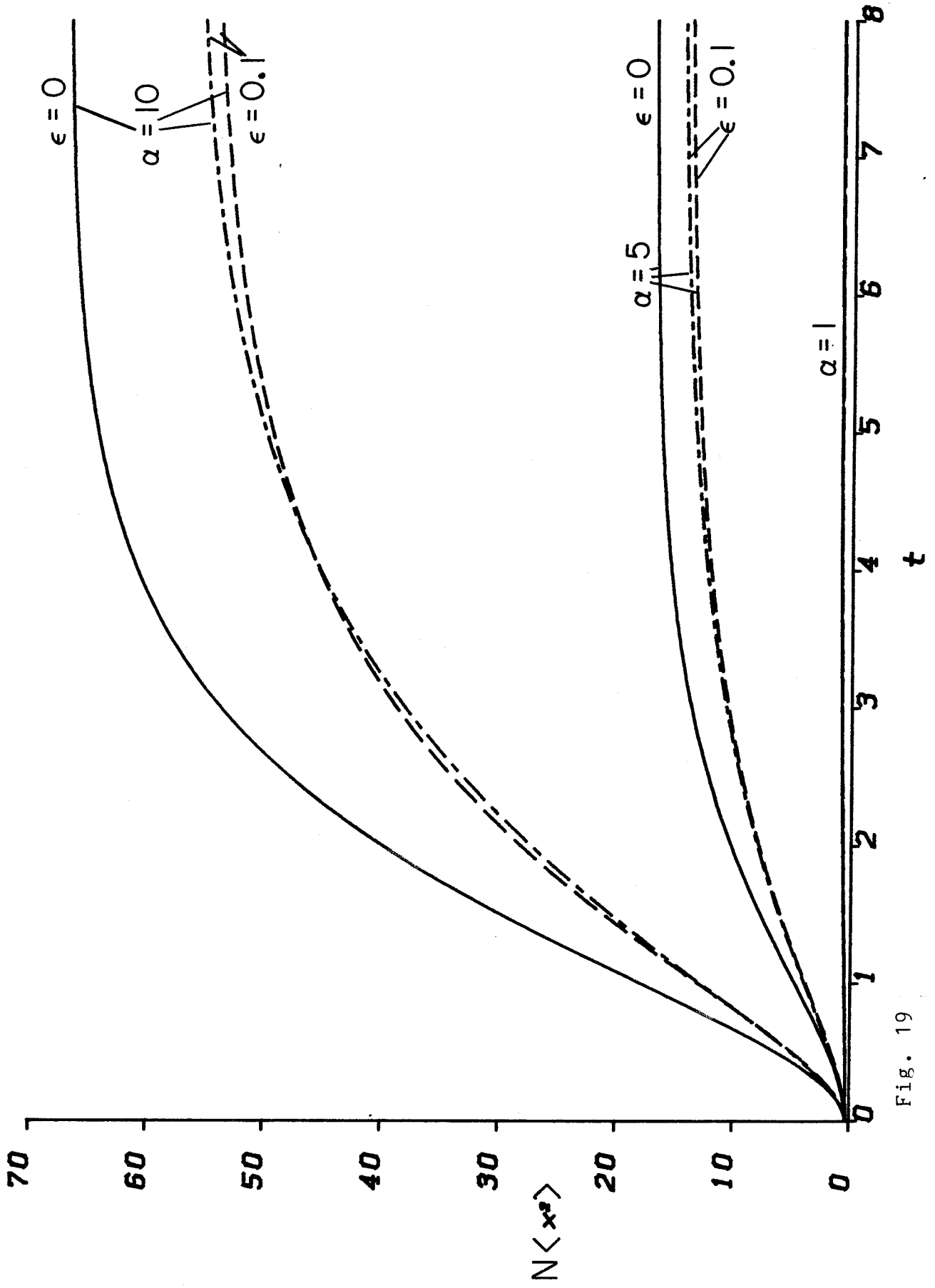

Fig. 19

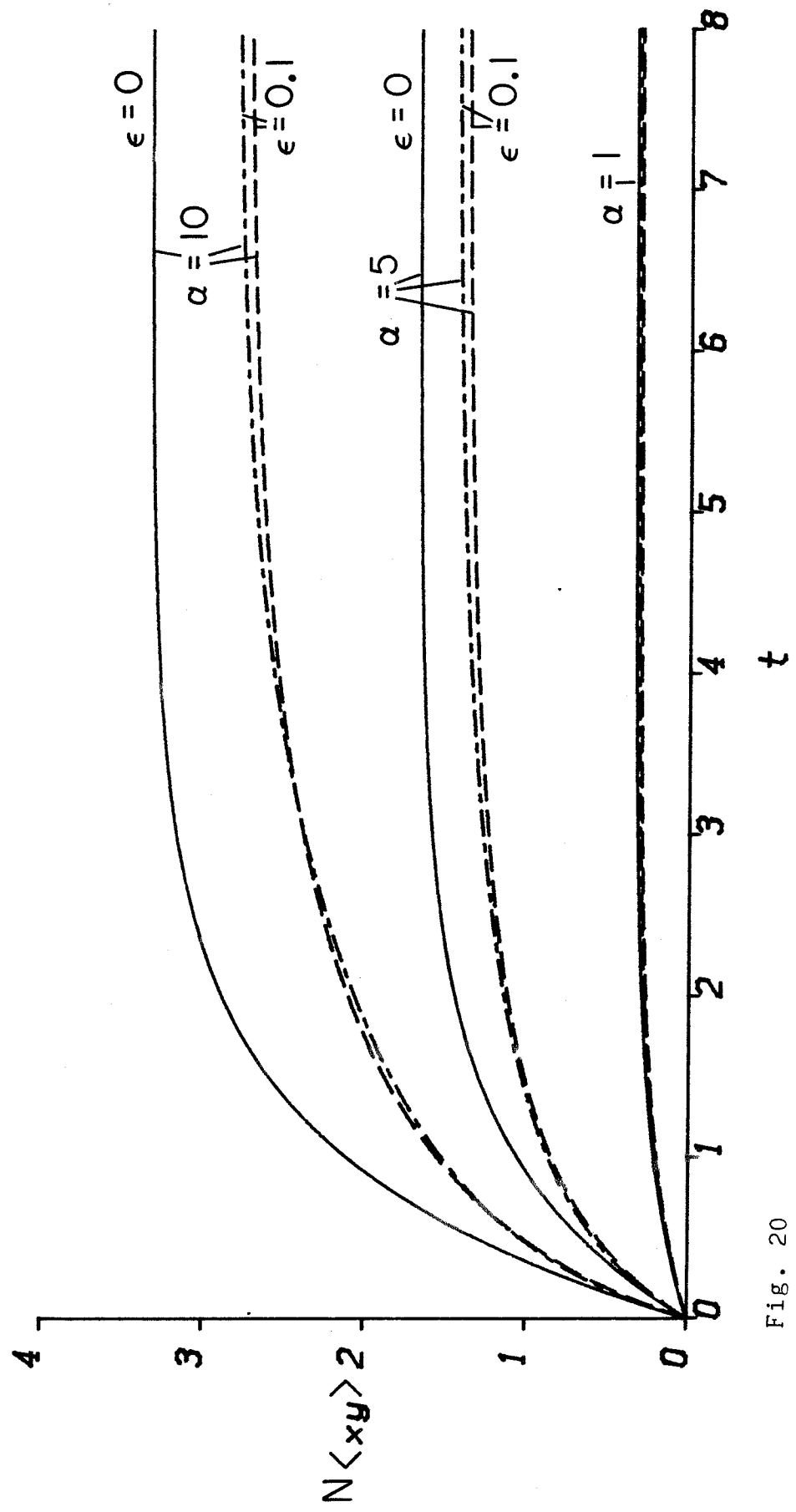

Fig. 20

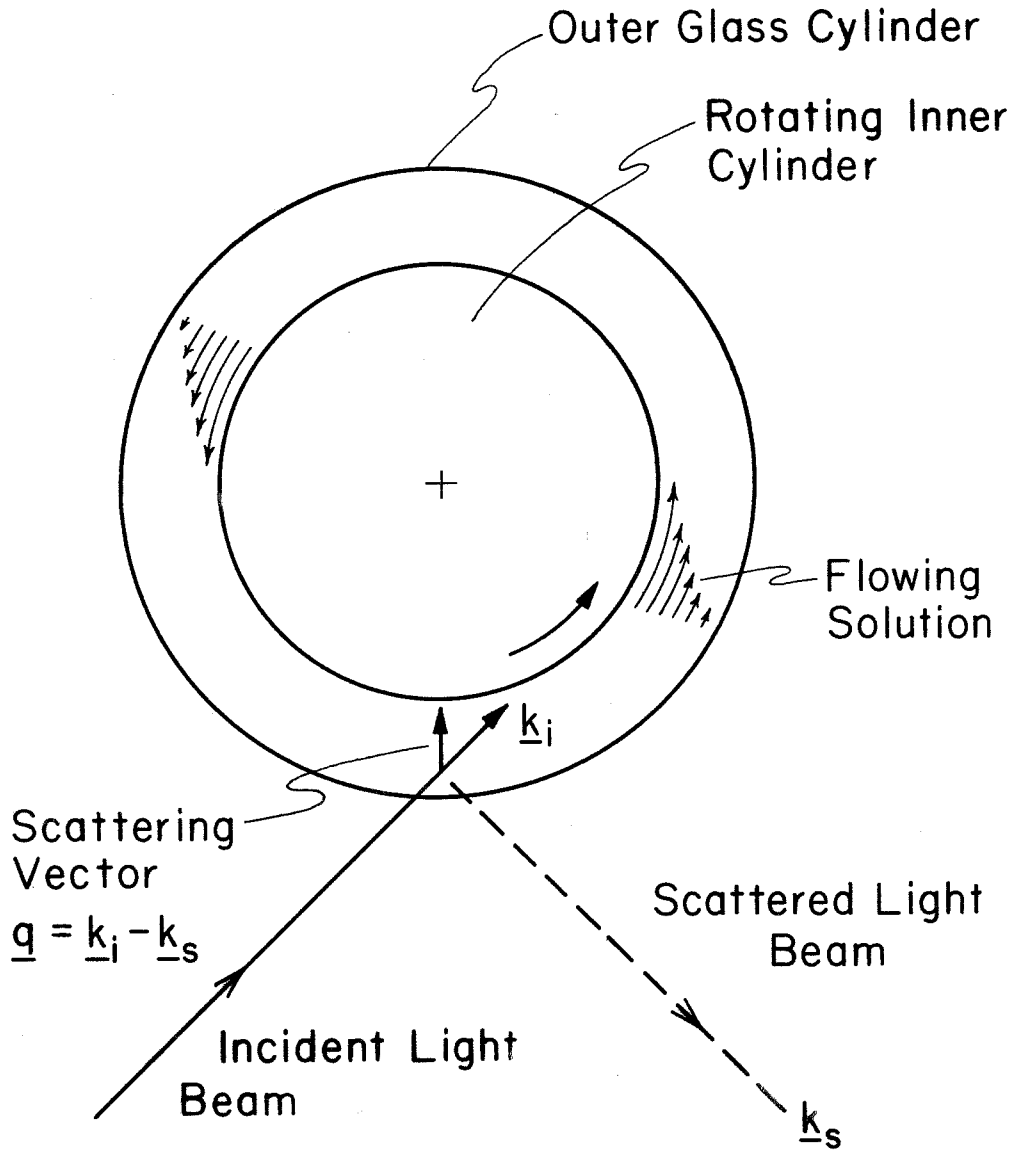
Outer Glass Cylinder
Rotating Inner Cylinder
Flowing Solution
$\underline{k}_i$
Scattering Vector
$\underline{q} = \underline{k}_i - \underline{k}_s$
Scattered Light Beam
Incident Light Beam
$\underline{k}_s$

Fig. 21

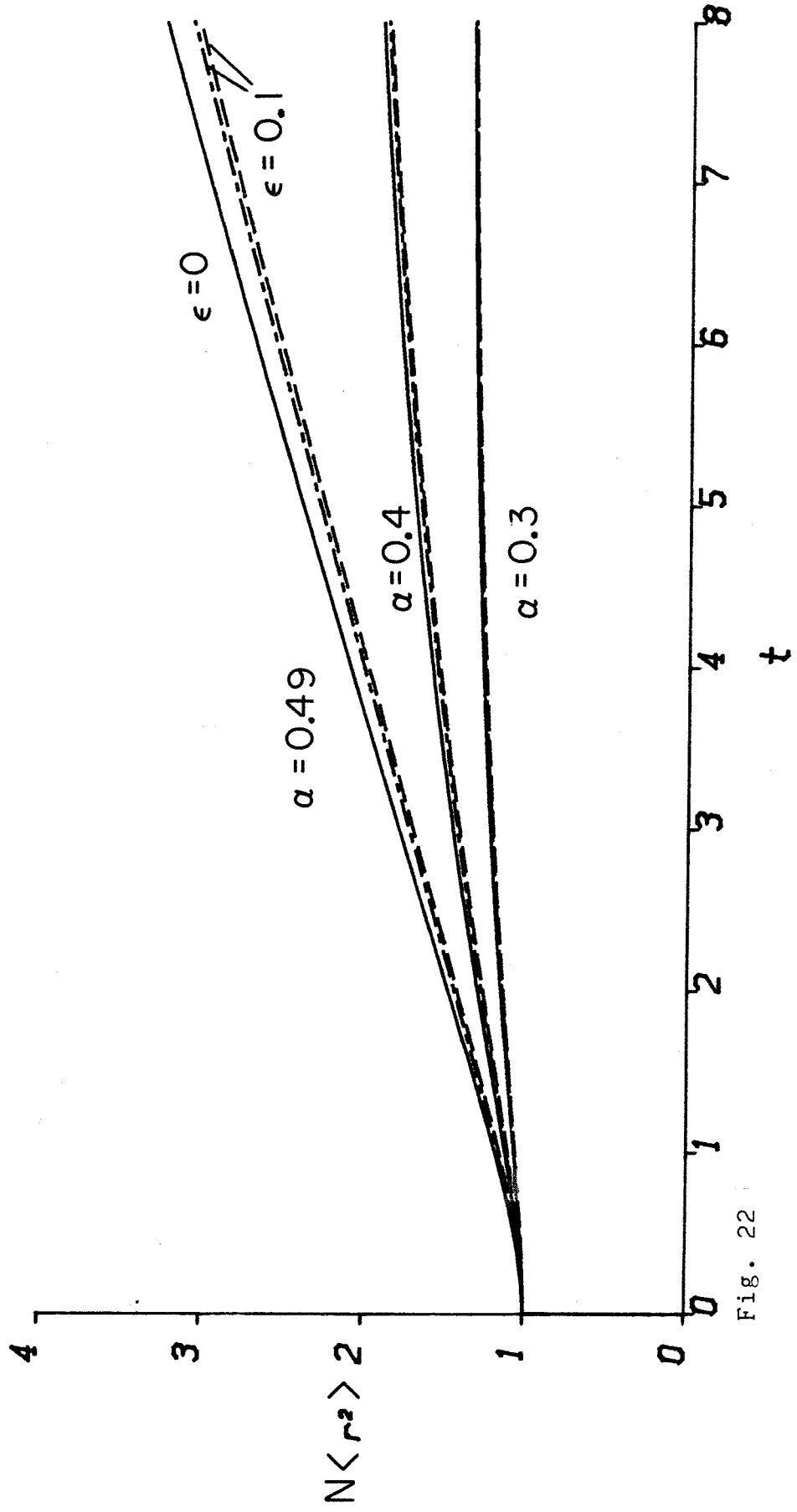

Fig. 22

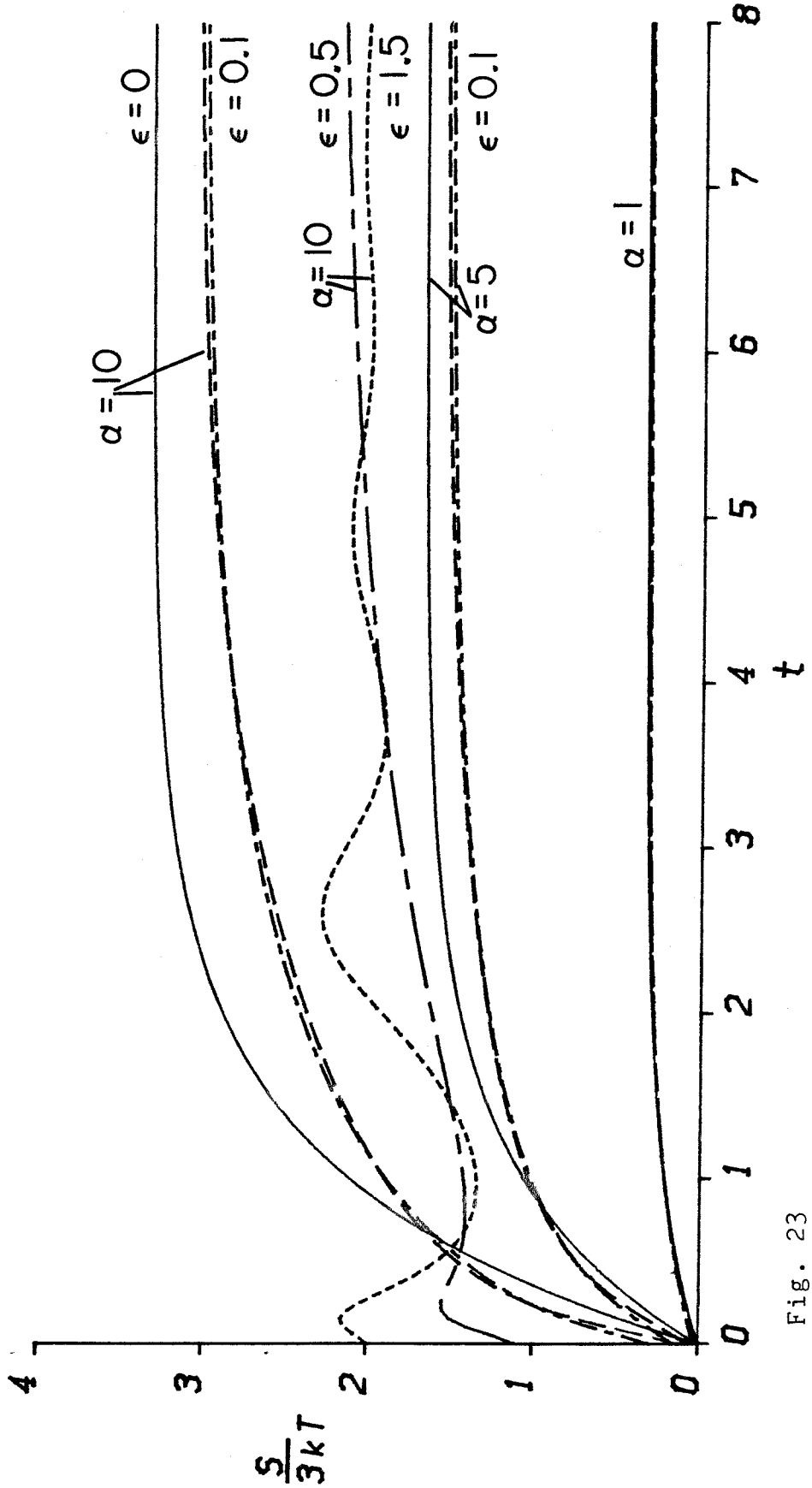

Fig. 23

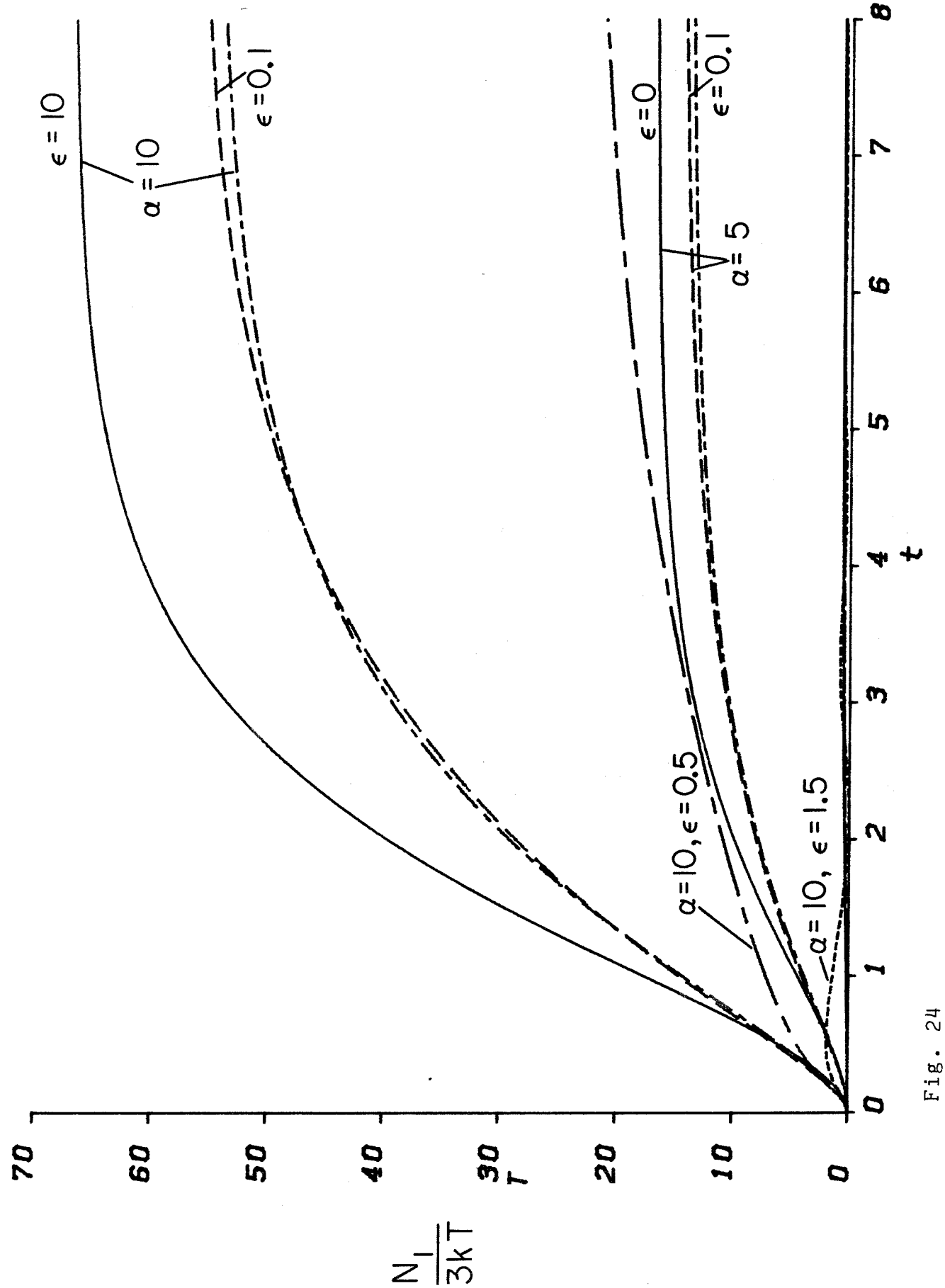
$\frac{N_1}{3kT}$
70
60
50
40
30
20
10
0
T
0
1
2
3
4
5
6
7
8
t
ε = 10
α = 10
ε = 0.1
ε = 0
α = 5
ε = 0.1
α = 10, ε = 0.5
α = 10, ε = 1.5

Fig. 24

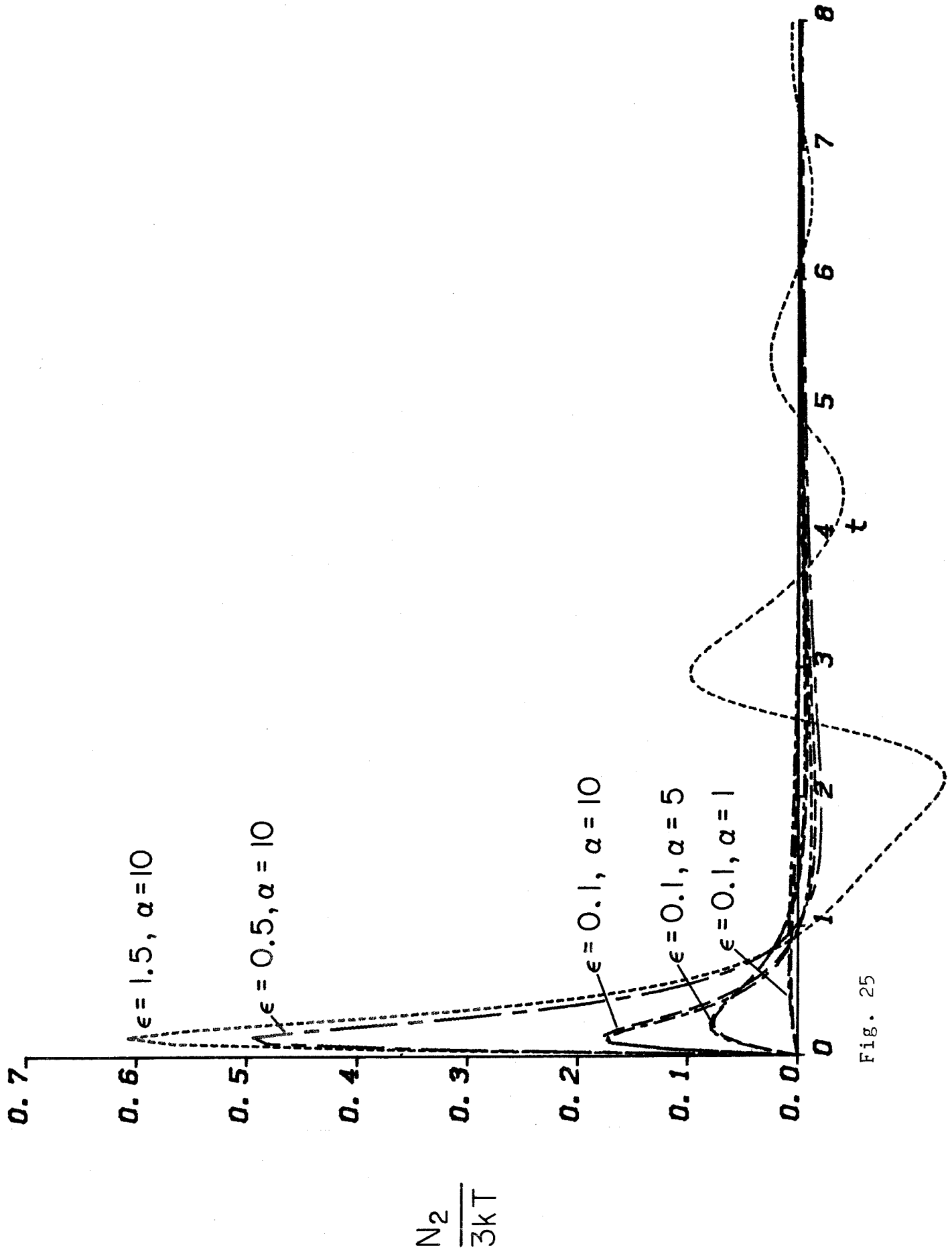
$\frac{N_2}{3kT}$
0.7
0.6
0.5
0.4
0.3
0.2
0.1
0.0
0
1
2
3
4
5
6
7
8
t
ε = 1.5, α = 10
ε = 0.5, α = 10
ε = 0.1, α = 10
ε = 0.1, α = 5
ε = 0.1, α = 1

Fig. 25

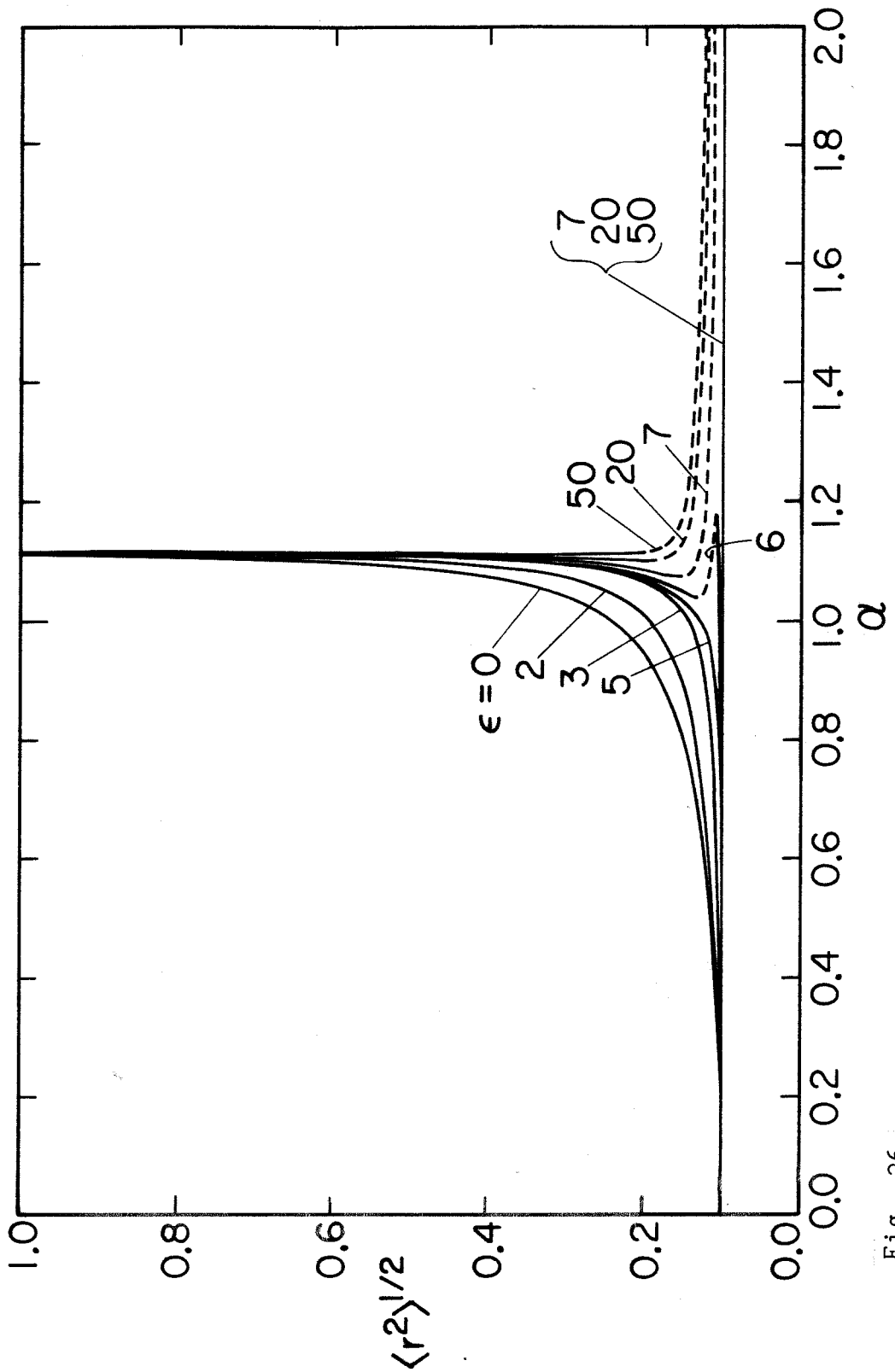
1.0
0.8
0.6
0.4
0.2
0.0
$\langle r^2 \rangle^{1/2}$
0.0
0.2
0.4
0.6
0.8
1.0
1.2
1.4
1.6
1.8
2.0
α
$\epsilon = 0$
2
3
5
6
7
20
50
7
20
50

Fig. 26

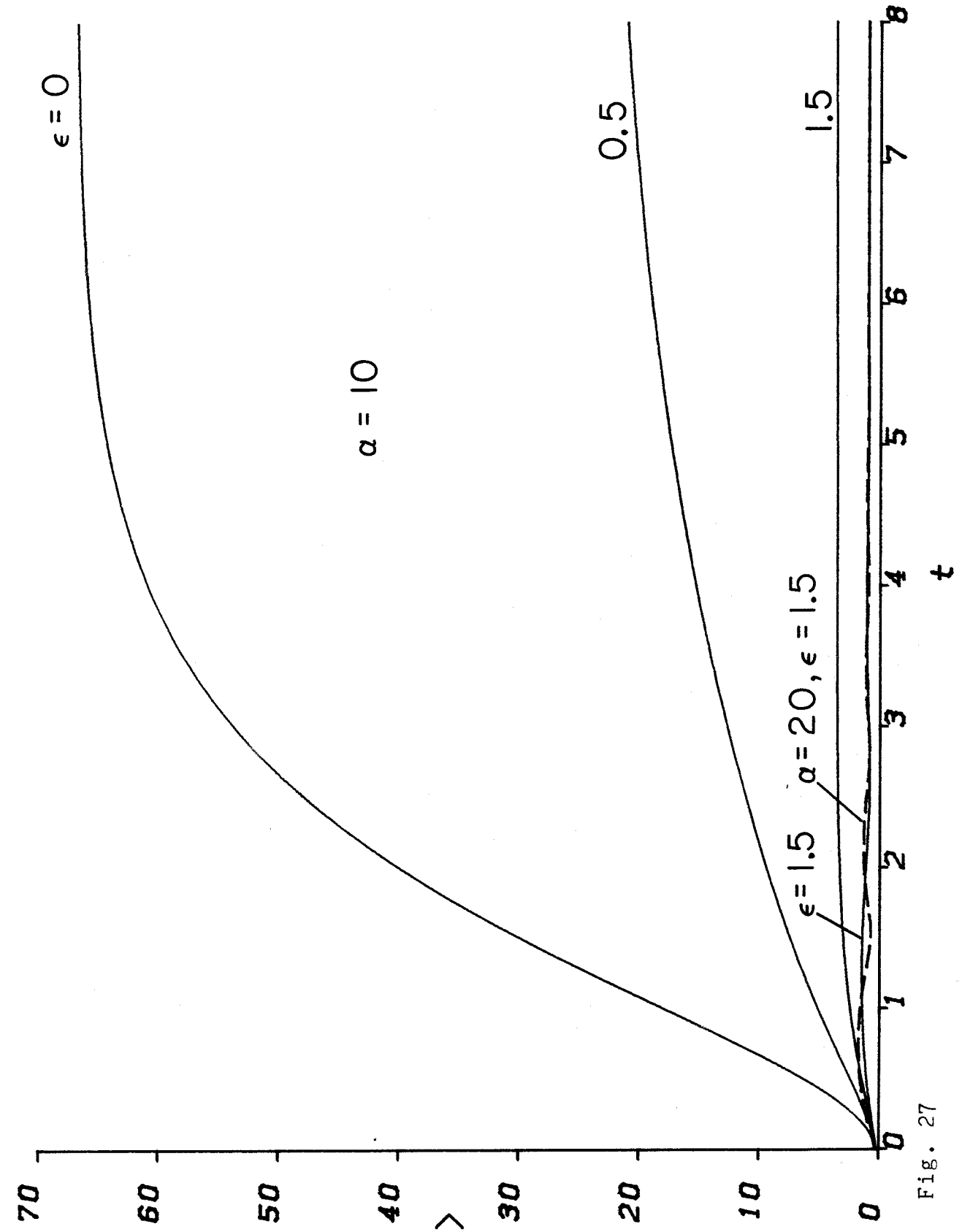

Fig. 27

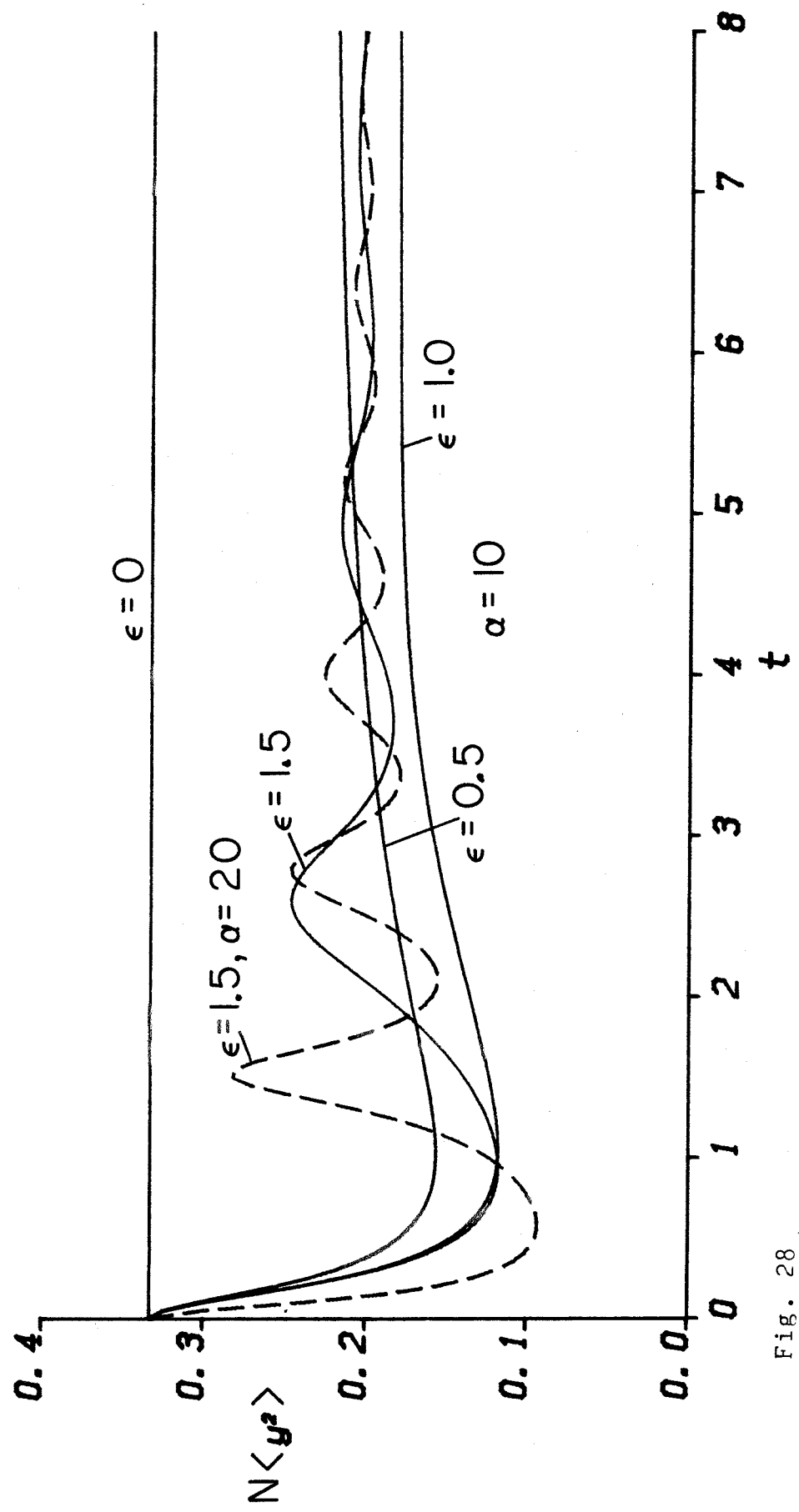

Fig. 28

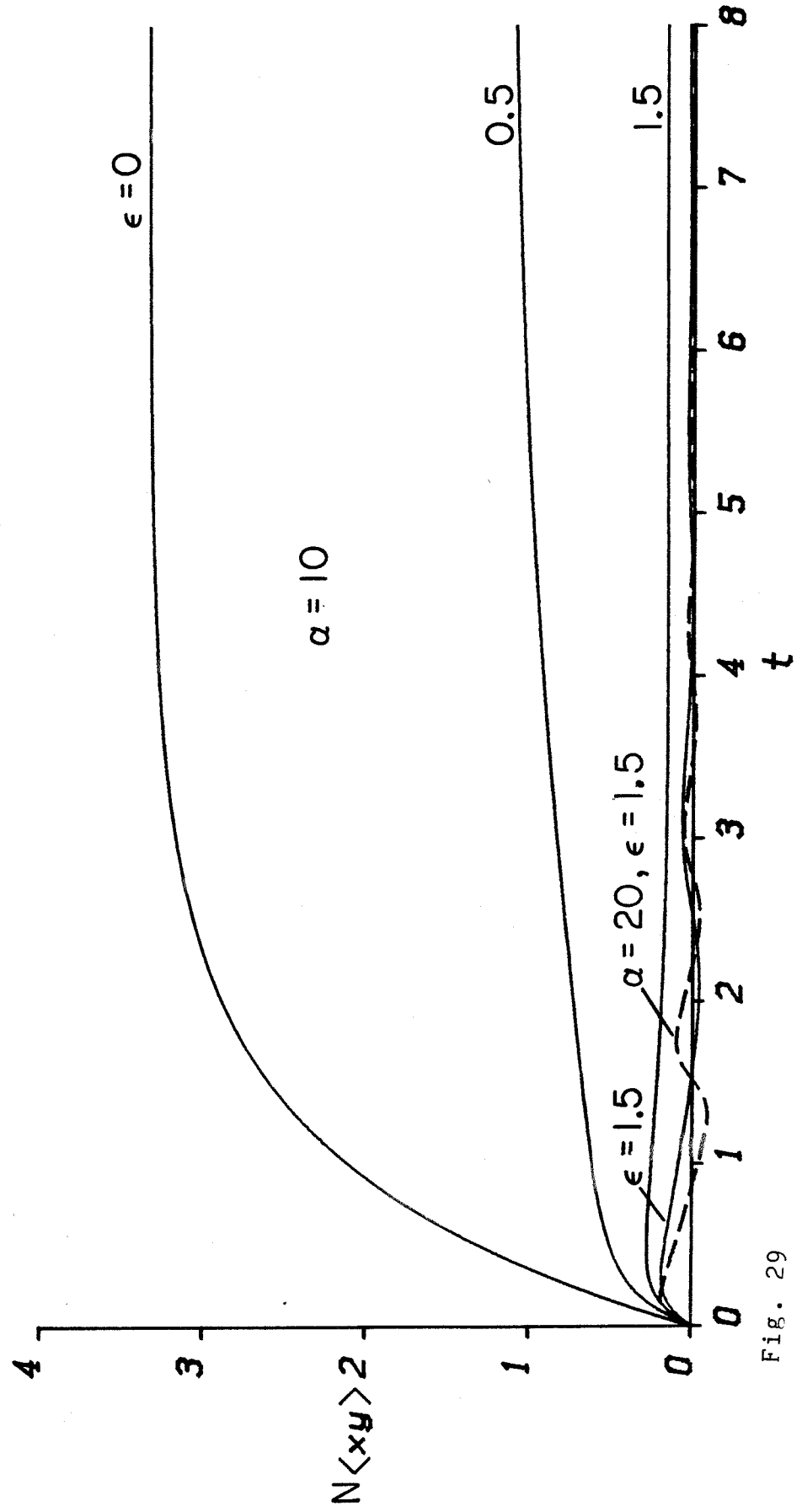

Fig. 29

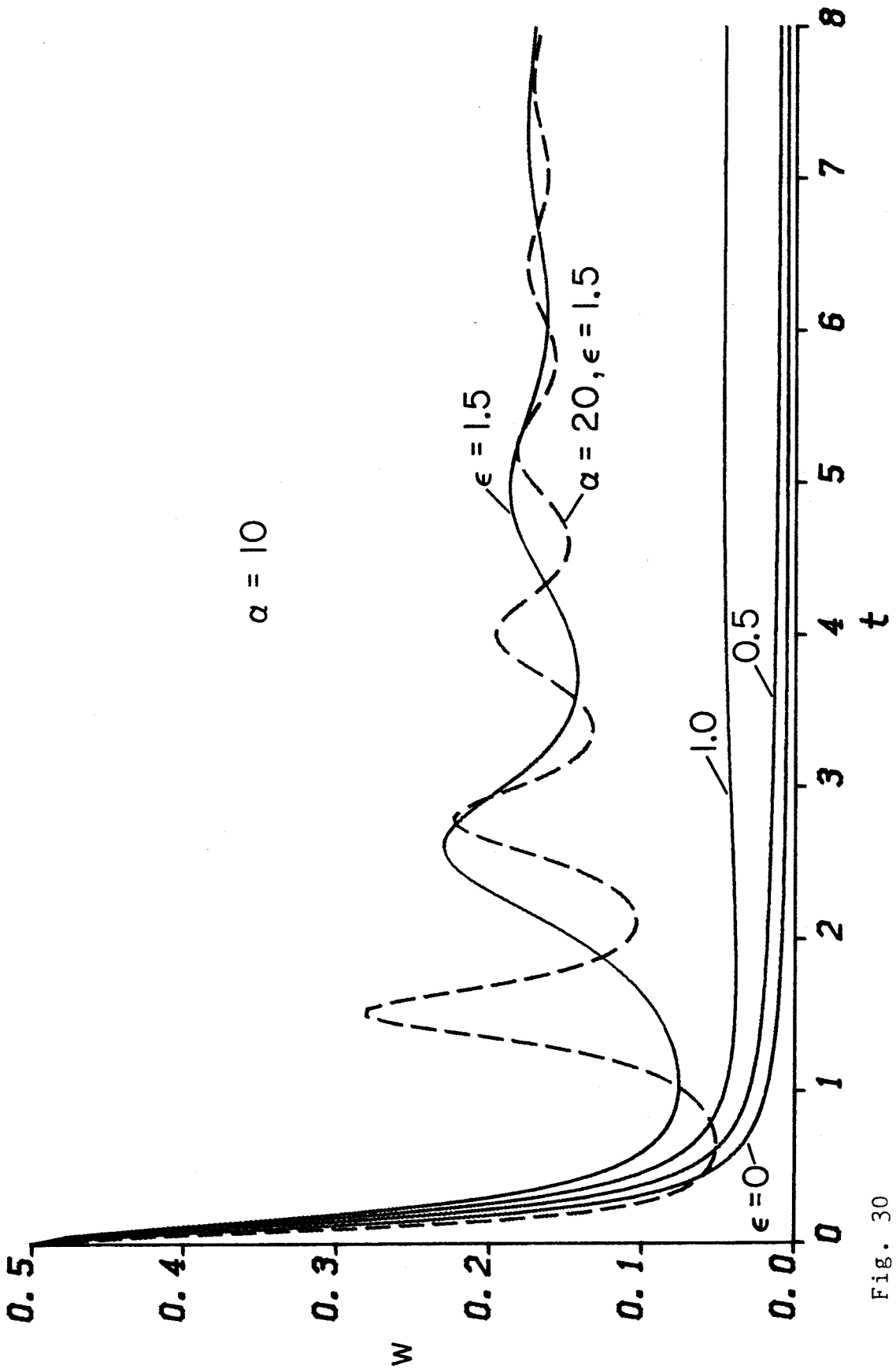

Fig. 30

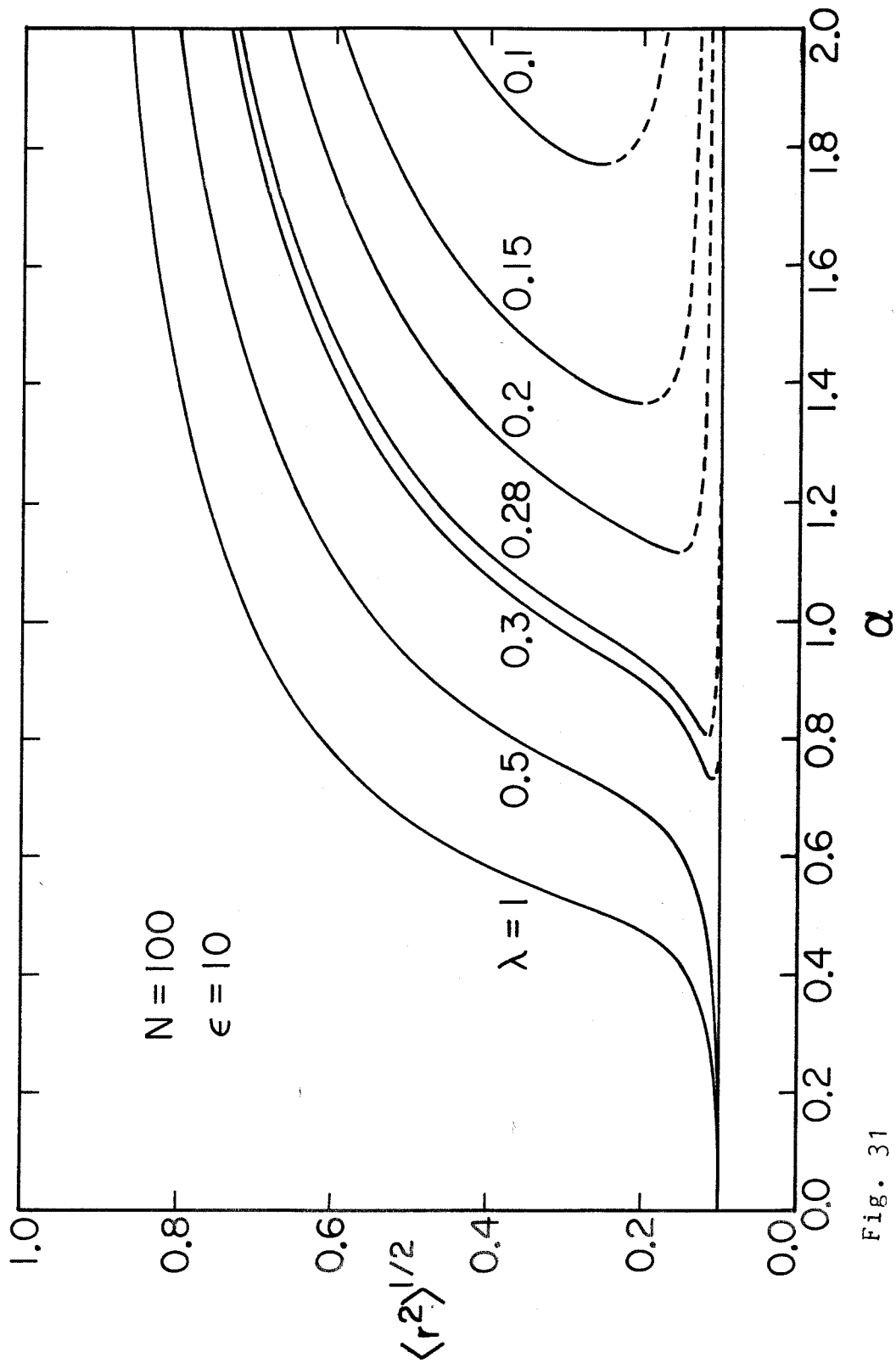
N = 100
ϵ = 10
λ = 1
0.5
0.3
0.28
0.2
0.15
0.1
⟨r²⟩^1/2
α
0.0
0.2
0.4
0.6
0.8
1.0
1.2
1.4
1.6
1.8
2.0

Fig. 31

The Measurement of Velocity Gradients by Homodyne Light Scattering Spectroscopy

by

G. G. Fuller, J. M. Rallison[†], R. L. Schmidt[‡] and L. G. Leal

Department of Chemical Engineering
California Institute of Technology
Pasadena, California 91125

[†]Permanent Address: Department of Applied Mathematics and Theoretical Physics, University of Cambridge.

[‡]Permanent Address: Chevron Oil Field Research, La Habra, California.

ABSTRACT

A technique for measuring of velocity gradients in laminar flows by homodyne light scattering measurements is presented. A theory which describes the light scattering spectrum is derived, and includes the effects of different types of linear flow fields, particle diffusion and the intensity profile in the scattering volume. The conditions which must be satisfied in order that the theory describe the experimental situation are outlined and complementary experiments are performed which both verify the theory and apply the technique. Verification is provided by the flow in a Couette device, and that due to a single rotating cylinder in a large bath of fluid. The technique is then applied to measure the spatial variation of the shear rate in a four roll mill.

I. INTRODUCTION

The development of an accurate experimental method for determination of velocity gradients in a flowing liquid is a problem of obvious practical importance. There is, of course, a variety of experimental techniques to determine the velocity in a flowing fluid, one of the most popular methods being laser doppler velocimetry. The use of laser light as a probe has the distinct advantage that it imparts essentially no disturbance to the velocity field. However, relatively little has been done which addresses the direct determination of velocity gradients.

The usual procedure for measuring velocity gradients using the laser doppler velocimeter (LDV) is to first measure the velocity as a function of spatial position and then differentiate the data. However, this procedure suffers from the inherent difficulties of differentiating experimental data and is particularly suspect in the regions of large velocity gradients which are likely to be of greatest interest. Not only may the region being studied be too thin to allow sufficient spatial resolution of the velocity field for differentiation with any reasonable accuracy [the LDV system yields an average velocity over the scattering volume which is typically about 0.5 mm in linear extent], but the LDV signal is also complicated by a large variation in velocity across the scattering volume and is difficult to interpret. In this paper, we demonstrate how the homodyne mode of light scattering spectroscopy may be used to directly measure the average velocity gradient in the scattering volume from a single in situ experiment, thereby minimizing both of these problems.

The paper consists of two main parts. In the first, we present the

theoretical developments which are necessary to determine the local velocity gradient from the homodyne spectrum of light scattered from small particles which are immersed in a flowing liquid. In the second, we report complementary experimental results which verify the method and illustrate its application. A primary objective of both the analysis and the experiments is to delineate the conditions which must be satisfied in order that the measurement of velocity gradients by homodyne light scattering be accurate and unambiguous. For this reason, our theoretical analysis considers not only the effect of a velocity gradient (and the corresponding variation in particle velocity across the scattering volume) on the observable frequency spectrum, but also the effects of different types of laminar motion, of variations in the light intensity profile of the incident beam in the scattering volume, and of random, diffusive motions of the scattering particles.

II. Theory

We consider the light scattered by small particles which are immersed in a liquid that is undergoing an arbitrary steady, laminar motion. The light scattering experiment is sketched in figure 1. The incident light is a single, monochromatic beam which is generated by a laser source, and the scattered light is viewed by a square-law detector (in our case, a photomultiplier tube) through two pinholes which serve to collimate the scattered beam, and thus define the extent of the scattering volume. The particles are assumed to be rigid, and small enough that their mean translational velocity is indistinguishable from the 'undisturbed'

velocity of the suspending liquid. Furthermore, they are assumed to be present at low concentration so that they neither alter the motion of the suspension as a whole, nor contribute to a significant level of multiple scattering events. Finally, the Rayleigh-Debye condition (Berne and Pecora 1976) is assumed to be satisfied, which requires an upper bound of $\lambda/4\pi|m - 1|$ on the average particle dimension, where λ is the wavelength of the incident light and m is the ratio of the solvent refractive index to that of the particles.

The frequency spectrum of the scattered light from the scattering volume V is determined by the motions of the scattering elements (both random and deterministic). By measuring the spectrum of the scattered light mixed with the incident light (heterodyne mode) it is possible to determine the mean velocity of the scattering centers in the scattering volume (Edwards et al. 1971). The effect of velocity gradients and of random motions due to diffusion is to broaden the heterodyne spectrum, but these are second-order effects compared to the doppler shift of the frequency which is caused by the mean motion of the particles in suspension.

The present paper is concerned with the frequency spectrum of scattered light when it is "mixed with itself" (i.e. the so-called homodyne mode). In this case, it will be seen that the effect of the mean velocity on the frequency correlation function can be neglected, relative to the effects of differences in the mean velocity across the scattering volume or of particle diffusion, provided only that the time scales associated with the mean velocity gradient, or with diffusion on the length scale $|\underline{q}|^{-1}$ (see, for example, figure 1) are sufficiently short

compared to the transit time of a particle across the scattering volume. In these circumstances, we shall see that the homodyne scattering experiment provides a direct measurement of either the mean velocity gradient or of the particle diffusivity, depending upon which of these dynamical processes is characterized by the shorter time scale.

The scattered light spectrum for the heterodyne mode is given by the heterodyne correlation function, F_1, which, in the time domain has the form (Berne and Pecora, 1976)

$$F_1(\underline{q},t) = \sum_{j=1}^{N} \left\langle E_j^*(0)E_j(t)e^{i\underline{q}\cdot\left[\underline{r}_j(t) - \underline{r}_j(0)\right]} \right\rangle . \qquad (1)$$

Here, $\underline{q}$ is the scattering vector which is defined in figure 1, $E_j(t)$ is the amplitude of the light scattered by particle j and $\underline{r}_j(t)$ is the position of the centroid of particle j with respect to an arbitrary origin in the scattering volume. The summation is over all particles in the scattering volume for a given realization of the scattering experiment and the angle brackets represent an ensemble average over many realizations.

Provided that the contribution of each particle to the scattered light is statistically independent of the other and randomly distributed, it may be shown (Berne and Pecora, 1976) that the homodyne spectrum, F_2, is related to the heterodyne spectrum by

$$F_2(\underline{q},t) = |F_1(\underline{q},t)|^2 \qquad (2)$$

It can be shown that this relation is also valid for the case of flowing particles where the deterministic motions dominate those due to random processes provided the time scale associated with the decay of the heterodyne

correlation function is sufficiently short compared to the reciprocal of the local velocity gradient γ^{-1}. This condition ensures that during the time scale of the experiment, any two particles will be statistically independent allowing the homodyne correlation function to be factored into the square modulus of the heterodyne correlation function as in equation (2). This condition is almost always satisfied under normal laboratory conditions. Thus, we shall first analyze the heterodyne spectrum via equation (1), and then use (2) to calculate the corresponding homodyne spectrum.

Equation (1) can be simplified if the amplitude function $E_j(t)$ and the phase factor $\exp\left(i\, \underline{g}\cdot[\underline{r}(t) - \underline{r}(0)]\right)$ vary on sufficiently different time scales. For spherical, optically homogeneous particles the amplitude function varies principally with the transit time of a particle across the scattering volume. If the particles are optically or geometrically anisotropic, the amplitude function will also vary on the additional time scale associated with particle rotation. However, we shall focus our attention for the moment on the simpler case of particles which are isotropic scatterers and return to the question of anisotropy at the end of the section. Thus, the amplitude factor will be assumed to vary on the transit time scale

$$\tau_t = L/U \tag{3}$$

where L is a length scale characteristic of the scattering volume, and U is the mean particle velocity in the volume. The phase factor, on the other hand, varies principally on the shortest of the possible time scales which is characteristic of particle displacement over a length scale, $|\underline{g}|^{-1}$. As we shall show later, this is usually

$$\tau_s \equiv (q\gamma L \cos\phi)^{-1} , \tag{4}$$

which is inversely proportional to the magnitude of the local velocity gradient. Here, ϕ is the angle between the scattering vector, $\underline{q}$, and the local mean velocity vector, $\underline{v}$. In order to minimize τ_s, this angle will normally be set to zero in the present application. Now, a typical magnitude for $|\underline{q}|$ is 10^5 cm^{-1}. Thus, by controlling the size of the scattering volume, L, the time scale, τ_s, of variations in the phase factor of (1) can be made quite short [say, $O(10^{-2})$ or smaller] relative to the time scale τ_t, of variations in the amplitude factor for most systems. We shall therefore assume the condition

$$\tau_t/\tau_s = q\gamma L^2/U >> 1 \tag{5}$$

to hold, thus implying that the particle moves only a short distance relative to L on the time scale τ_s. Under these circumstances, the amplitude factor in (1) is essentially constant over the time scale for decay of the correlation function (i.e. τ_s), and equation (1) can be approximated in the simpler form

$$F_1(\underline{q},t) = \sum_{j=1}^{N} I_j \left\langle e^{i\underline{q}\cdot[\underline{r}_j(t) - \underline{r}_j(0)]} \right\rangle = \sum_{j=1}^{N} I_j F_{sj}(\underline{q}t) \tag{6}$$

where $I_j \equiv \langle E_j(0)^* E_j(0) \rangle$ is the intensity of light scattered by particle j and F_{sj} is the so-called self-intermediate scattering function. We may note that for intermediate values of τ_t/τ_s, i.e. $\lesssim 1$, the phase and amplitude factors in (1) vary on comparable time scales, and experimental analysis of the frequency spectrum is impractical except in the opposite limit $\tau_t/\tau_s << 1$, where measurement of $F_1(\underline{q},t)$ corresponds to the single

beam velocimeter, described by Pike (1976).

We shall restrict our attention in the present communication to the limiting case (5) where the approximation (6) is valid. Further analysis of the correlation function thus reduces to a determination of the self-intermediate scattering function, $F_{sj}(\underline{q},t)$. This analysis is facilitated by first solving for the Fourier transform of F_{sj} (the Van-Hove self space-time correlation function)

$$G_{sj} \equiv \int d^3\underline{q}\, e^{-i\underline{q}\cdot\tilde{\underline{x}}_j} \left\langle e^{i\underline{q}\cdot[\underline{r}_j(t) - \underline{r}_j(0)]} \right\rangle \tag{7}$$

$$= \left\langle \delta\left[\tilde{\underline{x}}_j - [\underline{r}_j(t) - \underline{r}_j(0)]\right] \right\rangle$$

and then inverting to determine F_{sj}. It may be seen from (7) that G_{sj} is nothing more than the conditional probability density for a particle to be at a position $\underline{r}_j(t)$ at a time, t, given that it starts at $\underline{r}_j(0)$ at t = 0 (Berne and Pecora, 1976). Thus, G_{sj} represents the solution of the classical convective diffusion equation for the particle,

$$\frac{\partial G_{sj}}{\partial t} + \nabla\cdot\underline{v}_j G_{sj} - D\nabla^2 G_{sj} = 0 \tag{8}$$

subject to

$$G_{sj}(\tilde{\underline{x}}_j, 0) = \delta(\tilde{\underline{x}}_j).$$

Here, it should be emphasized that $\tilde{\underline{x}}_j$ is defined relative to a coordinate system with an origin at $\underline{r}_j(0)$. Once G_{sj} is known, the function F_{sj} can be determined by means of the inverse transform

$$F_{sj}(\underline{q},t) \equiv \frac{1}{(2\pi)^{3/2}} \int d^3\underline{x}\, e^{i\underline{q}\cdot\tilde{\underline{x}}_j} G_{sj}(\tilde{\underline{x}}_j, t).$$

The diffusion coefficient, D, has been taken as isotropic in (8) as a consequence of the earlier restriction to spherical particles.

Since the convection/diffusion process relevant to the light scattering experiment is characterized by a maximum length scale, L, corresponding to the scattering volume, we can approximate the velocity of particle j as

$$\underline{V}_j = \bar{\underline{V}}_j + \underline{\underline{\Gamma}}\cdot\tilde{\underline{x}}_j \tag{9}$$

where $\bar{\underline{V}}_j$ is the velocity of a particle in the scattering volume at the point $\underline{x} = \underline{r}_j$ and $\underline{\underline{\Gamma}}$ is the local velocity gradient tensor. Substituting (9) into (8) and taking the Fourier transform thus leads to

$$\frac{\partial F_{sj}}{\partial t} - i\bar{\underline{V}}_j\cdot\underline{q}F_{sj} - \underline{q}\cdot\underline{\underline{\Gamma}}\cdot\nabla_q(\underline{q}F_{sj}) + Dq^2F_{sj} = 0 \tag{10}$$

$$F_{sj}(\underline{q},0) = \frac{1}{(2\pi)^{3/2}}$$

The solution of (10) can be obtained by the method of characteristics. The result is

$$F_{sj}(\underline{q},t) = \frac{1}{(2\pi)^{3/2}}\, e^{-\int_0^t dt'[Dq'^2(t') + i\bar{\underline{V}}_j\cdot\underline{q}'(t')]} \tag{11}$$

$$\frac{d\underline{q}'}{dt} = -\underline{\underline{\Gamma}}^T\cdot\underline{q}', \quad \underline{q}'(0) = \underline{q}$$

In order to calculate the heterodyne correlation function $F_1(\underline{q},t)$, it is necessary to sum over all the particles in the scattering volume. Provided the number of such particles is large, this sum can be transformed to a volume integral giving

$$F_1(\underline{q},t) = \iiint d^3x\; I(\underline{x})\, e^{-\int_0^t dt'[Dq'^2(t') + i\bar{\underline{V}}(\underline{x})\cdot\underline{q}'(t')]} \tag{12}$$

where $I(\underline{x})$ is the intensity profile of the incident beam in the scattering volume, and $\underline{V}(x)$ is the velocity of the particles, which is approximated as

$$\underline{V}(x) = \underline{U} + \underline{\underline{\Gamma}}\cdot\underline{x} \tag{13}$$

Here $\underline{U}$ is the average particle velocity within the scattering volume, rather than the the mean velocity of the position of particle j at time zero as in (9). Substituting (13) into (12), the heterodyne correlation function then becomes

$$F_1(\underline{q},t) = e^{-\int_0^t \left[Dq'^2(t') + i\underline{U}\cdot\underline{q}'(t')\right]dt'} \iiint dx^3 I(\underline{x}) e^{-\int_0^t dt'\underline{q}'(t')\cdot\underline{\underline{\Gamma}}\cdot\underline{x}}$$

$$= e^{-\int_0^t \left[Dq'^2(t') + i\underline{U}\cdot\underline{q}'(t')\right]dt'} \tilde{I}\left(\int_0^t dt'\underline{q}'(t')\cdot\underline{\underline{\Gamma}}\right) \tag{14}$$

The corresponding homodyne correlation function, calculated from equation (2), is then

$$F_2(\underline{q},t) = e^{-2\int_0^t dt' Dq'^2(t')} \left| \iiint dx^3 I(x) e^{-i\int_0^t dt'\underline{q}'(t')\cdot\underline{\underline{\Gamma}}\cdot\underline{x}} \right|^2$$

$$= e^{-2\int_0^t dt' D q'^2(t')} \left| \tilde{I}\left(\int_0^t dt'\underline{q}'(t')\cdot\underline{\underline{\Gamma}}\right) \right|^2 \tag{15}$$

where $\tilde{I}$ is the Fourier transform of the intensity profile I, and

$$\frac{d\underline{q}'}{dt} = -\underline{\underline{\Gamma}}^T\cdot\underline{g}', \quad \underline{q}'(0) = \underline{q}$$

The homodyne correlation function differs from the heterodyne function

primarily in the fact that there is no dependence on the mean velocity $\underline{U}$. In particular, both functions involve the velocity gradient, $\underline{\underline{\Gamma}}$, and both therefore could, in principle, provide a basis for its experimental determination. As a practical matter, however, the homodyne mode provides a much superior technique. The response of the heterodyne correlation function with time will, in most cases, be dominated by the mean velocity term since the associated time scale, $(qU)^{-1}$ will usually be much shorter than either of the time scales, $(Dq^2)^{-1}$ or $(q\gamma L)^{-1}$, which are associated with diffusion or the velocity gradient, $\|\underline{\underline{\Gamma}}\| = \gamma$. Thus, except for extremely small values of U, determination of the velocity gradient from the heterodyne correlation function would be essentially impossible. The magnitude of the homodyne correlation, on the other hand, will normally be dominated by the velocity gradient term. Furthermore, the homodyne technique is much simpler to implement since no additional optics or alignment is required to deflect and mix the incident beam with the scattered signal.

The effect of the velocity gradient enters primarily through the Fourier transform, $\tilde{I}\left(\int_0^t dt' \underline{q}'(t') \cdot \underline{\underline{\Gamma}}\right)$, of the intensity profile of the incident beam in the scattering volume. By way of example, we have calculated the complete homodyne correlation function for two specific linear flows of the type (13). The first is simple shear flow where

$$\underline{\underline{\Gamma}} = \gamma \begin{pmatrix} 0 & 1 & 0 \\ 0 & 0 & 0 \\ 0 & 0 & 0 \end{pmatrix}$$

and

$$F_2(\underline{q},t) = e^{-2D\left[k^2\left(1 + \frac{1}{3}(\gamma t)^2\right) + \gamma t \cdot k\ell + \ell^2 + m^2\right]t} \left| \iiint d^3\underline{x}\ I(\underline{x}) e^{-i\gamma kyt} \right|^2 \tag{16}$$

and the second is plane, hyperbolic flow where

$$\Gamma \equiv \gamma \begin{pmatrix} 1 & 0 & 0 \\ 0 & -1 & 0 \\ 0 & 0 & 0 \end{pmatrix}$$

and

$$F_2(\underline{q},t) = e^{-2D\left[k^2\left(\frac{e^{2\gamma t} - 1}{2\gamma}\right) + \ell^2\left(\frac{1 - e^{-2\gamma t}}{2\gamma}\right) + m^2 t\right]} \left| \iiint d^3\underline{x}\ I(\underline{x}) e^{-ikx(1 - e^{\gamma t})} e^{i\ell y(1 - e^{-\gamma t})} \right|^2 \tag{17}$$

The components of $\underline{q}$ have been denoted as (k, ℓ, m) in (16) and (17). Examination of these expressions shows that the homodyne correlation function varies on three independent time scales

$$\tau_f \equiv \gamma^{-1}$$

$$\tau_D \equiv (q^2 D)^{-1}$$

and $\tau_s(\phi \equiv 0)$ which was defined in equation (4). Homodyne light scattering spectroscopy is practical as a means for determining the local velocity gradient, only when

$$\tau_s << (\tau_f, \tau_D) \ . \tag{18}$$

In this case, the expressions (16) and (17) can be approximated in the simpler forms

$$F_2(\underline{q},t) \sim \left| \iiint d^3\underline{x}\ I(\underline{x}) e^{-ik\gamma yt} \right|^2 \tag{19}$$

and

$$F_2(\underline{q},t) \sim \left| \iiint d^3\underline{x}\ I(\underline{x}) e^{-i\gamma kxt + i\gamma\ell yt} \right|^2 \tag{20}$$

respectively, and the time rate of decay of the correlation function provides a direct measure of the velocity gradient. In the case of a general linear flow subject to the same assumptions we obtain

$$F_2(\underline{q},t) = \left| \iiint d^3\underline{x}\ I(\underline{x}) e^{-i\ \underline{q}\ \cdot \underline{\underline{\Gamma}} \cdot \underline{x} t} \right|^2 . \qquad (21)$$

The expressions (19) - (21) provide the theoretical basis for determining the velocity gradient from a measurement of the homodyne correlation function, and will be used to analyze the experimental data of section 3 of this paper. If either of the conditions (18) or (5) is <u>not</u> satisfied for a given experimental set-up, the homodyne spectrum will reflect (or even be dominated by) additional contributions which arise from particle diffusion and/or translation across the scattering volume. In this case, the utility of homodyne scattering as a tool for determination of the local velocity gradient will be lost. Because of the importance of the relative magnitudes of the various time scales, τ_f, τ_s and τ_D, in establishing the domain of validity of the homodyne experiment as a method of measuring the velocity gradient, it is worthwhile to consider their relative values for typical experimental conditions. Thus, we have

$$\frac{\tau_f}{\tau_s} = q\ell \left(\frac{L}{\ell}\right)$$

and

$$\frac{\tau_D}{\tau_s} = \frac{Pe}{q\ell} \left(\frac{L}{\ell}\right)$$

where ℓ is the characteristic length scale of the particle and $Pe \equiv \gamma\ell^2/D$ is the particle Peclet number. Now, the ratio (L/ℓ) will typically be $O(10^3)$ or larger, whereas $q\ell$ is generally $O(1)$ or less in order that the Rayleigh-Debye

approximation be valid. Thus, $\tau_f/\tau_s \sim 0(10^3)$, while $\tau_D/\tau_s \sim 10^3$ Pe. The latter ratio, τ_D/τ_s, will be large provided Pe > 10^{-1} - 10^{-2}. For nonzero γ, this condition on Pe will almost always be satisfied. Thus, the condition (18) will be satisfied and the homodyne scattering experiment will almost always be dominated by the contribution of the velocity gradient in the form (19) - (21).

To complete the determination of the expected homodyne spectrum, when the conditions (5) and (18) are met, it is necessary to calculate the Fourier transform, (21), of the intensity distribution of the incident beam in the scattering volume. In general, however, this intensity profile will not be precisely known,† and it is thus important, if homodyne scattering is to be effective for determination of the local velocity gradient, that the spectrum be relatively insensitive to moderate variations in $I(\underline{x})$. For purposes of investigating this sensitivity, we have considered the following two intensity distributions for the beam geometry of figure 1 with $\underline{q} = (q,o,o)$

$$I^{(1)}(x'y'z') = \exp - (x'^2 + y'^2)/L^2 - z'^2/\alpha^2 L^2 \csc^2\theta \qquad (22)$$

and the 'tophat' profile

$$I^{(2)}(x'y'z') = e^{-z'^2/\alpha^2 L^2 \csc^2\theta} \begin{cases} 1 & (x'^2 + y'^2) \leq L^2 \\ 0 & (x'^2 + y'^2) \geq L^2 \end{cases} \qquad (23)$$

where θ is the scattering angle, $\underline{x}' = (x',y',z')$ is the beam coordinate system defined in figure 1, L is the length scale characteristic of the

†In spite of the fact that $I(\underline{x})$ can be measured in a reasonably straightforward manner, it will only stay fixed for about 24 hours, and accurate knowledge of $I(\underline{x})$ would thus require constant recalibration of the instrument.

width of the incident beam and α is the ratio of the length of the scattering volume in the z direction to the width L. With these expressions for the intensity profile, the equations (19) and (20) yield, respectively for shear flow, $\underline{q}\cdot\underline{\underline{\Gamma}}\cdot\underline{x}t = q\gamma yt$,

$$\text{(a) intensity profile } I^{(1)}\text{: } F_2(\underline{q},t) = e^{-q^2\gamma^2L^2t^2/2} \tag{24}$$

$$\text{(b) intensity profile } I^{(2)}\text{: } F_2(\underline{q},t) = \left[2J_1(q\gamma Lt)/q\gamma Lt\right]^2 \tag{25}$$

and for two-dimensional extensional flow, $\underline{q}\cdot\underline{\underline{\Gamma}}\cdot\underline{x}t = qx\gamma t$
$= qz'\sin\frac{\theta}{2}\gamma t + qx'\cos\frac{\theta}{2}\gamma t$

$$\text{(a) intensity profile } I^{(1)}\text{: } F_2(q,t) = \exp\left[-q^2\gamma^2L^2t^2\left(\cos^2\frac{\theta}{2} + \alpha^2\frac{\sin^2\theta/2}{\sin^2\theta}\right)\Big/2\right] \tag{26}$$

$$\text{(b) intensity profile } I^{(2)}\text{: } F_2(\underline{q},t) = \exp\left[-\frac{q^2\gamma^2L^2\alpha^2\sin^2\theta/2}{2\sin^2\theta}\right] \cdot\left[\frac{2J_1(q\gamma Lt\cos\theta/2)}{q\gamma Lt\cos\theta/2}\right]^2 \tag{27}$$

where J_1 is a Bessel function of the first kind.

Figure 2 compares the correlation functions described by equations (24) and (25). For large times, the behavior of the correlation function, $F_2(\underline{q},t)$, is fundamentally different for the two intensity distribution functions: $I^{(1)}$ produces monotonically decreasing correlation functions while those calculated for $I^{(2)}$ show time dependent oscillations. However, the characteristic time scale in both cases is proportional to $q\gamma L$ and in the region of primary experiment interest ($q\gamma Lt \leq 4$) the qualitative behavior produced by both $I^{(1)}$ and $I^{(2)}$ is the same. Comparison of (24) and (25) or (26) and (27) suggests that the principal influence of the <u>flow type</u> on $F_2(qt)$ is to alter the dependence of the characteristic decay time on the scattering

angle θ.

In general, the correlation function will be a function of more than one component of the velocity gradient tensor $\underline{\underline{\Gamma}}$, which has eight independent components if the fluid is incompressible. For the two specific flow types considered above and in the experiments described in the following section, the orientation of the vector $\underline{q}$ was chosen so that only one component of $\underline{\underline{\Gamma}}$ was projected onto $\underline{q}$. This will not in general be possible. However, the individual components of $\underline{\underline{\Gamma}}$ can still be measured, at least in principle, by creating an anisotropic scattering volume which has one length scale which is considerably larger than the other two. Thus, for example, we may consider an incident intensity distribution

$I(\underline{x}) = \delta(x)\delta(y)f(z)$, with $\delta(\ )$ a Dirac delta function,

in which it is assumed that the length scale of the scattering volume in the z direction is much larger than along x or y. In this case, the gradients in the velocity with respect to z will dominate the decay of the correlation function and each individual component of $\underline{\underline{\Gamma}}$ can be measured by independently varying the orientations of the scattering vector, $\underline{q}$, and the vector defining the largest length scale of the scattering volume.

All of the analysis of this section, from equation (3) onward, has been restricted to spherical particles, which are optically homogeneous and isotropic. If the particles are non-spherical or optically anisotropic, their rotational motions will influence the light scattering spectrum, both through the amplitude function and the phase factor of equation (1). The time scale of rotationally induced variations in the amplitude factor will be Ω^{-1} where Ω is the magnitude of the angular velocity of the particle. In order

to consider the role of rotations on the phase factor is necessary to include an integration over the internal coordinates of equation (11). For a rod-like particle of length ℓ and unit vector $\underline{p}(t)$ along the rod axis, the homodyne correlation function (neglecting diffusive motions) is

$$F_2(\underline{q},t) = \left| \iiint d^3x \; I(\underline{x}) e^{i\underline{q}\cdot\underline{\underline{\Gamma}}\cdot\underline{x}t} \right|^2 \left| \int_{-\ell/2}^{\ell/2} \iiint e^{i\underline{q}\cdot\left(r'\underline{p}(t) - r''\underline{p}(0)\right)} dr'dr'' \; d^2\underline{p}(0) \right|^2$$

Thus, the time scale of variations in the phase factor which are caused by particle rotation is

$$t_I = (q\ell\Omega)^{-1}.$$

Since the angular velocity Ω will be at most the same order as the velocity gradient γ, the time scales characteristic of rotations of anisotropic particles will in general be long compared to the velocity gradient time scale $(q\,\gamma L)^{-1}$ and so may be ignored.

The analysis can also be extended to include the effects of curvature in the velocity field $\frac{\partial^2 v_i}{\partial x_j \partial x_k}$. This may be important if there is a significant change in the velocity gradient over the scattering volume. For example, in the case of shear flow already considered, if the velocity field is actually

$$\underline{v} = (U + \gamma y + \beta y^2, 0, 0)$$

the homodyne correlation function becomes (using the Gaussian intensity distribution $I^{(1)}$ and the geometry of figure 1)

$$F_2(\underline{q},t) = \left| \iiint d^3x' I^{(1)}(\underline{x}') e^{iq\gamma yt + i\beta q y^2 t} \right|^2$$

$$= \sqrt{\frac{\pi}{1 + q^2\beta^2L^4t^2}} \quad \exp\left[- \frac{q^2\gamma^2L^2t^2}{2(1 + q^2\beta^2L^4t^2)} \right]$$

If $\beta^2L^2/\gamma^2 \ll 1$, the curvature effect will be unimportant and this expression reduces to the form (23) found earlier for a linear shear field. If this condition is not satisfied, on the other hand, the homodyne correlation function is no longer the square modulus of the Fourier transform of the intensity function and a new time scale $(q\beta L^2)^{-1}$ is introduced. Experimentally, the generally undesirable effects of curvature in the velocity field could thus be detectable, in principle, by the presence of an algebraic, rather than exponential, decay in the correlation function with a t^{-1} dependence if the intensity distribution is Gaussian.

III. Experimental

In the preceding section, we have considered theoretically the light scattering correlation function for the classical homodyne scattering experiment applied to a flowing suspension. We have shown that the dominant contribution, under normal circumstances, will derive from the mean velocity gradient in the scattering volume, thus suggesting the potential of applying the homodyne scattering experiment to the technological problem of actually measuring the magnitude of velocity gradients in flowing liquids.

In this section, we report the results of some exploratory experiments which were designed to test the validity of our theoretical results, and to explore the utility of homodyne light scattering as a method of measuring

velocity gradients. Thus, two sets of flow experiments were performed under conditions, discussed in the preceeding section, where the homodyne correlation function should decrease exponentially with time at a rate which depends principally on the local shear rate. In one case, the velocity gradient field is known, a priori , and the measurements serve to verify the utility and accuracy of the method. In the other, we study the experimentally important "four roller" flow device where the velocity gradient field was only approximately known before the present investigation. Additional experiments were also performed in order to investigate the effects of smaller values of the time scale ratio, τ_t/τ_s, illustrating a situation where the theory presented would not be applicable. These experiments also suggest the necessary conditions for the effects of diffusion to be measurable in the presence of flow.

The experiments were performed on two separate flow devices: the four-roll mill, illustrated in figure 3, which is used to approximate the two-dimensional, hyperbolic flow of equation (17); and a concentric cylinder, "Couette" device, shown in figure 4, which approximates the simple, shear flow of equation (16). The light source for both experiments was an argon ion laser operating typically in the neighborhood of 500 mW, and the scattered light was detected using an EMI 9789 photomultiplier tube. Two pinholes separated by about 10 inches were used to collimate the scattered light and thereby define the scattering volume. The pinholes had a diameter of 1/32 inch in the four-roll experiment, and 1/64 inch in the case of the Couette device, and the incident wavelengths of the light were 5145 Å and 4880 Å, respectively. The output of the photomultiplier tube was amplified by a Princeton Applied Research 113

preamplifier and processed with a Saicor 43 A 400 channel correlator. The computed correlation function was then output onto a Hewlett Packard 700 A X-Y recorder.

The dimensions of the four roll mill are shown in figure 5. All rollers were driven separately with independent motors and each could be removed to allow for a one or two roller operation. The top and bottom of the container were constructed of one-quarter inch pyrex through which the laser beam passed. A photographic study of the flow field generated by the apparatus was undertaken using a dilute suspension of glass spheres of mean diameter 100 μ in glycerin. A typical streakline photograph of the centerplane velocity field is shown in figure 6, from which it appears that the two-dimensional hyperbolic flow of equation (17) is reasonably well approximated in the central region between the four rollers. Assuming this to be true, the (uniform) velocity gradient in this region can be obtained by measuring the travel time Δt for a tracer particle to move from position (x_1,y_1) to (x_2,y_2). The velocity gradient for a two-dimensional, hyperbolic flow is

$$\gamma \equiv \ell n \left(\frac{x_2}{x_1}\right) \Big/ \Delta t = \ell n \left(\frac{y_1}{y_2}\right) \Big/ \Delta t \ . \tag{30}$$

This procedure[†] was carried out for rotation rates, w, of the rollers ranging from 1.4 to 35 sec^{-1}. The result was a <u>linear</u> relationship between roller speed and apparent velocity gradient,

$$\gamma = 0.678 \ w \ sec^{-1} \tag{31}$$

[†]Further details are reported by Fuller (1980).

as would be expected if the flow were truly given by equation (17). An interesting question, which we shall investigate later in this section, is whether detailed pointwise measurements of the velocity gradient field would support the conclusion of a very good approximation to the hyperbolic flow which is the obvious and strong inference of our streakline visualization studies. In the four roll mill, light scattering experiment, the incident beam was directed on to the flow device through its bottom by means of a front surfaced mirror, mounted on a rotation stage capable of 360° orientation to within 0.25 degrees. The rotation stage was in turn mounted on a translation stage capable of a twelve inch traverse to within 0.001 inch. Angular variation of the scattered light wave vector was provided by mounting the photomultiplier tube on a wide range vertical goniometer which could be positioned to within 0.01 degree. This capability of orienting the incident and scattered wave vectors separately allows the orientation and magnitude of the scattering vector $\underline{q}$ to be varied independently. In addition, the four-roll mill itself was mounted on a cross-slide rotary table which provides the capability of translating and rotating the flow device, while holding the optics stationary. Thus, scattering experiments at different positions and orientation relative to the flow are possible.

The Couette device was constructed of a rotating inner cylinder of black, anodized aluminum, enclosed by a heavy-walled, precision bore glass tube which was held stationary. The dimensions of the various components are indicated in figure 4. In this case, the incident laser light was introduced into the gap between the two cylinders through a solid lucite

cylinder which was cut to fit onto the outer glass cylinder such that the composite glass plus lucite wall formed a cylindrical section with its central axis at the center of the gap. This enabled the incident beam to enter the gap region with a minimum of refraction at the lucite/air interface. The Couette device was itself mounted on an x-y translation stage which, in turn, was fastened to the hub of a horizontal goniometer. The goniometer hub could be rotated independently of the rotating arm which supported the photomultiplier tube.

Experiments in both apparatus were conducted using a suspension of 100 ppmw of Dow Polystyrene Latex spheres in glycerin. The particle diameter was 0.091 μ and the viscosity of the glycerin was found to be 7 poise at 20°C. The water content of the glycerin was not known.

In order to use equation (20) to analyze the experiments, it is necessary to ensure that the dynamics of the light scattering process occur primarily on the shear rate time scale $(q\gamma L)^{-1}$. The data necessary to determine the various time scale ratios for the two experiments are listed in Table 1. In Table 2, we show the corresponding time scale ratios, τ_t/τ_s, τ_D/τ_s and τ_f/τ_s. It may be seen, in both cases, that the time scale τ_s, associated with the mean velocity gradient is very much the smallest, and it is thus expected that equation (21) should adequately represent the measured correlation functions.

To obtain absolute values for the shear rate from (20) and the measured correlation function, it is necessary to also measure the intensity profile of the beam, as we have already noted. However, this was not done in the present experiments. Instead, the characteristic

time, in each instance, was estimated as the time for decay of the correlation function to one-half its initial magnitude, and the shear rate was taken as being proportional to the inverse of this time. Thus, the velocity gradients obtained (and reported) are all relative values.

The first flow field studied was that generated by a single rotating cylinder and this was accomplished by removing all but one of the rollers in the four-roll mill. Analysis of an infinitely long cylinder of radius R, rotating with angular speed w, yields an r^{-2} dependence of shear rate on distance from the cylinder center

$$\gamma = -\frac{wR^2}{r^2} \quad . \tag{32}$$

Measurement of the spatial dependence of the velocity gradient should thus lead to the same radial dependence, provided that the flow device approximates an infinitely long cylinder.

The experimental arrangement for this case is shown in figure 6. The scattering vector $\underline{q}$ was oriented in the azimuthal direction and the experiment was carried out by holding the optics stationary while translating the flow device along the path indicated in figure 7. At each interval of translation, the correlation function was obtained and recorded. A typical correlation function is pictured in figure 8. The results of this procedure for two-roller speeds are shown in figure 7 where we have plotted the measured velocity gradient against the square of the reciprocal of the radial distance from the roller center. The linearity of the data, when plotted in this fashion, indicates that the measured velocity gradient is

consistent with the theoretical expression (32). Furthermore, the fact that the slope doubles when w is doubled is also consistent with (32). Both of these results support the validity of the homodyne scattering method as a way of measuring the velocity gradient.

The data do depart from linearity farther from the roller surface, but we attribute this to boundary effects associated with the finite cylinder length. The presence of a top and bottom on the four-roller container causes the velocity gradient to drop off faster than the analysis for an unbounded fluid would indicate. It is important to note that throughout the experiment, the shapes of the correlation functions were observed to remain constant. That is, by scaling the time, the correlation functions could be made to trace out a single curve. This verifies the assertion that the only quantity changing is the velocity gradient and that there is only a single time scale controlling the correlation function.

A second experiment was conducted using the Couette device, again intended to verify the homodyne method for measuring velocity gradients. In this apparatus, the flow field is a good approximation to simple shear flow and the velocity gradient should thus be nearly constant throughout the gap. The incident wave vector $\underline{k}_i$ was kept parallel to the direction of flow and correlation functions were obtained as a function of scattering angle. Care was taken to ensure that the centroid of the scattering volume remained fixed as the scattering angle was varied.

Taking the velocity to be locally in the direction of x and the gradient to be in the direction of y, the quantity $\underline{q}\cdot\underline{\underline{\Gamma}}\cdot\underline{x}t$ would be $2\gamma|\underline{k}_i|\sin^2\frac{\theta}{2}yt$. Therefore, the measured characteristic decay time for the z correlation

function should be linear with respect to the quantity $\sin^2\frac{\theta}{2}$. The data plotted in figure 9 show that this relationship is satisfied, thus again confirming the accuracy of the method for measurement of the velocity gradient.

Finally, as an indication of the kind of study which can be done in more complicated flows, we have used the homodyne scattering method to determine the velocity gradient profile for the four roll mill when it is supposed to be generating hyperbolic flow. These data are of some intrinsic interest as the four roller device has often been used in studies of particle and droplet deformation and orientation but has previously been characterized only via visual, streakline photography[†] (Pope and Keller, 1977, Rumscheidt and Mason, 1961, Taylor, 1934). The four roller device is usually designed to simulate two-dimensional extensional flow and it is important to know how well the device performs in actually creating this type of homogeneous flow. The most important feature of the flow, for most of the particle dynamics experiments, is the absence of spatial variation of the velocity gradient field.

As discussed in section 2, the scattered light spectrum will generally be influenced by all nonzero gradient components of the projected velocity $\underline{v}\cdot\underline{q}$. However, for the case of a single rotating clyinder, with the light scattering volume situated half way between the top and bottom of the cylinder, there is, at leading order, only a single, radial component of the velocity gradient, and there is therefore no ambiguity in interpreting what the experiment measures. However, in the more complex geometry of the four-roll mill, there will in general be more than one

---

[†]A more comprehensive study of the four-roller device are reported by Fuller (1980).

nonzero component of the velocity gradient. By making the scattering volume highly elongated one could, in principle, determine each velocity gradient component separately. We did not attempt this procedure here, but instead used symmetry of the flow field at the center plane and took measurements along the center streamline of the center plane with the scattering vector $\underline{q}$ parallel to the velocity component in the x direction. Along this center streamline, $\partial v_x/\partial y$ and $\partial v_x/\partial z$ are zero to at least a first-order of approximation, and the experiment thus yields values for $\partial v_x/\partial x$.

It may be anticipated that the velocity field in the four-roll mill contains a saddle point close to the position of closest approach between any two adjacent rollers. At these points the velocity gradient will vanish and the time scale ratio τ_t/τ_s will no longer be large enough for the correlation function to be related to the intensity profile by equation (20). Therefore, in the vicinity of these points one would expect the correlation function to change shape and to no longer be characterized by a single time scale which is inversely proportional to the velocity gradient. It was found, however, that the regions where there was a noticeable change in the shape of the measured correlation function was very small (less than one-tenth of an inch in the flow direction) and data in these regions are simply not included here.

The measured velocity gradient profile is pictured in figure 10. Data taken with the direction of the rollers reversed fell on the same curve. The profile clearly shows that the region of homogeneity in the flow field (constant velocity gradient) is confined to an area whose length is approximately equivalent to the gap width between the rollers. A study was also

undertaken of the dependence of the velocity gradient on roller speed with the scattering volume stationary at the center of the four roller device. This study showed that the dependence was linear over the entire range of roller speeds ($0 - 35\ sec^{-1}$).

A short investigation was also carried out in order to see whether conditions could be achieved where it would be possible to see the effects of the diffusion process in the scattering data. Such data would be of considerable interest since the rate of diffusion is sensitive to the conformation of the scattering particles (or molecules) and would provide information about flow-induced deformation or, in the case of rigid nonspherical particles, orientation. This study was carried out in both apparatus and involved an attempt to set the scattering vector $\underline{q}$ normal to the plane of flow so that $\underline{q}\cdot\underline{\underline{\Gamma}}\cdot\underline{x} \equiv 0$ everywhere in the scattering volume. In the Couette device, the vector $\underline{q}$ was oriented radially with a scattering angle of about 60°. In the four-roll mill experiment, $\underline{q}$ was set parallel to the z axis with a scattering angle of 120°. If equation (15) was appropriate and the orientation of $\underline{q}$ sufficiently precise, this configuration would eliminate the effect of the shear rate on the light scattering correlation function, leaving only the diffusion process. However, in the case of the Couette apparatus, the presence of a small but finite curvature in the streamlines and a nonzero mean velocity in the scattering volume caused the correlation function to be dominated still by flow effects and the measured time scale for the correlation function remained orders of magnitude faster than the diffusive time scale. In the four roll mill, on the other hand, the measured characteristic time scale was reduced to the same order of magnitude as the diffusive time scale. This was accomplished by

placing the scattering volume in the vicinity of the stagnation point in the flow and using a high scattering angle. There was, however, a small z component of velocity and an associated velocity gradient due to the effect of the top and bottom boundaries, and for this reason it would probably not be possible for the diffusive process to completely dominate the correlation function in the present system.

The criterion which must be satisfied in order that the diffusive effects dominate the spectrum is that

$$\tau_t/\tau_D = \frac{qD^2L}{U} >> 1 \ .$$

If the scattering volume is centered on the stagnation point, the velocity U will be of the order of γL and the ratio becomes

$$\tau_t/\tau_D = \frac{q^2D}{\gamma} = \frac{(q\ell)^2}{Pe} \ .$$

For most situations of interest, the Peclet number will be no larger than O(1). Therefore, in order to exhibit a dominant diffusive effect, the experiment would have to be performed at higher angle using relatively large particles. It would also be necessary, as in the present experiments, to have the scattering vector normal to the plane of flow and to have the scattering volume centered on the stagnation point.

Conclusions

We have examined the application of homodyne light scattering techniques to a laminar flow field, both theoretically and experimentally. Although many dynamic processes contribute to the frequency spectrum of the scattered light, we have seen that the dominant effect on the light scattering

correlation function will normally be due to the presence of velocity gradients in the scattering volume. Thus, we have shown theoretically, and confirmed via experiment, that the homodyne light scattering experiment provides a direct method to measure the velocity gradients.

In its present state of development, the most serious limitation of the method is that all components of the gradient of the projected velocity, $\underline{v}\cdot\underline{q}$, contribute to the spectrum. Although this deficiency may be overcome in principle by creating an anisotropic scattering volume, this was not pursued in the present investigation since the experiments studied had only one gradient component of velocity in the scattering volume. A second limitation is that the intensity profile of the beam must be known in order to quantify the gradients in an absolute sense. This information can be obtained experimentally without much difficulty. Unfortunately, however, the intensity profile will generally not be maintained for extended periods of time. The laser beam profile in our system was certainly stable for periods of the order of days, but often changed in as little as a week as the laser optics require cleaning and retuning.

The chief advantage of the homodyne light scattering technique relative to more conventional measurement techniques is that the shear rate can be obtained in a single, "noninvasive" experiment, without the need for accurate repositioning of the measurement point as would be required if one were to simply differentiate velocity data. The results are therefore more accurate and reliable than was previously possible. In addition, the present technique can be used in situations where the velocity changes rapidly in narrow regions (and in this case, the principal component of $\nabla\underline{u}$ is normal to $\underline{u}$, thus minimizing the major ambiguity of interpretation

which was discussed above).

In contrast, the usefulness of homodyne scattering experiments to determine anything of the diffusive motions (and, thus, indirectly the conformational state) of the scattering elements as is conventionally done in quiescent solutions or suspensions, would appear to be highly limited for flowing systems. The short investigation which we have carried out here suggests that it would be necessary for the scattering volume to be centered on a stagnation point of the flow, in order even to approach the necessary conditions for the correlation function to be dominated by the effects of Brownian diffusion. In addition, in order that $\tau_D/\tau_t < O(1)$, it is necessary that $q\ell > O(1)$ and this requires that the measurements be carried out at high scattering angles with relatively large particles. These various restrictions greatly reduce the potential utility of homodyne dynamic scattering for purposes other than measurement of the local mean velocity gradient in flowing systems.

ACKNOWLEDGMENT

This work was supported by a grant from the Office of Naval Research.

References

Berne, B. J. and Pecora, R., "Dynamic Light Scattering with Applications to Chemistry, Biology, and Physics", John Wiley and Sons, Inc., New York (1976).

Edwards, R. V., Angus, J. C., French, M. J. and Dunning, J. W., Jr., Spectral Analysis of the Signal from the Laser Doppler Flowmeter: Time Independent Systems , J. Appl. Phys. 42, 837 (1971).

Fuller, G. G., PhD Thesis, California Institute of Technology (1980).

Pike, E. R., Photon Correlation Velocimetry, in "Photon Correlation Spectroscopy and Velocimetry", Cummins, H. Z. and Pike, E. R. (ed.). Plenum Press, New York (1976).

Pope, D. P. and Keller, A., Alignment of Macromolecules in Solution by Elongational Flow, J. Colloid and Polymer Science 255, 633 (1977).

Rumscheidt, F. D. and Mason, S. G., Particle Motions in Sheared Suspensions XI. Internal Circulations in Fluid Droplets, J. Colloid Science 16, 210 (1961).

Taylor, G. I., The Formation of Emulsions in Definable Fields of Flow, Proc. Roy. Soc. A. 146, 501 (1934).

Table 1

	four roller	Couette
q	10^5 cm^{-1}	10^5 cm^{-1}
L	0.08 cm	0.04 cm
R	1 cm	1 cm
D	10^{-11} cm^2/sec	10^{-11} cm^2/sec
w	1 sec^{-1}	1 sec^{-1}

Table 2

	four roller	Couette
τ_t/τ_s	6.4×10^2	1.6×10^2
τ_D/τ_s	8×10^4	4×10^4
τ_f/τ_s	8×10^3	4×10^3

Figure Captions

1. Light scattering geometry. The vector $\underline{q}$ is orientated along the x axis in the laboratory frame.
2. Calculated homodyne correlation function for two choices of the light intensity profile in the scattering volume, using the scattering geometry of figure 1.
3. Light scattering set-up with the four roll mill.
4. Light scattering set-up with the Couette apparatus.
5. The four roll mill.
6. Streakline photograph of flow generated by the four roll mill. The particles were illuminated by a planar sheet of light at the mid-height of the rollers.
7. Measured shear rate as a function of the radial distance from a single rotating roller. The illustration in the upper left corner represents the experimental arrangement.
8. Typical correlation function for the single rotating roller experiment. Data taken at a scattering angle of 30°.
9. Characteristic frequency of the homodyne correlation function vs. $\sin^2\frac{\theta}{2}$. The flow is simple shear with the direction of flow parallel to the incident beam vector.
10. Characteristic frequency as a function of distance along the center streamline in the four roll mill simulating hyperbolic flow. The scattering angle was 50.7° and the rate of rotation of the rollers was 1.75 sec^{-1}. The large circles indicate the position of the rollers with respect to the bottom ordinate.

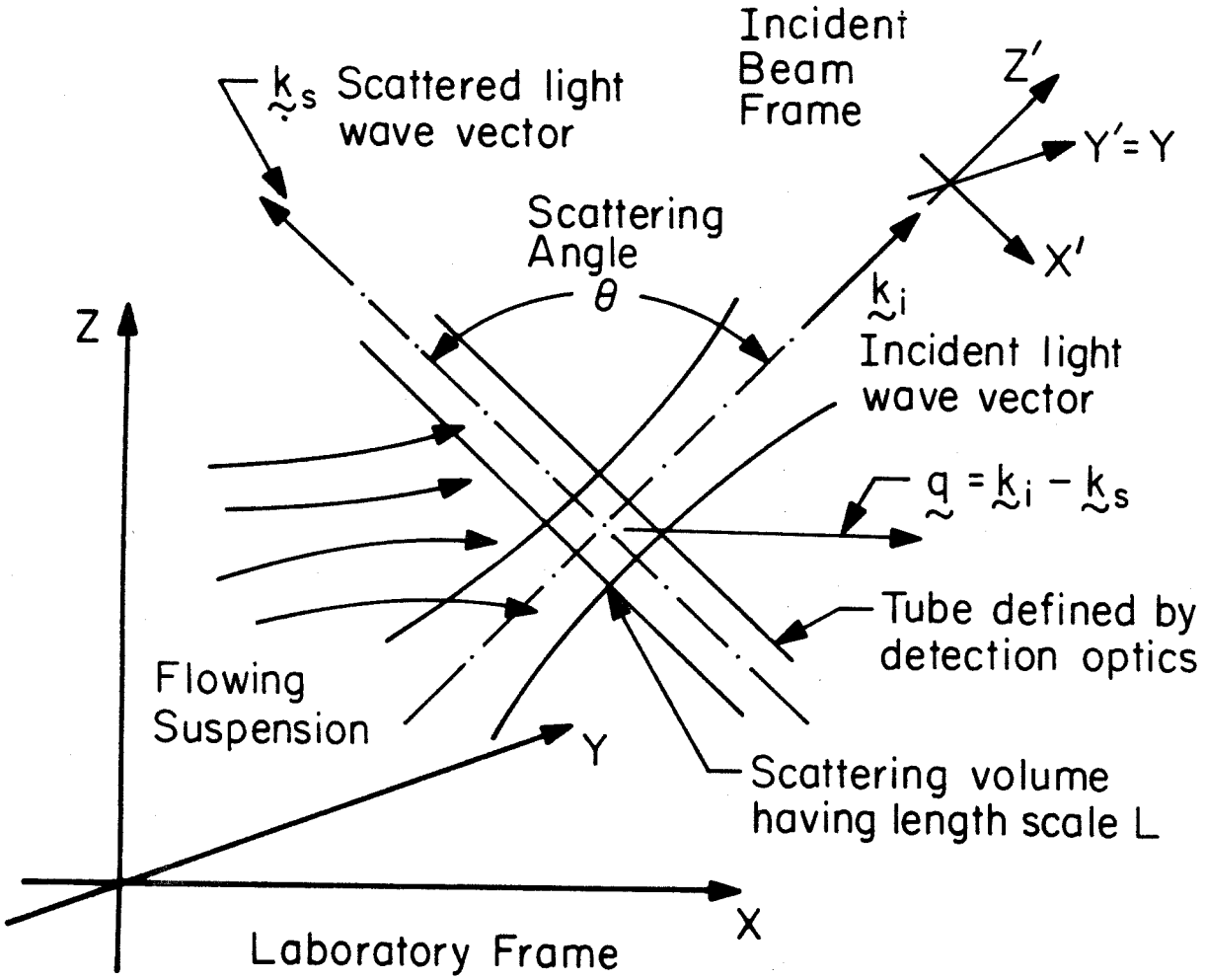
Incident
Beam
Frame
Z′
Y′= Y
X′
$\underset{\sim}{k}_s$ Scattered light
wave vector
Scattering
Angle
θ
$\underset{\sim}{k}_i$
Incident light
wave vector
Z
$\underset{\sim}{q} = \underset{\sim}{k}_i - \underset{\sim}{k}_s$
Tube defined by
detection optics
Flowing
Suspension
Y
Scattering volume
having length scale L
X
Laboratory Frame

Fig. 1

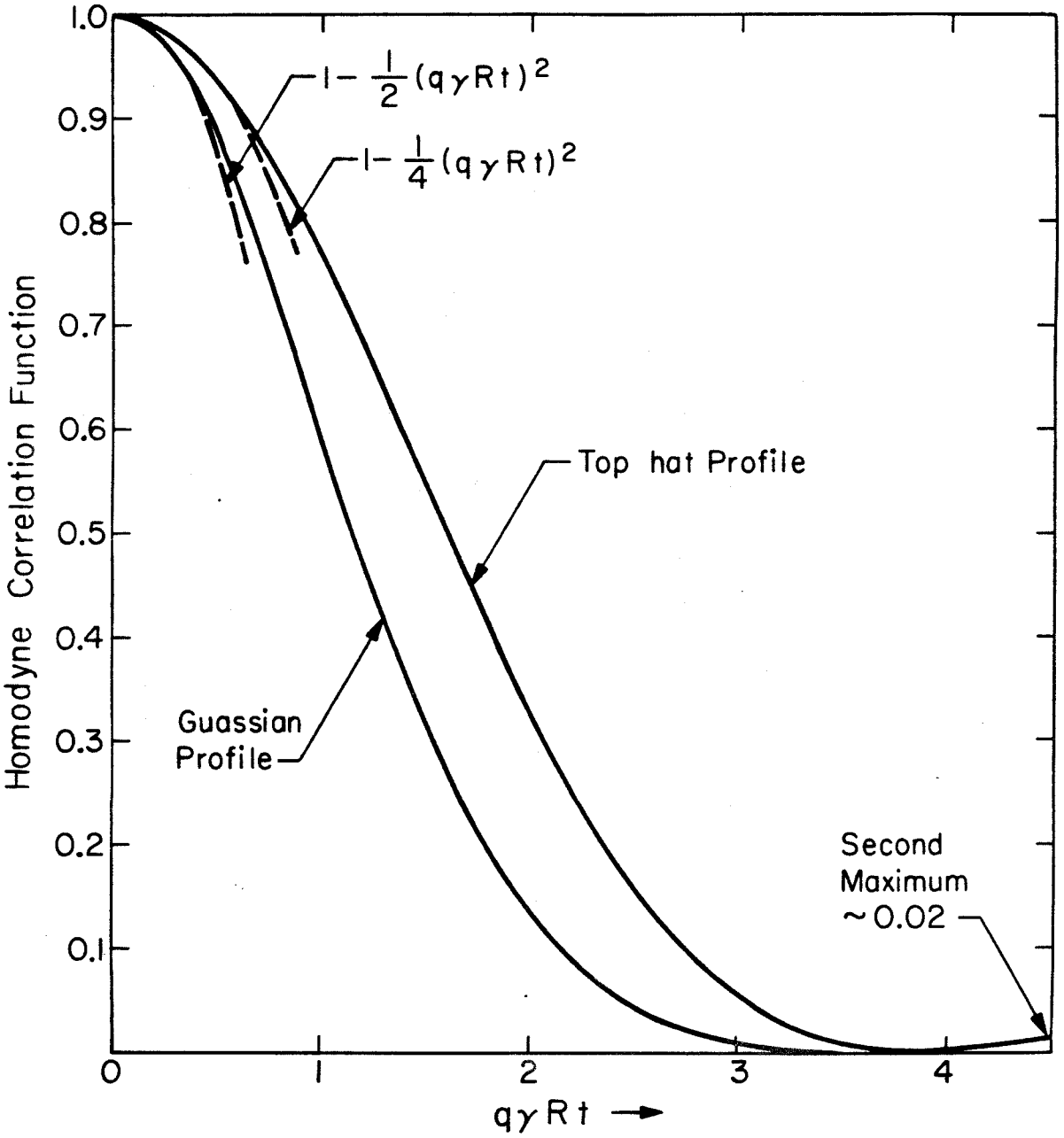
1.0
0.9
0.8
0.7
0.6
0.5
0.4
0.3
0.2
0.1
0
1
2
3
4
Homodyne Correlation Function
qγRt →
$1-\frac{1}{2}(q\gamma Rt)^2$
$1-\frac{1}{4}(q\gamma Rt)^2$
Top hat Profile
Guassian Profile
Second Maximum ~0.02

Fig 2

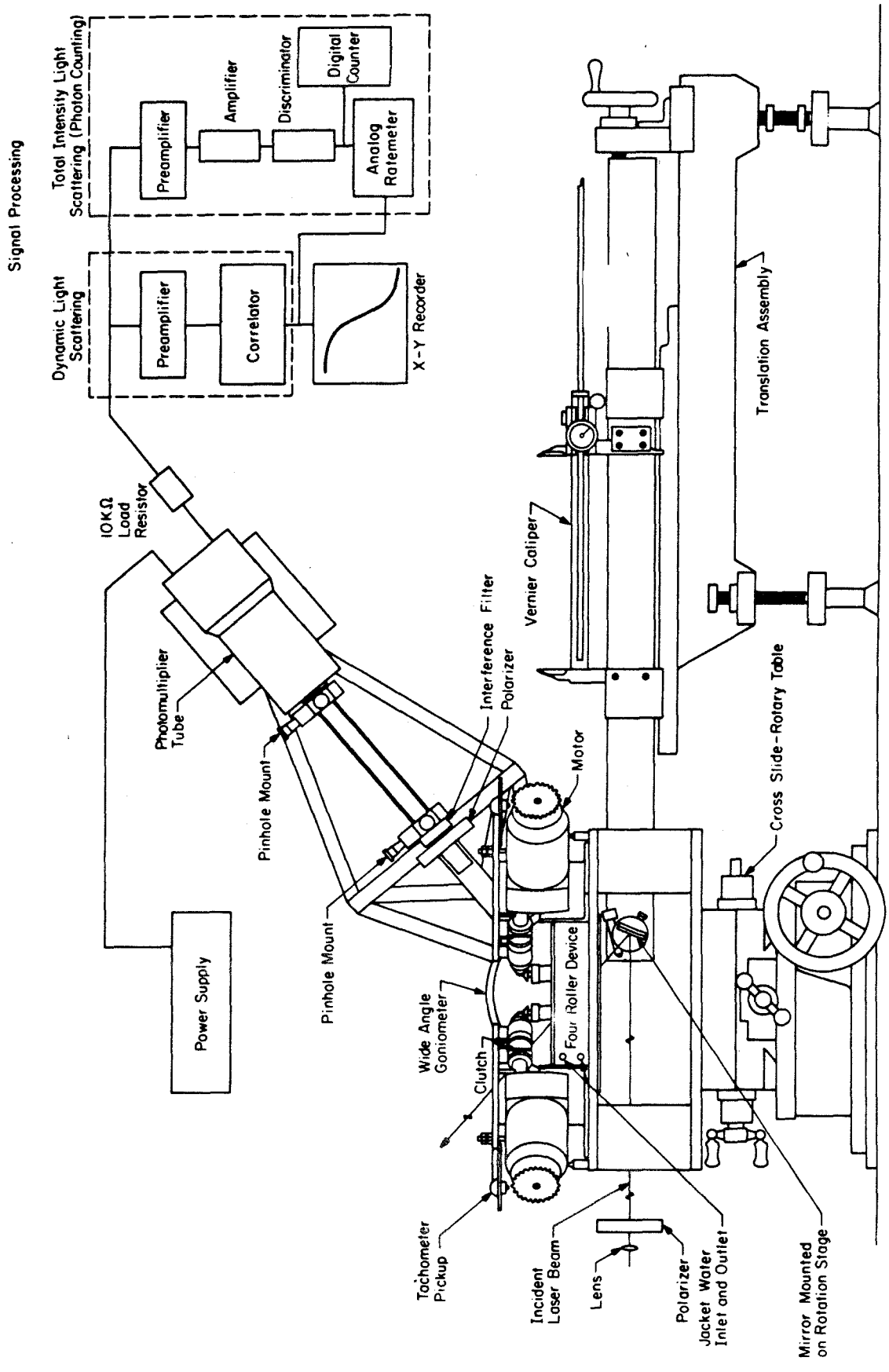
Signal Processing
Total Intensity Light Scattering (Photon Counting)
Preamplifier
Amplifier
Discriminator
Digital Counter
Analog Ratemeter
Dynamic Light Scattering
Preamplifier
Correlator
X-Y Recorder
10K Ω Load Resistor
Photomultiplier Tube
Pinhole Mount
Pinhole Mount
Interference Filter
Polarizer
Motor
Vernier Caliper
Translation Assembly
Cross Slide-Rotary Table
Power Supply
Wide Angle Goniometer
Clutch
Four Roller Device
Tachometer Pickup
Incident Laser Beam
Lens
Polarizer
Jacket Water Inlet and Outlet
Mirror Mounted on Rotation Stage

Fig. 3

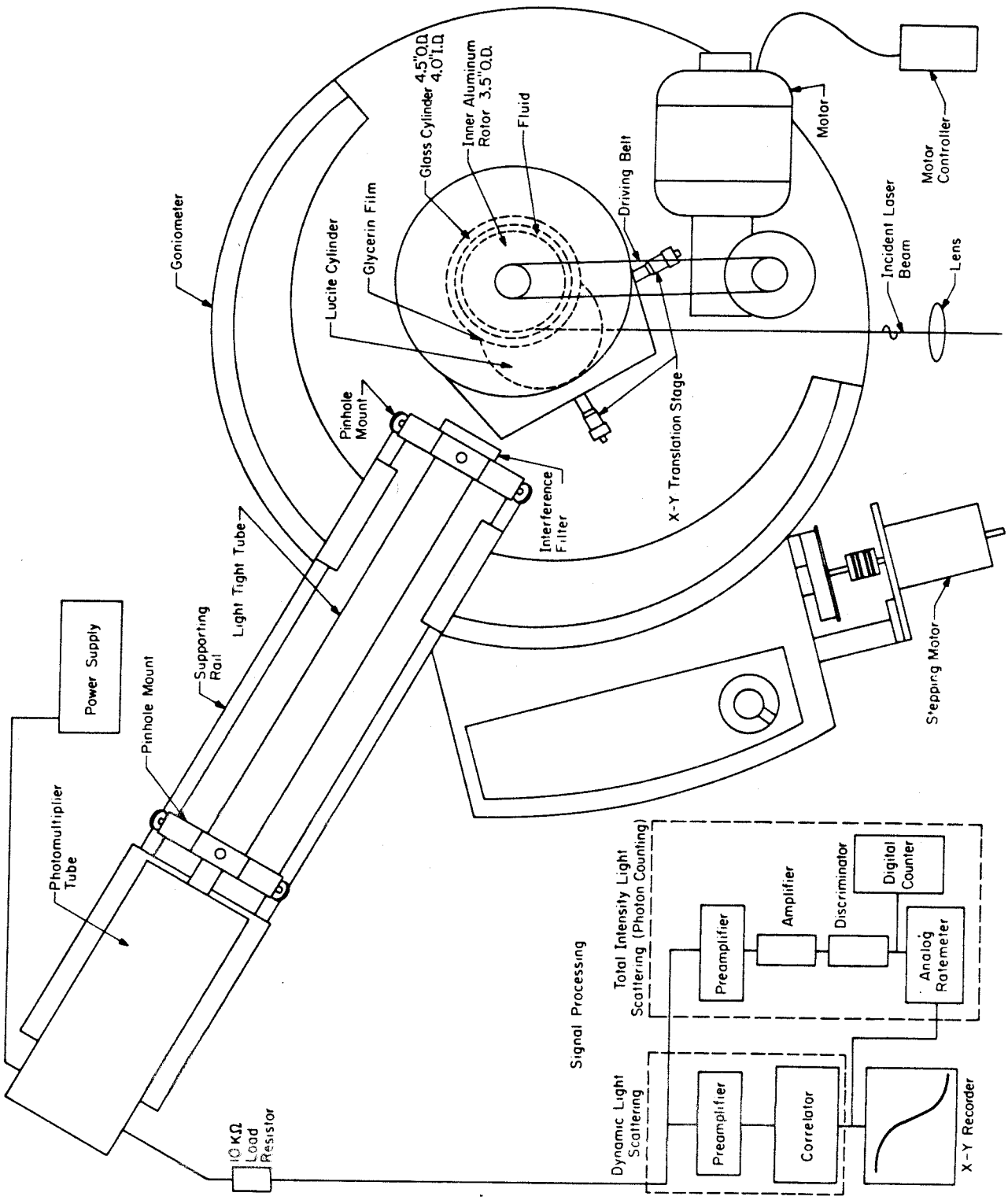
Goniometer
Glass Cylinder 4.5"O.D. 4.0"I.D.
Inner Aluminum Rotor 3.5"O.D.
Fluid
Driving Belt
Motor
Motor Controller
Incident Laser Beam
Lens
Lucite Cylinder
Glycerin Film
Pinhole Mount
Interference Filter
X-Y Translation Stage
Stepping Motor
Power Supply
Photomultiplier Tube
Pinhole Mount
Supporting Rail
Light Tight Tube
10 KΩ Load Resistor
Signal Processing
Dynamic Light Scattering
Preamplifier
Correlator
X-Y Recorder
Total Intensity Light Scattering (Photon Counting)
Preamplifier
Amplifier
Discriminator
Digital Counter
Analog Ratemeter

Fig. 4

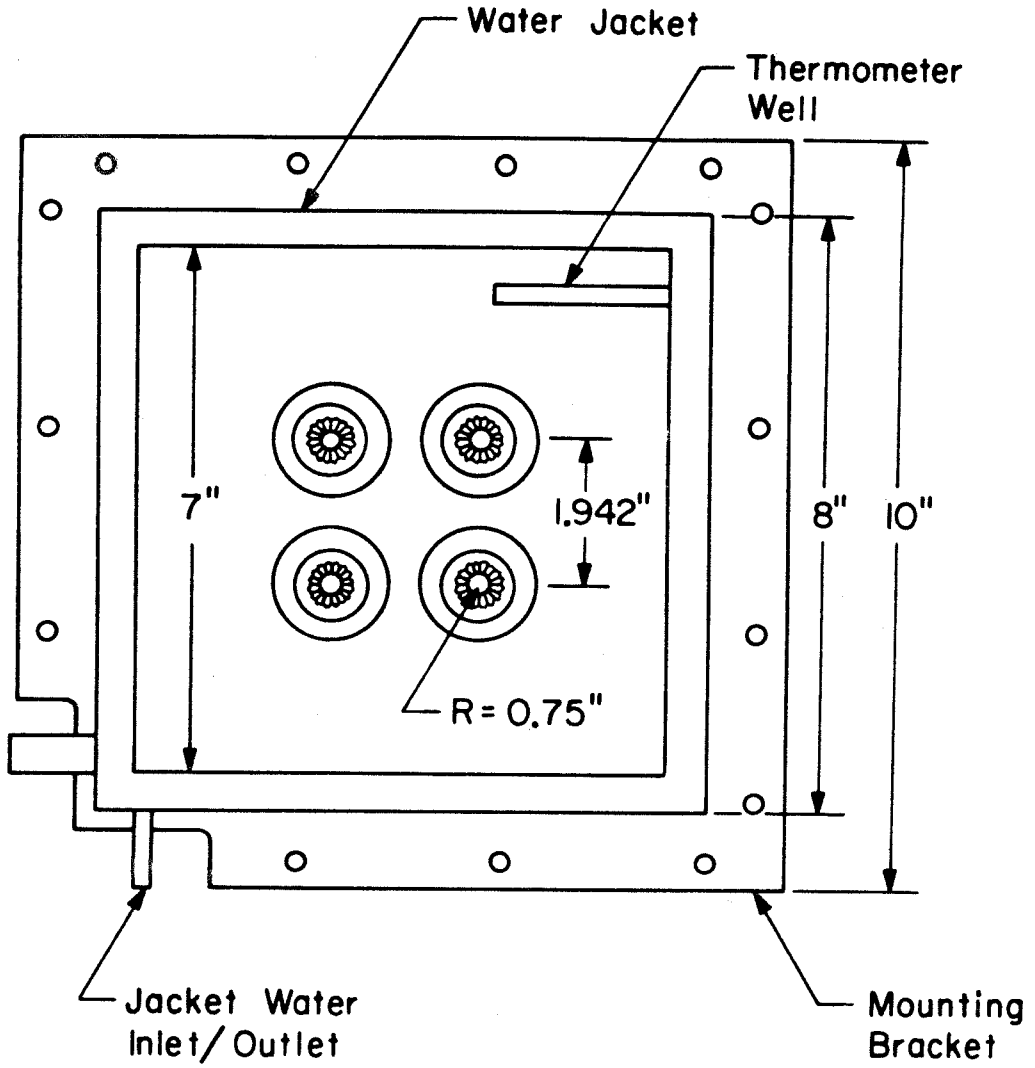
Water Jacket
Thermometer Well
7"
1.942"
8"
10"
R = 0.75"
Jacket Water Inlet/ Outlet
Mounting Bracket

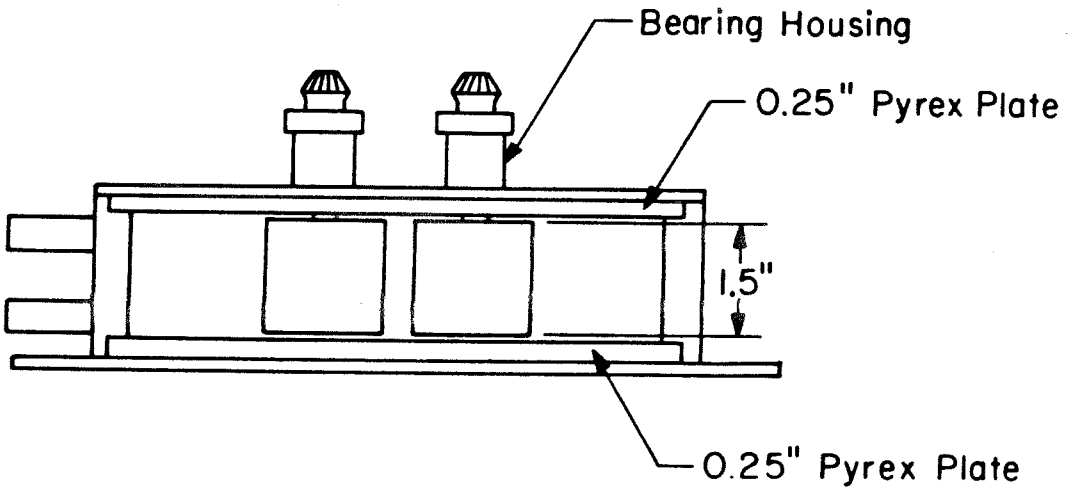
Bearing Housing
0.25" Pyrex Plate
1.5"
0.25" Pyrex Plate

Fig. 5

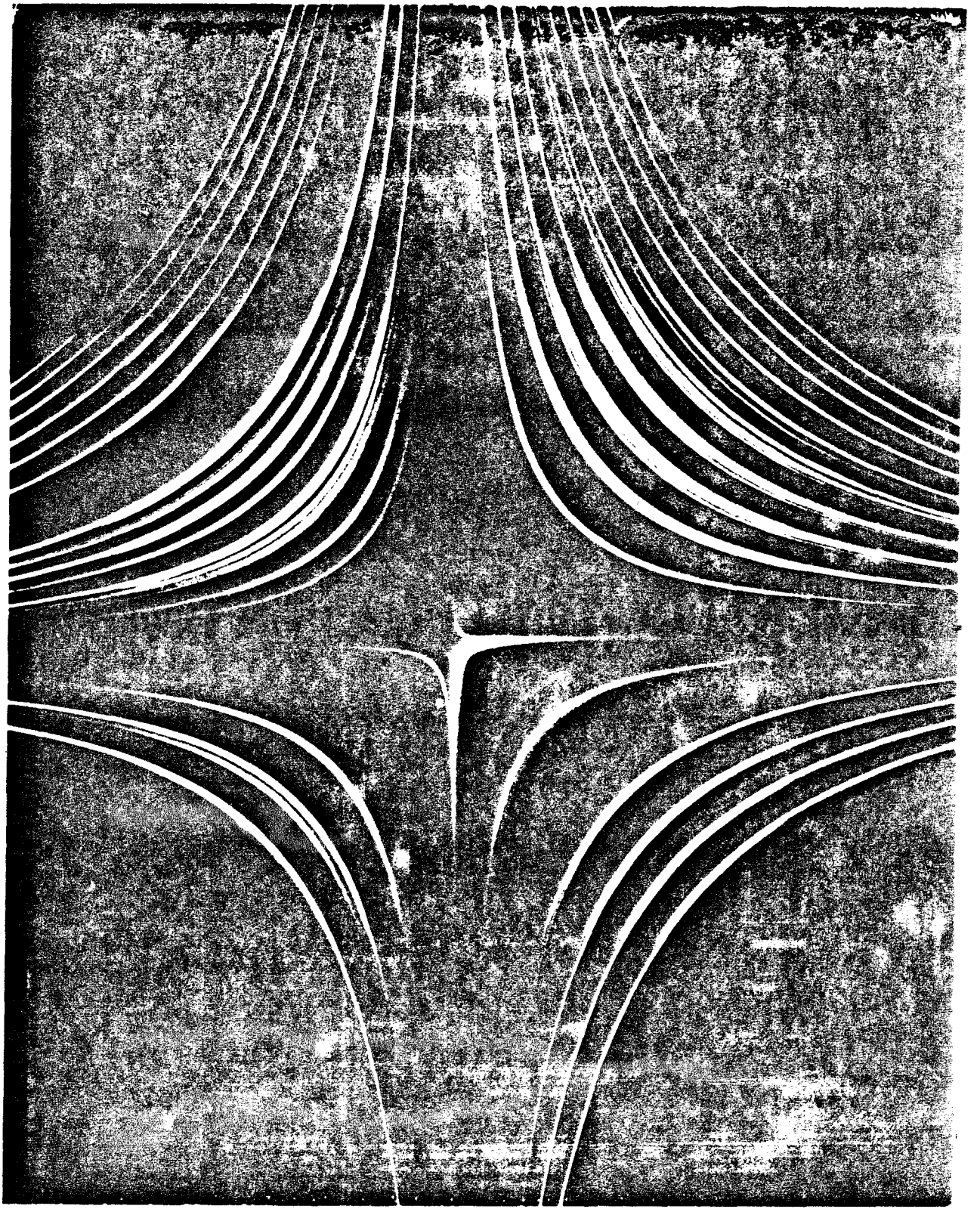

Fig. 6

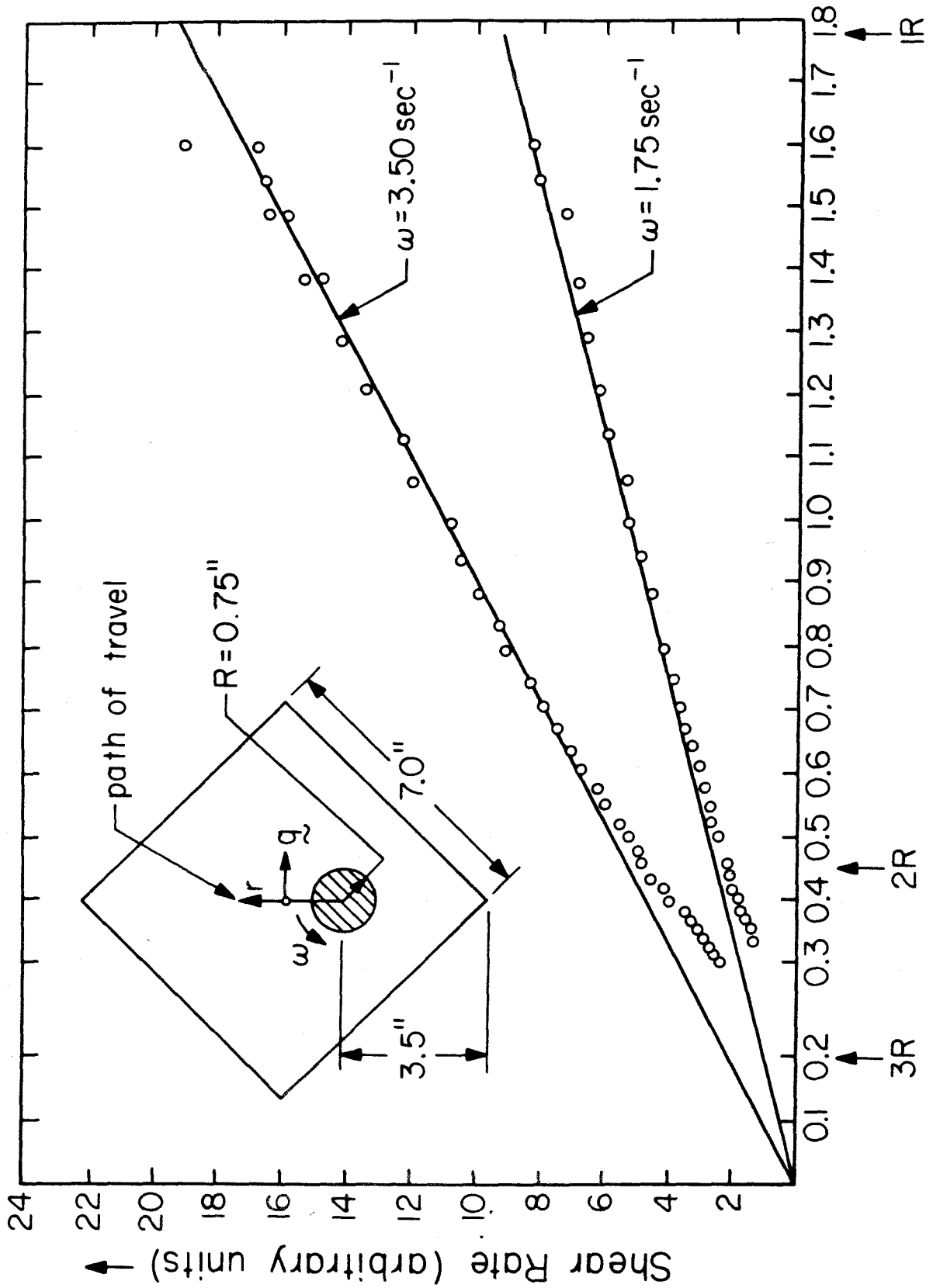
Shear Rate (arbitrary units) →
24
22
20
18
16
14
12
10
8
6
4
2
0.1
0.2
0.3
0.4
0.5
0.6
0.7
0.8
0.9
1.0
1.1
1.2
1.3
1.4
1.5
1.6
1.7
1.8
3R
2R
1R
1/r² (inches⁻²) →
ω=3.50 sec⁻¹
ω=1.75 sec⁻¹
path of travel
R=0.75"
7.0"
3.5"
r
q
ω

Fig. 7

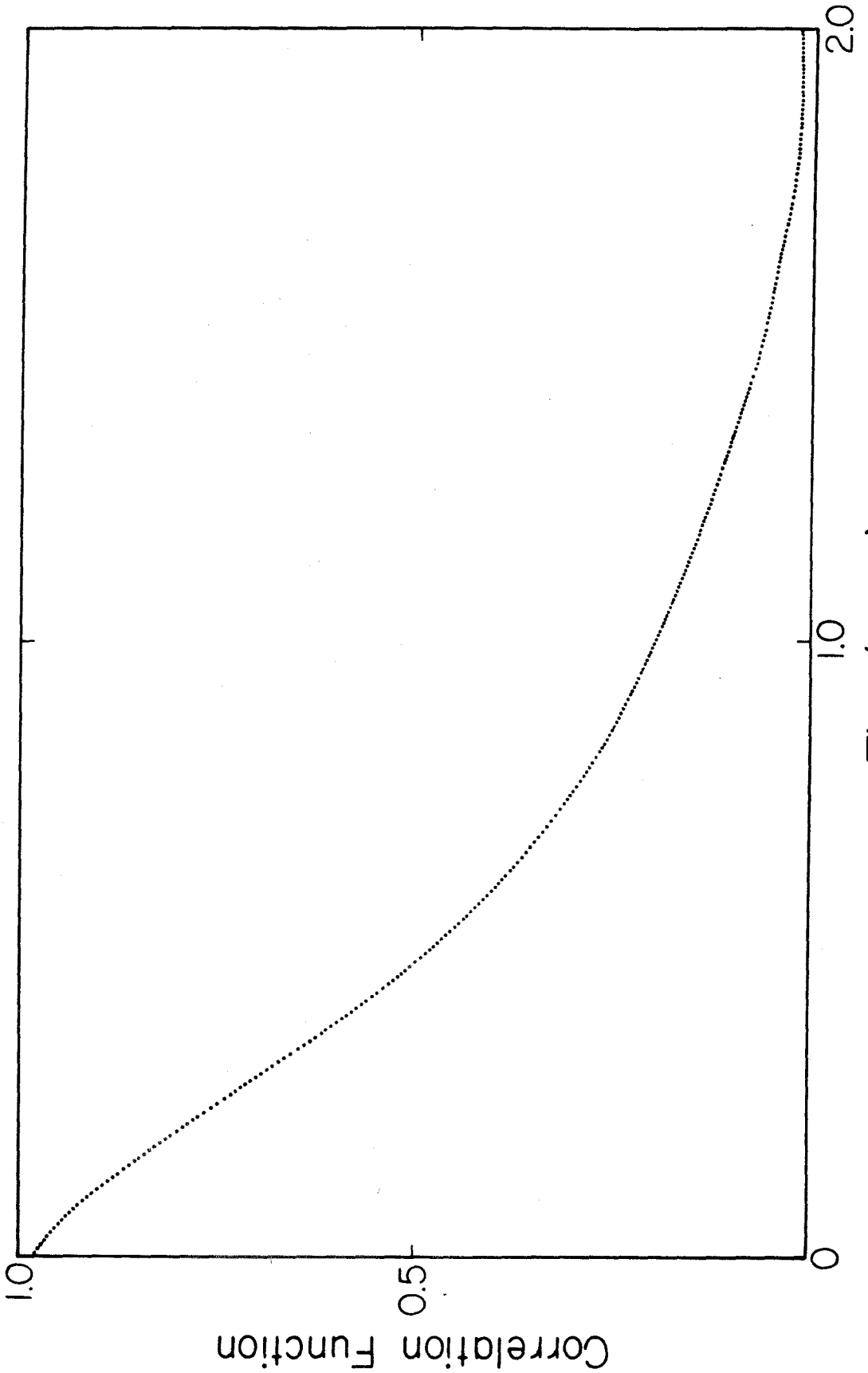

Fig. 8

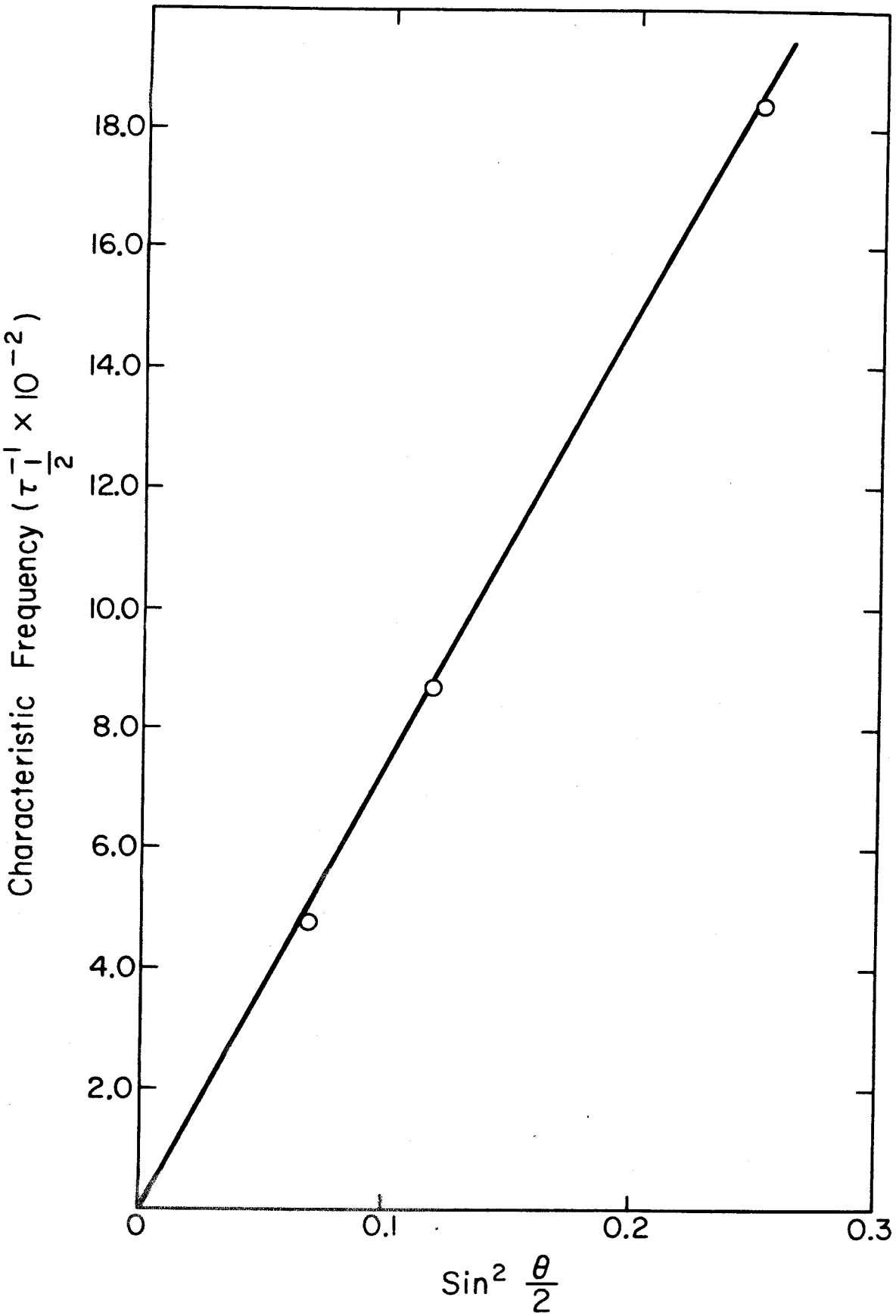
Characteristic Frequency ($\tau_{1/2}^{-1} \times 10^{-2}$)
18.0
16.0
14.0
12.0
10.0
8.0
6.0
4.0
2.0
0
0.1
0.2
0.3
$\sin^2 \frac{\theta}{2}$

Fig. 9

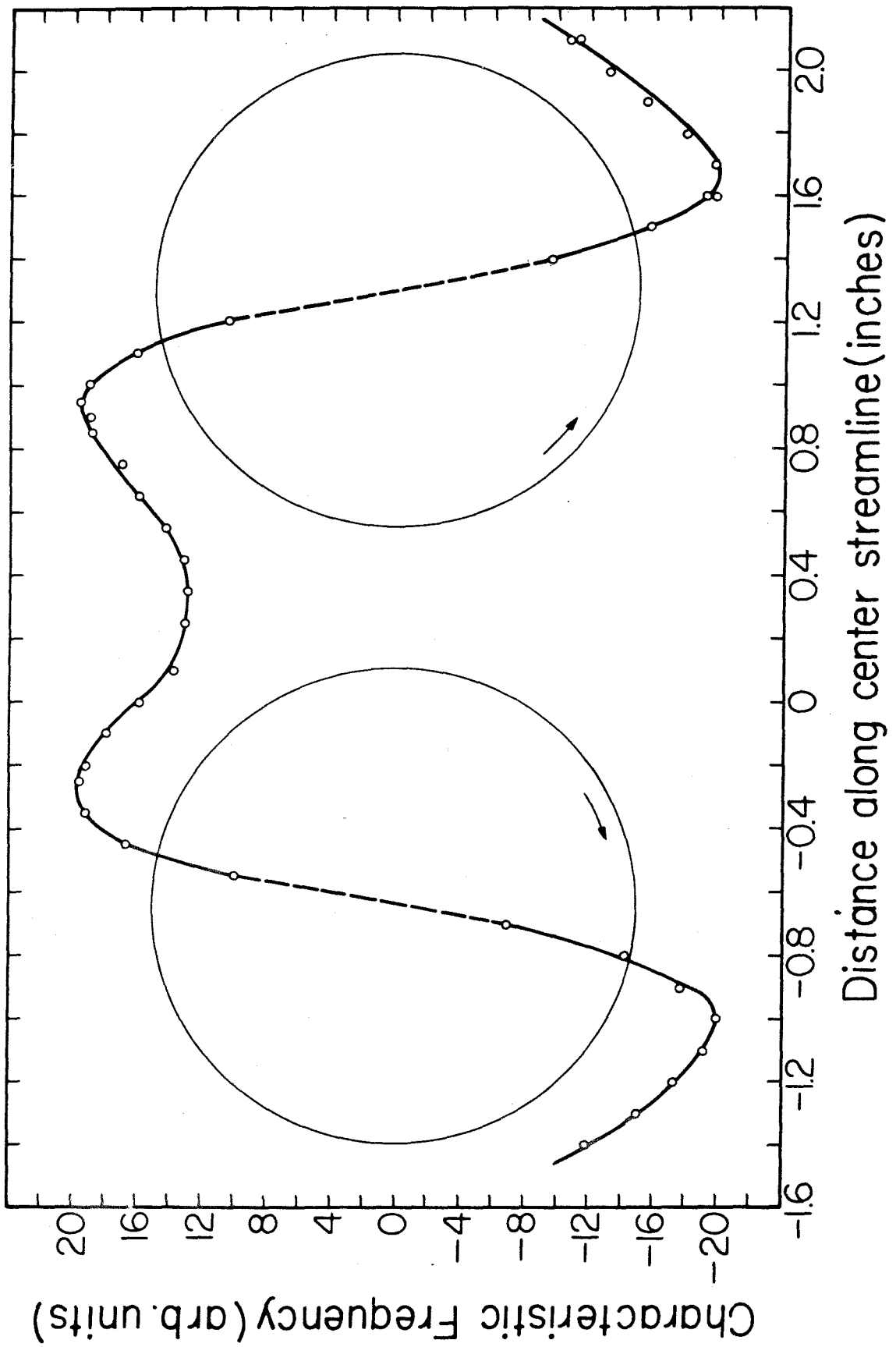
Characteristic Frequency (arb. units)
20
16
12
8
4
0
-4
-8
-12
-16
-20
-1.6
-1.2
-0.8
-0.4
0
0.4
0.8
1.2
1.6
2.0
Distance along center streamline(inches)

Fig. 10